

Springer Proceedings in Materials

R. Velmurugan  
G. Balaganesan  
Naresh Kakur  
Krishnan Kanny *Editors*

# Dynamic Behavior of Soft and Hard Materials, Volume 3

Proceedings of 13th International  
Symposium on Plasticity and Impact  
Mechanics 2022

 Springer

# Springer Proceedings in Materials

Volume 36

## Series Editors

Arindam Ghosh, Department of Physics, Indian Institute of Science, Bengaluru, India

Daniel Chua, Department of Materials Science and Engineering, National University of Singapore, Singapore, Singapore

Flavio Leandro de Souza, Universidade Federal do ABC, Sao Paulo, São Paulo, Brazil

Oral Cenk Aktas, Institute of Material Science, Christian-Albrechts-Universität zu Kiel, Kiel, Schleswig-Holstein, Germany

Yafang Han, Beijing Institute of Aeronautical Materials, Beijing, Beijing, China

Jianghong Gong, School of Materials Science and Engineering, Tsinghua University, Beijing, Beijing, China

Mohammad Jawaid , Laboratory of Biocomposite Technology, INTROP, Universiti Putra Malaysia, Serdang, Selangor, Malaysia

**Springer Proceedings in Materials** publishes the latest research in Materials Science and Engineering presented at high standard academic conferences and scientific meetings. It provides a platform for researchers, professionals and students to present their scientific findings and stay up-to-date with the development in Materials Science and Engineering. The scope is multidisciplinary and ranges from fundamental to applied research, including, but not limited to:

- Structural Materials
- Metallic Materials
- Magnetic, Optical and Electronic Materials
- Ceramics, Glass, Composites, Natural Materials
- Biomaterials
- Nanotechnology
- Characterization and Evaluation of Materials
- Energy Materials
- Materials Processing

To submit a proposal or request further information, please contact one of our Springer Publishing Editors according to your affiliation:

European countries: **Mayra Castro** ([mayra.castro@springer.com](mailto:mayra.castro@springer.com))

India, South Asia and Middle East: **Priya Vyas** ([priya.vyas@springer.com](mailto:priya.vyas@springer.com))

South Korea: **Smith Chae** ([smith.chae@springer.com](mailto:smith.chae@springer.com))

Southeast Asia, Australia and New Zealand: **Ramesh Nath Premnath** ([ramesh.premnath@springer.com](mailto:ramesh.premnath@springer.com))

The Americas: **Michael Luby** ([michael.luby@springer.com](mailto:michael.luby@springer.com))

China and all the other countries or regions: **Mengchu Huang** ([mengchu.huang@springer.com](mailto:mengchu.huang@springer.com))

This book series is indexed in **SCOPUS** database.

R. Velmurugan · G. Balaganesan · Naresh Kakur ·  
Krishnan Kanny  
Editors

# Dynamic Behavior of Soft and Hard Materials, Volume 3

Proceedings of 13th International Symposium  
on Plasticity and Impact Mechanics 2022

 Springer

*Editors*

R. Velmurugan  
Department of Aerospace Engineering  
Indian Institute of Technology Madras  
Chennai, India

G. Balaganesan  
Department of Mechanical Engineering  
Indian Institute of Technology Madras  
Chennai, India

Naresh Kakur  
Department of Materials Science  
and Engineering  
University of California  
Irvine, CA, USA

Krishnan Kanny  
Department of Mechanical Engineering  
Durban University of Technology  
Durban, South Africa

ISSN 2662-3161

ISSN 2662-317X (electronic)

Springer Proceedings in Materials

ISBN 978-981-99-6258-7

ISBN 978-981-99-6259-4 (eBook)

<https://doi.org/10.1007/978-981-99-6259-4>

© The Editor(s) (if applicable) and The Author(s), under exclusive license to Springer Nature Singapore Pte Ltd. 2024

This work is subject to copyright. All rights are solely and exclusively licensed by the Publisher, whether the whole or part of the material is concerned, specifically the rights of translation, reprinting, reuse of illustrations, recitation, broadcasting, reproduction on microfilms or in any other physical way, and transmission or information storage and retrieval, electronic adaptation, computer software, or by similar or dissimilar methodology now known or hereafter developed.

The use of general descriptive names, registered names, trademarks, service marks, etc. in this publication does not imply, even in the absence of a specific statement, that such names are exempt from the relevant protective laws and regulations and therefore free for general use.

The publisher, the authors, and the editors are safe to assume that the advice and information in this book are believed to be true and accurate at the date of publication. Neither the publisher nor the authors or the editors give a warranty, expressed or implied, with respect to the material contained herein or for any errors or omissions that may have been made. The publisher remains neutral with regard to jurisdictional claims in published maps and institutional affiliations.

This Springer imprint is published by the registered company Springer Nature Singapore Pte Ltd.

The registered company address is: 152 Beach Road, #21-01/04 Gateway East, Singapore 189721, Singapore

Paper in this product is recyclable.

# Preface

Volume 3 of Dynamic Behaviour of Soft and Hard Materials consists of chapters which are part of the papers submitted and presented at the 13th International Symposium on Plasticity and Impact Mechanics, held at Indian Institute of Technology Madras, Chennai, Tamil Nadu, India, during August 2022. These papers were reviewed by distinguished professors from leading institutions and scientists/engineers from research centres and establishments.

The book contains 29 chapters, containing different materials covering soft materials like polymer-based composites and hard materials like concrete reinforced with steel. There are papers which cover the experimental aspect of materials, some cover the theoretical aspects, and some papers consider both experimental and theoretical studies. The studies consider the different aspects of loading systems starting from quasi-static loading to high-velocity impact loading. There are some chapters which cover the thermal, high strain rate loading and other extreme loading conditions.

The book contains the topics which will be useful to the academicians, scientists/engineers, researchers and graduate students belonging to different engineering disciplines including civil, mechanical, aerospace, naval, chemical and electrical engineering. The topics are recent developments of new materials, manufacturing technologies and mechanics of materials which are very useful for many industrial applications.

Chennai, India  
Chennai, India  
Irvine, USA  
Durban, South Africa

R. Velmurugan  
G. Balaganesan  
Naresh Kakur  
Krishnan Kanny

# Contents

<b>Mechanical and Thermal Characterization of Materials</b>	
<b>Behaviour of Hard-to-Form Material in Friction Stir Incremental Forming Process</b> .....	3
D. Rajenthirakumara, R. Sridhar, N. Srinivasan, and S. Narayanan	
<b>Influence of Prestressing Force on Performance of Prestressed Concrete</b> .....	13
Vimal Kumar	
<b>Development of C<sup>1</sup> Smooth Basis in Isogeometric Analysis for Multi-Patch Domain</b> .....	23
Lokanath Barik and Abinash Kumar Swain	
<b>Modal Characterization of Additively Manufactured Chiral Structure: Suppression of Its Multiple Responses</b> .....	33
Rukmangad S. Barad, Akshay Pathania, B. K. Nagesh, and S. Anand Kumar	
<b>Premature and Extended Contact Behaviour of PA 6 and PA 6,6 Gears</b> .....	43
S. Vignesh and A. Johnney Mertens	
<b>Effect of Friction Coefficient and Feed Rates on Residual Stresses of Zr-4 Processed by Swaging</b> .....	53
Gaurav Singh, V. C. Raghuram, K. I. Vishnu Narayanan, Umesh Kumar Arora, and R. Jayaganthan	
<b>A Comparative Study of Cryorolling and Cryo-Cross Rolling Treatment on Tensile and Fracture Properties of Al 5052 Alloy</b> .....	63
Ruby Pant, Amit Joshi, Shushant Singh, Manoj Kumar Pathak, and Saurabh Gairola	

<b>A Study on Tensile Strength Attributes of Jute Fiber-Reinforced Polyester Composite</b> .....	75
B. S. Keerthi Gowda, B. E. Megha, G. L. Easwara Prasad, R. Abhishek, and R. Velmurugan	
<b>Residual Properties and Failure Characterization of Glass/Epoxy Laminates: Effect of Slender Filler Reinforcement</b> .....	99
Manoj K. Singh and R. Kitey	
<b>Potential of Development of Anti-Erosion Graphene-Reinforced Coatings for Wind Turbine Blades</b> .....	109
Nikesh Kuthe, Leon Mishnaevsky Jr., Puneet Mahajan, and Suhail Ahmad	
<b>An Entropy-Based Damage Model to Assess the Creep Behaviour of Nickel-Based Superalloys</b> .....	115
Sri Krishna Sudhamsu Kambhammettu, Ashish Pandey, and Lakshmana Rao Chebolu	
<b>Influence of Porosity and Temperature Load on Buckling Characteristics of Functionally Graded Material Plates</b> .....	123
K. Swaminathan, H. Sachin, and T. Rajanna	
<b>Experimental Investigation of the Behavior of Tubular T-Joint of Jacket Structures</b> .....	135
N. Murugan, Vadivuchezhian Kaliveeran, and Subrahmanya Kundapura	
<b>Numerical Investigation of Transient Heat Conduction Analysis in Functionally Graded Material (FGMs) Using MATLAB Partial Differential Equation (PDE) Toolbox</b> .....	147
Mansingh Yadav and Divyansh Krishana	
<b>Numerical Analysis of Structural and Thermal Characteristics of Automotive Disc Brake Rotor</b> .....	161
G. S. Abhiram, Aafis Aslam, K. Bhagavath Kumar, V. S. Amal Krishnan, and R. Kamal Krishna	
<b>Stress Analysis of Thin Rectangular Sections Subjected to Twisting Moment</b> .....	179
Saiarpan V. Joshi and Vadivuchezhian Kaliveeran	
<b>Stress Analysis of a Member of Jacket Structure with Different Types of Stiffeners</b> .....	193
T. S. Sreejith and Vadivuchezhian Kaliveeran	
<b>Structural Analysis of Non-prismatic Column Using Finite Element Approach</b> .....	205
Gautam Kumar and Vadivuchezhian Kaliveeran	



**2D and 3D Numerical Investigation of Delrin Spur Gear** ..... 217  
 A. P. Sugunesh and A. Johnney Mertens

**Study of Solid Particle Erosion Behaviour of Uncoated Superalloys of Turbine Application** ..... 227  
 M. S. Vinod Kumar, R. Suresh, N. Jagadeeswaran, and BSKeerthi gowda

**Evaluation of the Compression Properties of 3D Printed EPA-GF TPMS Structures** ..... 237  
 S. Jeyanthi, R. Prabhu, R. Arunkumar, Nivedhitha Ramesh, S. Vinoth Kumar, and L. Prince Jeya Lal

**Analysis and Design of Pre-engineered Building Structure Using SAP2000** ..... 251  
 Mrunali Surpam and Archana Tanawade

**Applicability of Meshfree Method in Computational Solid Mechanics** ..... 263  
 Kichu Paul and K. S. Babu Narayan

**Thermal Degradation of Kinetics of PET, PTT and PBT Hybrid Nanocomposites** ..... 275  
 Abjesh Prasad Rath, P. Santhana Gopala Krishnan, and K. Kanny

**Residual Stress Analysis of Additively Manufactured and Post Processed Inconel 718** ..... 287  
 O. V. Mythreyi and R. Jayaganthan

**Determination of Crystallinity of Natural Fibers—A Study with Spectroscopy** ..... 293  
 Akula Komuraiah, B. Satish Kumar, K. Shanker, N. Shyam Kumar, and B. Durga Prasad

**Studies on Thermal, Mechanical, and Morphological Properties of Aged XLPE Cables** ..... 311  
 Priya Selvamany, Gowri Sree Varadarajan, Naresh Chillu, Ramanujam Sarathi, Rengaswamy Jayaganthan, and Raman Velmurugan

**Numerical Investigation of Vertical Roller Mill Operation Using Discrete Element Method** ..... 323  
 Vinoth Dhanasekaran, Velmurugan Ramachandran, Praveenkumar Vijayakumar, and Harikrishnan Krishnamoorthy

**Effect of Gamma Irradiation on Mechanical and Thermal Properties of 3D-Printed PLAs** ..... 335  
 V. Yogeshwaran, J. Chandradass, M. Chinnapandi, and R. Velmurugan

# About the Editors

**Dr. R. Velmurugan** is Senior Professor of Aerospace Engineering at Indian Institute of Technology (IIT) Madras. His areas of research include composite materials, nano-materials, finite element analysis, structural crashworthiness, and impact mechanics. He has completed many consultancy and sponsored projects from DRDO Labs, ISRO centers, Government agencies, and Private industries. He has made numerous research articles in international journals and conferences and guided many students for Ph.D., M.S., and M.Tech. degrees. He has delivered invited lectures in many international and national conferences. He is Fellow of Aeronautical Society of India and Institution of Engineers and served as Member of the Editorial Board, for several journals of national and international repute.

**Dr. G. Balaganesan** pursued his bachelor's and master's in mechanical engineering and Ph.D. in aerospace engineering from the Indian Institute of Technology (IIT) Madras. He has more than 30 years of experience in the field of manufacturing and teaching. His active research is in the field of impact loading and repair of oil and gas pipelines using advanced composite materials. He has published 40 international peer-reviewed journal papers. He has presented his research work in more than 30 international conferences. He has filed 6 patents, and some of them are products of start-up companies incubated at IIT Madras. He is instrumental in setting up laboratory facilities of new IITs such as IIT Hyderabad in 2008, IIT Palakkad and Tirupati in 2015, and IIT Jammu in 2018. He has served as Faculty Member on deputation at the Department of Mechanical Engineering, IIT Jammu, from 2018 to 2020.

**Dr. Naresh Kakur** is currently Postdoctoral Scholar at the Department of Materials Science and Engineering, University of California, USA. He completed his dual degree (M.S. + Ph.D.) course at the Department of Mechanical Engineering, Indian Institute of Technology (IIT) Madras. His area of interest is on impact properties of bio-inspired glass/epoxy composites for wind turbine blade applications in collaboration with Helicoid Industries Inc. He has more than 40 research and review articles published in journals and conferences of national and international repute.

**Prof. Krishnan Kanny** holds a Ph.D. in Engineering and Science from TU, Alabama USA and an M.Sc. from *UKZN*, South Africa. He is professionally registered with the Engineering Council of South Africa (*ECSA*) and is a member of *SAIMechE*, *ASME*, and *AIAA*.

His areas of research is in Light Weight Materials and Nanotechnology. His interests are designing, processing, and testing of composite materials systems, reinforced thermosets, thermoplastics, and nano-infused structures for aerospace, naval and automotive applications.

Additionally, he is involved in computational and analytical modelling. Characterization & Morphological analysis include Scanning Electron Microscopy, Transmission Electron Microscopy, and X-ray Photoelectron Spectroscopy.

Professor Kanny is a recipient of many awards, amongst them is the Chair Professorship from the MG University in India.

# **Mechanical and Thermal Characterization of Materials**

# Behaviour of Hard-to-Form Material in Friction Stir Incremental Forming Process



D. Rajenthirakumara, R. Sridhar, N. Srinivasan, and S. Narayanan

**Abstract** The application of light metal alloys such as magnesium, aluminium and titanium alloys are expanding to reduce weight of various industrial products. As a result of a combination of attributes like corrosion resistance, high strength-to-weight ratio and biocompatibility, these materials are employed in diverse engineering applications. But it is difficult to form these materials at room temperature due to its high specific strength. Friction stir incremental sheet forming is a promising method for forming metal sheets, by which parts can be manufactured without the use of dedicated dies. In this work, the behaviour of titanium (hard-to-form material) formability is investigated using friction stir incremental forming process, in which forming is done under localized friction heating caused by high tool rotation. Series of experiments with cranial plate-forming process is carried out in a vertical machining centre with grade 5-Ti-6Al-4V alloy sheets of size 300 mm × 300 mm × 1.2 mm with hemispherical end forming tool. To determine the formability of the material, Erichsen cupping test is performed using cupping testing machine and the Erichsen cupping index is found. The effect of key process parameters, namely the rotation speed, the feed rate and the step depth is investigated. The mechanism for the enhanced mechanical properties during friction stir increment forming is addressed. The interactive effect of process parameters on mechanical properties of formed parts is studied because mechanical properties are key factors for evaluating the product performance before industrial applications. This work addressed the key issues encountered by researchers worldwide on friction stir incremental forming and it will provide useful guidance in improving the product quality formed by friction stir incremental sheet forming.

**Keywords** Forming · Formability · Friction stir · Incremental

---

D. Rajenthirakumara (✉) · R. Sridhar · S. Narayanan  
Department of Mechanical Engineering, PSG College of Technology, Coimbatore 641 004, Tamil Nadu, India  
e-mail: [drk.mech@psgtech.ac.in](mailto:drk.mech@psgtech.ac.in)

N. Srinivasan  
Department of Mechanical Engineering, Jansons Institute of Technology, Coimbatore 641 659, Tamil Nadu, India

## 1 Introduction

Incremental forming is a die-less technology for forming sheet metal. In this process, a sheet is essentially formed by the application of a small punch driven by a standard CNC milling machine. There are, however, several process issues that still need to be improved before a wider incremental forming industrialization can take place [1]. In the recent year, the capability of incremental forming in fabricating hard-to-form alloys has been investigated, by testing differing hybrid variations of the process. These variations involved heat-assisted forming. However, mindful of the objectives of maintaining process flexibility and cost efficiency, a direct heating method called friction stir incremental forming [2] is utilized in this research work. This method entails embossing the sheet by means of a tool spinning at relatively high speeds, causing frictional heating of the sheet. The inadequate geometric accuracy, excessive thinning and dissatisfied formed mechanical properties of this process still hindering its wide industrial application. Although substantial research work has been conducted on friction stir incremental forming, the interactive effect of process parameters has had little attention.

Further, the applications of this approach are mainly found in technical literature that focuses on aluminium and steel sheets [3]. There is a dearth of information on hard-to-form materials such as titanium alloys. This research work experimentally investigates friction stir incremental forming of titanium, while considering reasonable settings for the process variables. In the recent year, the capability of incremental forming in fabricating hard-to-form alloys has been investigated, by testing differing hybrid variations of the process [4–11]. These hybrid techniques exhibited significant improvements in material formability, but there is a substantial increase in the process complexity. However, in this work, a direct heating method called friction stir incremental forming [2] is utilized for maintaining flexibility. Further, so far, the applications of this approach are mainly focuses on aluminium and steel sheets. There is a dearth of information on hard-to-form materials such as titanium alloys. Although substantial research work has been conducted on the thickness distribution [12–14], the interactive effect of process parameters has had little attention. In addition, the mechanical properties of the sheet material after the process have not received sufficient attention yet. Therefore, in this work, experiments are planned to study the interactive effect of process parameters.

## 2 Illustrations

Ti-6Al-4V (Grade-5) sheet of dimension 300 mm × 300 mm × 1.2 mm with Rockwell hardness of 36 HRC is used in this study. It consists of 6% of aluminium, 4% of vanadium and remaining of titanium. Experiments are carried out in three axes vertical machining centre (Fig. 1) with clamping and backing plate of dimensions

300 mm × 300 mm × 20 mm. In order to clamp the sheet, four holes across the corner of the sheet is made using CNC laser cutting machine.

The fixture is then mounted on the machine table of VMC and the sheet metal is clamped in between the base plates on the fixture as shown in the Fig. 1. Then the tool is mounted on the collet chuck of spindle and centred with respect to the fixture and the forming process is carried out with initial lubricant (Beruplex LI-EP 2) in the surface of the sheet. In this work, a rigid tool with hemispherical end is used to deform the sheet into the desired shape. It helps in increasing the contact area of tool and will increase the overall formability of the sheet because of the friction caused. The forming tool made of high speed steel with diameter 25 mm (Fig. 2) is used for initial experimental work. For the subsequent experimental work, to ensure a wear-free tool, the same tool subjected to turning followed by chrome plating and buffing processes. Table 1 gives the input process parameters [rotation speed (n), feed rate (f) and the step size ( $\Delta z$ )] used for the experimental work.

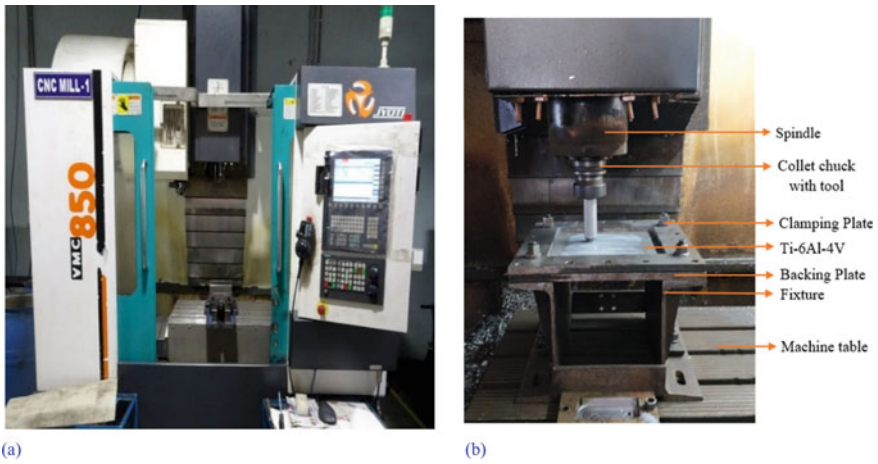


Fig. 1 Depiction of the forming setup: CNC table (a) and fixture (b)

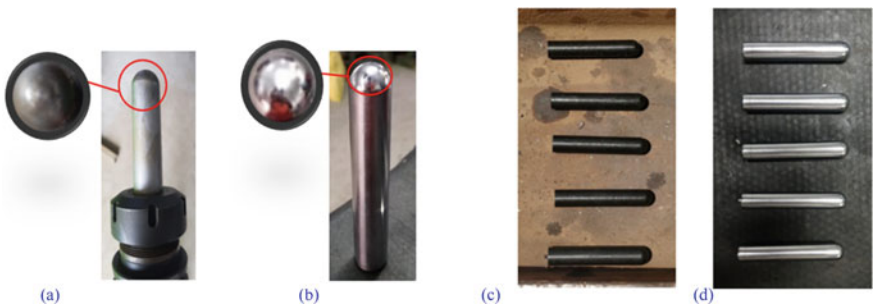


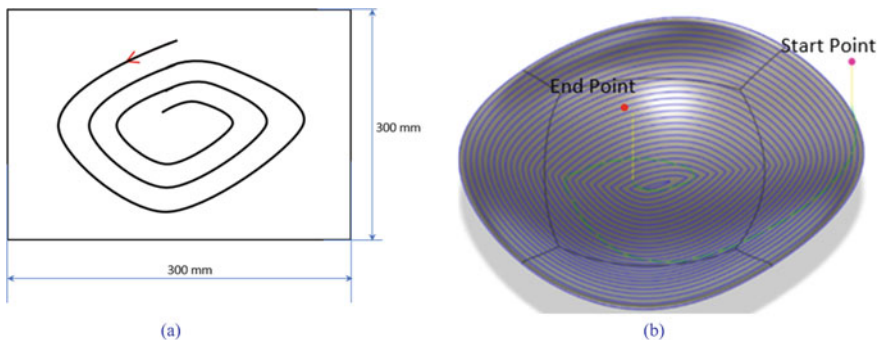
Fig. 2 Forming tools—tool tip condition before (a, c) and after buffing and other processes (b, d)

**Table 1** Process parameters used for the experimental work

Experimental trial no.	Sheet thickness (t) mm	Rotational speed (n) rpm	Feed rate (f) mm/min	Step size ( $\Delta z$ ) mm	Tool diameter (d) mm
1	1.2	1900	1050	0.4	25
2	1.2	500	1500	0.2	25
3	1.2	300	800	0.1	25
4	1.2	2000	1050	0.3	12

Regarding tool path and NC code (Fig. 3), a cranial plate with appropriate dimensions is used as the profile for this work. Model of cranial plate is developed using Fusion-360 software. The tool path is a crucial feature in determining the dimensional accuracy, trail time and surface quality. Contour tool path is chosen for this work as it has less lead time for the cranial plate geometry than the other tool paths. The contour tool path trails much like a topographic map, moving along a series of paths at incremental heights (step size). Master Cam software is used to generate contour tool path to develop the cranial plate, with appropriate parameters. The tool path is generated by input values such as plunge feed rate, spindle speed, step size and feed rate. The generated tool path was then converted to NC code using Master Cam, and the forming tool moved along this pre-defined path with given input parameters during the forming process.

The Erichsen cupping test [15] is used to evaluate the formability of a material. In this work, the Ti-6Al-4V (Grade-5) sheet is cut into 75 mm  $\times$  75 mm using wire EDM (MV2400S) and then punch of diameter 20 mm is used to force the sheet (1.2 mm), which is clamped between the frames or die, and the wheel is rotated until it touches the sheet. Then, the scale attached to the wheel is set to zero, and then a force is applied on the sheet through the cupping punch. A mirror is placed behind the punch and sheet to observe crack and know, where the force is to apply on a

**Fig. 3** Forming Illustration of tool path and its direction



punch and the scale is attached to the wheel to measure the depth of indent (Erichsen cupping index) in millimetres which is found to be 5.36.

### 3 Results and Discussion

In this work, three main process parameters are considered, namely rotational speed ( $n$ ), feed rate ( $f$ ) and step size ( $\Delta z$ ). The sheet material and its thickness are kept constant.

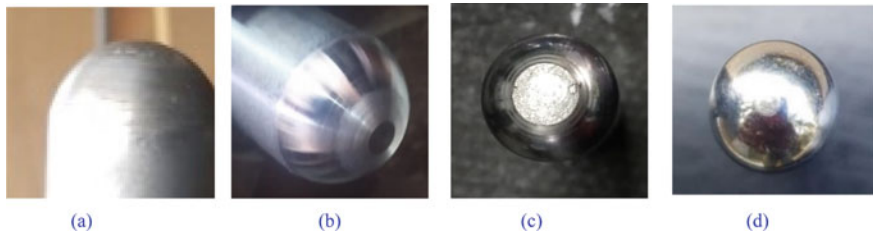
#### 3.1 Effect of Tool Rotational Speed

In this work, different rotational speed is chosen for each experimental trail. In the first trail, the experiment is carried out with the rotational speed ( $n$ ) of 1900 rpm, no overheating observed until the depth of 4 mm, but after that as the depth started to increase, there was a significant amount of heating observed and then conspicuously fire was observed after the depth of 6 mm; when the plunge took place. Due to the fire, the sheet was failed at the depth of 10.3 mm with poor surface finish which is observed through the naked eye (Fig. 4). During the start of the experiment, Beruplex LI-EP 2 (Lithium-based lubricant) is used, and once after the fire caused, coolant (WS 600N) is used but still the flame did not abate and so the sheet is failed. The tool tip faced just a minor wear.

As the rotational speed combined with the step size had a direct impact on the roughness of the surface, the rotational speed is reduced and set as 500 rpm in the second experimental trail. Due to this, there is a noteworthy improvement in the surface roughness, and as the rpm is low, there is no flame noted in the sheet but there was a minimal amount of heating which is somewhat nullified using the running coolant and the lubricant. Although there was a good improvement in the surface



**Fig. 4** Failure of sheet due to crack



**Fig. 5** Tool wear condition(s)

finish, the sheet failed at the depth of 7.6 mm due to the flatness of the tool tip (Fig. 5) which is resulted due to the low rpm and high step size. In the third experimental trail, the rotational speed is further reduced to 300 rpm. As the result of this, the tool became completely flat and the sheet failed due to the circumferential cracks at the depth of 7.3 mm.

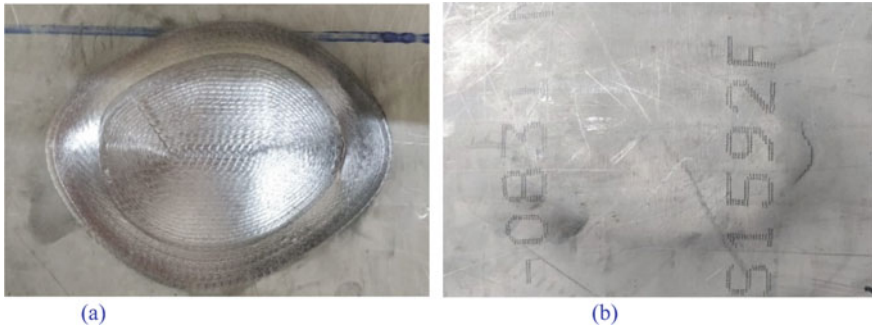
To improve the depth as well as the surface roughness of the sheet, the step NC programme is introduced to replace the tool in a uniform forming depth interval by demounting the tool and mounting a new tool in the fourth experimental trail. The rotational speed is increased to 2000 rpm. At the initial stages, average surface finish is observed and there is not even a minimal amount of heat. At the depth of 5 mm, there is a minor tool wear due to the high rotational speed and so it is replaced with the new one. However, a circumferential crack is observed at the sheet at 5.8 mm depth.

### **3.2 Effect of Feed Rate and Step Size**

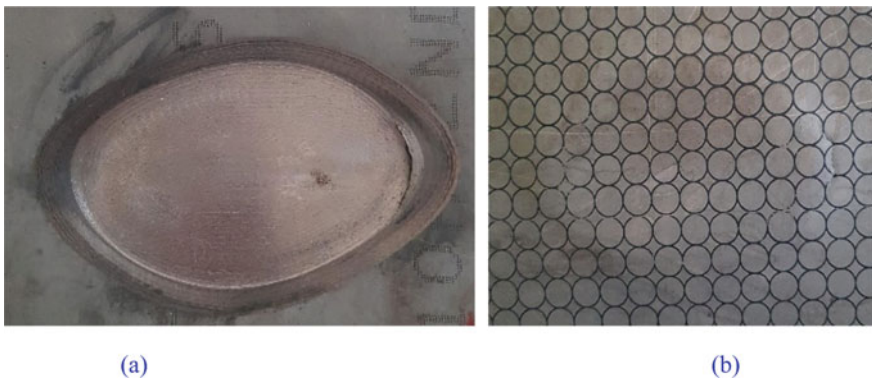
The feed rate and step size played a major role in determining the cycle time of the process. In the initial experimental work, the feed rate ( $f$ ) of 1050 mm/min and step size ( $\Delta z$ ) of 0.4 mm are used as the parameters. Here as the step size and feed rate are high, the total processing time is low, but with increased step size and feed rate, flame is noticed after a certain depth at the initial stages of the plunge and also the surface roughness is very poor.

In the later stages of the experimental work (Fig. 6), step size ( $\Delta z$ ) is reduced to 0.2 mm but the feed rate is increased to 1500 mm/min. As the step size is low the total processing time is high. The surface roughness value is improved when compared to the first experimental trail and also there is no significant heating observed. The improved surface roughness in this trial is due to the decreased step size. The sheet failed at 7.6 mm and the processing time at the time of failure is low.

In the third experimental trail (Fig. 7), the surface finish is very much improved because of the low step size of 0.1 mm and feed rate of 800 mm/min, but the total cycle time is increased. The sheet failed at 7.3 mm and the trail time at the time of failure is also in the higher side. But the tool is subjected to significant tool wear.



**Fig. 6** Results obtained from second experimental trial

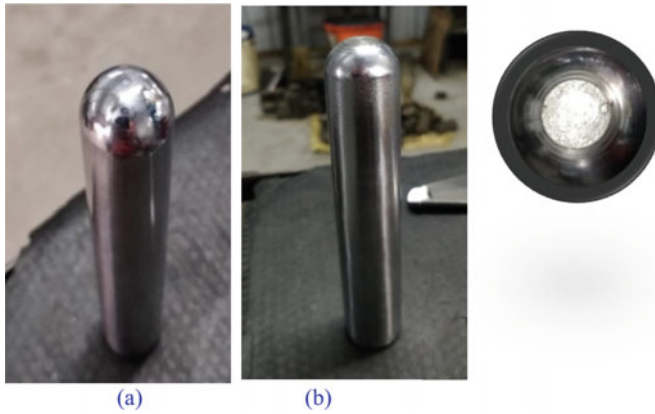


**Fig. 7** Results obtained from third experimental trial

The tool condition before and after forming is depicted in the Fig. 8. As the step size and feed rate are increased to 0.3 and 1050 mm/min in the fourth trial, there is an acceptable level of surface finish but still the total cycle time is high because of the reduction of the tool diameter from 25 to 12 mm. The sheet is failed at 5.8 mm due to the circumferential crack.

### **3.3 Effect of Tool Diameter and Friction**

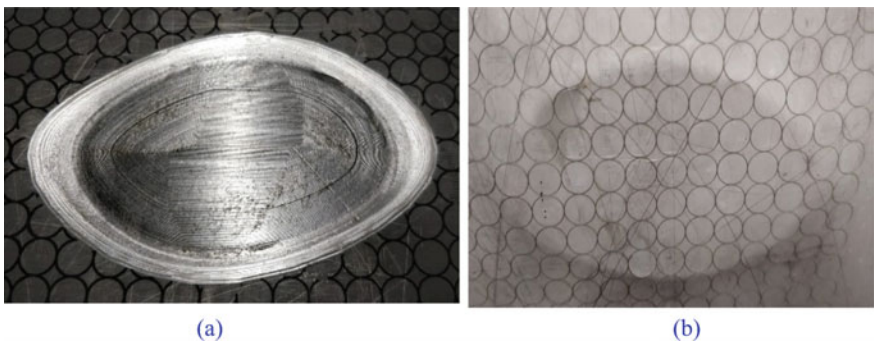
Overall, after performing the four experimental trials, it is inferred that if the rpm is low, amount of friction is at lower side and as a result minimal amount of heat is generated. During the fourth experimental trail (Fig. 9), when the tool diameter is changed to 12 mm, the area of contact reduced compared the tool of diameter 25 mm. This reduction in area of contact at the interface reduced the friction which resulted



**Fig. 8** Tool wear conditions–before (a) and after forming (b) process

in no overheating at the work piece and therefore it is observed that outer profile of cranial plate is better than other three trails but with average surface finish.

It is also inferred from first experimental trail that the flame caused at the interface due to very high amount of local friction generated between tool and the work piece will increase the tool wear and thus affects the surface finish and geometrical accuracy of the final part. This is prevented in successive trails by the use of lubricant and coolant which lowered the friction. As inferred from the available literature, if the rotational speed is increased above 2000 rpm for Ti-6Al-4V (Grade-5), it will result in sticking of titanium to the tooltip and in the worst-case scenario, friction welding of titanium sheet to the tooltip occurs. This is completely eliminated in all the experimental trails by using optimal process parameters, lubricant and running coolant.



**Fig. 9** Results obtained from fourth experimental trial

## 4 Conclusions

This work experimentally investigated the effect of process parameters in friction stir incremental forming of Ti-6Al-4V alloy sheets. The influences on the forming output of three key process parameters, namely the rotation speed ( $n$ ), the feed rate ( $f$ ) and the step size ( $\Delta z$ ), are studied along with the analysis of formability of Ti-6Al-4V with different tool diameters. Based on the experimental results obtained, the following conclusions are made: (i) tool rotation speed is a critical process parameter as it causes elevated temperature at the interface resulting in increase of the formability (ii) lubricant and running coolant are required to overcome the minimal amount of flame caused at the interface by high tool rotation speed and step size (iii) increased step size and feed rate helped to achieve maximum depth in cranial plate with a minimal amount of time but the surface roughness is very poor, inversely by decreasing step size and feed rate, good surface finish is obtained but the forming time was inflated (iv) using a smaller diameter tool with high tool rotation rate produces better outer profile (cranial plate) and resulted in low tool wear than larger diameter tool due to low area of contact but the sheet failed at a minimal depth.

Further, the cranial plate is not completely formed due to the circumferential cracks observed in all the four experimental trails. This occurrence of circumferential cracks can be related with the available literatures. It may be concluded that the titanium sheet with optimal thickness value of 1 mm will be used to form various complex parts by using friction stir incremental forming.

**Acknowledgements** The authors gratefully acknowledge the financial support of Department of Science and Technology [DST/TDT/AMT/2017/018(G)], Government of India and PSG college of Technology, Coimbatore, Tamil Nadu, India.

## References

1. Allwood JMM, Duncan SRR, Cao J, Groche P, Hirt G, Kinsey B, Kuboki T, Liewald M, Sterzing A, Tekkaya AEE (2016) Closed loop control of product properties in metal forming CIRP. Ann Manuf Technol 65(2):573–596
2. Buffa G, Campanella D, Fratini L (2013) On the improvement of material formability in SPIF operation through tool stirring action. Int J Adv Manuf Technol 66(9–12):1343–1351
3. Otsu M, Katayama Y, Muranaka T, Otsu TMM, Katayama Y (2014) Effect of difference of tool rotation direction on forming limit in friction stir incremental forming. Key Eng Mater 622(623):390–397
4. Fan G, Gao L (2014) Mechanical property of Ti-6Al-4V sheet in one-sided electric hot incremental forming. Int J Adv Manuf Technol 72(5–8):989–994
5. Fan G, Gao L, Hussain G, Wu Z (2008) Electric hot incremental forming: a novel technique. Int J Mach Tools Manuf 48(15):1688–1692
6. Fan G, Sun F, Meng X, Gao L, Tong G (2009) Electric hot incremental forming of Ti-6Al-4V titanium sheet. Int J Adv Manuf Technol 49(9–12):941–947
7. Liu R, Lu B, Xu D, Chen J, Chen F, Ou H, Long H (2016) Development of novel tools for electricity-assisted incremental sheet forming of titanium alloy. Int J Adv Manuf Technol 85(5–8):1137–1144

8. Mohammadi A, Vanhove H, Van Bael A, Duflou JR (2013) Influence of laser assisted single point incremental forming on the accuracy of shallow sloped parts. *NUMISHEET 2014*:864–867
9. Duflou JR, Callebaut B, Verbert J, De Baerdemaeker H (2007) Laser assisted incremental forming: formability and accuracy improvement. *CIRP Ann Manuf Technol* 56(1):273–276
10. Ambrogio G, Gagliardi F, Chamanfar A, Misiolek WZ, Filice L (2017) Induction heating and cryogenic cooling in single point incremental forming of Ti-6Al-4V: process setup and evolution of microstructure and mechanical properties. *Int J Adv Manuf Technol* 91(1–4):803–812
11. Grün PA, Uheida EH, Lachmann L et al (2018) Formability of titanium alloy sheets by friction stir incremental forming. *Int J Adv Manuf Technol* 99:1993–2003
12. Fan G, Li G (2014) Mechanical property of Ti-6Al-4V sheet in one sided electric hot incremental forming. *Int J Adv Manuf Technol* 72(5–8):989–994
13. Jeswiet J, Micari F, Hirt G, Bramley A, Duflou J, Allwood J (2005) Asymmetric single point incremental forming of sheet metal. *CIRP Ann Manuf Technol* 54(2):623–649
14. KimYH PJJ (2002) Effect of process parameters on formability in incremental forming of sheet metal. *J Mater Process Technol* 130:42–46
15. Cheong Z, Sorce FS, Ngo S, Lowe C, Taylor AC (2021) The effect of substrate material properties on the failure behaviour of coatings in the Erichsen cupping test. *Progr Org Coat* 151

# Influence of Prestressing Force on Performance of Prestressed Concrete



Vimal Kumar

**Abstract** In the present study, the performance of square prestressed concrete plates was investigated against drop impact. All the plate specimens were cast using the same concrete having 28 day's strength of  $48 \text{ N/mm}^2$ . The span length of the plates and thickness was kept the same for all the plates as 0.80 m and 0.10 m, respectively. The level of prestress in the plates varied between 0 and 30%. A known mass of 242.8 kg was lifted to 0.5 m and 1.0 m height and dropped freely to hit the target plates. The deflection, impact force, reaction, damage and energy absorbed were obtained through different sensors and studied. The finite element (FE) simulation of the problem was also carried out to understand the mechanics of deformation and for the reproduction of experimental findings. The metal plasticity and Holmquist-Johnson-Cook (HJC) models were used for steel (for tendon and reinforcement) and concrete, respectively. The prestress in the plates was noticed to have reduced the magnitude of deflection such that the highest deflection was noticed in plates with 0% prestress followed by 20% prestress and 30% prestress. The flexural deformation was dominant in plate having 0% prestress, while plates with 20% and 30% prestress have pronounced splitting damage. The energy absorbed by the plates induced with 20 and 30% prestress was found 5.4 and 6.3% higher compared to the plate with 0% prestress. The finite element simulation reproduced the response of the plates with a good correlation.

**Keywords** Prestressed concrete · Drop impact · Damage · Energy absorption · Finite element simulation

---

V. Kumar (✉)

Department of Civil Engineering, National Institute of Technology Hamirpur, Hamirpur 177005, India

e-mail: [panchariya.vimal@gmail.com](mailto:panchariya.vimal@gmail.com); [vimalkumar@nith.ac.in](mailto:vimalkumar@nith.ac.in)

## 1 Introduction

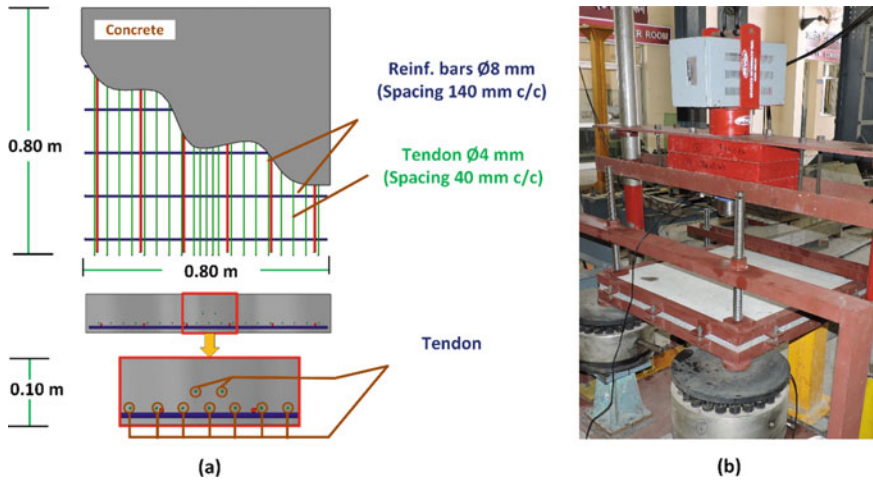
The prestressed concrete is a form of concrete in which internal compressive stresses of the desired extent are developed and distributed before it is subject to service load. The stresses thus induced usually balance the tensile stresses from external loading to a desired magnitude. The concrete has deficient tensile resistance which drove the idea for the development of prestressed concrete. This improved form of concrete, i.e., prestressed concrete makes it suitable for the construction of long-span bridges, slender members, lighter members, tanks and reservoirs, containments, railway sleepers, etc. Despite the significant applications of prestressed concrete in common as well as strategic structures of any nation, only limited research was carried out on the performance of prestressed concrete. Also, the available studies on prestressed concrete are primarily focused on the performance of prestressed concrete sleepers [1, 2]. The available studies on impact performance of concrete mostly targeted the reinforced concrete, fiber-reinforced concrete, high performance concrete, etc. The impact tests were performed on Preplaced Aggregate Fibrous Concrete (PAFC) and Slurry Infiltrated Fibrous Concrete (SIFCON) discs considering steel hooked end (2.5%) and macro polypropylene (8.0%) fibers [3]. The study reported up to 51% reduction in failure impact numbers for notched specimens compared to no-notch specimens. The performance of reinforced concrete beams and ultra-high-performance concrete (UHPC) strengthened-reinforced concrete beams was investigated under impact load [4]. The beams with UHPC attached to tension surface had shown the shear failure and reduced deflection instead of spalling of concrete. The influence of plastic waste (0–40%) on the engineering properties of concrete was studied under impact loading [5]. The study reported improved bending load, impact tub and inertia load for up to 20% replacement of fine aggregate with plastic waste. The response of Functionally graded Preplaced Aggregate Fibrous Concrete (FPAFC) employed with steel and polypropylene fibers was investigated under impact loading [6]. The study reported reduced impact strength for two-layer FPAFC compared to single layer concrete however which was governed by the proportion of steel and polypropylene fibers. The impact resistance of micro-steel fiber-reinforced self-compacting concrete was investigated under impact loading [7]. The failure modes, peak stress, impact resistance, ductility peak strain and elastic modulus of self-compacting concrete were influenced by strain rate and steel fibers content [7–9]. The improvement in the engineering properties was noticeably higher at failure stage than at cracking stage [7]. The performance of fire exposed specimens was investigated under impact loads [10] reported 80% loss in cracking and failure impact resistance when the concrete was exposed to 200 °C, and complete loss for the concrete exposed to 400–600 °C depending upon the compressive strength of concrete. In another study [11], the toughness of the concrete increased under impact loading due to inclusion of waste rubber in concrete mix. In another study [12], the use of nano-silica in concrete showed adverse effect on the engineering properties of concrete under impact loading when the amount of nano-silica was more than 2%.



Generally, it is assumed that the higher the prestress level, the better will be the performance of the specimen. But, it is not a universal fact. The stiffness of a structural member and its performance depends on many factors/parameters, their magnitudes and their combinations. Some of the factors may be length and thickness of the specimens; diameter, quantity, arrangement, strength and material of reinforcement and tendon; boundary conditions, bond strength, etc. For example, one typical failure mode of prestressed concrete is the ultimate sudden loss of prestress because of the fracture of tendons. Under this failure, the prestressed concrete would have a sudden reduction in strength and consequently result in sudden failure of the plates. Thus, the prestressed concrete under ultimate loss of prestress could become more dangerous compared to the plates with no/zero prestress. Although the ultimate failure was not observed in the present study; but it can occur for some combinations of parameters. Therefore, the presumption that the high prestress will always improve the overall performance of the concrete is not a universal conclusion. Also, it should not be assumed in absence of sufficient experimental results. In addition, the set of parameters and their magnitudes, for which the prestressed concrete would have better performance (compared to no prestress) under impact and vice versa, is not reported in the available literature. Hence, huge information is missing about their performance. As limited studies are available in the literature, an attempt is made in the present study to explore the performance of prestressed concrete plates against drop impact. The effects of magnitude of prestress in the concrete and height of drop were studied on deformation of the plate, impact force, reaction and energy absorption through experimental and finite element simulation. The metal plasticity and Holmquist-Johnson-Cook (HJC) models were used for steel and concrete, respectively, in the FE study.

## 2 Experimental Methodology

The experiments were performed on square prestressed concrete plates. The span of the plates was 0.80 m and the thickness was 0.10 m. The plates were cast using the same concrete having 28 day's strength of 48 N/mm<sup>2</sup>. The Ordinary Portland Cement, river sand and coarse aggregate were used for concrete mix proportioning. The maximum size of coarse aggregate was limited to 10 mm. The water-cement ratio was limited to 35 kg for each 100 kg of cement. The diameter of the reinforcing bar and tendon used in this study was 8 and 4 mm, respectively. The level of prestress in the plates varied between 0 and 30%. Zero percent (0%) prestress indicates the tendons were unstretched in the concrete. One-way prestressing of concrete was done. The prestressing was done using hydraulic jack in a robust prestressing bed of mild steel. The arrangement of tendons and reinforcement bars is presented in Fig. 1a. The yield strength of rebar and tendon was 609 and 1600 N/mm<sup>2</sup>, respectively. The concrete was placed in the plate molds once the tendons were stretched. It was cured in water for 28 days. The experiments were performed under a drop hammer setup. The slabs were first supported in the setup. The steel hammer was lifted to 0.5 m and

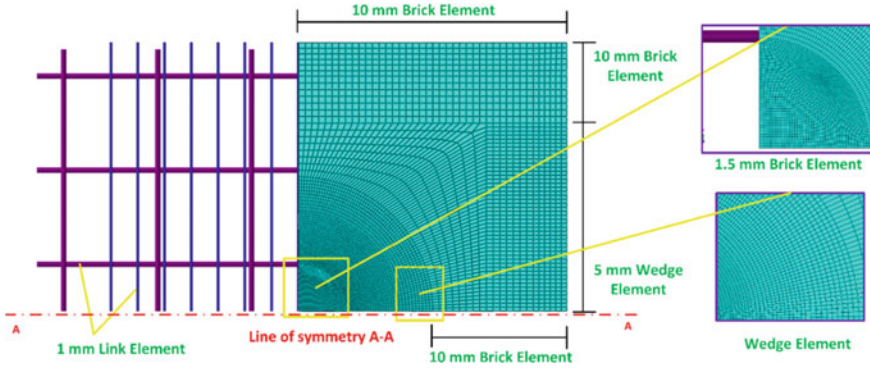


**Fig. 1** **a** Arrangement of reinforcement and tendon in a plate and **b** experimental setup

1.0 m height and dropped under gravity to hit the plate at the center. The mass of the steel hammer employed was approximately 0.243 tons. The various responses of the plate, i.e., force, reaction, deflection, energy and damage were obtained using load cells, displacement sensor and camera. The response from the sensor was obtained in a data logger at a sampling rate of 10 k samples per second. The experimental setup is presented in Fig. 1b.

### 3 Finite Element Model

The finite element simulations of the problem were carried out in ABAQUS software. All the constituents of the plate (concrete, rebar, tendon) were modeled as deformable parts, while the hammer was considered a rigid part. The different parts were discretized into eight node solid brick elements, six node solid wedge elements and two node link elements. The model was discretized such that finer meshing (i.e., 1.5 mm) was used at the center, while coarser meshing (i.e., 10 mm) was used at the boundary of the plate. The detail of meshing in the model is shown in Fig. 2. The tendons and reinforcing bars were discretized into mesh size 1 mm. This mesh configuration was adopted after carrying out a mesh convergence study. The Holmquist-Johnson-Cook model and metal plasticity models were employed for modeling concrete and steel (reinforcing bars and tendons), respectively. The models are discussed in detail in study [13–15]. The material parameters for concrete and steel are taken from study [13, 14, 16]. The HJC parameters used for concrete are mentioned in Table 1. A perfect bond was considered between reinforcing bars and concrete and also between tendon and concrete [14]. A penalty friction-based surface



**Fig. 2** Meshing in half finite element model

**Table 1** HJC material parameters used for concrete [14]

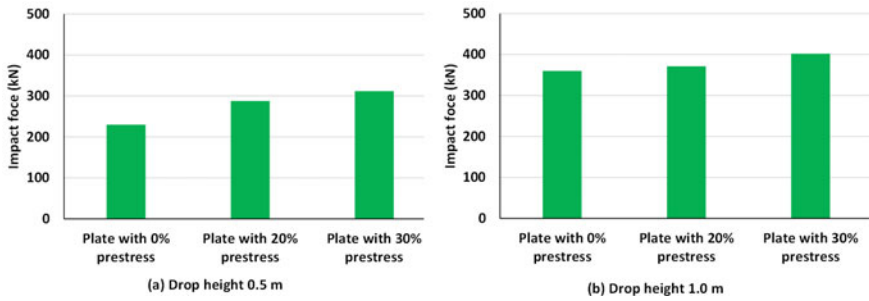
Material parameters	Values	Material parameters	Values
$\rho$ ( $\text{kg/m}^3$ )	2430	$D1$	0.04
$A$	0.79	$D2$	1
$B$	1.6	$P_{crush}$ (GPa)	0.016
$N$	0.61	$P_{lock}$ (GPa)	0.8
$C$	0.007	$\mu_{crush}$	0.001
$f_c'$ (MPa)	48	$\mu_{lock}$	0.1
$S_{MAX}$	7.0	$K1$ (GPa)	85
$G$ (MPa)	14,803	$K2$ (GPa)	-171
$T$ (MPa)	4.80	$K3$ (GPa)	208

to surface contact was used between concrete and steel hammers [14, 16]. The plate was assigned fixed boundary condition at corner. The hammer was given initial velocity corresponding to 0.5 and 1.0 m drop height in the direction of gravity, while its other degrees of freedom were arrested.

## 4 Results and Discussion

### 4.1 Impact Force in Plates

The impact force for the plates has been presented in Fig. 3a, b for drop heights of 0.5 and 1.0 m, respectively. The impact force was measured using load cell and a data logger. The impact force is nothing but the contact force between the hammer and a plate. Irrespective of the drop height the magnitude of peak impact force was noticed



**Fig. 3** Impact force in plates for **a** drop height 0.5 m, and **b** drop height 1.0 m

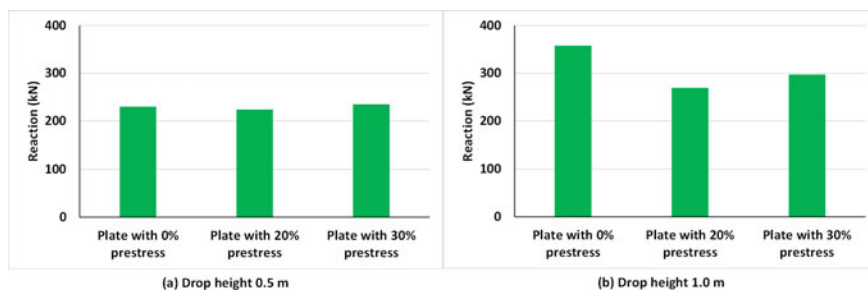
to have increased with an increase in the prestress in the concrete. For 0.5 m drop height, the impact force in the plate with 20 and 30% prestress was noticed to have increased by 25 to 35%, respectively, with respect to the plate with 0% prestress. The increase in the impact force could be due to the increase in the stiffness of the plate as a result of increased prestress. Similarly, the impact force in the plate with 20 and 30% prestress was noticed to have increased by 3.0 to 12.6% w.r.t. plate with 0% prestress, respectively, for 1.0 m drop height.

## 4.2 Reaction in Plates

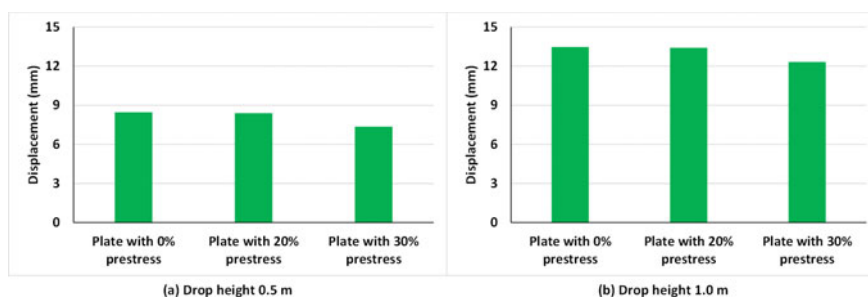
The reaction for the plates has been presented in Fig. 4a, b for drop heights of 0.5 and 1.0 m, respectively. The reaction was also measured using load cells and a data logger at the supports. For drop height 0.5 m, the plates were not found sensitive to reaction force as the magnitude of measured reaction was seen to be almost the same irrespective of the level of prestress. On the other hand, the plate with 0% prestress witnessed the highest peak reaction for 1.0 m drop height. The reaction was also noticed to have reduced with an increase in the prestress. The reaction was reduced by 25 and 17%, respectively, for 20 and 30% prestress in the concrete. This could be due to dominance of splitting damage for 20 and 30% prestress instead of flexural deformation.

## 4.3 Deflection in Plates

The displacement in plate has been presented in Fig. 5a, b for drop heights 0.5 and 1.0 m, respectively. The deflection was measured using the deflection sensor and the data logger at the center of the plate. In general, the plates with 0% prestress reported the highest peak deflection for both the drop heights. The deflection was reduced with an increase in the level of prestress in the concrete which could be due



**Fig. 4** Reaction in plates for **a** drop height 0.5 m, and **b** drop height 1.0 m

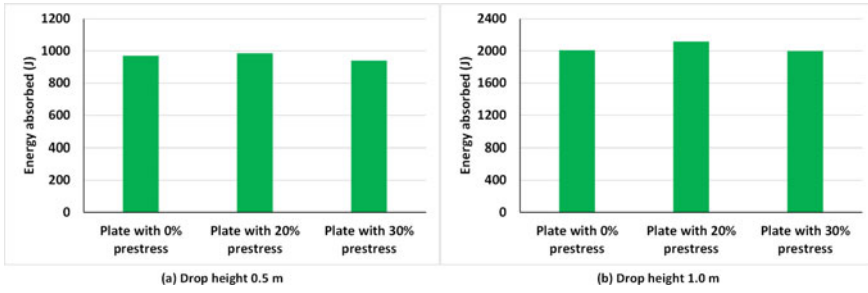


**Fig. 5** Deflection in plates for **a** drop height 0.5 m and **b** drop height 1.0 m

to the increase in the stiffness of the plate. The plates witnessed a nominal reduction in deflection for 20% prestress. However, the deflection was further reduced when the level of prestressed increased to 30%. For 30% prestress in the concrete, the plates witnessed 13% reduction in deflection of the plate.

#### 4.4 Energy Absorbed by Plates

The energy absorbed by the plates is shown in Fig. 6a, b for drop heights 0.5 and 1.0 m, respectively. The energy absorption was determined by calculating area between load and deflection curve. The results showed that the 20% prestress had the optimum energy dissipation among all the plates tested. In general, the plates with 20% prestress have shown the highest energy absorption under drop impact for both the drop heights. The concrete with 20% prestress has absorbed 986 and 2118 J energy, respectively, for 0.5 and 1.0 m drop height. For drop height 1.0 m, the energy dissipation was 2009 and 1997 J, respectively, for the plates with 0% and 30% prestress.



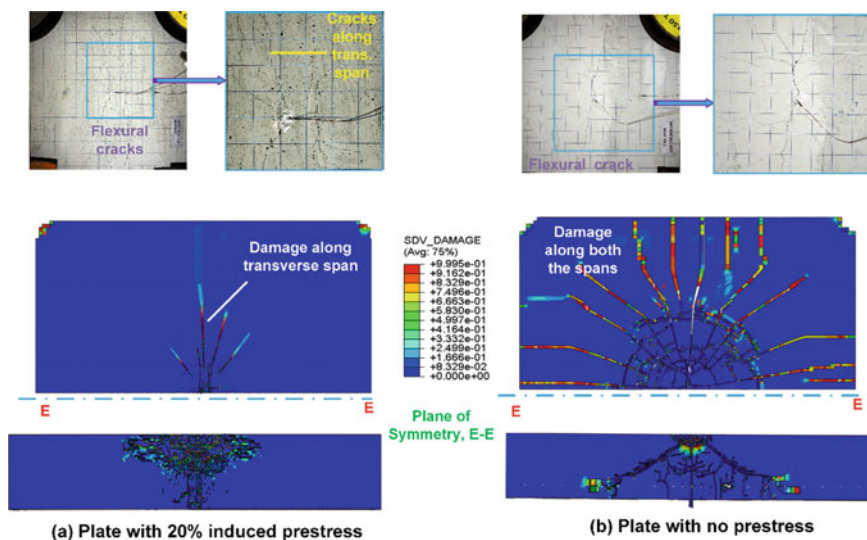
**Fig. 6** Energy absorbed by plates for **a** drop height 0.5 m and **b** drop height 1.0 m

#### 4.5 Damage in Plates

The damage in the plates has been presented in Fig. 7a, b for the plates with 20% prestress and plates with 0% prestressed, respectively. The 20% prestress concrete plates witnessed cracks at the center of the plate with some hairline cracks. The observed cracks were found to have primarily oriented along the direction of the tendon, which is the sign of the dominance of splitting crack in the plate with increase in the magnitude of prestress. Although, the better performance was seen for prestressed concrete for higher prestress level except the dominance of splitting damage. The splitting damage may invite severe consequences, (for example) if develop in a chemical storage structure, nuclear containment, railway sleeper, bridge, etc. The splitting crack can result premature failure of the prestressed concrete. On the other hand, the plate with no prestress (0% prestress) witnessed flexural cracks and relatively uniform crack distribution at the surface of the plate. The finite element simulations also witnessed the flexural cracking for 0% prestress and splitting damage for 20% prestress.

### 5 Conclusions

The prestressed concrete plates induced with 0–30% prestress in the concrete were subjected to drop impact from 0.5 and 1.0 m height. The impact force, deflection, reaction, damage and energy absorption were obtained and compared. The results show up to 25% increase in impact force for 20% prestress compared to plates with 0% prestress and up to 35% increase for 30% prestress in the concrete. In general, the plates with 20% prestress witnessed the smallest reaction and nominally higher energy absorption irrespective of the drop height of hammer. The induced prestress in the concrete increased the impact resistance of the plates such that the plate with 30% prestress witnessed the smallest deflection followed by the plate with 20% prestress and 0% prestress. The induced prestress in concrete was also noticed to have governed the failure mode of the plates. The plate with 20% prestress witnessed the flexural



**Fig. 7** Damage in the plates: **a** for 20% prestress, and **b** 0% prestress for 0.5 m drop height

cracks primarily oriented along the direction of tendons. Whereas, the plate with 0% prestress witnessed uniformly distributed flexural cracks in the plate. The finite element simulations reasonably reproduced the crack pattern in the plates.

**Acknowledgements** The author sincerely thank CBRI, Roorkee, India, and IIT Roorkee, India, for extending their experimental and computational lab support for this study.

## References

1. Kaewunruen S, Remennikov AM (2009) Impact capacity of railway prestressed concrete sleepers. *Eng Fail Anal* 16:1520–1532
2. Kaewunruen S, Remennikov AM (2010) Dynamic crack propagations in prestressed concrete sleepers in railway track systems subjected to severe impact loads. *ASCE J. Struct. Eng.* 136:749–754
3. K. Ramakrishnan, Depak SR, Hariharan KR, Abid SR, Murali G, Cecchin D, Fediuk R, Mugahed Amran YH, Abdelgader HS, Khatib JM (2021) Standard and modified falling mass impact tests on preplaced aggregate fibrous concrete and slurry infiltrated fibrous concrete. *Constr Build Mater* 298:123857
4. Wei J, Li J, Wu C, Liu Z, Fang J (2021) Impact resistance of ultra-high performance concrete strengthened reinforced concrete beams. *Int J Impact Eng* 158:104023
5. Al-Tayeb MM, Aisheh YIA, Qaidi SMA, Tayeh BA (2022) Experimental and simulation study on the impact resistance of concrete to replace high amounts of fine aggregate with plastic waste. *Case Stud Constr Mater* 17:e01324
6. Prasad N, Murali G (2021) Exploring the impact performance of functionally-graded preplaced aggregate concrete incorporating steel and polypropylene fibres. *J Build Eng* 35:102077. ISSN 2352-7102

7. Abid SR, Gunasekaran M, Ali SH, Kadhum AL, Al-Gasham TS, Fediuk R, Vatin N, Karelina M (2021) Impact performance of steel fiber-reinforced self-compacting concrete against repeated drop weight impact. *Crystals* 11:91
8. Li N, Jin Z, Long G, Chen L, Fu Q, Yu Y, Zhang X, Xiong C (2021) Impact resistance of steel fiber-reinforced self-compacting concrete (SCC) at high strain rates. *J Build Eng* 38:102212
9. Wang Z, Ma G, Ma Z, Zhang Y (2021) Flexural behavior of carbon fiber-reinforced concrete beams under impact loading. *Cement Concr Compos* 118:103910
10. Abid SR, Abbass AA, Murali G, Al-Sarray MLJ, Nader IA, Ali SH (2022) Repeated impact response of normal- and high-strength concrete subjected to temperatures up to 600 °C. *Materials* 15:5283
11. Feng W, Liu F, Yang F, Jing L, Li L, Li H, Chen L (2021) Compressive behaviour and fragment size distribution model for failure mode prediction of rubber concrete under impact loads. *Constr Build Mater* 273:121767
12. Zhang P, Sha D, Li Q, Zhao S, Ling Y (2021) Effect of nano silica particles on impact resistance and durability of concrete containing coal fly ash. *Nanomaterials* 11:1296
13. Holmquist TJ, Johnson GR, Cook WH (1993) A computational constitutive model for concrete subjected to large strains, high strain rates, and high pressures. In: Fourteenth international symposium on ballistics, Canada, pp 1–10
14. Kumar V, Iqbal MA, Mittal AK (2018) Study of induced prestress on deformation and energy absorption characteristics of concrete slabs under drop impact loading. *Constr Build Mater* 188:656–675
15. ABAQUS documentation
16. Kumar V, Kartik KV, Iqbal MA (2020) Experimental and numerical investigation of reinforced concrete slabs under blast loading. *Eng Struct* 206:110125



# Development of $C^1$ Smooth Basis in Isogeometric Analysis for Multi-Patch Domain



Lokanath Barik and Abinash Kumar Swain

**Abstract** Due to the ever-increasing need for computational accuracy, various new methodologies are being developed or improvised. One such advancement over the standard finite element analysis (FEA) is the isogeometric analysis (IGA) which is a spline-based technique with a framework of FEA. IGA provides the advantage of geometrical exactness and  $C^1$  continuous parametric space over the element domain. However, its continuity is compromised ( $C^0$ ) at patches represented by common boundaries ( $\prod_i$ ). This junction, in the parametric domain, is defined by the connecting point between two adjacent basis functions of adjoining patches whose end derivatives are discontinuous. Imposing  $C^1$  continuity can provide higher numerical accuracy and faster convergence. This study mainly focuses on generating new smooth basis functions, by manipulating the  $C^0$  basis of degree ( $p$ )  $\geq 2$  at neighboring patches in which two dissimilar  $p$ th degree curves are locally adjusted to satisfy continuity requirements. We have tested our model by solving Poisson and biharmonic equations that replicate governing differential equations of various structural mechanics problems. Its effectiveness is checked against conventional two patch domains in IGA through displacement plots and error estimates. Moreover, this novel approach can be extended to shell elements, phase-field models, and XIGA.

**Keywords** Isogeometric analysis · NURBS curve · Patch continuity · Structural mechanics

## 1 Introduction

Isogeometric analysis (IGA) is a NURBS augmented technique developed by Hughes et al. [1] that incorporates basis functions represented by knot vectors from CAD geometry. These basis functions are used for numerical analysis in finite element framework and possess higher order inter-element continuity. IGA has been extensively studied using a single knot vector called patches, where different refinement

---

L. Barik · A. K. Swain (✉)

Mechanical and Industrial Engineering Department, IIT Roorkee, Roorkee, India  
e-mail: [abinash.swain@me.iitr.ac.in](mailto:abinash.swain@me.iitr.ac.in)

schemes like  $h$ ,  $p$ ,  $k$  [2] and various spline techniques like RHT splines [3], T-splines [4], etc., have been tested for improving the solution space and overcoming problems with complex meshing. However, a single NURBS curve represented by a knot vector of specified degree may not be adequate for representing complex geometries of real-world structures owing to multiple curvatures and sharp edges. A higher degree curve can be a possible solution but it increases the computational time significantly due to larger numerical iterations. The trade-off between accuracy and time is critical. Hence, the mapping of complicated intrinsic geometry sometimes requires breaking down the physical domain into different sections at intervals denoted by patches. These geometries represented by multiple patches at their interfaces acquire  $C^0$  continuity. Higher-order differential equations governing the Kirchhoff–Love shell elements, Can–Hilliard phase field models, Euler–Bernoulli beam elements, etc., require a minimum of  $C^1$  continuity for numerical analysis. Hence, it is desirable to impose multi-patch continuity over the patch junction to solve these fourth-order differential equations [5].

Researchers have developed various patch continuity methods that can be broadly classified into weak and strong coupling. Kiendl et al. (2010) formulated a novel bending strip method where a so-called strip of fictitious material having a unidirectional bending stiffness was added to the adjoining patch junction, the direction of which was selected transverse to the patch interface [6]. Dornisch et al. (2011) studied the Lagrange multiplier method, these multipliers were the implementation of point and tangential continuity at the interfaces [7]. Lei et al. (2015) developed an additional penalty term which was incorporated in the weak form [8]. Nguyen et al. (2014) proposed Nitsche’s method for coupling patches at junctions. A novel Gauss point distribution technique was formulated that ensured coupling between adjacent patches at the interface [9]. Coox et al. (2017) proposed a direct elimination method [10], that incorporates a least square technique to formulate a master-slave interaction that was mesh dependent. Hirschler et al. (2019) introduced the primal mortar method for non-conforming patches, in which a master-slave relationship was established at the adjoining patch junction. The main objective of this approach was to formulate a relation matrix that could connect patches by static condensation, enforcing equal deformation to the control points of the patch interface [11]. All these formulations enforce additional modules either in variational form or patch segmentation.

Furthermore, Chui et al. [12] developed new basis as a linear combination of pre-existing bases at common boundaries shared by adjacent patches. The coefficients of the linear combination were determined by imposing continuity constraints in null space. However, the bases generated violated the partition of unity property which is essential for interpolatory nature of basis functions. Additionally, there were some regions where the basis function became negative which is not ideal for a well-conditioned stiffness matrix. In this study, we constructed special basis functions in a linear combination fashion of pre-existing  $C^0$  bases near patch junction by imposing tangent and point continuity in a much simpler yet elegant fashion. These newly formed basis functions not only satisfy  $C^1$  continuity but the partition of unity as and non-negativity property as well.

## 2 Preliminaries

This section presents NURBS concepts required to understand the  $C^1$  coupling of isogeometric patches. Let  $\mathbb{E}$  be a given knot vector, where  $\mathbb{E} = \{\xi_0, \xi_1, \xi_2, \dots, \xi_m\}$ , of degree  $p$ , having basis functions  $N_{i,p}$  with  $i = 1, \dots, m - p - 1$ . The basis functions are found iteratively by the Cox-de-boor algorithm defined as,

$$N_{i,0} = \begin{cases} 1 & \text{if } \xi_i \leq \xi < \xi_{i+1} \\ 0 & \text{otherwise} \end{cases} \quad (1)$$

$$N_{i,p}(\xi) = \frac{\xi - \xi_i}{\xi_{i+p} - \xi_i} N_{i,p-1}(\xi) + \frac{\xi_{i+p+1} - \xi}{\xi_{i+p+1} - \xi_{i+1}} N_{i+1,p-1}(\xi), \quad (2)$$

The parametric space  $\xi$  in 1D represents  $C^{p-k}$  continuous basis functions at knot  $u_i$  which have knot multiplicity  $k$  in the knot vector. In IGA, the basis function can be  $C^{p-1}$  continuous which is highly beneficial in solving higher order partial differential equations. The elements are defined over span of control points  $P_i \in R$ ,  $i = [0, 1, 2, \dots, n]$  in physical space and knot vector in parametric space.

The corresponding B-spline segment in  $\Pi$  is represented by,

$$G(\xi) = \sum_{i=0}^n N_{i,p}(\xi) \cdot P_i \quad (3)$$

Geometric mapping of this parametric space can be mapped to the physical domain  $\Omega$  such that  $G(\xi) = x$ .

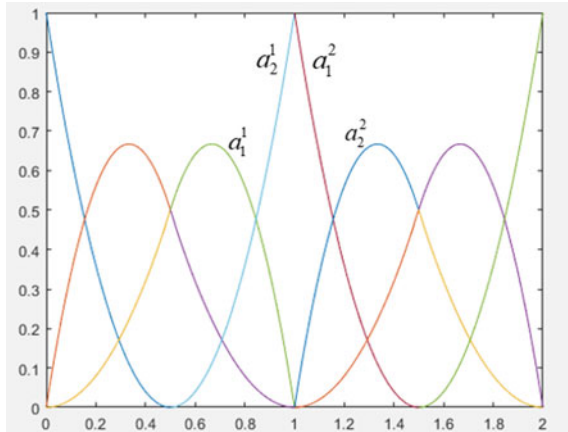
Moreover, the basis functions can be defined over  $\Omega$  following inverse geometric mapping [12],  $a_{i,p}(x) = N_{i,p}(\xi) \circ G^{-1}(x)$ , where  $a_{i,p}(x)$  is the basis functions represented concerning control points.

## 3 Preliminaries

To demonstrate our concept of  $C^1$  patch coupling, we introduce two arbitrary parametric domains  $\Pi^1$  and  $\Pi^2$  in 1D such that  $\Pi^1 \cap \Pi^2 = \Phi$  is represented by a knot vector  $\mathbb{E} = [0, 0, 0, 0.5, 1, 1, 1]$ . Its geometric mapping in physical space  $\Omega = (0 \rightarrow 2)$  where  $\Omega = \Omega^1(0 \rightarrow 1) \cup \Omega^2(1 \rightarrow 2)$  is represented over the boundary  $\Gamma = [0, 2] \cup [0, 2]$ , connected at  $P_i = 1$  as shown in Fig. 1 with  $x$  axis being the global parametric coordinate and  $y$  axis represents the corresponding basis function values. The basis function obtained in  $\Omega$  is represented as  $a_i^r$ ,  $r = 1, 2$  subdomains.

We construct our basis function as a linear combination of pre-existing bases having point continuity at patch interface, i.e.,  $a_1^1, a_2^1, a_1^2, a_2^2$  as shown in the Fig. 1. Our prime focus is maintaining partition of unity and non-negativity to the newly

**Fig. 1** Two patch domain basis functions in parametric space



developed  $C^1$  continuous bases  $\psi^1$  and  $\psi^2$ . Continuity conditions (5) and (6) are enforced at point  $P_t = 1$  taking in account neighboring sub-patch of  $\Pi^1$  and  $\Pi^2$  defined over the boundary (0.5, 1) and (1, 1.5), respectively.

$$\psi_1^1 + \psi_1^2 = \psi_1, \quad \psi_2^1 + \psi_2^2 = \psi_2.$$

$$\psi_1^1 = a \cdot a_1^1 + b \cdot a_2^1, \quad \psi_2^1 = c \cdot a_1^1 + d \cdot a_2^1 \quad (4)$$

$$\psi_1^2 = e \cdot a_1^2 + f \cdot a_2^2, \quad \psi_2^2 = g \cdot a_1^2 + h \cdot a_2^2$$

where  $\{a, b, c, d, e, f, g, h\}$  are the coefficients associated. Now, the continuity conditions are defined as,

$$\psi_1^1 = \psi_1^2, \quad \psi_2^1 = \psi_2^2 \text{ at } P_t \quad (5)$$

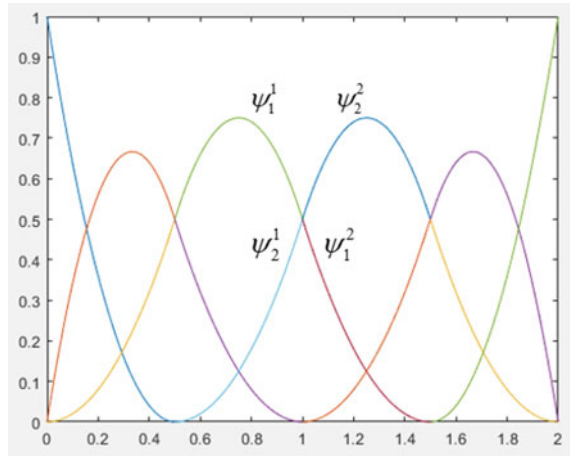
$$\frac{d(\psi_1^1)}{dx} = \frac{d(\psi_1^2)}{dx}, \quad \frac{d(\psi_2^1)}{dx} = \frac{d(\psi_2^2)}{dx} \text{ at } P_t \quad (6)$$

Henceforth, we determined the coefficients for constructing  $C^1$  smooth bases for the quadratic basis function, as in Fig. 2.

## 4 Model Problem

We demonstrate the effectiveness of our technique by solving Poisson and biharmonic equations, which are generally used to model real-life situations such as bar, beam, shell structures, etc.

**Fig. 2** Two patch domain  $C^1$  continuous basis functions in parametric space



### 4.1 Poisson’s Equation

It is a second-order differential equation denoted by,

$$\begin{aligned} -\nabla^2 u &= f \text{ in } \Omega \\ u &= g_0 \text{ in } \partial\Omega \end{aligned} \tag{7}$$

Its weak formulation is given as,

$$\alpha(u, v) = \int \nabla u \cdot \nabla v \, d\Omega, L(v) = \int f \cdot v \, d\Omega. \tag{8}$$

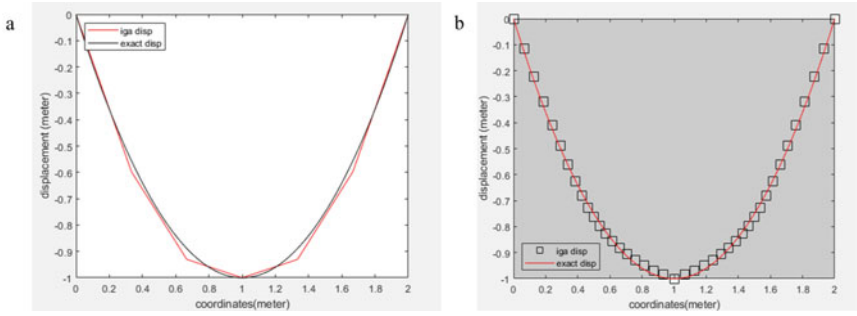
In our analysis, we have considered a problem  $\Delta u = -2$ , defined over the domain  $\Omega = [0, 2]$  with boundary conditions  $u : \Gamma \rightarrow R$ , given by,

$$u(x = 0) = u(x = l) = 0 \tag{9}$$

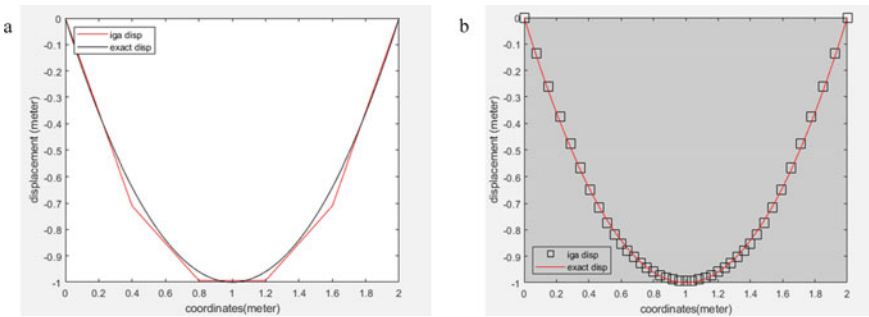
The exact solution is found to be,

$$u = -x(l - x), \quad x \in [0, 2] \tag{10}$$

We have considered two patch domains,  $\Xi^l = [0, 0, 0, 0.5, 1, 1, 1, 1]$  defined over  $\mathbb{I}$ , having quadratic basis functions. Figure 3 is obtained without enforcing patch continuity, and Fig. 4 is with patch coupling. Table 1 shows a comparative study of L2 error analysis for  $C^0$  and  $C^1$  continuity with different elements. By enforcing  $C^1$  continuity reduced error is obtained.



**Fig. 3** **a** Displacement plot for  $C^0$  continuous 2 patch domain; **b** displacement results of (a) interpolated



**Fig. 4** **a** Displacement plot for  $C^1$  continuous 2 patch domain; **b** displacement results of (a) interpolated

**Table 1** L2 error comparison between  $C^0$  and  $C^1$  continuous patch

Elements per patch	With $C^0$ continuity	With $C^1$ continuity
4	0.0163	0.0154
6	0.0099	0.0076
8	0.0078	0.0049

### 4.2 Biharmonic Equation

It is a fourth-order differential equation denoted by,

$$\begin{aligned}
 \nabla^4 u &= f \text{ in } \Omega \\
 u &= g_0 \text{ in } \partial\Omega \\
 n \cdot \nabla u &= g_1 \text{ in } \partial\Omega
 \end{aligned}
 \tag{11}$$

The biharmonic equation describes the behavior of a physical system that is subject to a balance of competing forces. In particular, it describes the equilibrium of a material subject to bending and stretching forces, such as a thin plate or a beam. Its weak formulation is given as,

$$\alpha(u, v) = \int \nabla^2 u \cdot \nabla^2 v \, d\Omega, L(v) = \int f \cdot v \, d\Omega. \tag{12}$$

In our analysis, we have considered a problem  $\Delta u = -24$ , defined over the domain  $\Omega = [0, 1]$  with boundary conditions  $u : \Gamma \rightarrow R$ , given by:

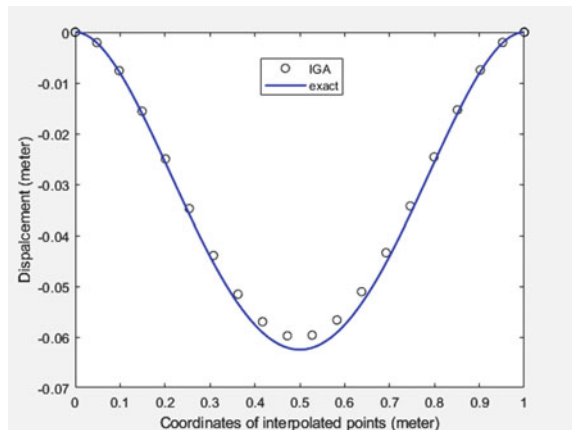
$$\begin{aligned} u(x = 0, l) &= 0 \\ \nabla u(x = 0, l) &= 0 \end{aligned} \tag{13}$$

The exact solution is found to be,

$$u = -x^2(l - x)^2, x \in [0, 2] \tag{14}$$

We have considered two patch domains,  $\Xi^l = [0,0,0,0,0.25,0.5,0.75,1,1,1,1]$  defined over  $\Pi$  having cubic basis functions and 4 elements in each patch, where  $l = (1, 2)$ . Figure 5 is the interpolated result obtained by enforcing patch continuity at the junction.

**Fig. 5** Displacement plot for  $C^1$  continuous, 2 patch domain



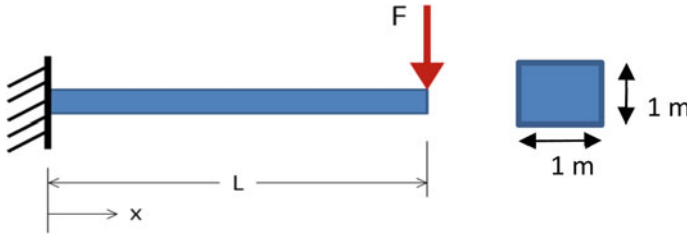
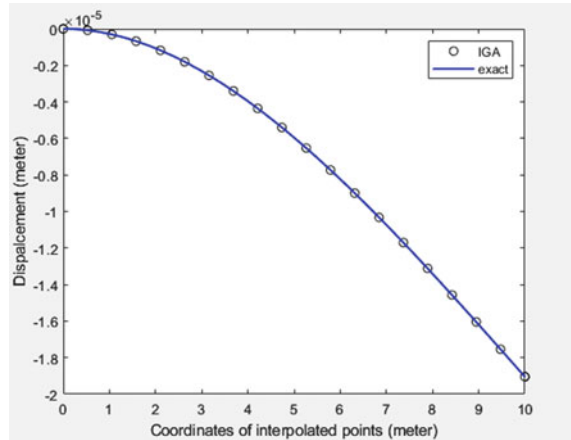


Fig. 6 Cantilever beam with point load of 1N at free end

Fig. 7 Displacement vs coordinate plot of the cantilever beam



### 4.3 Euler–Bernoulli Beam

We have taken an example of a cantilever beam of length 10 m with unit width and thickness. The Young’s modulus of the beam is 210 MPa, and it carries a point load on 1 N at the free end, as shown in Fig. 6. The beam is modeled with two identical NURBS patches having ten elements each, through uniform h-refinement. Figure 7 represents the displacement plot of the beam showing that the IGA results are in good agreement with the exact solution after implementing patch continuity.

## 5 Conclusion and Future Scope

This study develops a patch continuity methodology by replacing the  $C^0$  basis at the patch boundary, maintaining  $C^1$  continuity throughout the parametric space  $\bar{\Pi}$ . Our proposed bases satisfy the partition of unity and non-negativity properties idle for a NURBS patch under consideration. We demonstrated the effectiveness of our technique with 1D Poisson and biharmonic equations. A comparative study is presented



with ordinary bases and newly formed basis functions. The solutions obtained with displacement as a field variable are almost identical. After performing an error estimate for both the cases, it can be concluded that patch continuity offers better accuracy compared to its counterpart for degree  $p \geq 2$ . This technique can be further extended to 2D as well as 3D multi-patch domains for a variety of structural mechanics problems. Additionally, our method can be extended in solving shell structures, XIGA, and phase-field models.

## References

1. Hughes TJR, Cottrell JA, Bazilevs Y (2005) Isogeometric analysis: CAD, finite elements, NURBS, exact geometry and mesh refinement. *Comput Methods Appl Mech Eng* 194(39–41):4135–4195. <https://doi.org/10.1016/j.cma.2004.10.008>
2. Cottrell JA, Hughes TJR, Reali A (2007) Studies of refinement and continuity in isogeometric structural analysis. *Comput Meth Appl Mech Eng* 196(41–44):4160–4183. <https://doi.org/10.1016/j.cma.2007.04.007>
3. Nguyen-Thanh N et al (2017) Isogeometric analysis of large-deformation thin shells using RHT-splines for multiple-patch coupling. *Comput Meth Appl Mech Eng* 316:1157–1178. <https://doi.org/10.1016/j.cma.2016.12.002>
4. Beirão da Veiga L, Buffa A, Cho D, Sangalli G (2011) IsoGeometric analysis using T-splines on two-patch geometries. *Comput Meth Appl Mech Eng* 200(21–22):1787–1803. <https://doi.org/10.1016/j.cma.2011.02.005>
5. Paul K, Zimmermann C, Duong TX, Sauer RA (2020) Isogeometric continuity constraints for multi-patch shells governed by fourth-order deformation and phase field models. *Comput Meth Appl Mech Eng* 370. <https://doi.org/10.1016/j.cma.2020.113219>
6. Kiendl J, Bazilevs Y, Hsu MC, Wüchner R, Bletzinger KU (2010) The bending strip method for isogeometric analysis of Kirchhoff-Love shell structures comprised of multiple patches. *Comput Meth Appl Mech Eng* 199(37–40):2403–2416. <https://doi.org/10.1016/j.cma.2010.03.029>
7. Dornisch W, Klinkel S (2011) Boundary conditions and multi-patch connections in isogeometric analysis. *Pamm* 11(1):207–208. <https://doi.org/10.1002/pamm.201110095>
8. Lei Z, Gillot F, Jezequel L (2015) A C0/G1 multiple patches connection method in isogeometric analysis. *Appl Math Model* 39(15):4405–4420. <https://doi.org/10.1016/j.apm.2014.12.055>
9. Nguyen VP, Kerfriden P, Brino M, Bordas SPA, Bonisoli E (2014) Nitsche's method for two and three dimensional NURBS patch coupling. *Comput Mech* 53(6):1163–1182. <https://doi.org/10.1007/s00466-013-0955-3>
10. Cox L, Greco F, Atak O, Vandepitte D, Desmet W (2017) A robust patch coupling method for NURBS-based isogeometric analysis of non-conforming multipatch surfaces. *Comput Meth Appl Mech Eng* 316:235–260. <https://doi.org/10.1016/j.cma.2016.06.022>
11. Hirschler T, Bouclier R, Dureisseix D, Duval A, Elguedj T, Morlier J (2019) A dual domain decomposition algorithm for the analysis of non-conforming isogeometric Kirchhoff-Love shells. *Comput Meth Appl Mech Eng* 357. <https://doi.org/10.1016/j.cma.2019.112578>
12. Chan CL, Anitescu C, Rabczuk T (2019) Strong multipatch  $C^1$ -coupling for isogeometric analysis on 2D and 3D domains. *Comput Meth Appl Mech Eng* 357. <https://doi.org/10.1016/j.cma.2019.112599>

# Modal Characterization of Additively Manufactured Chiral Structure: Suppression of Its Multiple Responses



Rukmangad S. Barad, Akshay Pathania, B. K. Nagesh, and S. Anand Kumar

**Abstract** In this work, dynamic characterization of a simple cantilever embedded with a chiral lattice is investigated. The complex structure is realized through additive manufacturing technique. The inherent advantage of these lattices is offering a high strength-to-weight ratio. When embedded with vibration suppressing units at the nodes, these lattices aid in alleviating the overall dynamic response of the structure. The base structure is analyzed for its modal behavior by analytical and experimental means. These results are well correlated. This base lattice configuration is embedded with vibration suppression units at node locations in various spatial distribution patterns. All configurations have been subjected to dynamic characterization through experimental modal analysis and evaluated their effectiveness in suppressing the overall modal response. Finally, an optimal spatial distribution pattern is arrived, exhibiting the maximum benefit in terms of overall vibration reduction and with the most negligible weight penalty.

**Keywords** Additive manufacturing · Modal analysis · Chiral structure · Dynamic characterization · Impact loading

## 1 Introduction

Aerospace structures primarily are aimed with a primary design objective of improving the strength-to-weight ratio. Slender parts such as wings are prone to phenomena like resonance and flutter. As a designer, to control the overall response

---

R. S. Barad (✉)

Department of Mechanical Engineering, PES University, Bangalore 560085, India  
e-mail: [rukmandsanjaybarad@pesu.pes.edu](mailto:rukmandsanjaybarad@pesu.pes.edu)

A. Pathania · S. Anand Kumar

Additive Manufacturing Research Laboratory, Indian Institute of Technology, Jammu 181221, India

B. K. Nagesh

Gas Turbine Research Establishment, C.V. Raman Nagar, Bangalore 560093, India

of this structure, efforts are made to find mechanisms that enhance the damping or alter the vibration characteristics. The latter option may demand modifying the structure, which could be difficult in most cases. However, the former option of enhancing and localizing the energy dissipation mechanism could be appreciated as a feasible approach. This can reduce the overall response of the structure. With the rapid advent of additive manufacturing technology, one of the mechanisms to alleviate the overall vibratory response of the structure can be realized by introducing a chiral lattice structure with vibration suppression units embedded into this chiral lattice. The nomenclature employed in the present work is shown below.

### Nomenclature

OOP	out-of-plane
IP	in-plane
WoM	without mass
C	Central row
E1	Extreme 1 row
E2	Extreme 2 rows
T	triangular
TC	triangular with counterweights
F	Full

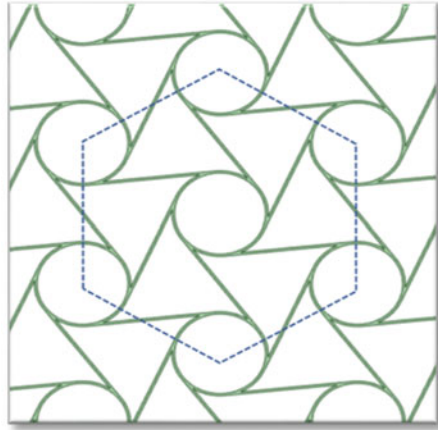
Several studies on chiral lattice structures and evaluation of its properties are reported in literature [1–3]. Specifically, the chiral lattices have an inherent advantage of high stiffness-to-weight ratio, high out-of-plane flexural bending stiffness and low in-plane stiffness. A literature survey indicates studies undertaken toward embedding these chiral lattices with vibration absorption units to suppress or alter the frequency response specific to the frequency and mode of interest [4]. These are popularly termed as tuned absorbers.

In the present work, efforts have been aimed toward alleviating the overall vibratory response of the structure. The structure has a hexagonal chiral lattice, which is embedded with various spatial distributions of vibration suppressing units. The dynamic response is evaluated for these various configurations through experimental modal analysis. These results have been analyzed further to arrive at an optimal spatial distribution so that a minimum weight penalty results in the maximum overall vibration reduction.

## 2 The Hexagonal Chiral Lattice

The fundamental unit of a hexagonal chiral lattice consists of circular nodes at all the hexagon vertices and the center of the hexagon. These nodes are coupled by ligaments that are tangential to these circular nodes, as shown in Fig. 1. The dynamic behavior of these unit cells is dictated by the ligament length, cross section area, a moment of inertia of cross section and the diameter of the circular node. These all parameters

**Fig. 1** Unit hexagonal chiral schematic



are considered at the design stage to arrive at the configuration of the chiral lattice structure for a given structure. Figure 1 describes a unit cell of a hexagonal chiral lattice. In this study, the dimensions of the chiral unit cell are 17.2 mm diameter node and a 21.25 mm ligament. The study uses a 1:1 scale for the finite-element model to the fabricated specimen.

### 3 Additive Manufacturing of Structure

Recent design methodologies enable more optimization techniques to arrive at a final geometry. These geometries are often complex and are difficult to be realized through conventional manufacturing techniques. With the advent of additive manufacturing technology, these parts can be realized easily. The present concept of embedding a chiral lattice in a structure falls in this category of complex geometries that are difficult to realize using conventional manufacturing processes.

The structure under consideration is realized through a fused deposition modeling (FDM) technique, wherein the part is built layer-by-layer from the bottom up by heating and extruding thermoplastic filament. The 'FDM Vantage' system from Stratasys, USA, is used.

To demonstrate this proof of concept, ABS plastic is used as it is durable and dimensionally stable. This ensures good accuracy and tight tolerancing. The geometric dimensions of the chiral lattice, specifically the thickness of the ligament, are arrived at after ascertaining the limitations in terms of realizing the minimum wall thickness that the FDM technique can print without any flaw. The other geometric parameters were fixed based on the Eigen frequency placements required for the studies. The structure is intentionally provided with a thick boundary wall of 5 mm so that there is no local deformation during vibration at the walls. The aim is to have maximum participation of the chiral lattice and the inertial masses to dissipate

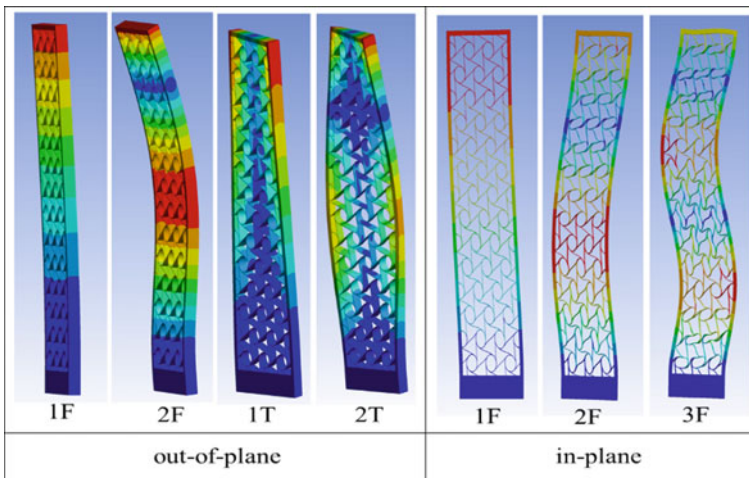
energy intentionally. In the present cantilever, the number of unit cells is dictated by the aspect ratio of the cantilever and the size of the unit cell.

## 4 Theoretical and Experimental Studies

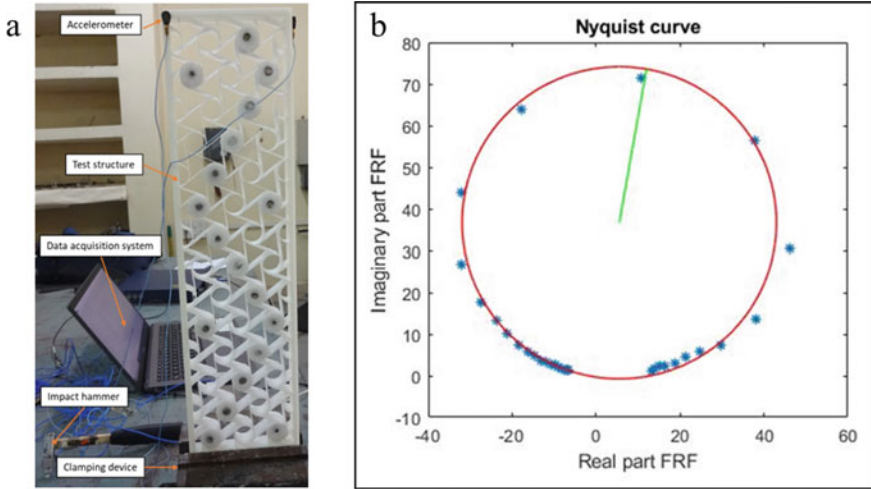
Prior to realizing the hardware, theoretical modal studies were performed using the ANSYS FEA software package. Multiple iterations were made to arrive at the final configuration of the geometry details. While considering various parameters, viz. placement of frequencies, the thickness of chiral ligaments, the diameter of the nodes, spacing between the nodes, structure wall thickness, 3D printing machine limitations, etc., after finalizing the geometry, the STL file was offered for additive manufacturing of the component.

Figure 2 shows the various mode shapes and their corresponding Eigen frequencies. The analysis ensured that there is no local deformation on the supporting wall and the majority of deformations for the various modes lie in the chiral lattice.

An experimental modal analysis was performed using a standard impact hammer technique on the FDM fabricated structure. This is rather a simple technique and is popular for lightly damped structures. This technique is preferred in the industry because of its simplicity and flexibility. The structure was excited in the in-plane and out-of-plane modes at the tip, using an instrumented impact hammer to measure the input force. The corresponding transient vibratory responses were measured using miniature accelerometers positioned at fixed locations see Fig. 3a. This response location was maintained throughout the experiment for various configurations of the spatial distribution of vibration suppressing units. Based on the measurement of



**Fig. 2** Various mode shapes of the baseline structure in the present study



**Fig. 3** a Experimental modal analysis setup; b circle fit technique used to establish damping

impulse excitation force and the transient time response of the structure, the frequency response function (FRF) is arrived. A typical FRF for one of the tests is displayed in Nyquist plot format as depicted in Fig. 3b. Using the single degree of freedom circle fit technique, these measured FRFs were used to arrive at the modal frequencies and corresponding damping factors.

## 5 Correlation Studies

With the experimental and analytical studies undertaken for the base configuration, further correlation studies were undertaken to ensure that the results were satisfactory. The theoretical model can be further extended for response predictions. These studies have not been brought out in the present paper for various configurations. However, the experimental results for various configurations tested are discussed in detail. As observed in Table 1, a good correlation exists between the experimental and theoretical results.

With this established correlation, further experimental studies were undertaken for various configurations with various spatial distribution patterns of vibration suppressing units in the chiral lattice.

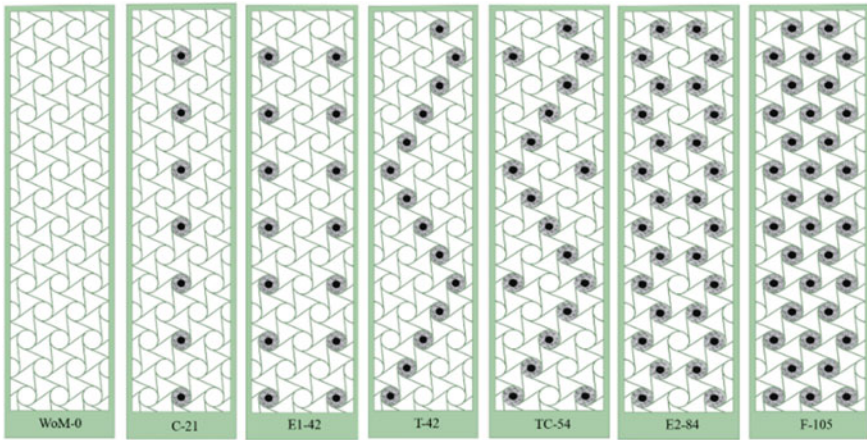
**Table 1** Modal details for the base configuration and Eigen frequency correlation with analytical results

Natural mode	Description	Theoretical frequency (Hz)	Experimental frequency (Hz)	Frequency deviation (%)	Damping (%)	Amplitude (g/N)
OOP-1F	Out-of-plane 1st Flexural	15.86	15.73	-0.82	1.36	4.26
OOP-1T	Out-of-plane 1st Torsional	43.14	42.63	-1.19	0.97	3.46
OOP-2F	Out-of-plane 2nd Flexural	101.82	102.50	0.66	0.92	2.60
OOP-2T	Out-of-plane 2nd Torsional	168.1	167.93	-0.10	0.81	3.42
IP-1F	In-plane 1st Flexural	39.84	32.03	-24.38	1.40	2.53
IP-2F	In-plane 2nd Flexural	125.54	112.90	-11.19	0.95	1.86
IP-3F	In-plane 3rd Flexural	227.08	221.25	-2.64	1.13	0.62

## 6 Suppressing Vibratory Responses and Optimization

This study is undertaken through experimental means as the procedure is well established and the component was already realized. Theoretical studies regarding this were already undertaken and brought out in the previously published work [5]. The damping values established through experimental studies were incorporated in the theoretical model through Rayleigh damping coefficients estimated. This model was then subjected to harmonic response studies. In this case, studies were undertaken to understand the response characteristics for various configurations.

The present work extends the previous, however, this is brought out through experiments. The vibration suppressing units are made of a central metal core surrounded by a soft (Styrofoam) material. This ensured that apart from the flexibility of the chiral ligaments, these inertial masses act as dissipative vibration elements in the system, thereby reducing the overall vibratory response of the system. The system does differ from a classical tuned vibration absorber, wherein one intentionally tunes the other spring mass system to match one of the system frequencies. However, in the present case, efforts were aimed to suppress multiple modes. In the sense, this is a mechanism acting as an inertial damping mechanism. This composite unit is then located inside various nodes of the chiral lattice. Figure 4 shows the various spatial distribution patterns of these units. For convenience, in this paper, the nomenclature for these spatial distribution patterns is denoted by the type of distribution followed by the magnitude of mass in grams. For example, C-21 represents ‘Central row-21g’. All these configurations are subjected to experimental modal studies.

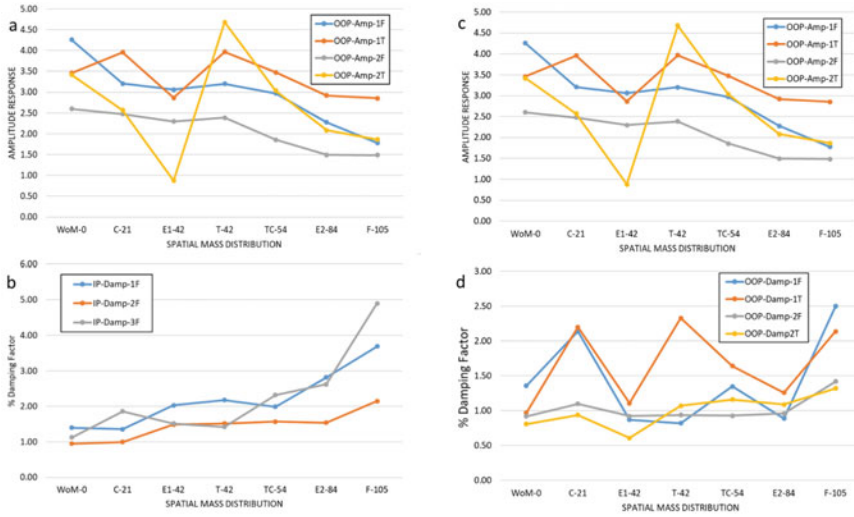


**Fig. 4** Various configurations tested

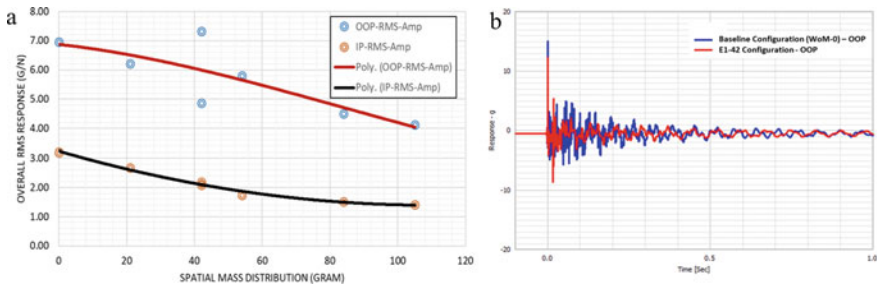
In order to study its effectiveness, the structure has been embedded with various special distribution patterns. These different configurations as shown in Fig. 5 have been subjected for experimental modal analysis (EMA). All the impact points and response points are maintained at same location throughout the experiment so as to aid in fair comparison and ease of ascertaining the influence of various parameters. Figure 6 gives the magnitude of response and damping measured for various configurations for in-plane and out-of-plane modes. As observed from the figure, the overall vibratory response in the in-plane mode decreases with an increase in vibration suppressing units. The modal damping also shows a progressive increase with the number of inertial units. However, in the case of the out-of-plane excitation and response measurement, though a global trend is similar to the in-plane observation but, for torsional mode 2T and T-42 spatial distribution of masses, a significant increase in the response is observed. However, the E1-42 configuration showed a significant drop in the response amplitude for the same mode. It is attributed to the mode-specific distribution of amplitude response at various nodes. It is observed that specific to the torsional modes 1T and 2T, the increase in the response is attributed to a decrease in the number of effective masses for these modes. The modal pattern in Fig. 2. indicates that the central nodes are relatively ineffective in these specific modes, and one needs to concentrate more on the extreme nodes for this mode, i.e., E1-42 configuration.

Intuitively, the placement of masses at all the nodes of the chiral lattice so that the maximum benefit in terms of damping and lowest response is expected. However, there is a penalty in terms of weight which may be crucial in the case of aerospace structures. As observed from these results, the optimal solution with the least number of masses is the E1-42 configuration, wherein an optimal benefit is obtained. As observed from the plots, an increase in the masses further does not offer significant benefits.





**Fig. 5** Modal amplitude responses and damping for various configurations. **a** In-plane amplitude, **b** in-plane damping, **c** out-of-plane amplitude, **d** out-of-plane damping



**Fig. 6** **a** Effect of special mass distribution on overall modal response, **b** time domain response for the baseline and E1-42 configuration

Further analysis of these results indicates that the best way to obtain the overall benefit in terms of responses is to plot the overall RMS response of all the modes of interest. This overall response, when plotted along with the mass, shows the best visualization for an optimal point. As observed from Fig. 6a, the optimal mass is 42 g. To be more specific the E1-42 pattern, this is applicable for the in-plane and out-of-plane modes. This can be observed in the raw time domain response plot for the base configuration and E1 configuration in Fig. 6b. The overall decay rate is quite significant in the E1-42 configuration, indicating that the overall damping is quite effective.

As a spin-off of these results, if one is interested in reducing modal responses of specific modes of interest as in the case of flutter of a wing or specific resonances of

the structure. The mass units can be spatially distributed in such a way that maximum benefit is achieved. However, while doing so, one needs to look at the responses of other modes. There could be a chance that the responses may increase. A judicious decision in this regard has to be taken by introducing suitable checks and keeping in mind the strength-to-weight ratio parameter. This work can be well extended to unmanned air vehicles or any other structure, where the main goal is to reduce the overall vibratory response without much structural weight penalty. In addition, these chiral embedded structures have a great potential to absorb the transient vibration in case of impact loads.

## 7 Conclusions

It is clear from this study that the placement of vibration suppressor units at the right location is the key to obtain optimal point of benefit. This is dictated by the various modes of interest and their modal displacement patterns. To understand the global response reduction, it is better to plot the RMS response levels considering all the modes of interest. This offers a better tool for selecting an optimal point. Also, one could observe the raw time domain response plot to confirm the decay rate. In case of a requirement to suppress a specific mode of interest as in flutter or resonance, one could tune these vibration suppressing units to act as tuned absorbers. As observed during the experiment, increasing the mass excessively results in slight stiffening of the assembly, in which case the modal frequency shifts to a slightly higher value.

During the design stage, it should be ensured that the external frame has sufficient strength so that there is no local deformation in the structure, but rather the deformations or energy dissipation is concentrated in the chiral lattice structure and inertial units. In addition to this, it is advisable to consider constraints from 3D printing processes in terms of minimum thickness achievable, finishing operations, high-stress points, etc. There are no high-stress concentration points and weaknesses in the ligaments. Further, a good survey of the material in terms of thermal sensitivity and other environmental conditions needs to be taken into account.

This particular innovative concept of suppressing a mode/s-specific response/s by introduction of a chiral lattice with tuned absorbers, can be exploited in practical applications of UAV wings, structures for impact absorption and other applications that demand a high strength-to-weight ratio. Further, the usage of the AM technology in realization of such complex structures makes it possible to achieve the optimal configuration.

**Acknowledgements** The author acknowledges the help extended by GTRE, Bangalore, in realizing the chiral lattice structure during my internship work at GTRE, Bangalore.

## References

1. Chen L, Yi H (2020) Optimization of natural frequency for hexachiral structure based on response surface method. *J Vibroeng* 22(7)
2. Spadoni A, Ruzzene M (2007) Numerical and experimental analysis of the static compliance of chiral truss-core airfoils. *J Mech Mater Struct* 2(5)
3. Airoidi A, Bettini P, Zazzarini M, Scarpa F. Failure and energy absorption of plastic composite chiral honeycombs, *WIT transactions on the built environment*, vol 126, *Structure under shock and impact XII* 101
4. Wu W et al (2019) Mechanical design and multifunctional application of chiral mechanical metamaterial: review. Elsevier, *Materials and Design*
5. Barad RS, Nagesh BK, Barad S, Suresh TN (2020) Influence of chiral lattice on modal characteristics of structures. In: *Proceedings of the 3rd national aerospace propulsion conference NAPC-2020*, December 17–19

# Premature and Extended Contact Behaviour of PA 6 and PA 6,6 Gears



S. Vignesh and A. Johnney Mertens

**Abstract** Recently, plastic gears are given higher importance due to their reduced weight, cost-effectiveness, lower noise, and vibration. Among the plastic gears, polyamide (PA) gears are primarily used because of their ability to run under dry conditions. However, while running under such conditions, the lower stiffness of the polymer induces the load-carrying teeth to deform elastically during the engagement. As a result, an extension to the path of contact occurs, i.e. an initial contact at the beginning and a pro-longed contact at the end of the meshing cycle. This extended contact affects the load-sharing ratio, contact stress, and bending stress induced in the gear pair. Furthermore, the contact between the deformed tooth and the adjacent tooth gives rise to pitch line fractures (PLFs) and flank wear. In this work, simulations were done to study the deflection behaviour of the common polymer gear materials, PA 6 and PA 6,6, under elastic loading conditions. The effect of the extended contact on the gear tooth's bending and contact stress behaviour was also investigated.

**Keywords** Finite element analysis · Polyamide gears · Pre-mature contact · Extended contact · Contact stress · Bending stress

## 1 Introduction

Modern gear industry requirements, such as design flexibility, noise reduction, vibration control, and cheap cost, encourage designers to utilize polymer gears for improving performance. However, the sensitivity of the polymer gears, as well as the weaker mechanical characteristics, induces a variety of failure modes [1–3]. Scoring (also known as scuffing) is a type of gear tooth failure caused by the elastic deformation of the gear tooth during dry running conditions.

For a polymer gear, each pair of gear teeth would enter contact earlier than the actual contact and will leave the contact later than the actual end of contact. This

---

S. Vignesh · A. J. Mertens (✉)

Department of Mechanical Engineering, National Institute of Technology Puducherry, Karaikal, India

e-mail: [johnney.m@nitpy.ac.in](mailto:johnney.m@nitpy.ac.in)

initial and pro-longed contact occurring at the start and end of the mesh cycle results in pitch line fractures in the gear tooth.

Seager [4] was the first to investigate the extended contact in gear caused by excessive deflection. The investigation provides an optimal separation distance between two gear teeth was calculated to avoid extended contact. Also, the study insisted on the importance of extended contact in gear scoring failure tests. Wink and Serpa [5] developed a method to estimate the static transmission errors of spur and helical gears due to extended contact. The research concluded that the evaluation of gear transmission error might be inaccurate if the effect of extended contact is neglected.

Lin et al. [6] studied the effect of tooth deflection and flexibility in the static transmission error of gear pair. The impact of pre-mature contact is higher for gears with a higher contact ratio because the extended contact region increases the contact ratio above 2. Walton et al. [7] used the finite element analysis method for contacting gear models to study the gear tooth deflection and contact patterns. Walton et al. [8] also studied the tooth deflection occurring in the plastic gears and suggested backlash allowances to avoid such extended contacts. Singh et al. [9] examined the effects of polymer gear's offline action contact on the contact ratio and load distribution.

Ma et al. [10] developed a finite element model of a geared rotor system with tooth root fracture (TVMS) to examine the impact of extended tooth contact and tooth root crack on time-varying mesh stiffness. The work implied that developing a model that considers the effect of extended teeth is more effective in practice because it could deal with multiple teeth meshing circumstances under high torques and fracture depths. Kirupasankar et al. [11] developed an in-built gear test setup to investigate the effect of deflection on the performance of injection moulded PA 6 and PA 6 nanocomposite gears at different torque levels. The addition of nano-clay to PA 6 reduced the ductility of the polymer gear while enhancing its efficiency. Karimpour et al. [12] conducted a detailed finite element method investigation on the behaviour of Delrin polymer gears. It was stated that the conventional gear-rating standards were not valid for high-friction dry running polymer gears. The report showed an increase in roll angle because of the pre-mature contact. Hoskins et al. studied the effect of friction and temperature at the pitch point and around the region of pre-mature contact for PEEK gears [12].

Transmission error refers to the deviation in the path of contact for a gear pair under loading conditions. Hence, the pre-mature and extended contact plays a significant role in estimating transmission error in polymer gears. Various researchers have mentioned the additional contact of the polymer gears. However, very little work was done to enquire about the behaviour of the gear tooth in the extended contact region. In this article, an extensive investigation was done on the PA 6 and PA 6,6 gears to study the behaviour of gear teeth in the pre-mature contact region. The path of the pre-mature and pro-longed contact was traced, and its effect on the roll angle of the gears was examined. Also, the contact and bending stress induced in each gear tooth pair due to the pre-mature and extended contact were studied.

## 2 Methodology

Table 1 describes the material properties of PA 6 and PA 6,6, and Table 2 describes the specifications of the two-dimensional spur gear model. Only five meshing teeth were modelled to decrease the simulation's computing duration. The following basic assumptions were made during the simulation.

- The material is isotropic.
- The material is linear and elastic.
- The coefficient of friction between the contacting gear teeth is zero.

Planar 2D element was chosen, and plane stress with thickness condition was selected since the face width of the gear is required to calculate the contact stress developed in the gear tooth during meshing. The elastic modulus of PA 6 and PA 6,6 is 2760 MPa and 818.2 MPa, respectively [13, 14]. The Poisson's ratio for both materials is 0.4.

The load was selected such that the contact stress induced in the gear tooth is within the proportional limit of the PA 6 and PA 6,6 gears, respectively. A contact was given between each pair of meshing gear teeth. The driven gear was arrested in all directions, whereas the driver gear was arrested in the horizontal direction. A torque of 4.5 Nm and 15 Nm was applied to the driving PA 6 and PA 6,6 gears, respectively, as shown in Fig. 1.

A mesh convergence study was done, as shown in Figs. 2 and 3, with the surface of the mating teeth meshed to a higher mesh density to allow precise data extraction. A mesh size of 0.03 mm and 0.1 mm was finalized in the contacting gear tooth surface

**Table 1** Material properties

Material	PA 6	PA 6,6
Elastic modulus	2760	818.2
Poisson's ratio	0.4	0.4

**Table 2** Specifications of the meshing gears

Parameter	Driving gear	Driven gear
Pressure angle	20°	20°
Module	2 mm	2 mm
Number of teeth	30	30
Pitch circle diameter	60 mm	60 mm
Base circle diameter	56.5 mm	56.5 mm
Addendum circle diameter	64 mm	64 mm
Dedendum circle diameter	55 mm	55 mm
Face width	17.4 mm	17.4 mm
Gear Hub diameter	28 mm	28 mm

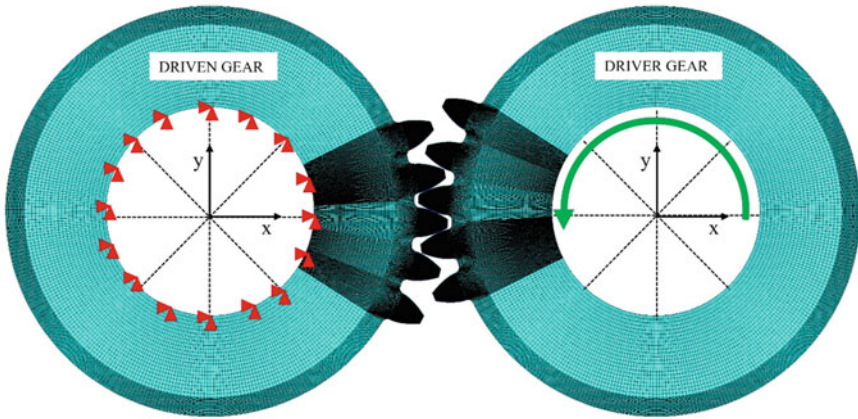


Fig. 1 Boundary conditions of the meshing gears

and the root, respectively. The other gear regions were given an equal mesh size of 0.5 mm.

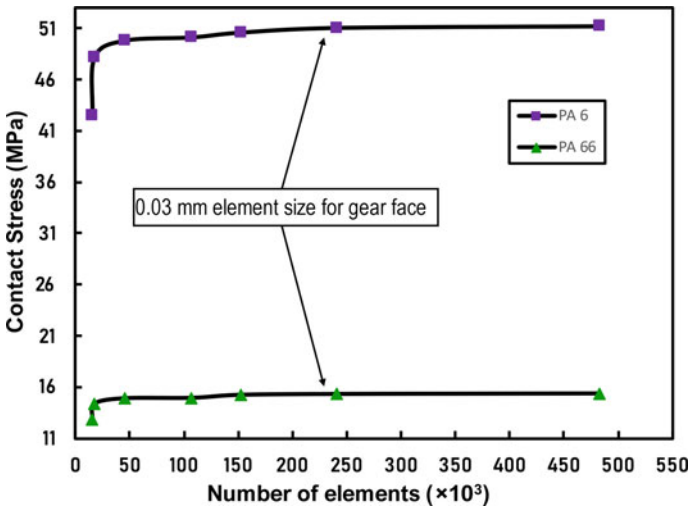


Fig. 2 Mesh convergence study of contact stress for a PA 6, b PA 6,6

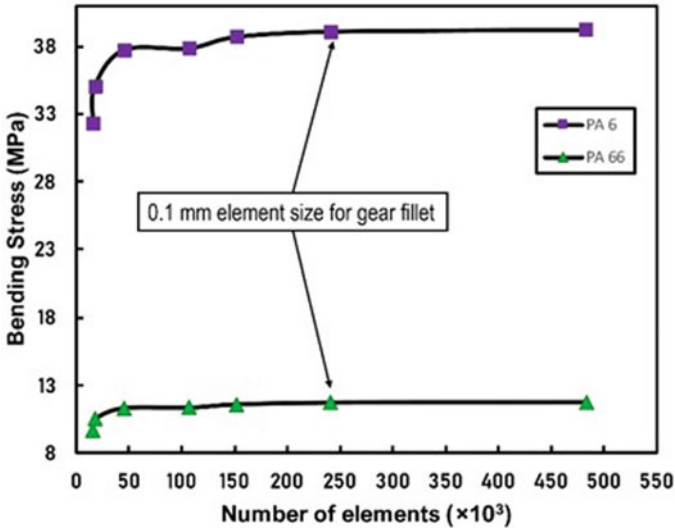


Fig. 3 Mesh convergence study of bending stress for a PA 6, b PA 6,6

### 3 Results and Discussion

Simulations were done for different roll angles of the meshing gear pair with an equal interval of one degree, and the corresponding stresses (contact and bending stress) were computed. Also, simulations were run for roll angles beyond the theoretical value to predict the occurrence of external contact. A mechanism explaining the pre-mature and extended contact phenomena in polymer gears are illustrated in Fig. 4.

#### 3.1 Roll Angle

It was observed that there is an extension in roll angle beyond the theoretical value for both materials. The theoretical roll angle was calculated as  $20.85^\circ$  (per the standards). However, by simulation results, both PA 6 and PA 6,6 gears indicate a roll angle value of  $22.2^\circ$ . An increase of about 6.47% in the roll angle for both the polymer gears was observed. The increased roll angle is a result of higher tooth deflection. The deflected tooth makes contact with the flank of the neighbouring tooth, causing the roll angle of the overall meshing cycle to increase. The result agrees well with Karimpour et al.'s result [12].



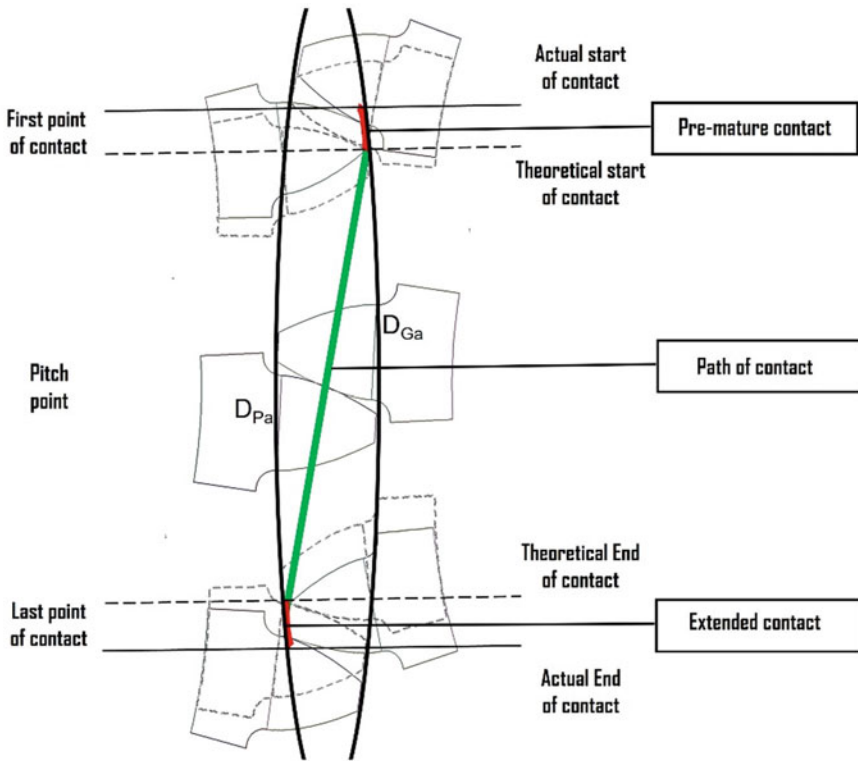


Fig. 4 Pre-mature and extended contact in the PA 6 and PA 6,6 gears

### 3.2 Contact Stress

The nodes in the contact region were extracted, and the maximum contact stress graph was plotted. Fig. 5 shows the contact stress for different roll angles of one complete mesh cycle between the gear pair. Initially, the contact stress rises to 50% of the maximum value and then falls to a minimum in the extended contact region. In the actual contact region, the stress gradually increases and decreases symmetrically to the pitch point, with a maximum contact stress value of 50.5 MPa and 15.2 MPa for PA 6 and PA 6,6, respectively. After the theoretical end of the meshing cycle, the stress value reaches up to 45% of the maximum stress value and again falls to the minimum.

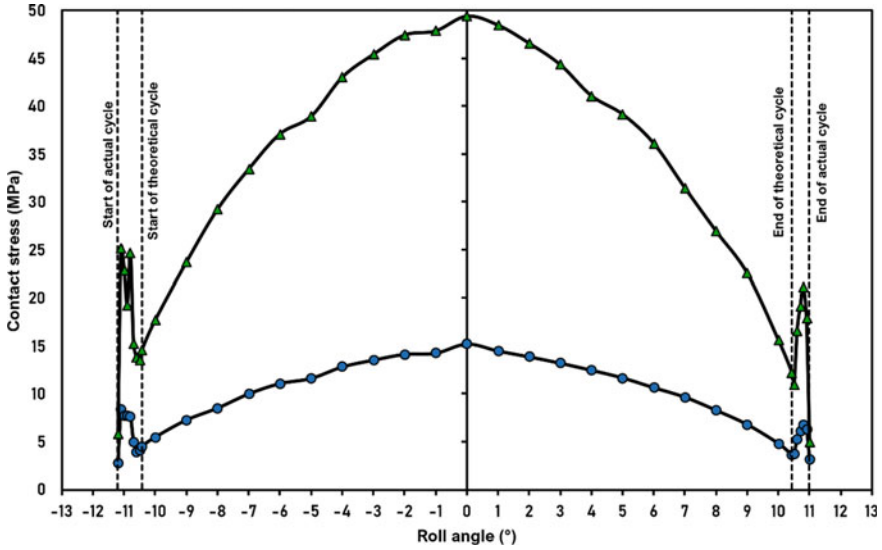


Fig. 5 Comparison of contact stress for PA 6 and PA 6,6 gears

### 3.3 Bending Stress

The same procedure was repeated for plotting bending stress. Nodes were selected from the gear tooth's root region, and the maximum stress during the engagement was plotted. The bending stress predicted by the simulation versus the roll angle is shown in Fig. 6. The graph shows a similar trend to the contact stress. The maximum bending stress occurs at the pitch point with a value of 38.7 MPa and 11.8 MPa for PA 6 and PA 6,6 gears, respectively. Correspondingly, the extended contact in the meshing cycle induces additional bending stress in the root region.

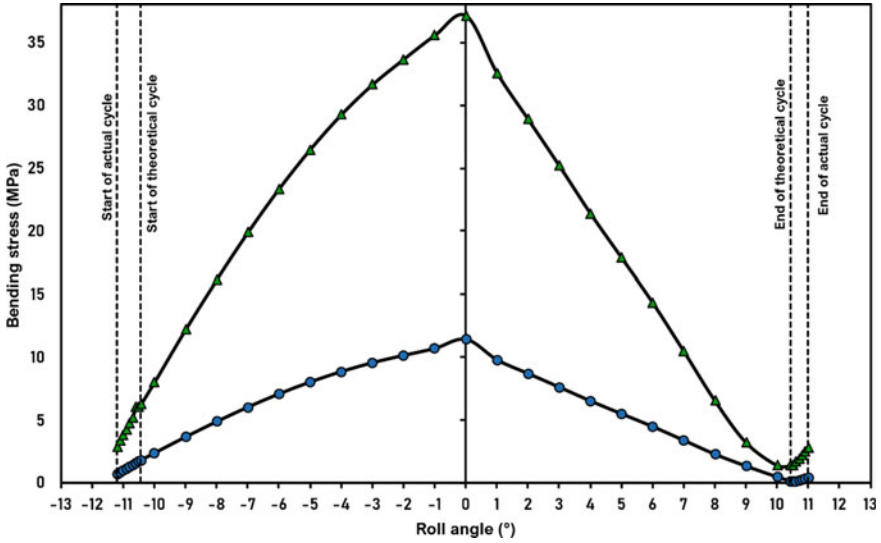


Fig. 6 Comparison of bending stress for PA 6 and PA 6,6 gears

### 4 Conclusion

This article explains the occurrence of pre-mature and extended contact in polyamide gears under dry-running conditions. It also investigates comparing the increased line of contact before and after the meshing cycle for PA 6 and PA 6,6 gears. The detailed results from the simulation are given in Table 3, and the conclusions from the simulation are given below.

- The roll angle had been increased for both materials for a value of  $1.35^\circ$ , i.e. an increase of  $0.773^\circ$  at the start and  $0.573^\circ$  at the end of the cycle.
- Even though both materials have yield strength in a similar range, PA 6 requires a higher load to produce the same amount of extended contact than PA 6,6.

**Table 3** Results of the simulation

Material	Young's Modulus (MPa)	Elastic limit (MPa)	Torque (Nm)	Contact stress (MPa)	Bending stress (MPa)	Theoretical roll angle (°)	Theoretical roll angle (°)		Obtained roll angle (°)	
							POA	POR	POA	POR
PA 6	2760	50	15	50.5	38.7	20.85	10.427	10.427	11.2	11
PA 6,6	820	60	4.5	15.2	11.6	20.85	10.427	10.427	11.2	11

## References

1. Senthilvelan S, Gnanamoorthy R (2004) Damage mechanisms in injection molded unreinforced, glass and carbon reinforced nylon 66 spur gears. *Appl Compos Mater* 11:377–397. <https://doi.org/10.1023/B:ACMA.0000045313.47841.4e>
2. Černe B, Petkovšek M, Duhovnik J, Tavčar J (2020) Thermo-mechanical modeling of polymer spur gears with experimental validation using high-speed infrared thermography. *Mechan Machine Theory* 146. <https://doi.org/10.1016/j.mechmachtheory.2019.103734>
3. Singh PK, Siddhartha AK (2018) Singh, An investigation on the thermal and wear behavior of polymer based spur gears. *Tribol Int* 118:264–272. <https://doi.org/10.1016/j.triboint.2017.10.007>
4. Seager DL (1976) Separation of gear teeth in approach and recess, and the likelihood of corner contact. *ASLE Trans* 19:164–170. <https://doi.org/10.1080/05698197608982790>
5. Wink CH, Serpa AL (2005) Investigation of tooth contact deviations from the plane of action and their effects on gear transmission error. *Proc Inst Mech Eng C J Mech Eng Sci* 219:501–509. <https://doi.org/10.1243/095440605X16983>
6. Lin HH, Wang J, Oswald FB, Coy JJ (1994) Effect of extended tooth contact on the modeling of spur gear transmissions. *Gear Technol* 11:18–25. <https://doi.org/10.2514/6.1993-2148>
7. Walton D, Tessema AA, Hooke CJ, Shippen JM (1994) Load sharing in metallic and non-metallic gears. *Proc Instn Mech Engrs* 208:81–87. [https://doi.org/10.1243/PIME\\_PROC\\_1994\\_208\\_104\\_02](https://doi.org/10.1243/PIME_PROC_1994_208_104_02)
8. Walton D, Tessema AA, Hooke CJ, Shippen J (1995) A note on tip relief and backlash allowances in non-metallic gears. *Proc Inst Mech Eng C J Mech Eng Sci* 209:383–388. [https://doi.org/10.1243/PIME\\_PROC\\_1995\\_209\\_169\\_02](https://doi.org/10.1243/PIME_PROC_1995_209_169_02)
9. Singh A, Houser DR (1994) Analysis of off-line of action contact at the tips of gear teeth. *SAE Tech Papers*. <https://doi.org/10.4271/941761>
10. Ma H, Pang X, Feng R, Song R, Wen B (2015) Fault features analysis of cracked gear considering the effects of the extended tooth contact. *Eng Fail Anal* 48:105–120. <https://doi.org/10.1016/j.engfailanal.2014.11.018>
11. Kirupasankar S, Gnanamoorthy R, Velmurugan R (2010) Effect of apparent area, load, and filler content on sliding friction characteristics of polymer nanocomposites. *Proc Inst Mech Eng, Part J: J Eng Tribol* 224:133–138. <https://doi.org/10.1243/13506501JET648>
12. Karimpour M, Dearn KD, Walton D (2010) A kinematic analysis of meshing polymer gear teeth. *Proc Inst Mech Eng, Part L: J Mater: Des Applications* 224:101–115. <https://doi.org/10.1243/14644207JMDA315>
13. Mohamadi M, Alavitabari S, Aliasghary M (2021) Prediction of mechanical and thermal properties in bronze-filled polyamide 66 composites using artificial neural network. *Polym Bull*. <https://doi.org/10.1007/s00289-021-03751-5>
14. Bernasconi A, Cosmi F (2011) Analysis of the dependence of the tensile behaviour of a short fibre reinforced polyamide upon fibre volume fraction, length and orientation. *Proc Eng* 10:2129–2134. <https://doi.org/10.1016/j.proeng.2011.04.352>

# Effect of Friction Coefficient and Feed Rates on Residual Stresses of Zr-4 Processed by Swaging



Gaurav Singh, V. C. Raghuram, K. I. Vishnu Narayanan,  
Umesh Kumar Arora, and R. Jayaganthan

**Abstract** Zirconium alloy has been extensively used as a cladding material in nuclear power reactors due to its low neutron absorption cross section, excellent tensile properties, fracture strength, and corrosion resistance. The influence of swaging parameters, feed rate (1.25 and 2 m/min), die angle (2–12°), friction coefficient (0.15, 0.2, 0.25, 0.3), and deformation (0–40%) on residual stress induced in Zirconium alloys is investigated numerically and experimentally in the present work. The residual stress in cold worked materials affects significantly their microstructural characteristics, tensile, fracture, and impact properties. The experimental hole drilling method is used to determine the residual stresses on swaged zirconium alloy. A three-dimensional finite element model was implemented in FEA software deform 3D to determine the residual stress in swaged zirconium alloys at different die angles. The residual stress is found to be decreasing with the increasing friction coefficient at the center of the specimen but it increased at the surface of the specimen. The nature of residual stress is compressive at the surface and tensile at the center for all friction coefficients at both feed rates. The optimum swaging parameters (die angle, feed rate, and friction coefficient) were proposed for improving production, achieving better mechanical properties, and lowering residual stresses.

**Keywords** Swaging · DEFORM 3D · Zircaloy-4

---

G. Singh (✉) · V. C. Raghuram · R. Jayaganthan (✉)  
Department of Engineering Design, IIT Madras, Chennai, India  
e-mail: [pankaj.gaurav.singh@gmail.com](mailto:pankaj.gaurav.singh@gmail.com)

R. Jayaganthan  
e-mail: [pankaj.gaurav.singh@gmail.com](mailto:pankaj.gaurav.singh@gmail.com)

K. I. Vishnu Narayanan · U. K. Arora  
NFC Hyderabad, Hyderabad, India

## 1 Introduction

Zirconium alloy has been extensively used as a cladding material in nuclear power reactors due to its low neutron absorption cross section, excellent tensile properties, fracture strength, and corrosion resistance. Zr-2, Zr-4 and Zr-2.5 Nb are the main alloys used as cladding materials. Zr-4 alloy is the main cladding material in pressurized heavy water reactors and it is used as a tube, end caps, end plates, spacer, and pencils. The end caps are manufactured by a rotary swaging process [1, 2]. Due to the high demand for end caps, the influence of swaging parameters has become important in nuclear power reactors. In feed rotary swaging, the workpiece is fed axially inside the set of dies but in the recess swaging process, the workpiece is not fed axially forward or outward [3].

There are several swaging parameters such as feed rate, die angles, friction coefficient, and die stroke that affect the microstructural, mechanical properties, and residual stresses of materials. The die angle has a direct effect on sinking and forging. It can also change the coordinates of the neutral plane according to the material flow. The section of the die has a direct relationship with the feed rate and homogeneity of deformation on the specimen's surface. The important factors in the swaging process such as total force, die angle, type of friction, and value of the coefficient friction could have a principal role in microstructure hardness, material flow, residual stress, and the amount of increased strength of the specimen. There are several works carried out in predicting residual stresses using FEM. Ghai et al. [4] used the finite element to model the rotary forging of the tube and showed that increases in axial feed tend to increase the axial stresses. The increase in residual stress was observed without the mandrel as compared to the mandrel. In another study, Ghai et al. [5] reported that the axisymmetric model provides better prediction of residual stresses in the case of without mandrel as compared to with mandrel. Ameli et al. [6] developed a 3D finite element model for the simulation of radial forging of tubes. This result showed the increase in die pressure and load with increasing friction coefficient. Rong li et al. [3] have studied the effect of feed rates on the strain field of rotary swaging of magnesium alloy using FEM-based modeling. The axial feed velocity can be maximized (to 1.83 m/min) but surface roughness needs to be maintained. S. Ortmann-Ishkina et al. [7] studied the development of residual stresses by infeed rotary swaging with different die angles and calibration lengths. They found that an increase in the die angle caused an increase in the tensile residual stresses but with a decrease in the compressive residual stresses. Liu et al. [8] built a 2D axisymmetric model and investigated the plastic deformation history with friction coefficient values ( $\mu = 0.10$  to  $\mu = 0.35$ ). Material flow and plastic deformation are controlled by the friction coefficient conditions. Liu et al. [9] have studied plastic deformation histories of both aluminum and steel tubes. Higher friction coefficient values results in high plastic strain and good lubrication provide the homogenous distribution of plastic deformation; while poor lubrication leads to more work hardening at the surface as compared to good lubrication.

It is essential to optimize the friction coefficient for achieving lower compressive residual stresses in Zr-4 alloy. There are very few studies on the effect of friction coefficient on residual stresses and no study has been carried out on Zr-4 alloy. This alloy is one of the prominent cladding materials for nuclear applications, so it is essential to carry out this work for a more thorough understanding of the effect of different swaging parameters on residual stresses. Therefore, the present work is focused on simulating the effect of different friction coefficients on residual stress induced into Zr-4 alloy during swaging. In this work, FEM simulation is used to study the effect of friction coefficient and different swaging passes on residual stresses of Zr-4 alloy. The simulation result is also compared with the experimental measured residual stress.

## **2 FEM Simulation**

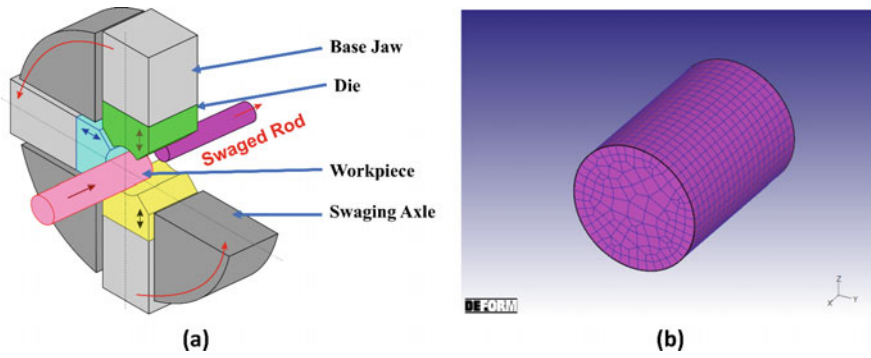
### **2.1 Rotary Swaging**

Rotary swaging (RS) is an incremental forming process used to produce the bars, tubes, wires, and other cylindrical workpieces with reduced cross section, schematically shown in Fig. 1. A series of dies (often 2 to 8) move radially and compress the enclosed workpiece at high frequencies that range from 6800 to 12,000 times per minute. Rotary swaging is considered one of the severe plastic deformation processes. Due to the 2-axial compression and uniaxial tension stress applied to the swaged material, which can efficiently refine the microstructures and enhance the mechanical properties of metallic materials. The advantages of the rotary swaging process are low tooling costs, better surface finish, and more precise dimensional tolerance, saving materials, reducing lead time, and improving product quality [10–12]. Several zones are inside the dies based on the workpiece and die. The sinking zone, the forging zone, and the sizing zone are three sections inside the dies, where the workpiece can be categorized, and the dies can be classified into three sections: reduction, calibration, and exit zones.

### **2.2 Processing Parameters and Simulation Steps**

The integrated manufacturing module of Deform 3D software was used for performing swaging simulation of the test sample. To analyze the residual stress of Zr-4 alloy for various friction coefficients and feed rates, a 3D FEM based on plastic and elastic–plastic formulation is developed using the commercial finite element software DEFORM 3D (12.1, Scientific Forming Technologies Corporation Columbus, Ohio, United States). DEFORM 3D is used to solve large-scale deformation problems





**Fig. 1** a Schematic of swaging process, and b the mesh element is shown in the workpiece of Zr-4 alloy

using the FEM approach, and an automatic mesh generator (AMG) automatically generates an optimum remeshing capability.

The preparation of the FEM model is extensive work and therefore followed a set of guidelines, parameters, and boundary conditions as a process, pass table in the Deform 3D software. The following inputs were given to the pass table to process our simulation run as given in Table 1. A total of 5 passes were defined to reduce the sample diameter from 21 mm to 16.2 mm. We have used Zr-4 alloy as the billet material with an Elastic Modulus of 99 GPa and Poisson’s ratio of 0.37. A rotation of 10° was given after each bite, and a rotation of 180° after each pass was maintained across passes. The object type was elastic–plastic (Assumed strain brick mesh) and the rod was chosen as a diameter of 21 mm and length was 500 mm. The strain brick mesh was used in this simulation with a seed size of 0.5 mm. A contact condition was created, where a shear friction coefficient value of 0.15, 0.20, 0.25, and 0.30 was assigned to the contact surface of the billet and die. Lagrangian incremental criteria were taken in the simulation control module, and deformation mode 0.2 was assigned to the sub-stepping control for max polygon length.

**Table 1** Process parameters for FEM simulation for swaging process

Process parameters	Present case
Die angle	4°
Diameter reduction	21–16.2 mm
Number of passes	5
Feed rates	1.25 m/min and 2 m/min
Friction coefficient ( $\mu$ )	0.15, 0.2, 0.25, and 0.3
Die speed (in the Z direction)	250 mm/second
Rotation per bite	10°
Rotation per pass	180°

### 2.3 Residual Stress Analysis Using DEFORM 3D

Residual stresses in the workpiece are introduced during different passes (5) of swaging processes. The point tracking technique predicts the residual stresses of simulated swaged Zr-4 alloy rods. A total of 20 measuring points were chosen along the diameter of the swaged rod. Firstly, we simulated 5 passes of swaging at a particular feed rate and friction coefficient and then removed the dies from the workpiece. This provides enough time to recover the elastic part of the formulation. After the relaxation phase, the residual stress in the rod was considered the residual stress.

## 3 Experimental Methodology

The through-thickness residual stresses are measured by the hole drilling technique using ASTM E837-13a [13]. This test has been carried out in 4 different steps [14]. The first step is to drill a reference hole at the particular location using gun drilling. The second step is to measure the diameter of the reference hole at specific angles for every 1 mm increment in the depth direction. The third step is to trepanned free of materials away from the reference hole using an electric discharge machine. The final step is to again measure the diameter of the reference hole that helps in calculating the magnitude of residual stress of the material from the degree of deformation seen in the inner core column of the trepanning operation.

The residual stress of 5th passes swaged zircaloy-4 ( $\varnothing 16.2\text{mm}$ ) is measured using this experimental technique and compared with the numerically simulated results for 0.15 friction coefficient and 2 m/min feed rates.

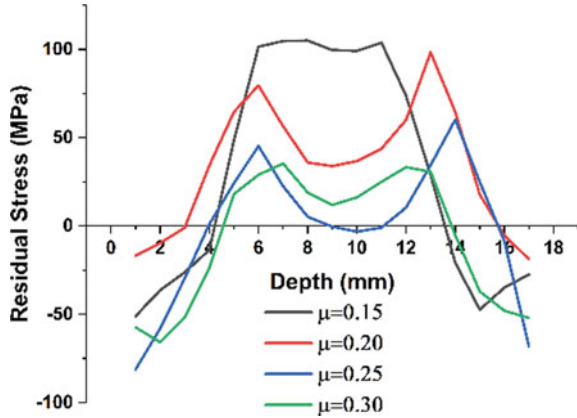
## 4 Results and Discussion

### 4.1 FEM Results

The maximum residual stress decreases with an increased friction coefficient for a 2 m/min feed rate as shown in Fig. 2 till 0.25. It again increases for 2 m/min feed rates, while maximum residual stress decreases with increasing friction coefficient from 0.15 to 0.30 as given in Table 2. This might be due to less contact time between dies and workpieces for higher feed rates while applying more lubricant during swaging process leads to a decrease in maximum residual stress. Residual stresses are observed to increase with increasing the feed rate for each friction coefficient (Table 2). It is due to more strokes of dies on the workpiece and leads to higher residual stress for higher feed rates.

The maximum residual stress values increase from the third to fourth pass and then decreases after the fifth pass (Table 3). On changing the feed rate from 1.25 m/

**Fig. 2** Residual stress variation from surface to center for 2 m/min feed rate and **a** friction coefficient 0.3, **b** friction coefficient 0.25, **c** friction coefficient 0.2, **d** friction coefficient 0.15



**Table 2** Comparison of residual stresses at the center for different friction coefficients

Friction coefficient	Maximum residual stress (MPa)	
	1.25 m/min	2 m/min
0.3	29.48	35.35
0.25	51.0403	60.10
0.2	69.82	98.27
0.15	67.35	104.86

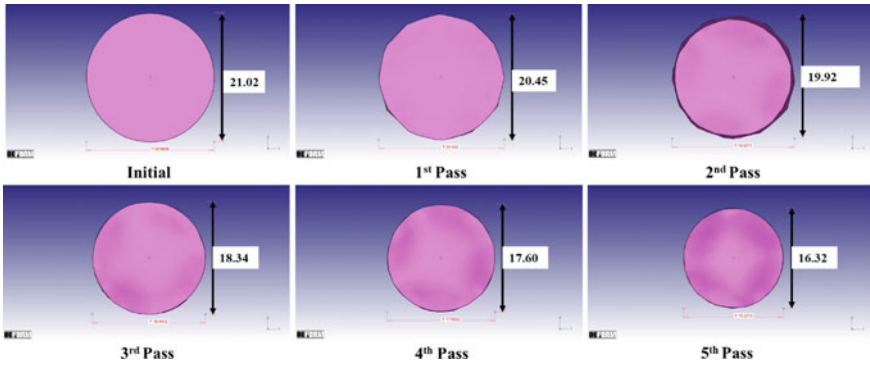
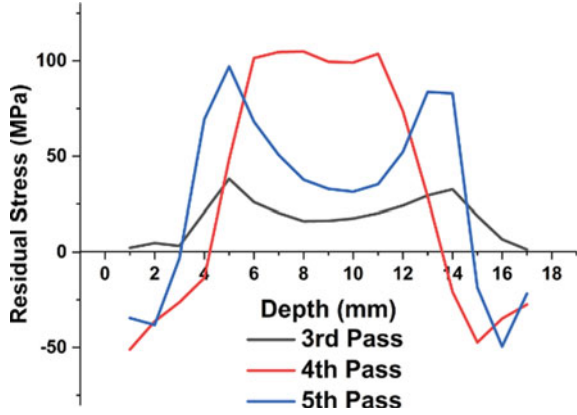
min to 2 m/min, the magnitude of stress values seems to increase after the fourth and fifth pass while it decreases after the third pass (Table 3). With an increase in the number of passes, the magnitude of residual stress becomes uniform from surface to center and again from center to surface. It is also showing compressive residual stresses at the surface and tensile residual stresses at the center (Fig. 3). There is no significant difference in residual stress between the 3rd and 4th pass of swaging as given in Table 3.

For checking the uniformity during the swaging process, the billet’s diameter is measured and compared with the expected diameter. Figure 4a–f shows the billet cross-sectional view after each pass and the diameter is measured in 2 perpendicular directions for the feed rate of 2 m/min and friction coefficient of 0.3. The samples with a friction coefficient of 0.15 resulted in the billet having the closest final diameter to the expected one for both feed rates. The samples with higher friction coefficient

**Table 3** Maximum residual stress comparison at different swaging passes at  $\mu = 0.15$

Swaging pass	Maximum residual stress (MPa)	
	1.25 m/min	2 m/min
3rd	29.48	38.16
4th	67.98	104.86
5th	63.32	97.01

**Fig. 3** Residual stress variation from surface to center for 2 m/min feed rate and friction coefficient 0.3 after **a** third pass, **b** fourth pass, **c** fifth pass



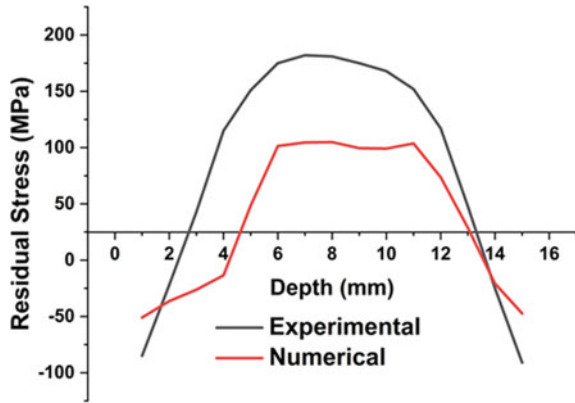
**Fig. 4** Uniformity in final dimension after **a** initial, **b** 1st Pass, **c** 2nd Pass, **d** 3rd Pass, **e** 4th Pass, and **f** 5th pass of swaging

values can reach diameters closer to the expected diameter in the earlier passes. The lower feed rate sample tends to reach the final diameter slower than the higher feed rate case. This effect is more pronounced when using lower friction coefficients.

### 4.2 Numerical Versus Experimental

Experimental and simulation studies of residual stresses are shown in Fig. 5. Residual stress predicted by simulation is comparable with the deep hole drilling technique for 16.2 mm swaged Zr-4 alloy samples (with 0.15 friction coefficient). For swaged alloy with a 0.15 friction coefficient value, the findings of the hole drilling show the tensile stress in the center and compressive stresses at the surface. Numerical modeling for the swaged alloy also indicated tensile stresses in the center and compressive stresses at the surface (in the radial direction). Quantitative measurements of the residual

**Fig. 5** Comparison between experimental and numerical predicted residual stresses at 0.15 friction coefficient



stress magnitude at the surface of the swaged rod using experimental and numerical techniques are comparable.

## 5 Conclusion

In this study, a 3D finite element model based on elastic–plastic formulation is developed using the commercial finite element software DEFORM 3D to analyze the effect of friction coefficient (0.15, 0.20, 0.25, and 0.30) and feed rates (1.25 m/min and 2 m/min) on residual stress induced in Zr-4 alloy. The results of this study can be summarized as follows:

- The maximum residual stress decreases with an increased friction coefficient for 2 m/min feed rate till 0.25 and then again increases for 2 m/min feed rates, while maximum residual stress decreases with increasing friction coefficient from 0.15 to 0.30. This could be possible due applying more lubricant during swaging process leads to a decrease in maximum residual stress.
- Residual stresses are observed to increase with increasing the feed rate for each friction coefficient, so lower feed rates (1.25 m/min) are chosen for the rod without crack. It is due to more strokes of dies on the workpiece and leads to higher residual stress for higher feed rates.
- With an increasing number of passes, the magnitude of residual stress becomes uniform and shows compressive residual stresses at the surface and tensile residual stresses at the center.
- The samples of friction coefficient 0.15 resulted in the billet having the closest final diameter to the expected one for both feed rates. The samples with higher friction coefficient values can reach diameters closer to the expected diameter in the earlier passes. The lower feed rate sample tends to reach the final diameter slower than the higher feed rate case.

- Experimental results show good agreement in the trend of residual stress with numerically predicted residual stresses using DEFORM 3D.

**Acknowledgements** The authors would like to thank the Board of Research in Nuclear Sciences (BRNS), Mumbai, India, for sponsoring this work.

**Funding** This research was funded by the Board of Research in Nuclear Sciences (BRNS), Mumbai, India (Grant no. EDD/16/17/034/BRNS/RJAG).

## References

1. Singh G, Verma R, Vishnu Narayanan KI, Arora UK, Jayaganthan R (2022) Effect of swaging feed rate and annealing phenomena on tensile, fracture toughness and microstructural evolution of Zr-4 alloy. *Mater Sci Eng A* 831:142219. <https://doi.org/10.1016/j.msea.2021.142219>
2. Murty KL, Charit I (2006) Texture development and anisotropic deformation of zircalloys. *Prog Nucl Energy* 48:325–359. <https://doi.org/10.1016/j.pnucene.2005.09.011>
3. Rong L, Nie ZR, Zuo TY (2006) FEA modeling of the effect of axial feeding velocity on strain field of rotary swaging process of pure magnesium. *Trans Nonferrous Met Soc China (English Ed)* 16:1015–1020. [https://doi.org/10.1016/S1003-6326\(06\)60370-1](https://doi.org/10.1016/S1003-6326(06)60370-1)
4. Ghaei A, Movahhedy MR (2008) Finite element modelling simulation of radial forging of tubes without mandrel. *Mater Des* 29:867–872
5. Ghaei A (2007) Die design for the radial forging process using 3D FEM. *J Mater Process Technol* 182:534–539
6. Ameli A, Movahhedy MR (2007) A parametric study on residual stresses and forging load in cold radial forging process. *Int J Adv Manuf Technol* 33:7–17. <https://doi.org/10.1007/s00170-006-0453-2>
7. Svetlana Ortmann-Ishkina BK, Charni D, Herrmann M, Liu Y, Epp J, Schenck C (2021) Development of residual stresses by infeed rotary swaging of steel tubes. *Archive Appl Mech* 91:3637–3647
8. Liu Y, Herrmann M, Schenck C, Kuhfuss B (2019) Plastic deformation components in mandrel free infeed rotary swaging of tubes. *Proc Manuf* 27:33–38. <https://doi.org/10.1016/j.promfg.2018.12.040>
9. Liu Y, Herrmann M, Schenck C, Kuhfuss B (2017) Plastic deformation history in infeed rotary swaging process. *AIP Conf Proc* 1896. <https://doi.org/10.1063/1.5008093>
10. Singh G, Kalita B, Vishnu Narayanan KI, Arora UK, Mahapatra MM, Jayaganthan R (2020) Finite element analysis and experimental evaluation of residual stress of Zr-4 alloys processed through swaging. *Metals (Basel)*. (n.d.). <https://doi.org/10.3390/met10101281>
11. Singh G, Jayaganthan R, Arora UK, Vishnu Narayanan KI, Srivastava D (2020) Texture analysis and fracture behavior of zircaloy-4 processed through swaging. *Metallogr Microstruct Anal.* <https://doi.org/10.1007/s13632-020-00634-5>
12. Singh G, Tiwari A, Agarwal V, Jayaganthan R, Vishnu Narayanan KI, Arora UK, Srivastava D (2020) Tensile and fracture behaviour of Zr-4 alloy processed through swaging. *Trans Indian Inst Met* 73 (2020) 955–965. <https://doi.org/10.1007/s12666-020-01874-3>
13. ASTM (2008) Determining Residual Stresses by the Hole-Drilling Strain-Gage Method, *Stand. Test Method E837-13a*. i 1–16. <https://doi.org/10.1520/E0837-13A.2>
14. Taraphdar PK, Mahapatra MM, Pradhan AK, Singh PK (n.d.) Evaluation of through-thickness residual stresses in narrow gap dissimilar weld joint of ferritic to austenitic stainless steel

# A Comparative Study of Cryorolling and Cryo-Cross Rolling Treatment on Tensile and Fracture Properties of Al 5052 Alloy



Ruby Pant, Amit Joshi, Shushant Singh, Manoj Kumar Pathak, and Saurabh Gairola

**Abstract** In present study, Al 5052 alloy was cross rolled at cryogenic temperature up to a true strain of 2.3. The impact on microstructure, mechanical, and fracture behaviour is then examined. The microstructure is characterised through optical microscopy and TEM, which shows the formation of ultrafine-grained (UFG) structure in cryo-cross rolled (CCR) samples. Reduction in grain size of CCR samples leads to improvement in tensile properties as a direct consequence of the Hall–Petch effect. As the UFG structure is formed, CCR samples demonstrate a simultaneous increment in tensile strength and fracture toughness compared to solution treated (ST) samples and high dislocation density formed during cryo-cross rolling. The conventional rolling at a cryogenic temperature known as cryorolling (CR) was also performed on Al 5052, and the results were compared with CCR. CCR samples revealed higher ductility enhancement from 7.38% to 10.64% for all sample conditions with respect to CR samples because of the change in strain path and recrystallized microstructure. Due to higher dislocation density, the CCR sample indicates higher hardness from 112 to 128HV as compared to CR sample.

**Keywords** Cryo-cross rolling · Tensile strength · Fracture toughness

---

R. Pant · S. Singh

Department of Mechanical Engineering, Uttarakhand University, Dehradun, Uttarakhand 248001, India

A. Joshi (✉) · M. K. Pathak

Department of Mechanical Engineering, G. B. Pant Institute of Engineering and Technology, Pauri 246194, India  
e-mail: [amitiitrebsd@gmail.com](mailto:amitiitrebsd@gmail.com)

S. Gairola

Department of Engineering Design, Indian Institute of Technology, Madras, Chennai 600036, India

## 1 Introduction

Aluminium 5052 is a non-heat treatable aluminium alloy based on magnesium [1]. Due to its combined properties like good strength-to-weight ratio, easy to weld, and high corrosion resistance, aluminium 5052 is used in armour plates, and naval plates [1]. Aluminium 5052 is widely accepted as a replacement for conventional Al 5083 alloy in armour plates. It is a good choice for applications in the marine sector due to its excellent strength and corrosion resistance. [2]. Bergquist et al. [3] compared the static and dynamic response of three aluminium alloys (Al 5059, Al 5083, Al 7039) which are potential candidates for armour plates, and he reported the highest tensile strength in Al 7039, but Al 5059 shows the best combination of strength and corrosion resistance. Izadi et al. [4] have investigated grain development patterns and Hall–Petch strength in Al 5059 samples processed by friction stir welding (FSW) and reported the formation of fine-grained structure in FSW samples. Due to its use in armour plating and ships, a lot of research has been dedicated towards ballistic performance [5] and weld joints [4, 5] of aluminium 5059 alloy, but efforts for improving the mechanical properties are scarce in literature.

The strength of non-heat treated alloys can be improved by using strain hardening and solid solution strengthening [6]. Aluminium 5052 alloy derives its superior tensile strength from high magnesium concentration [7]. Although magnesium is soluble in aluminium, a large amount of magnesium in the alloy causes lower ductility and low corrosion resistance [6, 7]. As a result, strain hardening emerges as the most viable option for enhancing the mechanical characteristics of Al 5052 alloy. A wide range of severe plastic deformation (SPD) processes, such as multi-axial forging (MAF) [8, 9], accumulative roll bonding (ARB) [10], and cryorolling (CR) [11–13], have been developed in recent decades for improving the mechanical properties of metals/alloys. SPD process induces high dislocation density which leads to the formation of UFG structure and thereby improves the mechanical properties [14]. Cryorolling is a relatively simple and inexpensive SPD technique that is used to produce UFG structure in various Al alloys [15, 16] and it has the additional benefit of producing output in sheet form as required in the armour plates. Rangaraju et al. [17] have reported the formation of UFG structure in cryorolled commercially pure aluminium which leads to an increase of 134% in tensile strength. Nikhil et al. [15] have reported an increase of 71.17% in the ultimate tensile strength of Al 5052 alloy accompanied by a simultaneous 600% decrease in ductility. Similar results have been observed in Al 6063 alloy by Panigrahi et al. [18]. An increase of 123% in ultimate tensile strength and a decrease of 600% in ductility is observed after cryorolling. These studies show the increase in mechanical properties like tensile strength, and hardness comes at the expense of ductility. The researcher has demonstrated that the ductility of cryorolled samples can be increased by post-rolled annealing or ageing treatment [14, 16]. Annealing improves the ductility of samples by recrystallization and improves the grain size, but as a direct consequence of this increase in grain size, the tensile strength of samples decreases in annealed samples. Despite cryorolling and post-rolled annealing, a new method known as cryo-cross rolling (CCR) has



emerged for enhancing the strength and ductility of metals/alloys at the same time. The CCR method combines the benefits of cross rolling with cryorolling to give deformed materials the best mechanical qualities under a variety of situations.

Despite the potential of improving mechanical properties by UFG formation in Al 5052 alloy, the literature on SPD processing of Al 5052 alloy by use of the CCR method is really scarce. The present work is focused on improving the mechanical and fracture behaviour of Al 5052 alloy by CCR treatment and correlating the changes in mechanical properties and fracture behaviour with microstructural features. Microstructure in the present study is studied using optical microscopy, and tunnelling electron microscopy (TEM) was used to characterise, the tensile and fracture behaviour after CR and CCR treatment is analysed through the tensile test and three-point bend test, respectively.

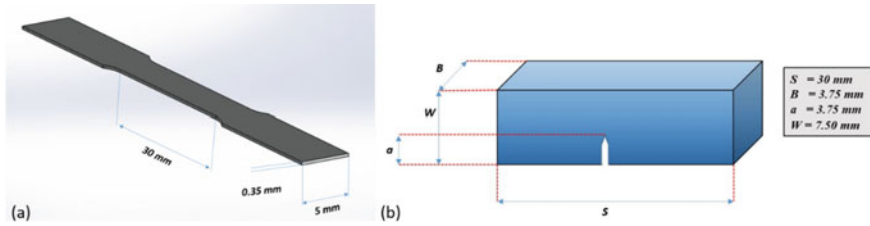
## 2 Materials

For present study, aluminium 5052 was procured in the form of 40 mm thick sheets in T6 temper condition from BAM, Maharashtra, India. The chemical composition of aluminium 5052 alloys is given in Table 1. The samples of 40 mm (length) \* 30 mm (width) \* 10 mm (thickness) were cut from 170 mm (length) \* 110 mm (width) \* 40 mm (thickness) plates. After that, the samples were solution treated for 2 h at 540 °C before being quenched in room temperature water.

These samples were immersed in liquid N<sub>2</sub> for fifteen minutes before going through the rollers, then dipped again for 10 min before each pass until an effective true strain of 2.3 was achieved. Researchers have utilised a similar cryorolling process to create the UFG structure [19]. The microstructure of cryorolled and cross rolled samples was observed through optical microscopy and tunnelling electron microscopy (TEM). Optical microscopy samples were polished using varied grit emery paper sizes up to 2000, followed by cloth polishing using a polishing cloth and an abrasive slurry of MgO. These samples were then etched through Poultons reagent and observed under Leica DMI 5000 using polarised light. As for analysis by TEM, samples were prepared through mechanical grinding using emery paper of various grit size ranging from 250 to 1200 followed by polishing through ion beam milling. At 120 V, TEM was performed on a Philips CM 12 microscope. Various tests, including as tensile tests, hardness tests, and 3-point bend test, are used to find out the mechanical and fracture behaviour of CR and CCR samples. Tensile test samples were manufactured and analysed according to the ASTM E8 sub-size standard on H25K-S Tinius Olsen using a strain rate of  $5 * 10^{-4}$ . Detailed specifications

**Table 1** Composition of aluminium 5052 alloy

Element	Si	Fe	Cu	Mn	Mg	Cr	Zn	Al
Composition (wt. %)	0.21	0.37	0.11	0.09	2.34	0.29	0.11	Balance



**Fig. 1** Specification of: **a** tensile sample and **b** three-point bend sample

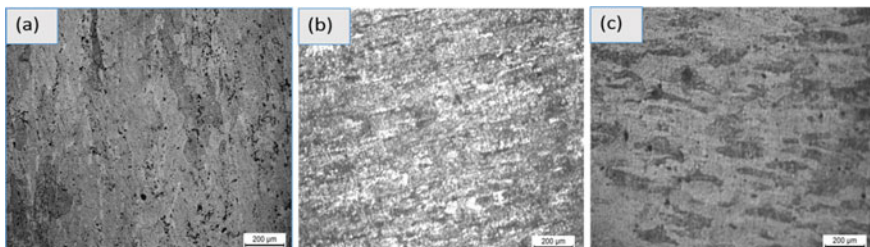
of tensile samples are shown in Fig. 1a. Vickers hardness testing rig was used to measure the hardness of samples by using a five kilogram-force load for a dwell time of fifteen seconds. Hardness is measured in different locations in individual samples, and an average of five readings is taken as a final result. Three-point bend samples were prepared as per American Society for Testing and Materials (ASTM) standard, and the test was performed on H25K-S Tinius Oslen using the special attachment. Specification of 3-point test specimens is shown in Fig. 1b. Field emission scanning electron microscopy (FESEM) study shows the fracture surface after tensile and 3-point bend tests.

### 3 Experimental Procedure

#### 3.1 Microstructure Characterisation

##### 3.1.1 Optical Microscopy

After solution treatment and cryorolling, the microstructure of aluminium 5052 is characterised through optical microscopy and TEM analysis. Figure 2 shows the optical microscopy of samples in different processing conditions. Solution treatment of Al 5052 alloy led to the formation of a uniformly distributed equi-axed structure with an average grain size of  $200\ \mu\text{m}$ , as seen in Fig. 2a.



**Fig. 2** Optical microscopy in diverse processing conditions: **a** ST, **b** CR 90%, and **c** CCR 90%.

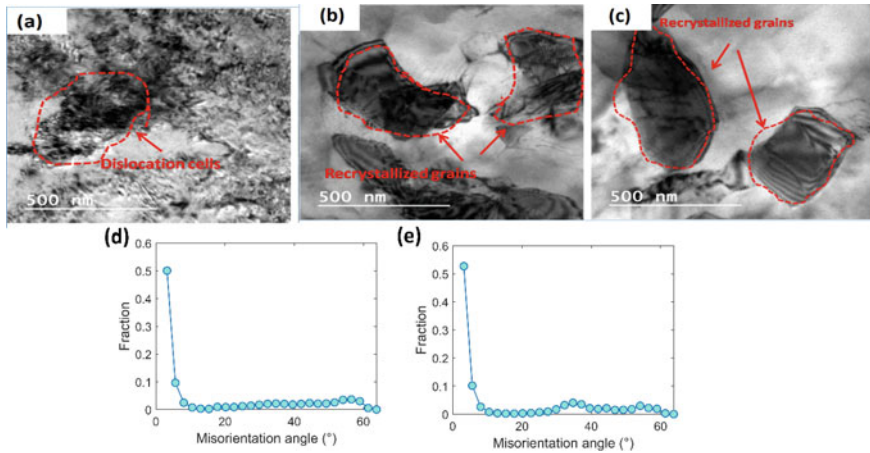
After CR up to 90% thickness reduction, grains become elongated in the rolling direction, as seen in Fig. 2b. Cryorolling leads to the deformation of well-defined grain boundaries formed during solution treatment and converts them into ill-defined deformation cells as described by many researchers [6, 14], but due to the limited magnification of optical microscopy, we need TEM to observe the formation of UFG structure after cryorolling. The optical microstructure of CCR samples with 90% thickness reduction is shown in Fig. 2c. CCR samples showed ill-defined grain boundaries. However, the thickness of the grains is slightly more as compared with CR 90% samples. This may be due to the cross rolling effect resulting wider grain structure as observed in Fig. 2b.

### ***3.2 Tunnelling Electron Microscopy (TEM), and Electron Back-Scattered Diffraction (EBSD) Analysis***

TEM results of CR 90% samples subjected to the true strain of 2.3 are shown in Fig. 3a. CR samples showed entangled dislocation cells and substructures elongated in rolling direction surrounded by an ill-defined grain boundary. The size of these dislocation substructures is well within the UFG regime, as seen in Fig. 3a. Areas with high dislocation density, which is a characteristic feature of all SPD processes can be seen distributed over the whole surface of CR samples [9]. The microstructure of annealed samples differs significantly from that of cryorolled samples. Figure 3c and d depicts the TEM results of CCR samples subjected to a true strain of 2.3. The density of dislocations has decreased even further in these samples, while the size of the dislocation sub-structure has increased. These samples show a significantly lower dislocation density compared to the CR samples, as shown in Fig. 3d. The size and width of grains increases due to the cross rolling effect, as observed in these figures. The misorientation distribution of the cryorolled and cross-cryorolled samples is depicted in Fig. 3e and f, respectively. Misorientation distribution of both CR and CCR samples shows a very high fraction of low-angle grain boundaries (LAGB, grain boundaries less than  $15^\circ$ ). The high fraction of the LAGB can be attributed to the formation of the deformation substructures such as sub-grains in CR and CCR samples.

### ***3.3 Mechanical Behaviour***

Figure 4 and Table 2 show the mechanical properties of Al 5052 alloy in different processing conditions. Aluminium 5052 alloy in ST condition has a yield strength of 81 MPa and ultimate tensile strength of 170 MPa. After cryorolling, yield strength and ultimate tensile strength increase to 157.11 MPa and 289 MPa. So, an increase of 94.35% in yield strength and 70.51% in ultimate tensile strength is observed after

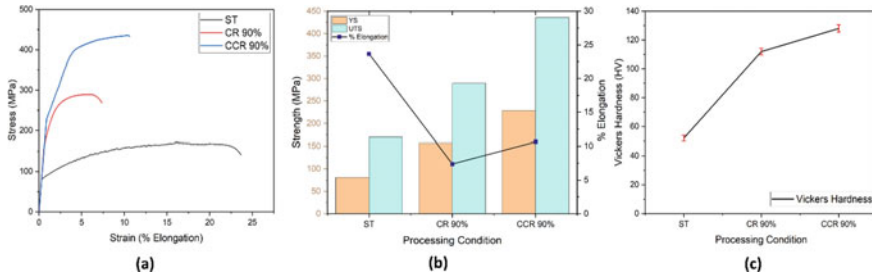


**Fig. 3** TEM micrograph for: **a** CR 90%, **b** and **c** CCR 90%. Misorientation distribution of **a** CR 90% and **b** CCR90%

CR treatment. The main reason behind this increase in tensile strength is the fact that CR leads to suppression of dynamic recovery and results in high dislocation density, as confirmed by TEM analysis. The formation of UFG structure after CR treatment also contributes to this increase in tensile strength, as explained by the famous Hall–Petch relationship, but this increase in tensile strength is at the cost of a decrease in ductility. The ductility of Al 5052 alloy decreased by 68.79% (from 23.65% to 7.38%) after CR treatment compared to ST samples. To neutralise these adverse effects of CR treatment, the samples were subjected to cryo-cross rolling (CCR) treatment. Cryo-cross rolled samples show an increment in yield strength (229 MPa) and ultimate tensile strength (436 MPa), and simultaneously an enhancement in ductility (from 7.38% to 10.64%) is also observed in comparison with CR processed samples. Recrystallization and grain enlargement after CCR treatment can be attributable to these changes in mechanical characteristics, as proven by TEM investigation. So, the CCR samples show a significant increase in ductility with simultaneous enhancement in the strength.

The hardness of the aluminium 5052 alloy follows the same trend as seen in the tensile behaviour of different processing conditions. The hardness variation of Al 5052 alloy under different production conditions is shown in Fig. 4c. Cryorolled samples have more hardness as compared with the solution-treated samples. Vickers hardness of solution treated samples comes out to be 52HV, and after cryorolling, it becomes 112HV. The hardness of Al 5052 alloy is increased to 128 HV after CCR treatment. This increase in hardness is due to higher dislocation density and the creation of UFG structure in cryorolled samples. Similar results have been found for different materials subjected to cryorolling [14].

Scanning electron microscopy (SEM) fractography of tensile samples for different processing conditions is shown in Fig. 5. Figure 5a shows the fracture surface of



**Fig. 4** a Stress–strain curve for ST and CR 90%, CCR 90%. b Variation in tensile properties of Al 5052 for all processing conditions. c Variation of hardness of Al 5052 for all processing conditions

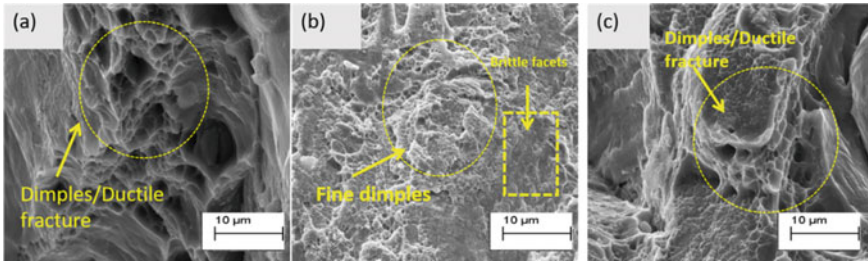
**Table 2** Mechanical properties of Al 5052 alloy under the different processing conditions

Processing condition	YS (MPa)	UTS (MPa)	Elongation at fracture (%)	Vickers hardness (HV)	$K\alpha$ (MPa $\sqrt{m}$ )
ST	81	170	23.65	52	19.45
CR 90%	157	289	7.38	112	23.32
CCR 90%	229	436	10.64	128	34.41

tensile test specimen of solution treated samples. This increase in hardness is due to higher dislocation density and the creation of UFG structure in cryorolled samples. The dimples in the fracture surfaces of samples subjected to various processing condition are marked by the yellow sphere in Fig. 5. In CR samples, the dimples size is significantly lower compared to the solution treated samples which is a clear indication of the formation of UFG structure in CR samples. In addition to the fine size dimples, fracture surface of CR samples also has some areas with fine facets which is indicated by a yellow rectangle in Fig. 5b. So, mode of fracture in CR samples is mixed mode. Cross rolling improves the grain size of CR samples by recrystallization and this has a direct consequence on dimple size obtained in SEM fractograph of tensile samples. Cross rolling increases grain size and hence the dimple size also increases as seen in Fig. 5c. This increase in grain size of dimples is accompanied by decrease in the density of areas with flat facets. These changes in CCR sample clearly depict the higher tendency of cross rolled samples towards ductile fracture.

### 3.4 Fracture Behaviour

Fracture toughness of Al 5052 alloy in different reconditioning condition was analysed through single edge notch bending specimen (as shown in Fig. 1) using three-point bend test. Load-extension curve for the different condition is shown in Fig. 6a. Fracture toughness represents the ability of any material to resist fracture in the presence of a crack. Fracture toughness of aluminium 5052 under different processing

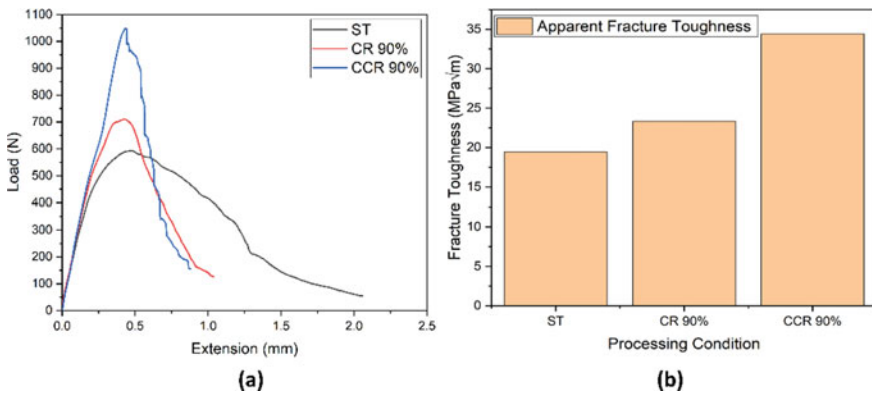


**Fig. 5** Fracture surface morphology of Al 5052 alloy after tensile test: **a** ST; **b** CR 90%; and **c** CCR 90%

condition is shown in Fig. 6b. The procedure used in present study for the determining fracture toughness has already been used by various researchers for different alloys [6, 12, 15]. In three-point bend test, high-intensity tri-axial stress is induced in the samples resulting in failure under low loads.

$$B = 2.5 \left( \frac{K_Q}{\sigma_0} \right)^2 \tag{1}$$

B obtained from the above equation must be lower compared to other parameters like crack length (a), specimen thickness (B) and unbroken ligament (b) If this criterion is met, the calculated fracture toughness is known as plane strain fracture toughness; if the samples do not match the criteria, the fracture toughness is known as apparent fracture toughness.  $K_Q$  in the above equation is calculated by the following formula:



**Fig. 6 a** Comparison of force versus displacement diagram for different processing condition; **b** Comparison of apparent fracture toughness in different processing condition

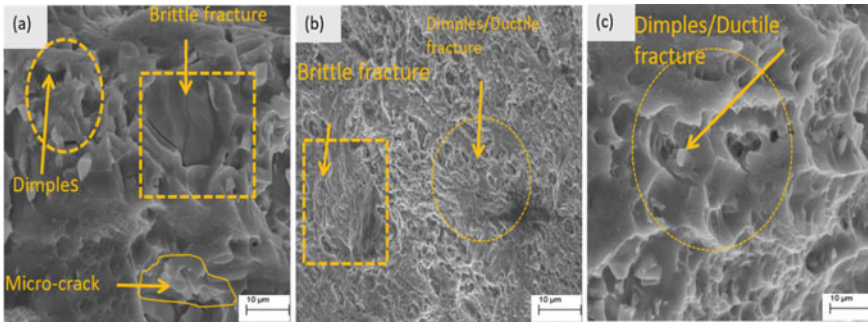
$$K_Q = \frac{P_Q \cdot S}{B \cdot W^{1.5}} \left[ 2.9 \left( \frac{a}{w} \right)^{0.5} - 4.6 \left( \frac{a}{w} \right)^{1.5} + 21.8 \left( \frac{a}{w} \right)^{2.5} - 37.6 \left( \frac{a}{w} \right)^{3.5} + 38.7 \left( \frac{a}{w} \right)^{4.5} \right] \quad (2)$$

Substituting the values of KQ in Eq. 2 or solution treated samples comes out to be 19.45 MPa $\sqrt{m}$ . From Eq. 1, the value of B for all sample conditions comes out to be greater than the thickness of specimen and hence samples prepared in the current study fail to satisfy the criteria and hence fracture toughness obtained in the present study is apparent fracture toughness. Apparent fracture toughness for all processing conditions is shown in Fig. 6b.

Fracture toughness of Al 5052 alloy is improved after CR and CCR treatment. This increment might be due to formation of UFG structure and dislocation tangle zones in the CR and CCR samples as shown by TEM results. However, CCR samples showed the higher fracture toughness parameter (apparent fracture toughness) in comparison with CR and ST samples. According to numerous researchers, high dislocation density and dislocation tangles in CR samples promote a delay in fracture onset [20, 21]. The smaller size of grain in CR samples offers increased resistance to the movement of dislocation during loading leading to higher fracture toughness in cryorolled samples as compared to ST samples. CCR treatment further increases the fracture toughness due to the increase in grain size resulting improvement in crack propagation phase. The improved crack propagation phase leads to the enhanced fracture toughness of CCR alloys as compared to CR and ST alloy.

### 3.5 Fractograph After Three-Point Bend Test

The fracture surface of aluminium 5052 alloy under different processing conditions was characterised by SEM fractography. Figure 7 shows the fracture surface morphology of ST, CR, and CCR samples subjected to a three-point bend test. Solution-treated samples of the fracture surface are shown in Fig. 7a. The fracture surface of solution-treated samples shows a mixture of dimples, brittle facets, and micro-cracks which shows fracture in mixed mode the solution-treated samples. CR sample shows a mixture of flat facets and fine dimples as seen in Fig. 7b which shows the mixed mode of fracture. It might be due to the fact that crack initiation has become easy on account of softening caused by recovery which lowers the fracture toughness values as compared to CCR sample. After CCR, large amount of fine dimples is observed in the fracture surface as seen in Fig. 7c. This indicates that significant amount of plastic deformation has taken place before the failure has occurred in CCR sample resulting significant improvement in resistance to crack initiation and crack propagation phases due to which the fracture toughness of the CCR sample has improved dramatically. It could be related to the establishment of the UFG structure following CCR. A similar observation was made by Joshi et al. [6] during cryorolling and followed by annealing of Al 2014 alloy.



**Fig. 7** Fracture surface morphology of Al 5052 alloy after 3 PB test: **a** ST; **b** CR 90%; and **c** CCR 90%

## 4 Conclusion

The effects of CR and CCR treatment on the aluminium 5052 alloy were explored in this study, and the following results were reached:

- Cryorolled samples have significantly higher tensile strength than ST samples. After cryorolling, YS is increased by 94.34%, while UTS is increased by 70.51%, and this rise in tensile strength is accompanied by a loss in ductility, which has decreased from 23.65% to 7.38 per cent. The formation of UFG structure and high dislocation density is the key factors behind these change in mechanical characteristics.
- The hardness of samples shows a similar trend as tensile strength. The hardness of Al 5052 is increased from 52 to 112 HV after CR, and the value of 128 HV is achieved for CCR-treated samples. This extraordinary improvement in tensile strength and hardness of Al 5052 alloy is attributed to the formation of UFG structure and high dislocation density in cryorolled samples.
- The fracture toughness of samples is also improved after CR and CCR treatment. Apparent fracture toughness value of  $34.41 \text{ MPa}\sqrt{m}$  is obtained in CCR-treated samples and  $23.32 \text{ MPa}\sqrt{m}$  in CR samples. Reduction in grain size after CR and CCR treatment increases resistance to crack initiation in Al 5052 alloy.

## References

1. Yogesha KK, Joshi A, Kumar N, Jayaganthan R (2017) Effect of cryo groove rolling followed by warm rolling (CGW) on the mechanical properties of 5052 Al alloy. *Mater Manuf Process* 32(12):1336–1344
2. Khademian N, Peimaei Y (2020) Lightweight materials (LWM) in transportation especially application of aluminum in light weight automobiles (LWA). In *International conference on interdisciplinary studies in nanotechnology*, pp. 1–22



3. Perez-Bergquist SJ, Rusty Gray III GT, Cerreta EK, Trujillo CP, Perez-Bergquist A (2011) The dynamic and quasi-static mechanical response of three aluminum armor alloys: 5059, 5083 and 7039. *Mater Sci Eng A* 528(29–30):8733–8741
4. Izadi H, Sandstrom R, Gerlich AP (2014) Grain growth behavior and Hall–Petch strengthening in friction stir processed Al 5059. *Metall Mater Trans A* 45(12):5635–5644
5. Showalter DD, Placzankis BE, Burkins MS (2008) Ballistic performance testing of aluminum alloy 5059-H131 and 5059-H136 for armor applications. Army Research Lab Aberdeen Proving Ground MD, 2008
6. Joshi A, Yogesha KK, Kumar N, Jayaganthan R (2016) Influence of annealing on microstructural evolution, precipitation sequence, and fracture toughness of cryorolled Al–Cu–Si alloy. *Metallogr Microstruct Anal* 5(6):540–556
7. Gubicza J, Chinh NQ, Horita Z, Langdon TG (2004) Effect of Mg addition on microstructure and mechanical properties of aluminum. *Mater Sci Eng A* 387:55–59
8. Kapil R, Jayaganthan R, Gairola S, Verma R (2019) Improvement of fracture toughness of ultra fine grained Al–Li 8090 alloy processed through multi axial forging. *Mater Res Express* 6(8):085064
9. Joshi A, Kumar N, Yogesha KK, Jayaganthan R, Nath SK (2016) Mechanical properties and microstructural evolution in Al 2014 alloy processed through multidirectional cryoforging. *J Mater Eng Perfor* 25(7):3031–3045
10. Jamaati R, Naseri M, Toroghinejad MR (2014) Wear behavior of nanostructured Al/Al<sub>2</sub>O<sub>3</sub> composite fabricated via accumulative roll bonding (ARB) process. *Mater Des* 59:540–549
11. Gairola S, Joshi A, Gangil B, Rawat P, Verma R (2019) Correlation of tensile properties and fracture toughness with microstructural features for Al–Li 8090 alloy processed by cryorolling and post-rolled annealing. *Trans Indian Inst Met* 72:1743–1755
12. Pathak MK, Joshi A, Mer KKS, Jayaganthan R (2019) Mechanical properties and microstructural evolution of bulk UFG Al 2014 alloy processed through cryorolling and warm rolling. *Acta Metall Sinica (English Letters)* 32(7):845–856
13. Pathak MK, Joshi A, Mer KKS (2019) Evaluating tensile properties and fracture toughness of Al 2014 alloy processed by different rolling methods. *Mater Res Express* 6(10):105012
14. Joshi A, Yogesha KK, Jayaganthan R (2017) Influence of cryorolling and followed by annealing on high cycle fatigue behavior of ultrafine grained Al 2014 alloy. *Mater Charact* 127:253–271
15. Yogesha KK, Kumar N, Joshi A, Jayaganthan R, Nath SK (2016) A Comparative study on tensile and fracture behavior of Al–Mg alloy processed through cryorolling and cryo groove rolling. *Metallogr Microstruct Anal* 5(3):251–263
16. Pathak MK, Joshi A, Mer KKS (2021) Improvement of tensile and fracture toughness properties of Al 2014 alloy processed by different rolling method followed by post-ageing treatment. *Trans Indian Instit Metals* 74(3):679–689
17. Rangaraju N, Raghuram T, Vamsi Krishna B, Prasad Rao K, Venugopal P (2005) Effect of cryo-rolling and annealing on microstructure and properties of commercially pure aluminium. *Mater Sci Eng: A* 398(1–2):246–251
18. Panigrahi SK, Jayaganthan R (2008) A study on the mechanical properties of cryorolled Al–Mg–Si alloy. *Mater Sci Eng: A* 480(1–2):299–305
19. Pathak MK, Joshi A, Mer KKS, Gupta A (2021) Comparative analysis of tensile properties and fracture toughness of Al 2014 alloy processed by warm rolling and cryo-groove rolling. *Mater Today: Proc* 44 (2021): 1841–1847
20. Pant R, Joshi A, Singh S, Raturi A (2023) Influence of cryo-cross rolling and post-rolled annealing on microstructure and high cycle fatigue properties of Al-5052 alloy. *Metall Microstruct Anal* 12(3):505–514. <https://doi.org/10.1007/s13632-023-00961-3>
21. Pant R, Singh S, Joshi A, Joshi K, Saxena KK (2022) Mechanical performance and characteristics evaluation of material through Cryo rolling process: a review. *Mater Today: Proc* 62:3086–3096. <https://doi.org/10.1016/j.matpr.2022.03.245>

# A Study on Tensile Strength Attributes of Jute Fiber-Reinforced Polyester Composite



**B. S. Keerthi Gowda, B. E. Megha, G. L. Easwara Prasad, R. Abhishek, and R. Velmurugan**

**Abstract** Natural fiber have shown great advantages over synthetic fibers due to the ease of its availability. The alkali treatment for these fibers enhances the surface modification, which improves the adhesion between fiber and matrix in turn greatly enhances the tensile strength. In the present study, tensile strength attributes of alkali-treated jute fiber-reinforced polyester composites of 3-mm and 5-mm thickness were discussed. Here, the NaOH concentration ranges for the treatment of fibers from 5 to 15% at a soaking period of 3 h to 15 h is reported. Results have shown that the optimum tensile strength is obtained for 10% NaOH-treated jute fiber which is soaked for 9 h. Statistical analysis of experimental results contributes to predicting tensile strength at desired fiber volume fraction, NaOH concentration and soaking period. The usage of natural fibers as reinforcement during the manufacturing of composites increases the usage of agricultural debris and byproducts, and farmers can get the benefits from this. Here the artificial neural network (ANN) approach is also adopted to predict the tensile strength attributes beyond the experimental investigation ranges. It resulted in the characterization of tensile strength attributes of jute polymer composite less expensive. ANN exhibited a similar trend as experimental investigation.

**Keywords** Natural fiber · ANN · Mechanical strength · Alkali treatment · Material characterization · Polymer

---

B. S. Keerthi Gowda (✉)  
Dept of Civil Engineering VTU CPGS, Mysuru, India  
e-mail: [keerthigowda@vtu.ac.in](mailto:keerthigowda@vtu.ac.in)

B. E. Megha  
Research Scholar, MITE, Moodbidri, India

G. L. E. Prasad  
Director, MITE, Moodbidri, India

R. Abhishek  
Research Scholar, Dept of Civil Engineering VTU CPGS, Mysuru, India

R. Velmurugan  
Dept of Aerospace Engineering IIT Madras, Chennai, India

## 1 Introduction

The utilization of biodegradable materials in engineering applications has been advancing nowadays due to advancement in science and material technologies. Many researchers are interested in utilizing such recyclable, biodegradable materials as a part of construction materials. The materials which possess certain significant mechanical properties are sufficient for this purpose. Natural polymers like banana, sisal, hemp, flax, bamboo, ramie, jute and other fibers exhibit biodegradable properties. Jute is a natural, eco-friendly fiber material excessively used for the manufacture of several composite materials due to its ease of availability, low cost and its moderate mechanical properties [1]. Jute fiber is one of the most economical and strongest of all natural fibers and the second most produced all around the world. India, Bangladesh, China and Thailand are the major producers of jute in the financial year 2021, India produces over 962 thousand metric tons of jute [2]. West Bengal contributes more jute production all over India along with Bihar, Assam, Orissa, Andhra Pradesh, Tripura and Meghalaya [2]. A major drawback of this fiber is that it absorbs a lot of water and this affects the actual mechanical properties of the fiber. However, natural fibers are elongated structures, as the length of fiber increases it adversely affects the tensile strength property of fiber. Therefore, many research works were carried out to enhance the mechanical property of natural fibers. One of the simplest ways to improve the properties of fiber is by alkali treatment. The different alkalis used for the treatment process are NaOH, KOH, HCL and H<sub>2</sub>SO<sub>4</sub> [3, 4]; these alkali treatments greatly improve the mechanical properties of fiber-reinforced composites, and also it improves the adhesion between fiber and matrix interface. The increase in mechanical strength is obtained by eliminating cellulose, hemicellulose and lignin contents from the fiber through a chemical treatment process. Various chemical treatments like alkali, acetylation and isocyanides improve the adhesive property of fiber and the matrix and also reduce the water absorption capacity of fiber within the reinforced composite.

Alkali treatment of natural fiber on the mechanical properties of composites was studied by Benyahia et al. [5]; they observed improved tensile and flexural properties in the reinforced fiber composite at 7% NaOH concentration. This treatment improves the tensile strength by 30% and the flexural strength by 50% as compared to untreated. The effect of the treated woven jute-reinforced composite was experimentally studied by Karabulut et al. [6]; here, the fibers are soaked in NaOH solution of 0 to 15% concentration for 15 days at room temperature. Mechanical properties like tension, compression and shear properties are analyzed experimentally and statistically by adopting Weibull distribution at an 85% reliability level. The results of this study indicate that surface modification has greatly influenced the mechanical properties of jute fiber-reinforced composites. The effect of alkali treatment of jute fiber on mechanical strength was also studied by Singh et al. (2019) [7], and the NaOH concentration used in their study varies from 1 to 9% at a 2% increase rate. The results of this analysis indicate that the optimum dosage of NaOH required for better performance ranges between 5 and 7% concentration levels. Yasir Khalid et al. [8] have

investigated the tensile strength behavior of composite materials consisting of natural jute fiber and synthetic glass fiber. They analyzed the effect of different sequencing patterns of jute and glass fiber hybrid composite by hand layup method. The experimental results indicated that the achieved tensile strength is directly proportional to the amount of fiber concentration. In other words, at lesser jute fiber concentration, the development of strength will be insignificant. They concluded that the effect of stacking one jute laminate with four laminate layers of glass fiber is equivalent to five layers of glass fiber laminate. Gowda et al. [9] investigated the effect of basalt and pineapple polyester fiber on the mechanical strength development of composites. The origin of basalt fiber is mainly from igneous rock; hence, it can withstand high temperatures. Therefore, in this study, the fire-resistant property of basalt fiber composite is also investigated at different fiber volume fractions (10 to 45%). The theoretical modulus of elasticity was also determined by using the Halpin Tsai Model. The result of this study shows that there is an increase in the properties of fibers with an increase in the fiber volume fraction, on the other hand, increased fiber volume fraction reduces the linear burning rate. Bindusara et al. [10] studied the effect of symmetrical and asymmetrical woven jute fiber orientation on the mechanical properties of the composite. The different types of specimens with different orientation angles like 0°, 15°, 30°, 45°, 60°, 75° and 90° are cast and tested as per ASTM standards. The results of this study conclude that the woven jute-reinforced composite shows better mechanical properties than randomly distributed fiber composite and also they concluded that the strength of the composite increases with the increase in the number of layers and fiber orientation angles, meanwhile it decreases the modulus of elasticity of composite. Prasad et al. [11] studied the mechanical properties of both jute- and banana-reinforced fiber composite. Two different thicknesses 3-mm and 5-mm composite specimens are cast by banana and jute fibers of length 10 mm, which are blended with polyester resin matrix at different fiber volume fractions varying from 5 to 25% and tested for their tensile and flexural strengths. The results of this study indicate that compared to banana-reinforced fiber composite jute exhibits better performance. They finally concluded that the optimum fiber volume fraction required to get better mechanical properties for jute- and banana-reinforced composite fibers is 20% and 25%, respectively. Krishna et al. [12] investigated the mechanical properties of banana and jute hybrid composite at different fiber volume fractions like 5%, 10%, 15%, 20% and 25% by maintaining banana and jute fibers in equal proportion. The optimum fiber volume fraction for tensile strength and flexural strength is 15% and for impact is 25%, respectively. Finally, they concluded that the thickness of composite material has a direct influence on the mechanical strength of the composite. Ramesh et al. [13] have investigated the mechanical properties of natural and synthetic fibers in combination. The tensile, flexural and impact strengths of sisal–jute–glass fiber were investigated in this study. The surface characteristics are observed through scanning electron microscopy, and the results of this analysis indicate that the mixing of natural fiber jute with glass fiber improves the mechanical property of composites. The effect of polyester and epoxy resin matrix embedded with treated jute fibers on the mechanical properties of composite materials was investigated by Gopinath et al. [14], the test specimen consists of 5- and 6-mm-length jute

fibers. These jute fibers are pre-treated with NaOH solution by immersing them in 5% and 10% concentrated solution of NaOH for 24 h. The composite specimens are tested for their hardness, tensile strength, flexure and impact strengths. The results of this analysis show that the 5% NaOH-treated jute-reinforced epoxy composite shows better performance over polyester jute-reinforced composites.

In the field of artificial intelligence, soft computing is the new emerging technology that is used to reduce the complexities associated with real-world problem. Soft computing involves various techniques such as artificial neural network (ANN), machine learning (ML), fuzzy logic (FL) and genetic algorithms (GA). Learning from existing data is the basic working principle for all these techniques. It collects the information that exists within the experimental data set and then it correlates the input with the target data. This information stored is then can be used to predict or forecast the new data sets. Sometimes the conduction of experimental works becomes a tedious process, it consumes more manpower and a lot of time. Therefore, to reduce the risks involved in the practical testing process and also to efficiently utilize the materials and time, many of the researchers were adopting soft computing techniques for their research works. It helped them a lot during analysis and evaluation problems. Ramkumar et al. [15] analyzed the mechanical properties of natural fiber composite such as rigidity, bending and tensile strength of a composite by convolution neural network (CNN). Different natural fibers such as jute, sugar cane, pineapple and banana fibers are examined in this study. By using vacuum-assisted resin molding technique, the specimens are prepared by incorporating nano-fillers to maintain the dimensional stability of the composite. The data required for the CNN model are pre-processed by finite element analysis. The genetic algorithm (GA) is also used to optimize the results obtained from CNN. The accuracy of the model is assessed by using mean square error and absolute percentage error. The results of this analysis show that the developed CNN model along with GA optimizer predicts the fraction volume of composite material; therefore, they suggested that the adoption of the CNN model with GA optimization in the field of materials and structural design is useful. Sulthan et al. [16] have adopted soft computing techniques in their experimental work to predict the mechanical properties of jute fiber-reinforced concrete. They implemented different soft computing techniques like- artificial neural network, support vector regression, and response surface methodology. The statistical investigation of this study shows that the support vector regression performs better than the response surface methodology, and the accuracy of developed ANN models is verified by statistical approaches. Mentges et al. [17] have developed an ANN model to predict the elastic properties of short fibers. Finite element analysis and orientation averaging approaches are also implemented to enhance the prediction accuracy along with the ANN. The results of this study show that in comparison to experimental results, the ANN model provides better elastic properties for short fiber. Rami and Faris [18] implemented the double-integrated artificial neural network approach for the prediction of the mechanical properties of natural fibers. At first, they developed a back propagation neural network (BPNN) model for the prediction of the mechanical properties, and then they developed another model based on a shallow neural network (SNN) for classification purposes. The developed model contains 20

hidden layers and 11 outputs that include Young's modulus, tensile strength, elongation, cellulose and moisture contents. The developed model shows 95.6% prediction accuracy; hence, they concluded that ANN is a robust prediction approach for the determination of mechanical properties of fiber composite.

From the previous research, it is observed that the pre-treatment of fiber enhances the mechanical property of the overall composite and the ANN performs better as a prediction tool in predicting the mechanical properties of composites. Therefore, in this present research work, an attempt is made to predict the tensile strength property of jute fiber-reinforced composite materials whose fiber volume fractions range from 5 to 30% and the jute fibers are pre-treated with 5 to 15% concentration NaOH solution at a soaking period of 3 to 15 h. The soft computing approach of artificial neural networks is also implemented to interpret the experimental data.

## 2 Materials and Methodology

### 2.1 Materials

In this present study, the jute fibers are pre-treated with sodium hydroxide solution, and these fibers are embedded in a polyester matrix. Jute fiber is a biodegradable natural fiber (Fig. 1); therefore, sometimes it is called "green fiber." It is generally used in textile industries for the manufacture of gunny bags, ropes and likewise other products. These plants usually grow up to 12 to 15 feet in height within 3 months of the crop period.

Sodium hydroxide is commonly known as caustic soda. It is an inorganic compound consisting of sodium and hydroxide ions. At ordinary temperatures, it decomposes proteins. It is generally used for pulping wood to make paper and to extract fibers. It bleaches and separates lignin from cellulose in fibers. Care should be taken while handling this alkali solution since it causes chemical burns and it exhibits corrosive nature in the presence of water.

Polyester resins are synthetic condensed resins. It mainly consists of organic acids and polyhydric alcohols. Unsaturated polyester resins are commonly used in sheet molding, bulk molding and laser printing. The main advantage of this resin is its water-resistant characteristic. It is also resistant to chemical attacks, weathering and aging actions. They can withstand high temperatures up to 80 °C. In this present

**Fig. 1** Jute fiber



study, methyl ethyl ketone peroxide and cobalt naphthenate were used as catalysts and hardeners, respectively, with polyester resin to make matrix material.

## 2.2 Methodology

### 2.2.1 Extraction of Jute Fiber

Jute is one of the rainy season crops. It is harvested in the month from June to September. It grows exuberantly in warm and humid climates and requires temperatures between 24 °C and 37 °C. It is best to harvest the plants as early as possible to get good healthy fibers. The plant from 8- to 12-feet high is cut with stickles at or close to the ground level. The harvested plants are left in the field for 3 days to make leaves to shed. The stems are then made up into bundles for steeping in water. Steeping is carried out immediately after harvesting is over. The jute fibers are beneath the bark and it is surrounded by a woody central part of the stem. To extract these fibers, the following step-by-step procedures are adopted which are shown in Fig. 2.

In retting, the bundles of jute stalks are steeped in water at a depth of 60 cm to 100 cm for a period of 8–30 days. It is an intensive process that takes place within the tank where the fibers are loosened and separated from woody stalks. Once the bars separate out easily from the stick or wood and the fibers are ready for extraction. Basic methods include dew retting and water retting. Stripping is the process of removing the fibers from the stalks after the completion of retting. Extracted fibers are then

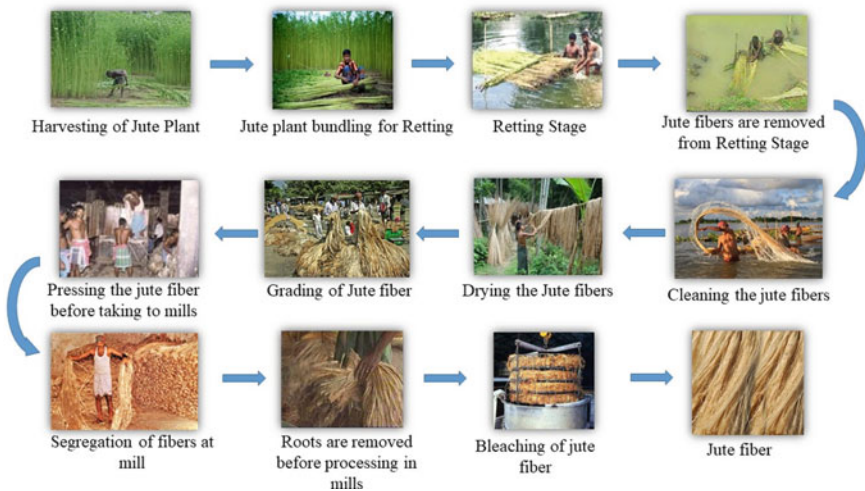


Fig. 2 Extraction process of jute fiber. Source <http://indianjute.blogspot.com/p/jute-jute-cultivation-and-fibre.html>

washed in clean water. The dark color of fibers can be removed by dipping them in tamarind water for 15–20 min and again washed in clean water. After squeezing excess water, the fibers are sun drying for 2–3 days over bamboo railings. After drying, jutes are taken to mills where it is converted into jute yarn.

### **2.2.2 Preparation of Composites**

In the present study, the composite specimens were cast by the compression molding technique. Here, the composite laminates of 3 mm and 5 mm thick were fabricated by using 10-mm-long treated and untreated jute fibers individually. The fiber volume fraction varied from 5%, 10%, 15%, 20%, 25% and 30% to characterize its tensile strength attributes. The treatment of fibers was carried out by soaking them in the NaOH solution for 3, 6, 9, 12 and 15 h of soaking period. This treatment helps to improve the adhesion properties between jute fiber reinforcement and polymer matrix, thereby enhancing the mechanical strength of composites. Treated fibers are then blended with the polyester resin matrix and compressed between two non-sticky plates at the top and bottom. Cobalt naphthenate and methyl ethyl ketone peroxide were used as hardeners and catalyst in the fabrication process, respectively. The mixing ratio of 1:1:100 is adopted for the catalyst, hardener and resins, respectively, to prepare the matrix. To disperse the fibers uniformly the matrix mix was thoroughly agitated, and then it was compressed in a compression molding machine which is preheated to 82 °C.

### **2.3 Tensile Strength Test**

After molding the specimen, it was cut according to ASTM D-3039 by using a laser cutting machine. The testing coupons of 250 mm length and 25 mm width were used to compute the tensile strength of the composites. The tensile strength of composite is conducted by using a computerized universal testing machine (UTM) of 50 kN capacity. The test coupons were placed in the UTM jaws (gripper) and then it is loaded at the rate of 2 mm/min with uniform tensile force until coupon fracture. Care should be taken to avoid any slippage due to poor fixity.

### **2.4 Artificial Neural Network (ANN)**

In the present study, an ANN model was implemented to predict the tensile strength of treated jute fiber-reinforced composite. The ANN is a biologically inspired technique generally used to solve various complex problems where the development of mathematical models becomes difficult. The neural network is modeled based on

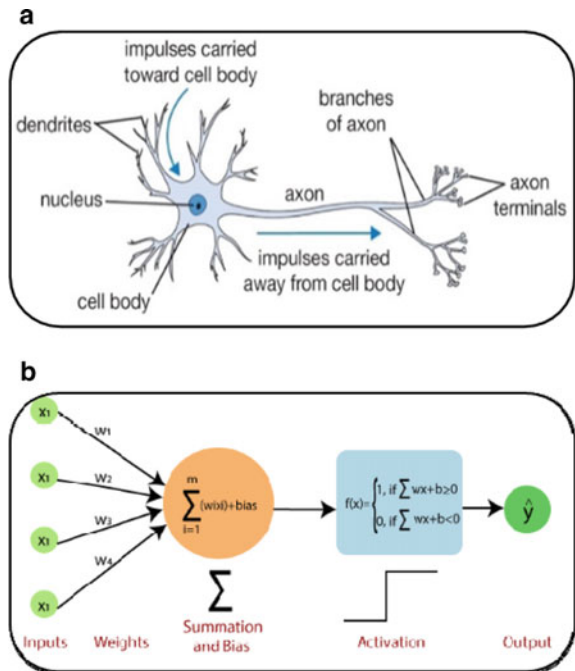


relationships that exist within the domain of variables. Once the model is suitably trained and tested then it is possible to predict the desired experimental data.

A simple artificial neural network consists of 3 layers, an input, a hidden and an output layer. These are very similar to the functioning of dendrites, cell body and axons as in the case of biological neurons work principle, respectively. The overall mechanism of ANN is inspired by the biological functioning of neural networks in human beings. A simple representation of a biological neuron is shown in Fig. 3a, and a simple ANN model with sigmoid activation function is represented in Fig. 3b.

The input layer is the first layer where all the input data are fed to the developed ANN model. The next layer is the hidden layer. It may be a single or group of hidden layers. This hidden layer contains a number of hidden neurons which depends upon the amount of input and output variables and also depends on the accuracy of the desired results. The ANN process initiates from the input layer and ends at the output layer. The data provided by the input layer are multiplied by a suitable weight matrix and then it is passed toward hidden layers. The bias of the network should also be taken into account along with weights. This process is generally referred to as the summation process. After the summation process, outputs obtained are then passed through the activation function, where the interpretation of output data is performed. There are several activation functions employed in ANN; in that, the sigmoid activation function is the most efficient function used for the prediction

**Fig. 3 a** Representation of biological neuron. *Source* [https://www.cs.toronto.edu/~lczhang/aps360\\_20191/lec/w02/terms.html](https://www.cs.toronto.edu/~lczhang/aps360_20191/lec/w02/terms.html). **b** Representation of a simple ANN with sigmoid activation function. *Source* [https://pub.towardsai.net/perceptron-a-basic-neural-net-work-model-for-deep-learning-21aea56e3216](https://pub.towardsai.net/perceptron-a-basic-neural-network-model-for-deep-learning-21aea56e3216)



purpose in the engineering field. Then, the required output is obtained through the output layer [19].

## 2.5 Performance Evaluation Parameter

The performance of the developed ANN model is generally assessed by mean square error (MSE), correlation coefficient (R) and mean absolute percentage error (MAPE). An average error between predicted and actual data is called the mean absolute error (MAE). The correlation coefficient is used to predict the accuracy of the developed model. The value of “R” normally varies between –1 and 1. An accurate prediction of the outputs can be achieved when the “R” value approaches unity. MAPE is a measure of the average percentage error between the predicted and experimental output. The statistical parameters used for the evaluation of the developed model are represented in Eqs. 1 , 2, 3 and 4 [20–22].

$$MSE = \frac{\sum_{i=1}^n (Y_{exp} - Y_{pre})^2}{n} \quad (1)$$

$$MAE = \frac{\sum_{i=1}^n |Y_{exp} - Y_{pre}|}{n} \quad (2)$$

$$R = \sqrt{1 - \frac{\sum_{i=1}^n (Y_{exp} - Y_{pre})^2}{\sum_{i=1}^n (Y_{exp} - \bar{Y}_{exp})^2}} \quad (3)$$

$$MAPE = \sum_{i=1}^n \left| \frac{(Y_{exp} - Y_{pre})}{Y_{exp}} \right| \quad (4)$$

where  $Y_{exp}$ ,  $Y_{pre}$  and  $\bar{Y}$  denote experimental values, predicted Values and mean of experimental values, respectively, and “ $n$ ” represents the number of data involved in statistical analysis.

## 3 Result and Discussions

The results of tensile strength properties of treated and untreated jute fiber-reinforced composites at different fiber volume fractions are discussed in this section. Both experimental and analytical procedures are discussed for each composite specimen.

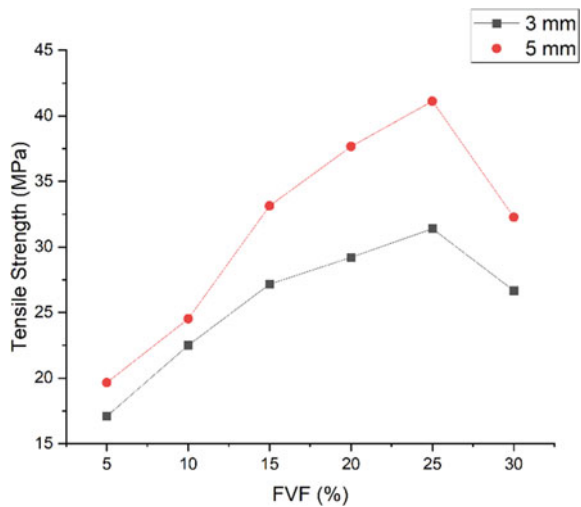
### 3.1 Tensile Properties of Composites

#### 3.1.1 Untreated Jute Composite

Tensile strength of 3-mm and 5-mm-thick composites incorporated with untreated jute fibers at different fiber volume fractions (FVF) of 5% to 30% is determined using a computerized universal tensile testing machine. The effect of variation of FVF on tensile strength properties is represented graphically in Fig. 4. The figure depicts the variation in tensile strength for both 3- and 5-mm-thick specimens. It is evident in the graph that by increasing the fiber content in composites, there is an increase in tensile strength, up to a 25% FVF content. With the increasing thickness of specimens, tensile strength also increases. The optimum tensile strength is 31.39 MPa and 41.11 MPa for both 3-mm and 5-mm-thick fiber composites at 25% fiber volume fraction, respectively.

Up to 10% FVF, both specimens have shown a uniform rate of increase in tensile strength, but between 10 and 25%, 5-mm-thick specimens have shown an enormous increase in their tensile strength compared to 3-mm-thick specimens. Here at 25% FVF, 5-mm-thick specimen recorded 30.96% more tensile strength compared to a 3-mm-thick specimen. Further, both specimens depict a decreasing trend of tensile strength.

**Fig. 4** Experimental tensile strength of untreated jute fiber composite

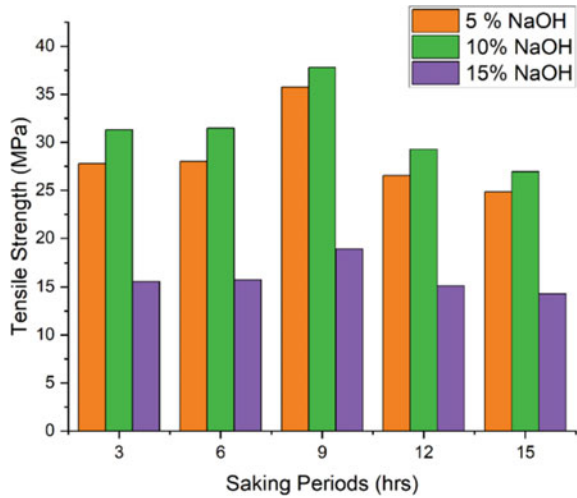


### 3.1.2 Treated Jute Composite

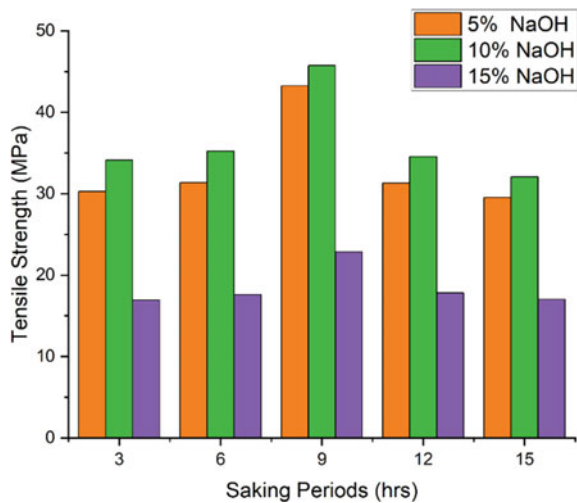
The 25% FVF-treated jute composite gives better results, as evidenced by Figs. 5 and 6. These figures represent the optimum NaOH concentration and the ideal soaking period for 25% FVF-treated jute composite specimens in the 3 mm and 5 mm range.

To analyze the tensile strength behavior of both 3- and 5-mm-thick jute fiber-reinforced polyester composites, a NaOH (alkali) treatment strategy was adopted. Here, NaOH concentration varied as 5%, 10% and 15% for the different soaking periods (3 h, 6 h, 9 h, 12 h and 15 h). Here, FVF of each composite coupon varied from 5%, 10%, 15%, 20%, 25% and 30%, respectively. Figure 6 shows the optimum

**Fig. 5** Experimental tensile strength of treated jute fiber composite of 3 mm



**Fig. 6** Experimental tensile strength of treated jute fiber composite of 5 mm



tensile strength results of 25% FVF-treated jute fibers, this is achieved by soaking the jute fibers in 10% NaOH for 9 h of the time period.

Figure 5 illustrates the tensile strengths of a 3-mm-thick treated jute fiber-reinforced composite. There is a loss of tensile strength of the composite after 9 h of soaking due to higher levels of leaching. The graph also shows that tensile strength increases with increasing NaOH concentration up to 10%. However, above that concentration, tensile strength decreases. The optimum tensile strength value for the composite specimen of 3 mm thickness containing jute which was treated for nine hours in 10% NaOH is 37.80 MPa, which is 20.42% higher than for the untreated jute specimen.

Figure 6 reports the tensile strength of a 5-mm-thick composite containing jute fiber-reinforced composite. The variation is similar to that of a 3-mm-thick jute fiber-reinforced composite. There are significant improvements in tensile strength up to 9 h of soaking time and 10% of FVF. Thereafter, the strength of the composite specimen decreases. The jute fiber treated in 10% NaOH concentration solution and soaked for 9 h duration gives the optimum tensile strength of 45.74 MPa, which is 11.26% more tensile strength compared to untreated specimens.

## 3.2 ANN Modeling

The experimental test results of treated jute fiber-reinforced composites were used to create an artificial neural network (ANN) model. These experimental data are tabulated and separated into two data sets by selecting individual data sets at random for testing and training.

### 3.2.1 Input Values

Out of 180 data sets, 164 were used to create the ANN model. The percentage of NaOH concentration which was used for pre-treatment of fiber and the duration of time in which the fibers are soaked are considered as input parameters along with fiber volume fraction (FVF) and thickness of specimens. The input parameters which were considered for 3 mm thick and 5 mm thick are the same as shown in Fig. 8. Three distinct forms, five different mathematical operators and six different colors are used to interpret the ternary graph. Each shape indicates a different concentration of sodium hydroxide. The square shape is used to represent 5% NaOH concentration, the circle is used to represent 10% NaOH concentration, and the triangular shape represents 15% NaOH concentration. The different soaking hours are represented by using different mathematical symbols which were inscribed within the respective shapes. Each color describes the different fiber volume fractions, all the above-said symbols and their meanings are shown legend of Fig. 7.

Consider a necessary point on the graph to comprehend it. Take, for illustration, the 25<sup>th</sup> value. It has a square form, which reflects a concentration of 5% NaOH. The

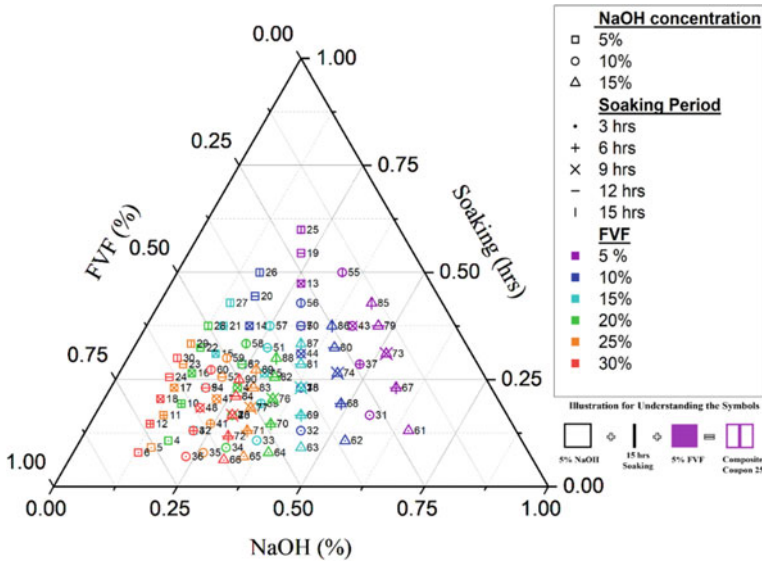


Fig. 7 Ternary diagram representing input parameters of the training process

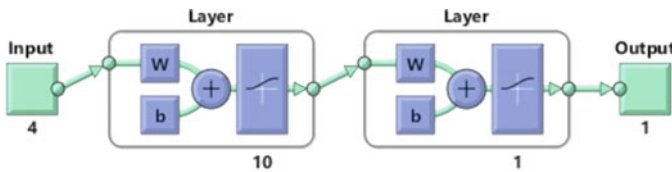


Fig. 8 Neural network architecture

15-h soaking period is shown by the vertical bar inside the square. Finally, the purple color shows that the composite specimen contains a 5 percent fiber volume fraction. All other points on the graph are read in the same way. All input parameters are arranged into a  $164 \times 4$  matrix. This shows four different parameters from 164 data sets that are used as ANN network inputs. This information is saved in the MATLAB workspace for the construction of ANN models.

### 3.2.2 Target Values

The tensile strength of jute fiber-reinforced composite for the respective input parameters is determined from the experimental procedure, and these are used as target values for modeling the neural network in the prediction process. There are 164 target data grouped in a matrix of size  $164 \times 1$  matrix and it is stored inside the workspace to develop an ANN model.

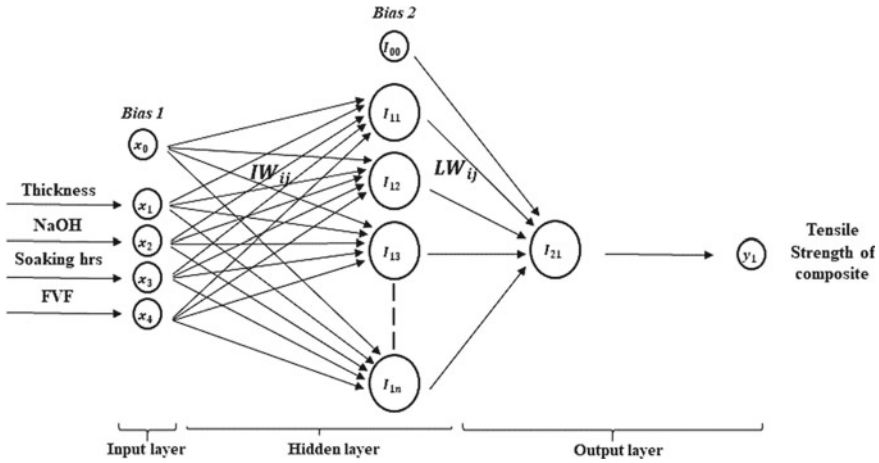


Fig. 9 Developed ANN model architecture

### 3.2.3 Network Architecture

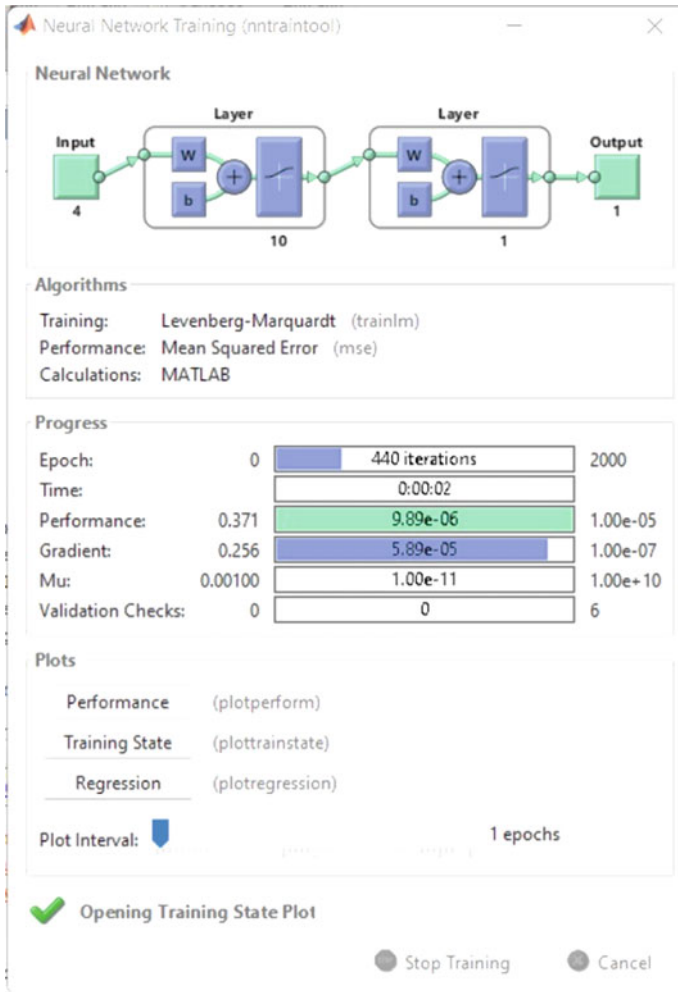
Artificial neural network (ANN) is an effective way to prognosticate the outputs where the mathematical modeling becomes tedious. In this present study, the ANN model is developed by using 164 data sets. The developed model contains 4 inputs in the network, 10 neurons in the hidden layer and one neuron in the output layer. Therefore, the architecture of the developed model is represented as a structure of 4-10-1 which is shown in Fig. 8.

The developed ANN model requires 4 inputs, such as fiber volume fraction (FVF), thickness of composite material and soaking period and NaOH concentration adopted during the pre-treatment of jute fiber. The output required is the tensile strength of the jute-reinforced composite (Fig. 9). For the given input data, the number of hidden neurons is varied until the best fit of data is obtained which contains minimum error between the target and predicted data.

### 3.2.4 Training

Usually, the architecture of the ANN model is decided based on the performance of that model during the training process. The well-trained model shows greater efficiency; therefore, training becomes an important aspect of developing the models. In this present study, the training is done through the Levenberg–Marquardt learning algorithm. The performance is evaluated by using the mean squared error operator. The graphical user interface of MATLAB software is shown below in Fig. 10.

The training is an iterative process; iteration has to be stopped when the desired accuracy is achieved. In the present study, the training process is stopped at the 440<sup>th</sup> epoch by obtaining the best performance at the  $9.8898 \times 10^{-06}$  MSE range. The



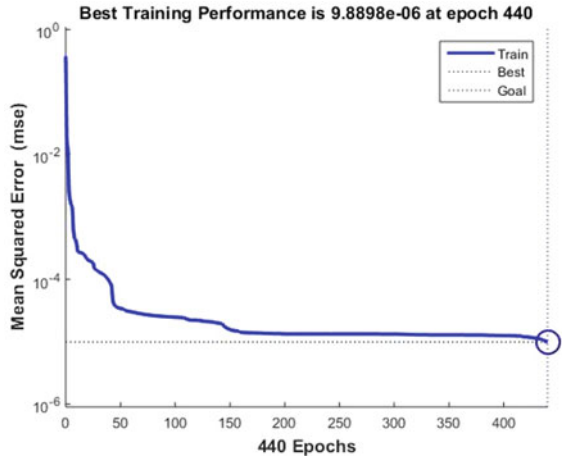
**Fig. 10** The graphical user interface of MATLAB software during training

performance plot is shown in Fig. 11. This illustrates the MSE values at every epoch until the best performance or desired goal is met. The gradual decrease in the slope of the curve indicates the achievement of better performance from the model.

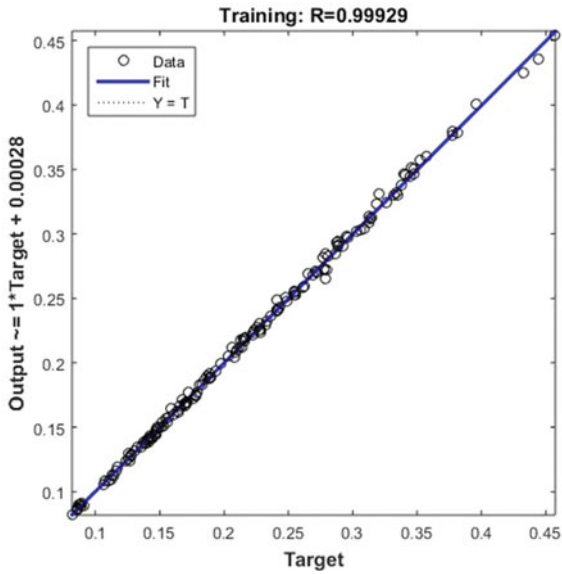
The performance of the developed model is evaluated based on the correlation obtained between the target and the predicted outputs. If the correlation coefficient “R” approaches unity, then the predicted results will be very nearer to actual values. If it is exactly equal to 1, then the predicted results are as same as the actual values. The regression graph for the training data sets is shown in Fig. 12. It represents the better correlation obtained from the developed model.



**Fig. 11** Performance plot for training data sets

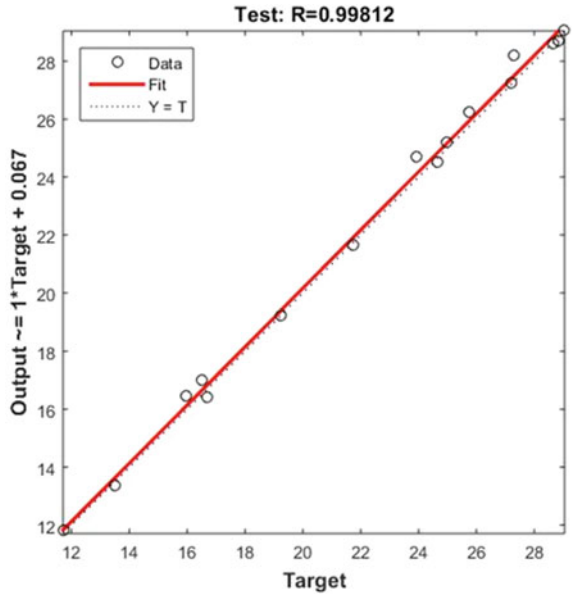


**Fig. 12** Regression plot for the training data set



The correlation coefficient of 0.99929 is obtained during the training process of the ANN network. It is very nearer to unity; therefore, the developed model predicts accurate outputs which are very close to actual/experimental values. Hence, this model is finalized for testing. Testing is conducted for this model to determine the efficiency of the developed model in predicting new data sets which were not used during the training process.

**Fig. 13** Regression plot for the testing data set

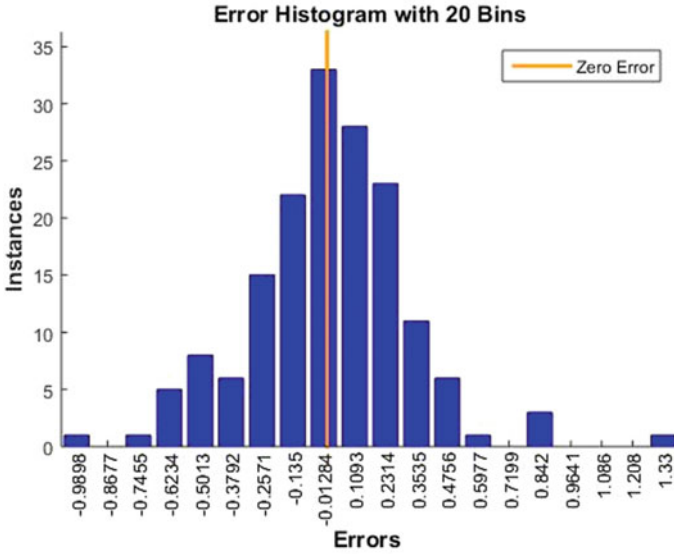


### 3.2.5 Testing and Validation

Once the model achieves the required goal parameters and once depicts fewer MSE values with a correlation coefficient nearer to unity, then that model should be tested and validated for other sets of data which were not used during the training process. This process decides the actual efficient model that best suits the present domain of data sets. In this present work, about 16 data sets were used for testing. Therefore, it serves as a set of new data sets that are going to be inferred from the developed model, to compare the theoretical procedures with the soft computing techniques. The regression plot for the testing process is shown in Fig. 13. The developed model predicts the outputs accurately as compared with actual data sets. The correlation coefficient of 0.99812 is obtained for testing data sets.

### 3.2.6 Model Validation

Statistical parameters were used to validate the performance and efficiency of the developed model, which are shown in Eqs. 1, 2, 3 and 4. Analyzing the differences between actual and predicted values is the most valid way of determining the efficiency of ANN. Figure 14 shows the histogram illustrating the discrepancy between actual and predicted experimental results. Errors involved here were grouped into 20 bins. It is concluded that the predicted values of the developed model are more accurate because the maximum errors cluster nearby the zero axis line.



**Fig. 14** Error histogram

**Table 1** The results of the statistics parameter of ANN testing and training

Statistical error parameter	Training	Testing
MSE	$9.8898 \times 10^{-06}$	$15.2691 \times 10^{-06}$
R <sup>2</sup>	0.99929	0.99812
MAE	0.232997	0.276703
MAPE (%)	1.09002	1.323619

Table 1 represents the statistical analysis of error parameters. The mean squared error (MSE) between experimental and predicted values for training data is  $9.8898 \times 10^{-06}$  and for testing is  $15.2691 \times 10^{-06}$ . The correlation coefficients (R<sup>2</sup>) for training and testing are 0.99929 and 0.99812, respectively. The mean absolute error (MAE) is 0.232997 and 0.276703, and the mean absolute percentage errors are 1.09002 and 1.323619 for training and testing, respectively. Here, it is observed that the absolute errors are less than 2%; hence, it is concluded that the developed model predicts the outputs very accurately.

### 3.3 Model Outputs

Experimental values and the predicted values from the developed ANN model are represented in the form of ternary diagrams as shown in Figs. 15a and 16a for

3-mm and 5-mm-thick composites, respectively. The ternary graph Fig. 15a represents the maximum experimental tensile strength values for 3-mm-thick coupons at different FVF and NaOH concentrations at their respective soaking periods, and the values which are in the parentheses indicate the maximum ANN predicted tensile strength. The experimental and predicted values are similar to each other. The absolute percentage errors between maximum experimental and predicted values are depicted in Fig. 15b. It showed that a 3% error was involved in predicting the tensile strength of 3-mm-thick composite specimens. Therefore, it is concluded that the developed ANN model predicts the output at an accuracy of 97%.

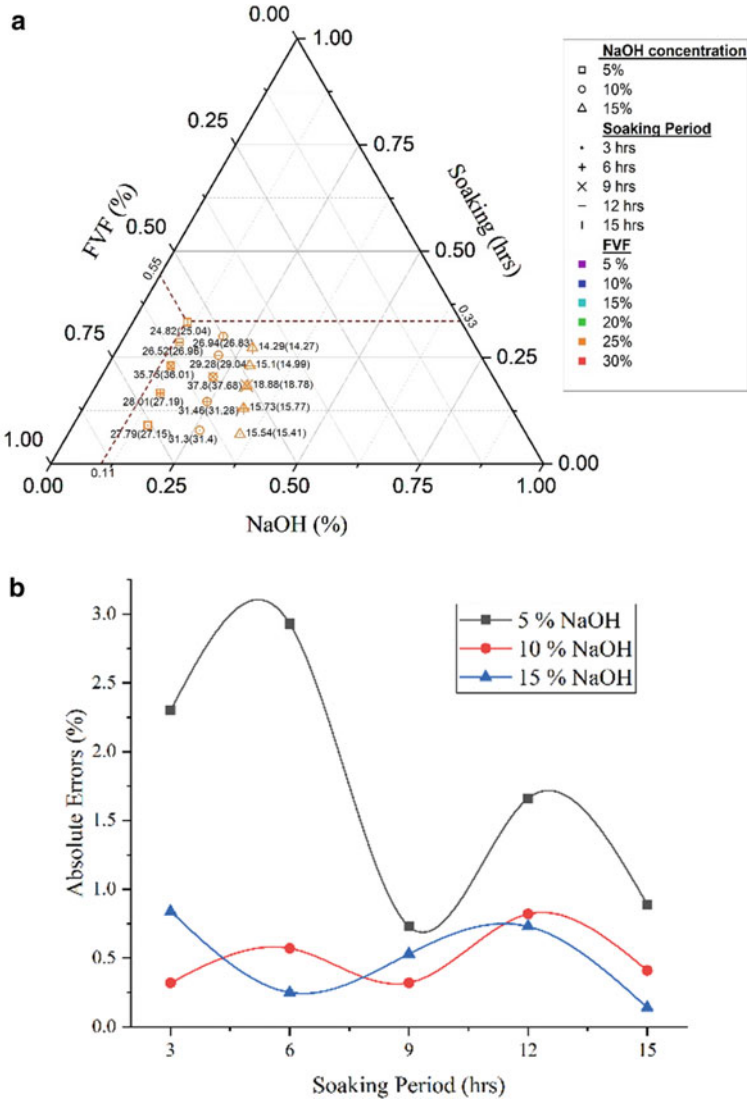
Figure 16a depicts the experimental and predicted values of maximum tensile strength for 5-mm-thick treated jute composite specimens at their respective FVF, NaOH concentration and soaking periods. The predicted results are similar to that of actual values which were indicated within the parenthesis. The absolute percentage errors developed while predicting the tensile strength results of the 5-mm-thick treated composite were depicted in Fig. 16b. The maximum errors involved in the predicted results are less than 3.5%. Hence, the developed model is accepted as an efficient model for predicting tensile strength of 3-mm and 5-mm-thick alkali-treated jute fiber-reinforced polyester composites.

## 4 Conclusions

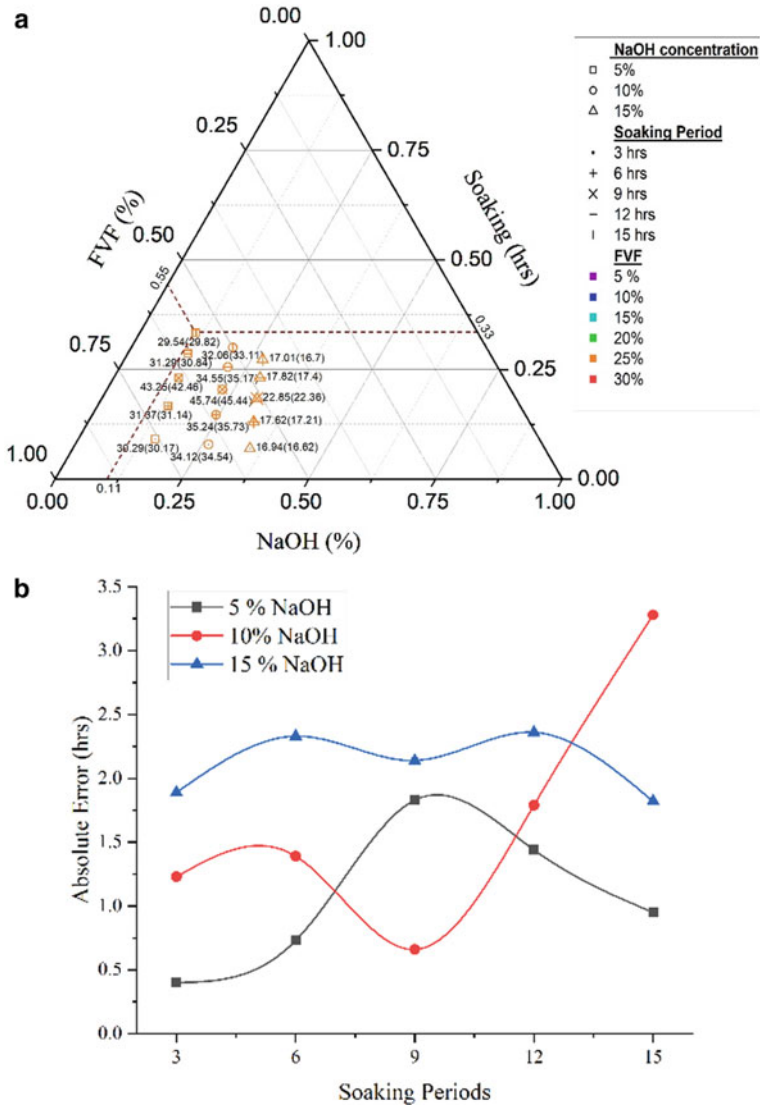
In the present study, an experimental method and an ANN approach are used to determine the tensile strength properties of jute fiber-reinforced composites. A composite specimen of 3 mm and 5 mm thickness were casted and tested at different fiber volume fraction of 5%, 10%, 15%, 20%, 25% and 30%. Pre-treatment of fibers was done by soaking in 5%, 10%, and 15% NaOH solution for 3, 6, 9, 12 and 15 h of soaking period.

The tensile strength of the untreated fiber-reinforced polyester composite increases with the increase in fiber content up to 25% FVF. The optimum tensile strength of 31.39 MPa and 41.11 MPa is obtained for the 25% fiber volume fraction of 3-mm and 5-mm-thick composite specimen, respectively. The treatment of fiber further enhances the tensile strength of a composite by 20.42% and 11.26% which is 37.80 MPa and 45.74 MPa for 3-mm and 5-mm-thick composites, respectively. In the training and testing process, the model has the lowest MSE value of  $9.8898 \times 10^{-6}$  and  $15.2691 \times 10^{-6}$  (i.e., the predicted outputs are closer to actual values). It shows a linear relationship between predicted and experimental results since the correlation coefficients for training and testing are very close to unity.

Taking into account that the MAE and MAPE values of training and testing are less than 2%, the developed model predicts output with 98% accuracy. Using the ANN model, the anticipation of the outcome saves time and energy [23].



**Fig. 15 a** Experimental and predicted tensile strength representation for 3-mm-thick composite. **b** Absolute errors for 3-mm-thick treated jute composite specimen



**Fig. 16 a** Experimental and predicted tensile strength representation for 5-mm-thick composite. **b** Absolute errors for 5-mm-thick treated jute composite specimen

**References**

1. Hossain MR, Islam MA, Van Vuurea A, Verpoest I (2013) Tensile behavior of environment friendly jute epoxy laminated composite. *Procedia Eng* 56:782–8. <https://doi.org/10.1016/j.proeng.2013.03.196>
2. Ministry of textile govt. of India. Production volume of jute goods in india. Stat Res Dep n.d.

3. Latip NA, Sofian AH, Ali MF, Ismail SN, Idris DMND (2019) Structural and morphological studies on alkaline pre-treatment of oil palm empty fruit bunch (OPEFB) fiber for composite production. *Mater Today Proc* 17:1105–11. <https://doi.org/10.1016/j.matpr.2019.06.529>
4. Kalia S, Kaith BS, Kaur I (2009) Pretreatments of natural fibers and their application as reinforcing material in polymer composites-a review. *Polym Eng Sci* 49:1253–72. <https://doi.org/10.1002/pen.21328>
5. Benyahiaa A, Merrouchea A, Rokbib M, Zkouadri C (2013) A study the effect of alkali treatment of natural fibers on the mechanical behavior of the composite unsaturated Polyester-fiber Alfa Abstract : 21ème Congrès Français de Mécanique 2013:1–6.
6. Karabulut N, Aktaş M, Balcıoğlu HE (2019) Surface modification effects on the mechanical properties of woven jute fabric reinforced laminated composites. *J Nat Fibers* 16:629–43. <https://doi.org/10.1080/15440478.2018.1431995>
7. Singh JIP, Singh S, Dhawan V (2020) Effect of alkali treatment on mechanical properties of jute fiber-reinforced partially biodegradable green composites using epoxy resin matrix. *Polym Polym Compos* 28:388–97. <https://doi.org/10.1177/0967391119880046>
8. Khalid MY, Al Rashid A, Arif ZU, Sheikh MF, Arshad H, Nasir MA (2021) Tensile strength evaluation of glass/jute fibers reinforced composites: An experimental and numerical approach. *Results Eng* 10:100232. <https://doi.org/10.1016/j.rineng.2021.100232>
9. Gowda BSK, Naresh K, Ilangovan S, Sanjay MR, Siengchin S (2022) Effect of fiber volume fraction on mechanical and fire resistance properties of basalt/polyester and pineapple/polyester composites. *J Nat Fibers* 19:6074–88. <https://doi.org/10.1080/15440478.2021.1904479>
10. Bindusara TS, Keerthi Gowda BS, Velmurugan R (2018) A study on mechanical properties of symmetrical and asymmetrical woven jute fiber composite polymer. *IOP Conf Ser Mater Sci Eng* 2018:376. <https://doi.org/10.1088/1757-899X/376/1/012070>
11. Easwara Prasad GL, Megha BE, Keerthi Gowda BS (2019) Study of mechanical characteristics of banana and jute fiber reinforced polyester composites. In: Thakre PR, Singh RP, Slipher G, editors. *Mech. Compos. Hybrid Multifunct. Mater.* Vol. 5, Cham: Springer International Publishing; 2019, p. 23–9
12. Krishna Adhikari R, Keerthi Gowda BS (2017) Exploration of mechanical properties of banana/jute hybrid polyester composite. *Mater Today Proc* 4:7171–6. <https://doi.org/10.1016/j.matpr.2017.07.043>
13. Ramesh M, Palanikumar K, Reddy KH (2013) Mechanical property evaluation of sisal-jute-glass fiber reinforced polyester composites. *Compos Part B Eng* 48:1–9. <https://doi.org/10.1016/j.compositesb.2012.12.004>
14. Gopinath A, Senthil Kumar M, Elayaperumal A (2014) Experimental investigations on mechanical properties of jute fiber reinforced composites with polyester and epoxy resin matrices. *Procedia Eng* 97:2052–63. <https://doi.org/10.1016/j.proeng.2014.12.448>
15. Ramkumar G, Sahoo S, Anitha G, Ramesh S, Nirmala P, Tamilselvi M, et al. (2021) An unconventional approach for analyzing the mechanical properties of natural fiber composite using convolutional neural network. *Adv Mater Sci Eng* 2021:2021. <https://doi.org/10.1155/2021/5450935>
16. Sultana N, Zakir Hossain SM, Alam MS, Islam MS, Abtah MA Al (2020) Soft computing approaches for comparative prediction of the mechanical properties of jute fiber reinforced concrete. *Adv Eng Softw* 149:102887. <https://doi.org/10.1016/j.advengsoft.2020.102887>
17. Mentges N, Dashtbozorg B, Mirkhalaf SM (2021) A micromechanics-based artificial neural networks model for elastic properties of short fiber composites. *Compos Part B Eng* 213:108736. <https://doi.org/10.1016/j.compositesb.2021.108736>
18. Al-Jarrah R, AL-Oqla FM (2022) A novel integrated BPNN/SNN artificial neural network for predicting the mechanical performance of green fibers for better composite manufacturing. *Compos Struct* 289:115475. <https://doi.org/10.1016/j.compstruct.2022.115475>
19. Howard D, Mark B (2004) Neural network toolbox documentation. *Neural Netw Tool* 2004:846
20. Paulson AJ, Prabhavathy RA, Rekh S, Brindha E (2019) Application of neural network for prediction of compressive strength of silica fume concrete. *Int J Civ Eng Technol* 10:1859–67

21. Asteris PG, Mokos VG (2020) Concrete compressive strength using artificial neural networks. *Neural Comput Appl* 32:11807–26. <https://doi.org/10.1007/s00521-019-04663-2>
22. Kulkarni P, Londhe SN, Dixit PR (2019) A comparative study of concrete strength prediction using artificial neural network, multigene programming and model tree. *Chall J Struct Mech* 5:42. <https://doi.org/10.20528/cjsmec.2019.02.002>
23. Solanki S, Gangwal S (2019) Prediction of compressive strength of high-volume fly ash concrete using artificial neural network. *Int J Sci Res Eng Trends* 5



# Residual Properties and Failure Characterization of Glass/Epoxy Laminates: Effect of Slender Filler Reinforcement



Manoj K. Singh and R. Kitey

**Abstract** Effect of slender filler reinforcement on post-impact residual properties of beam specimens, prepared by woven glass fabrics, is studied. The epoxy matrix is reinforced with slender glass fibers at low volume fractions and used to prepare the laminates. The specimens machined from unreinforced (UR) and slender filler-reinforced (SFR) laminates are subjected to 5 J and 12.5 J impact energies. While at lower energy, the influence of short fiber reinforcement on impact resistance and elastic characteristics is only marginal, a significant rise in damage resistance and elastic response of SFR laminate is observed at higher energy level. The quasi-static flexural tests conducted on pristine and impacted samples reveal significant improvement in residual mechanical properties due to the slender filler reinforcement. Micrographic analysis exhibits lesser damage in SFR laminate as compared to unreinforced one, especially at higher impact energies when multiple interlaminar delaminations are observed in the laminate.

**Keywords** Glass fiber · Laminated composite · Slender filler · Impact · Residual properties

## 1 Introduction

Glass fiber-reinforced polymer composite is extensively employed in various high-performance usages including aerospace, naval and wind turbine industries, owing to its higher specific mechanical characteristics. Their weaker transverse attributes remain a consistent nagging challenge, especially under the low-velocity impact, which usually produces unobtrusive damage to the structure. These damages deteriorate the load transferring ability of the structure, therefore raising concern about structural integrity and reliability. Several techniques, such as z-pinning [1, 2], three

---

M. K. Singh (✉) · R. Kitey

Department of Aerospace Engineering, Indian Institute of Technology Kanpur, Kanpur 208016, India

e-mail: [manojmsk@iitk.ac.in](mailto:manojmsk@iitk.ac.in)

3-D weaving and braiding [3, 4], micro and nano size particle reinforcement [5–7], are used to enhance out of plane mechanical, fracture and post-impact residual characteristics of the laminates. Whereas to access the post-impact residual properties usually compression after impact, test protocol is used [6]. Santiuste et al. [8] studied beam impact and flexural after impact behavior of glass fiber/polyester laminated composite. They reported that impact damage dissipation energy increases with increase in incident energy while flexural strength reduces. They also reported matrix crack and fiber fracture as major damage mechanisms above a critical impact loading. Recently, Hu et al. [9] used very thin multi-wall carbon nanotubes (MWCNTs), micro and nano size aramid fibers, chopped poly (phenylene-2,6-benzobisoxazole) (PBO) fibers, and 3–8-nm-thick multilayer graphene as reinforcement in carbon/epoxy laminate. They conducted low-velocity plate impact and reported, micro and nano size aramid fibers, PBO fibers and MWCNTs reinforcement reduces impact damage significantly. They also outlined that while all types of reinforcement enhance residual strength, the greatest compressive strength was noticed for aramid fiber and MWCNT-reinforced laminate before and after the impact, respectively. Jefferson et al. [10] investigated the impact behavior of plain weave glass fabric/epoxy laminate reinforced with chopped glass fiber mat in the interlaminar region. They used two types of laminate configuration, alternatively stacked randomly oriented chopped glass fiber mat and woven fabric, chopped fiber core sandwich laminate. They reported that alternatively stacking of chopped fiber mat offers better hindrance to damage propagation, while sandwich laminate gives better impact and post-impact residual tensile properties. Hu et al. [11] utilized chopped kevlar fibers of 3 mm length to reinforce epoxy system of carbon prepreg laminate at an equivalent weight of 10 g/m<sup>2</sup> and conducted low-velocity impact test. They reported higher damage area at higher impact energy, with no effect of reinforcement on it. Whereas kevlar fiber reinforcement shows higher residual compressive strength at all impact energies.

From the literature survey, it is learned that numerous techniques have been used to improve impact characteristics of laminated composites, where reinforcing matrix of laminated composites by using slender fillers is sparsely traced. Usually, compression after impact (CAI) tests are performed to estimate residual properties of laminates, even though it requires a sophisticated robust, and precise testing system. In this investigation, a simple, new flexural after impact (FAI) testing method is used to characterize the post-impact flexural behavior of the slender glass filler-reinforced laminated composite.

## 2 Experimental Details

### 2.1 Materials and Laminate Fabrication

Plain weave glass fabric of area density 450 gm/m<sup>2</sup> is used to prepare 16-ply polymer-reinforced laminated composite. Reinforced epoxy system is developed by embedding it with slender glass fibers of 6 mm in length and 16 μm in diameter. First, Diglycidyl Ether of Bisphenol-A (DGEBA) resin is degassed and impregnated with the slender fillers at the requisite quantity. Then Methyl Tetra Hydrophthalic Anhydride (MTHPA) curing agent is added to the resin-fiber mixture at 1:1 resin/curing agent weight ratio. A little amount of 2,4,5-tris[(dimethylamino)methyl]-Phenol is used to accelerate polymerization process. Glass slender fibers are added at 3% volume fraction of the matrix. Prepared matrix system is employed to fabricate laminate using hand layup technique and cured in a vacuum-assisted hot press machine. Two types of matrix systems are used in this investigation, unreinforced matrix and 3% slender filler-reinforced matrix and denoted as “UR” and “SFR,” respectively, in the manuscript.

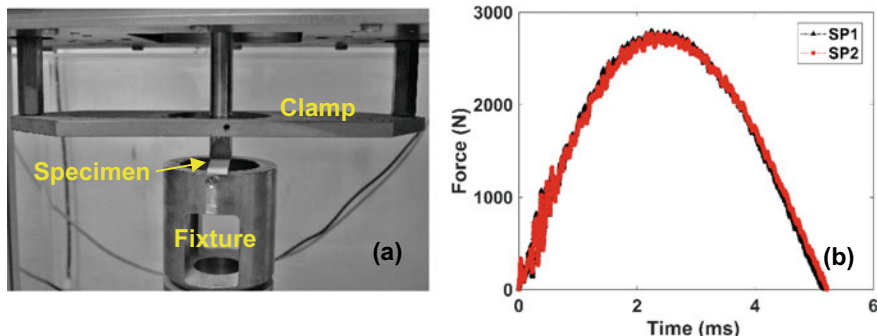
### 2.2 Impact Test

Low-velocity impact tests on beam samples are performed following ASTM D7136 standards [12] using INSTRON CEAST 9340 machine. Beams of dimension 110 × 16 × 4.5 mm are cut from the prepared laminates. Samples are clamped on the fixture with a circular opening of 75 mm diameter and impacted at mid-span similar to three point bend configuration. Impactor tip insert of V-shape with 6 mm nose diameter and 20 mm width are used to impact the specimen at two impact energies viz. 5 J and 12.5 J. Figure 1a depicts fixture of the machine with mounted specimen in unclamped position. At least three specimens are impacted for each case and data are acquired from instrumented Tup at a sampling rate 100 kHz. Force history retrieved at 5 J loading shown in Fig. 1b, illustrates well-shaped curve with excellent repeatability of test data. Following Eqs. (1), (2), and (3) are used to calculate velocity (v(t)), displacement (δ(t)) and energy absorbed (E(t)), respectively, from the force history.

$$v(t) = v_0 + gt - \int_0^t \frac{F(t)}{m} dt \quad (1)$$

$$\delta(t) = \delta_0 + v_0 t + \frac{gt^2}{2} - \int_0^t \left( \int_0^t \frac{F(t)}{m} dt \right) dt \quad (2)$$

$$E(t) = \frac{1}{2} m v_0^2 - \frac{1}{2} m (v(t))^2 + mg \delta(t) \quad (3)$$



**Fig. 1** a Specimen mounted (unclamped position) on impact test fixture b repeatability of force history at 5 J loading

where variables with subscript “0” represents their value at beginning of the impact event, i.e., at time  $t = 0$ , when the impactor tip meets the specimen at first. The integration in all the above equations is performed following Simpson’s 1/3rd rule.

### 2.3 Four-Point Bend Test

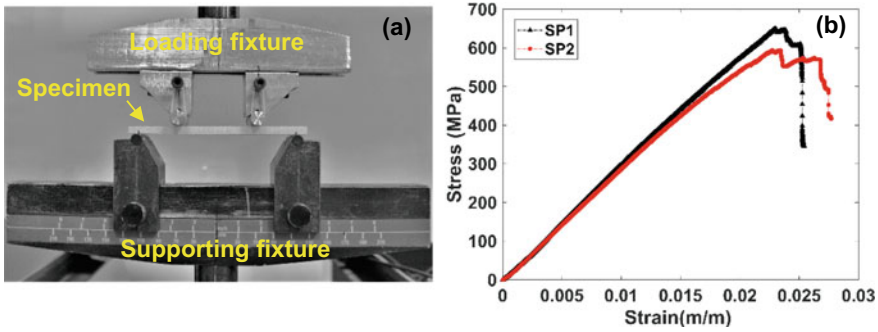
Symmetric four-point bend tests on impacted and pristine samples are conducted following ASTM standards [13]. Specimen is mounted on the fixture with 88 mm and 44 mm support and loading span, respectively, in a configuration so that the impacted surface is under flexural tension as shown in Fig. 2a. Minimum three specimens are tested for each case, in stroke governed mode at a rate of 1 mm/min. Following Eqs. (1) and (2) are used to calculate flexural stress and strain, respectively, from force–displacement history obtained from the tests. Figure 2b represents flexural stress–strain curve for UR pristine laminate, where initial linear relation between stress and strain along with very good repeatability in the data is observed.

$$\sigma_f = (3 P L / 4 b h^2) \tag{4}$$

and,

$$\varepsilon_f = 6 \delta h / L^2 \tag{5}$$

In the above equations,  $b$  and  $h$  represent specimen width and thickness, respectively. Whereas  $P$ ,  $L$  and  $\delta$  stand for force, support span and specimen deflection at loading point, respectively.



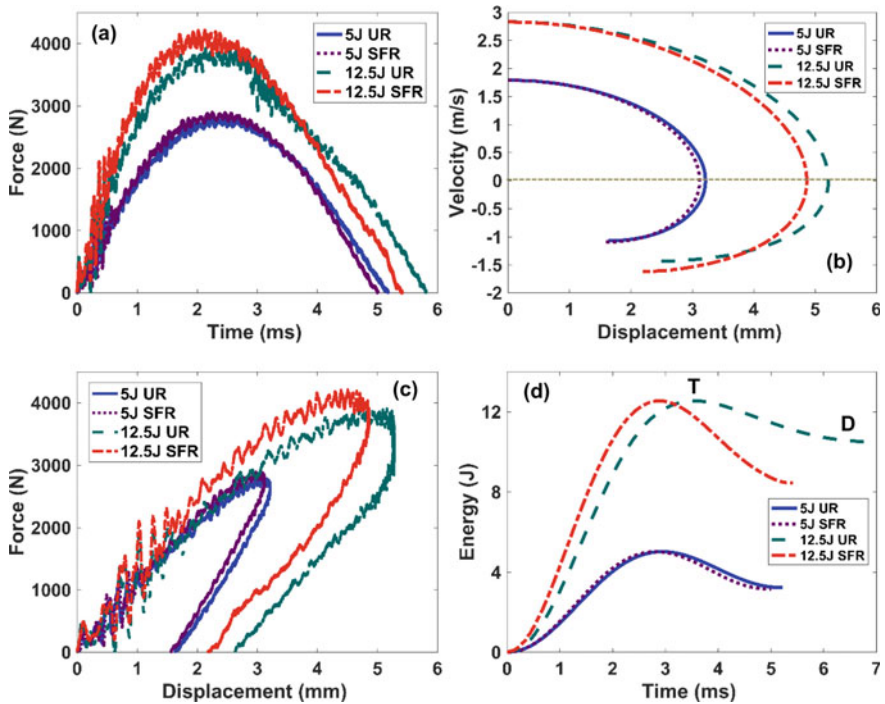
**Fig. 2** a Specimen configuration in four-point bend test fixture, b flexural stress–strain plot of unreinforced pristine sample

### 3 Discussion on Test Results

#### 3.1 Low-Velocity Impact Behavior

Figure 3a represents force–time history at 5 J and 12.5 J incident energies. Multiple oscillations in the ascending part of the curve indicate initiation and/or propagation of the damage in the laminate, where the first significant minor peak suggests the first failure in the laminate. While increased amplitude of these undulations at higher impact energy is observed (see Fig. 3a), slender fillers reinforcement exhibits negligible effect. Relatively smoother descend in force history at 5 J loading suggests lesser damage in the laminate. At higher impact loading, notable fluctuation is seen near peak force, these fluctuations are sustained for a comparatively larger duration with marginally greater amplitude (see Fig. 3a) in UR laminate. This suggests more damage to the UR laminate. Force begins to decrease after maximum force as the impactor reverses and goes to zero when impactor detaches from the specimen. Lesser contact duration is noticed for SFR laminate at both the impact energies. Table 1 shows that maximum force increases with increase in impact energy. While SFR exhibits a marginal effect on maximum resistance force at lower impact loading, 11% rise is noticed at 12.5 J loading when compared to UR case. In velocity–displacement plot (see Fig. 3b), velocity at time  $t = 0$  is the incident velocity, whereas zero velocity is the point from where impactor reversal begins.

Plot illustrates that velocity decreases from the incident point while specimen deflects, curve follow an elliptical path. In the reversal process, velocity again increases and attains maximum reversal velocity which is much lesser than incident one in any case, suggesting damage dissipation in the specimen. While maximum reversal velocity remains the same for UR and SFR laminate at 5 J loading, a noticeable increase at 12.5 J loading is visible for SFR case (Fig. 3b). Maximum displacement tabulated in Table 1 shows subdued value for SFR case, especially at higher loading suggesting higher stiffness. Force–displacement trace delineated in Fig. 3c



**Fig. 3** Various impact variable plots **a** force–time history, **b** velocity–displacement curve, **c** force–displacement plot and **d** absorbed energy–time trace

**Table 1** Impact test and residual properties parameters

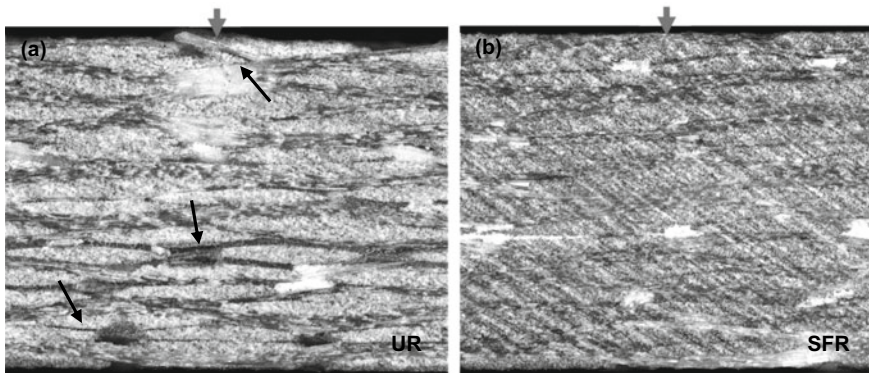
Incident energy	Laminate Type	Max. Force (N)	Max. Disp. (mm)	Elastic energy (J)	Flex. Modulus (GPa)	Flex. Strength (MPa)
0 J	UR	–	–	–	30.67 ± 1.6	615 ± 49
	SRF	–	–	–	30.38 ± 0.8	661 ± 89
5 J	UR	2780 ± 18	3.3 ± 0.18	1.7 ± 0.08	28.90 ± 1.3	582 ± 52
	SRF	2908 ± 17	3.1 ± 0.02	1.74 ± 0.07	29.67 ± 2.3	638 ± 44
12.5 J	UR	3931 ± 90	5.6 ± 0.4	2.53 ± 1	21.11 ± 2.6	327 ± 7
	SRF	4194 ± 143	5 ± 0.1	3.80 ± 0.6	28.97 ± 1.4	450 ± 81

reveals a nearly linear relationship in the rising part of the curve with numerous fluctuations till peak value, thereafter it decreases with displacement and reaches to its zero value. The remnant displacement at zero force suggests permanent damage in the specimen. The area encompassing the force–displacement curve represents energy dissipation in the fracture mechanism [14]. Plot shows greater energy dissipation

at higher impact loading. Again, at lower impact energy slender filler reinforcement shows marginal reduction in dissipation energy, significantly lower dissipation energy is observed at higher impact loading. Figure 3d shows an energy–time plot calculated by employing Eq. (3). The figure depicts that the total energy absorbed by the specimen increase with time and attains a peak value denoted by the letter “T” which is almost equal to impact energy in all the cases. Therefore, other frictional losses in the impact are assumed to be negligible. This total absorbed energy mainly goes into fracture dissipation and elastic deformation. From the peak energy value, the rebound of the impactor begins utilizing elastically stored energy; therefore, energy decreases and attains a plateau value denoted by the letter “D” which represents dissipated energy, whereas the difference between total absorbed energy and dissipated energy is the elastic energy (assuming negligible energy loss). Elastic energy tabulated in Table 1 shows marginal effect of slender filler reinforcement at 5J loading, there occurs 51% enhancement at 12.5 J loading.

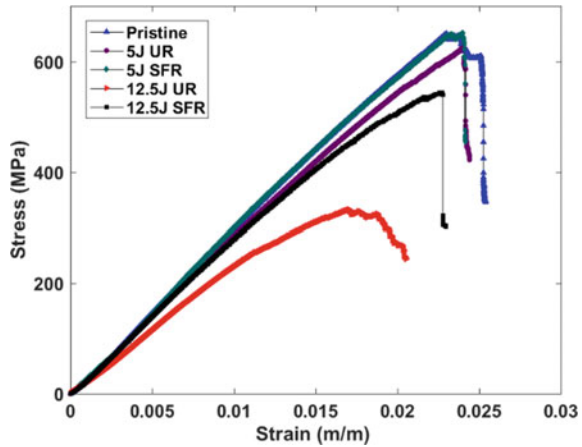
### 3.2 Visible Impact Damage

To assess the extent of impact-induced damage, the free surface of the 12.5 J impacted beams are imaged in the thickness direction by using Zeiss Axio Zoom V16 microscope as represented in Fig. 4, where the brown color (thicker one) arrow indicates impact location. Figure 4a reveals severe damage at impacted location along with multiple delaminations distributed through the thickness indicated by the black arrow imprint in UR laminate. Whereas no damage was visible in SFR laminate at the same loading as delineated in Fig. 4b. At 5 J loading a localized damage is seen only in UR laminate, no delamination is observed in any case.



**Fig. 4** Micrograph showing various damages in the 12.5 J impacted samples **a** unreinforced (UR) laminate **b** slender filler-reinforced (SFR) laminate

**Fig. 5** Post-impact residual flexural stress–strain curves



### 3.3 Residual Flexural Characteristics

Representative flexural stress–strain curves of UR and SFR laminates are plotted in the Fig. 5 along with pristine UR sample. Flexural properties of all types of impacted as well as pristine samples are calculated using Eqs. (4) and (5) and tabulated in Table 1. While flexural modulus remains nearly the same for UR and SFR pristine samples, 8% higher flexural strength is observed in the case of SFR laminate when compared to UR one. Plot and table show that post-impact flexural strength and modulus reduces with increase in impact energy for both UR and SFR laminates, where a lower rate of reduction in SFR case is noticed which correlates with visual damage in the specimen. At 5 J loading, SFR laminae show only a marginal increase in post-impact residual modulus as compared to UR laminate, about 10% rise in flexural strength is witnessed. Whereas, at higher impact loading, 37% and 38% increase in residual flexural strength and modulus is observed in SFR laminate.

## 4 Conclusion

Sixteen ply woven glass fabric/epoxy laminated composite are fabricated by using hand layup technique. Slender filler-reinforced (SFR) epoxy laminates are prepared by dispersing slender glass fillers into the epoxy system at requisite quantities. Beam specimens are machined from the cured laminate. Specimens are clamped in a circular fixture with 75 mm opening and impacted at mid-span at 5 J and 12.5 J impact energies. The filler-reinforced laminate exhibits higher impact resistance and stiffness as compared to unreinforced laminate. While impact-induced energy dissipation increases with increase in impact energy, the slender filler laminate shows consistently lower energy dissipation. At 12.5 J impact loading, the filler-reinforced



laminates shows 51% rise in the elastic energy in comparison to unreinforced laminate case. Symmetric four-point bend tests indicate that at lower incident energy, the residual mechanical properties of the laminates increase only marginally. However, at 12.5 J the post-impact flexural modulus and strength are enhanced by more than 35%. The impact site micrographs reveal significant damage with multiple delaminations in the unreinforced laminates at higher impact energy, whereas the damage is not distinct in the SFR laminate cases, which correlates quite well with the measured post-impact residual properties of the laminate.

## References

1. Zhang X, Hounslow L, Grassi M (2006) Improvement of low-velocity impact and compression-after-impact performance by z-fibre pinning. *Compos Sci Technol* 66:2785–94. <https://doi.org/10.1016/j.compscitech.2006.02.029>
2. Mouritz AP (2020) Review of z-pinned laminates and sandwich composites. *Compos Part A: Appl Sci Manuf* 139:106128. <https://doi.org/10.1016/j.compositesa.2020.106128>
3. Mouritz AP, Bannister MK, Falzon PJ, Leong KH (1999) Review of applications for advanced three-dimensional fibre textile composites. *Compos Part A: Appl Sci Manuf* 30:1445–61. [https://doi.org/10.1016/S1359-835X\(99\)00034-2](https://doi.org/10.1016/S1359-835X(99)00034-2)
4. Hart KR, Chia PXL, Sheridan LE, Wetzel ED, Sottos NR, White SR (2017) Comparison of compression-after-impact and flexure-after-impact protocols for 2D and 3D woven fiber-reinforced composites. *Compos Part A: Appl Sci Manuf* 101:471–9. <https://doi.org/10.1016/j.compositesa.2017.07.005>
5. Richardson MOW, Wisheart MJ (1996) Review of low-velocity impact properties of composite materials. *Compos Part A: Appl Sci Manuf* 27:1123–31. [https://doi.org/10.1016/1359-835X\(96\)00074](https://doi.org/10.1016/1359-835X(96)00074)
6. Cantwell WJ, Morton J (1991) The impact resistance of composite materials—a review. *Composites* 22:347–62. [https://doi.org/10.1016/0010-4361\(91\)90549-V](https://doi.org/10.1016/0010-4361(91)90549-V)
7. Tang Y, Ye L, Zhang Z, Friedrich K (2013) Interlaminar fracture toughness and CAI strength of fibre-reinforced composites with nanoparticles—A review. *Compos Sci Technol* 86:26–37. <https://doi.org/10.1016/j.compscitech.2013.06.021>
8. Santiuste C, Sanchez-Saez S, Barbero E (2010) Residual flexural strength after low-velocity impact in glass/polyester composite beams. *Composite Structures* 92:25–30. <https://doi.org/10.1016/j.compstruct.2009.06.007>
9. Hu Y, Wei Y, Han G, Zhang J, Sun G, Hu X et al (2022) Comparison of impact resistance of carbon fibre composites with multiple ultra-thin CNT, aramid pulp, PBO and graphene interlayers. *Compos Part A: Appl Sci Manuf* 155:106815. <https://doi.org/10.1016/j.compositesa.2022.106815>
10. Jefferson AJ, Srinivasan SM, Arockiarajan A (2019) Effect of multiphase fiber system and stacking sequence on low-velocity impact and residual tensile behavior of glass/epoxy composite laminates. *Polym Compos* 40:1450–62. <https://doi.org/10.1002/pc.24884>
11. Hu Y, Liu W, Shi Y (2019) Low-velocity impact damage research on CFRPs with Kevlar-fiber toughening. *Compos Struct* 216:127–41. <https://doi.org/10.1016/j.compstruct.2019.02.051>
12. ASTM D7136/D7136M-12 (2012) Standard test method for measuring the damage resistance of a fiber-reinforced polymer matrix composite to a drop-weight impact event

13. ASTM D6272–10 (2010) Standard test method for flexural properties of unreinforced and reinforced plastics and electrical insulating materials by four point bending. ASTM International
14. Singh MK, Kitey R (2022) Enhancing dynamic fracture behavior of laminated composite by short fiber reinforcement. In: Jonnalagadda K, Alankar A, Balila NJ, Bhandakkar T, (ed.) *Advances in structural integrity*. Singapore: Springer Singapore, pp 243–253. [https://doi.org/10.1007/978-981-16-8724-2\\_22](https://doi.org/10.1007/978-981-16-8724-2_22)

# Potential of Development of Anti-Erosion Graphene-Reinforced Coatings for Wind Turbine Blades



Nikesh Kuthe, Leon Mishnaevsky Jr., Puneet Mahajan, and Suhail Ahmad

**Abstract** The wind turbine blade coating is a protective layer that experiences repetitive raindrop impact. The impact causes cyclic stresses, fatigue, and erosion of the coating. The presence of voids in the coating leads to stress concentration and enhances erosion. A finite element model (FE) of the matrix containing a void and a layer of Graphene nano-platelets (GNP) was developed in ABAQUS using Python scripting, Boolean operation, and embedded element technique. A pressure pulse is applied on the top surface of RVE to imitate raindrop impact on the wind turbine blade coating for investigating the local stress concentration around the voids in the coating. It is observed that stresses around voids are reduced as the GNP layer reflects and scatters the stress wave. This can lead to enhanced fatigue life of the coating.

**Keywords** Wind Turbine blades (WTB) · Coating · Voids · Graphene nano-platelets (GNPs) · Embedded elements · Finite element technique

## 1 Introduction

Graphene has been widely studied in different areas of engineering since its discovery in 2004. Graphene, being the thinnest, strongest, and highly conductive material, is used as reinforcement to enhance the mechanical properties of other materials [11]. These characteristics of Graphene make it ideal for composing the impeccable protective anti-erosion coating layer.

Leading-edge erosion of wind turbine blade (WTB) coating is one of the exceedingly reviewed problems in recent years. Given that, a protective coating layer of WTB experiences repetitive raindrop impacts and so causes cyclic stresses, fatigue, and erosion of the leading edge of the blade coating. The presence of voids in the

---

N. Kuthe (✉) · P. Mahajan · S. Ahmad

Department of Applied Mechanics, Indian Institute of Technology Delhi, Hauz Khas, New Delhi 110016, India

e-mail: [Nikesh.Girdhari.Kuthe@am.iitd.ac.in](mailto:Nikesh.Girdhari.Kuthe@am.iitd.ac.in)

L. Mishnaevsky Jr.

Department of Wind Energy, Technical University of Denmark, Roskilde, Denmark

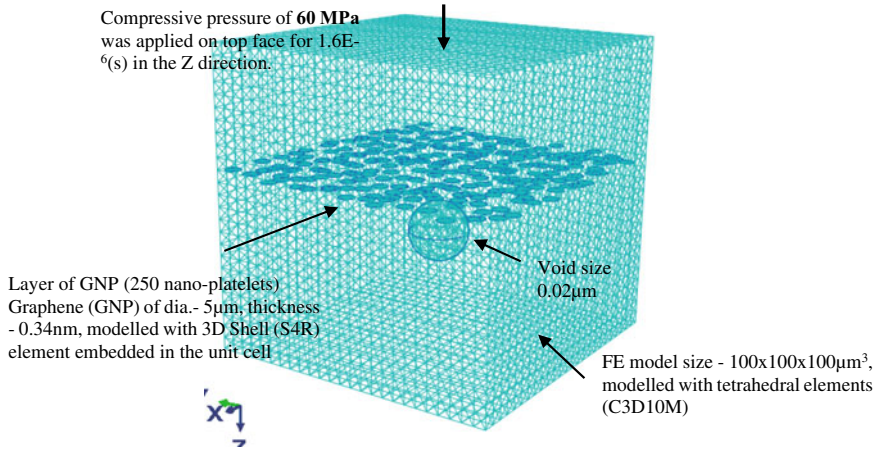
coating leads to stress concentration and enhances erosion. This erosion can cause an increase in the drag coefficient and reduction in lift coefficient resulting in reduced performance of the WT [1, 3]. In India, the annual monsoon with high-intensity rain makes the problem more critical. It is confirmed that the addition of nanoparticles like Graphene can significantly improve the mechanical, thermal, and impact properties of the polymers. A small weight percentage of up to 0.5% of Graphene nano-platelets (GNP) was introduced in the matrix to improve erosion resistance of polymer coating [4, 7].

In this work, we demonstrate that GNP can prevent damage initiation by reducing the local stress concentration around the voids by reflecting and scattering the stress waves. A finite element simulation of a GNP-reinforced coating sample (considered as a unit cell) subjected to impact loading imitating the raindrop impact is performed to study this effect. Numerical simulations show that high-stress concentration in the vicinity of voids can cause damage initiation from the voids in the coating, which can be prevented by the reinforcement Graphene nano-platelets. This will ultimately lead to enhanced fatigue life of the WT blade coating.

## 2 Methodology

### 2.1 Finite Element Model of GNP-Reinforced Coating

A FE model of size  $100 \times 100 \times 100 \mu\text{m}^3$  with a layer of GNPs and a void in Polyurethane (PU) matrix is developed using Python scripting in ABAQUS is shown in Fig. 1. The study was carried out to understand the phenomenon of stress wave reflection and scattering caused by GNP reinforcement. The GNP has a diameter of  $5 \mu\text{m}$  and a thickness of  $1 \text{ nm}$ . An interface of thickness  $1 \text{ nm}$  exists between the GNP and matrix. The interface and matrix are modelled with brick elements, and shell elements are used for the platelets. Both the interface and platelet are embedded in Polyurethane (PU) matrix using the embedded element technique in ABAQUS to maintain a good aspect ratio. The layer of GNP is made using Boolean operations in ABAQUS, wherein the GNPs are placed at randomly generated coordinates and merged to develop a unit cell with a layer of GNP. A pulse load of  $60 \text{ MPa}$  for  $1.6 \times 10^{-6} \text{ (s)}$  was applied on the upper face  $Z = 0 \mu\text{m}$  to mimic the raindrop impact on WT blade coating. It is observed that the GNPs reflect the part of the stress wave impacting it; as a result, stresses around voids are reduced due to the presence of a GNP layer in the coating.

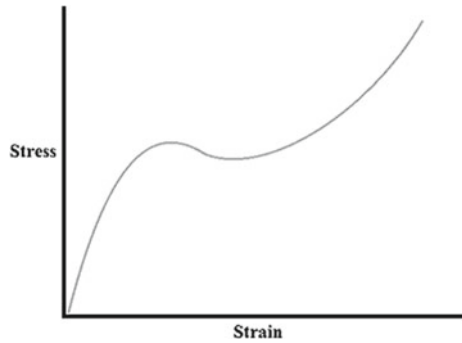


**Fig. 1** Unit cell with a layer of GNP and a void modelled in PU matrix

## 2.2 Material Model

The coating material, soft Polyurethane with Young’s modulus of 3.5 GPa, Poisson’s ratio of 0.3 considering Drucker–Prager elastoplastic constitutive law is used in ABAQUS/Explicit to exhibit significantly more complex post-yield behaviour of engineering polymers as shown in Fig. 2, Stress–strain data available in the literature [9] is used to model plasticity. GNP is given with the Elastic modulus ( $E$ ) = 1 TPa, Poisson’s ratio ( $\nu$ ) = 0.4 and Density ( $\rho$ ) = 2250 kg/m<sup>3</sup> [7], while interface is assigned with the Elastic modulus ( $E$ ) = 5.5 GPa and Poisson’s ratio ( $\nu$ ) = 0.33 [10].

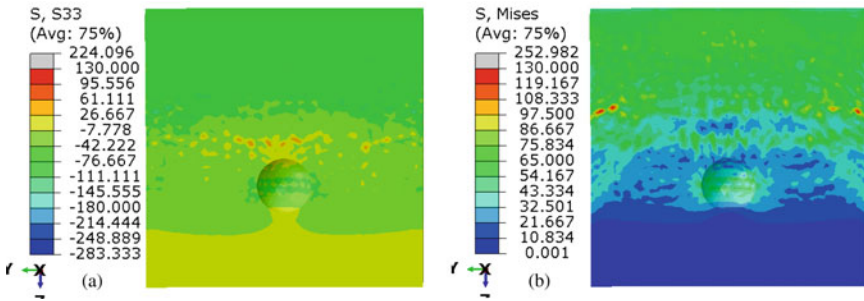
**Fig. 2** Typical complex high deformation plasticity as exhibited by polymer materials (Reprinted from [8, 9])



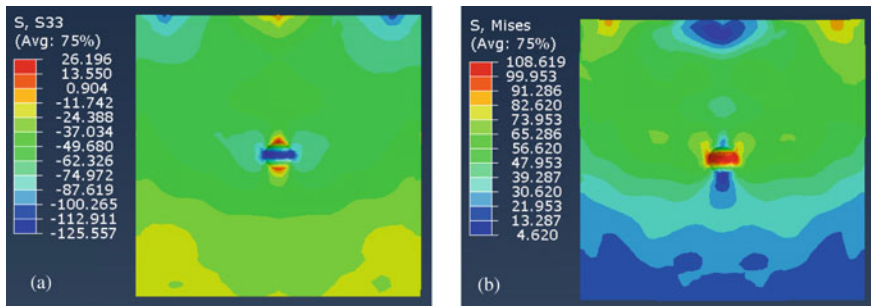
### 3 Results

The preliminary study to comprehend the phenomenon of stress wave reflection and scattering caused by GNP reinforcement was accomplished in [6] and showed that the compression wave of 50 MPa gets reflected from the single GNP as a compressive wave in the material. It was learned that when the stress wave interacts with GNP, the Mises stress in the interface and matrix approximately doubles in the vicinity of GNP and then decreases to 50 MPa after reflection. As Graphene has a very high Modulus of 1 TPa, it behaves as a rigid body, and therefore deformation in the elements is negligible (no strain), so stresses are negligible in GNP. Furthermore, it was noticed that the stress wave during interaction with GNP produces stress concentration in the matrix at the vicinity of the edges of GNP.

Figure 3a and b reveal that the layer of GNP in the RVE reduce the local stress concentration (by 50%) in the void (S33 reduced to  $-60$  MPa) by blocking the stress wave propagation towards the void whereas, without reinforcement of GNP layer, stress (S33) concentration in the void is  $-125$  MPa as observed in Fig. 4.



**Fig. 3** a Stress:  $S_{33}$  (MPa) wave at  $5.00 \times 10^{-8}$  (s) in the matrix (cross-section) blocked by GNP layer b von-Mises stress



**Fig. 4** Local stress distribution in the polymer with void without GNP reinforcement a Stress:  $S_{33}$  (MPa) wave b von-Mises stress (MPa)

## 4 Conclusion

The study was conducted to discover the behaviour of Graphene nano-platelets (GNP) reinforced in PU matrix subjected to dynamic loading. A layer of (GNP) was modelled with void using Python scripting and embedded element technique in ABAQUS. It was recognized that GNP act as a rigid particle in the matrix due to its high stiffness, consequently it reflects the incoming dynamic stresses in the matrix. From the results, it was interpreted that layer of GNP can reduce the local stress concentration in the voids by reflecting the stress wave produced during impact, and GNP reinforcement in the coating will prevent the damage initiation from the manufacturing defects like void due to repetitive impacts of the raindrops.

**Acknowledgements** The authors kindly acknowledge the financial support of the Ministry of Foreign Affairs of Denmark, in the framework of Danida grant 19-M02-DTU “Maintenance and Repair Strategy for Wind Energy Development”.

## References

1. Doagou-Rad S, Mishnaevsky L (2020) Rain erosion of wind turbine blades: computational analysis of parameters controlling the surface degradation. *Meccanica* 55:725–743. <https://doi.org/10.1007/s11012-019-01089-x>
2. Amirzadeh B, Louhghalam A, Raessi M, Tootkaboni M (2017) A computational framework for the analysis of rain-induced erosion in wind turbine blades, part II: Drop impact-induced stresses and blade coating fatigue life. *J Wind Eng & Ind Aerodyn*, Elsevier Ltd 163:44–56. <https://doi.org/10.1016/j.jweia.2016.12.007>
3. Mishnaevsky Jr L, Bech JI (2019) Micromechanisms of leading-edge erosion of wind turbine blades: X-Ray tomography analysis and computational studies. *Wind Energy*:1–16. <https://doi.org/10.1002/we.2441>
4. Jespersen KM, Monastyrckis G, Mishnaevsky Jr L (2020) On the potential of particle engineered anti-erosion coatings for leading-edge protection of wind turbine blades: Computational studies. In: 41st Risø Symposium, IOP Conference series: Materials science and engineering, vol 942, No 1, p 012027. <https://doi.org/10.1088/1757-899X/942/1/012027>
5. Mishnaevsky Jr. L (2019) Toolbox for optimizing anti-erosion protective coatings of wind turbine blades: Overview of mechanisms and technical solutions. *Wind Energy*:1–18. <https://doi.org/10.1002/we.2378>
6. Kuthe N, Mahajan P, Ahmad S, Mishnaevsky Jr L. Engineered anti-erosion coating for wind turbine blade protection: Computational analysis. *Mater Today Commun* 31:103362. ISSN 2352-4928. <https://doi.org/10.1016/j.mtcomm.2022.103362>
7. Johansen NFJ, Mishnaevsky L Jr, Dastkar A, Williams NA, Silvello A, Cano IG, Hadavinia H (2021) Nanoengineered graphene reinforced coating for leading-edge protection of wind turbine blades. *Coatings* 11(9):1104. <https://doi.org/10.3390/coatings11091104>
8. Claus CE (2013) Effects of leading-edge erosion on wind turbine efficiency & innovative erosion protection solutions. *Wind Power Monthly—Blade Insp, Damage Repair*, Hamburg.
9. Keegan MH Wind turbine blade leading edge erosion: An investigation of rain droplet and hailstone impact-induced damage mechanisms. Ph.D. thesis, Wind Energy Systems Centre for Doctoral Training, Department of Electronic & Electrical Engineering, University of Strathclyde, Glasgow, Scotland

10. Spanos KN, Anifantis NK (2016) Finite element prediction of stress transfer in graphene nanocomposites: The interface effect. *Compos Struct* 154:269–276. <https://doi.org/10.1016/j.compstruct.2016.07.058>
11. Chandraa Y, Adhikaria S, Saavedra Floresb EI, Figielc L (2020) Advances in finite element modelling of graphene and associated nanostructures. *Mater Sci & Eng R* 140:100544. <https://doi.org/10.1016/j.mser.2020.100544>



# An Entropy-Based Damage Model to Assess the Creep Behaviour of Nickel-Based Superalloys



Sri Krishna Sudhamsu Kambhammettu, Ashish Pandey,  
and Lakshmana Rao Chebolu

**Abstract** Unified mechanics theory employs an entropy-based damage parameter (known as thermodynamic state index) to track damage in a material that is subjected to variety of mechanical, thermal, electrical and other kinds of loads. The fundamental and consistent approach followed in defining and in evolving this “thermodynamic state index” enables reliable estimation of material damage, even when multiple competing damage mechanisms are involved. In this paper, uniaxial creep behaviour of Inconel 600 nickel-based superalloy is modelled by modifying the Norton power law for creep to accommodate the entropy-based damage parameter. The resulting model is calibrated and verified using available uniaxial tensile creep data at different creep loads.

**Keywords** Creep · Nickel-based superalloys · Damage model · Unified mechanics theory

## 1 Introduction

Nickel-based superalloys are known for their excellent creep resistance and hence are commonly used in aero engines at high operating homologous temperatures (Pollock and Tin [10] in spite of their excellent creep resistance, creep damage is unavoidable particularly at high homologous temperatures [1]. In order to estimate the failure due to creep, historically, researchers have on models developed based on the continuum damage mechanics (CDM) [4] framework. These models contain constitutive relations that determine the material behaviour (stress–strain–time behaviour) in various stages of damage evolution. The damage corresponding to any given time is tracked

---

S. K. S. Kambhammettu (✉)  
National Institute of Technology Jamshedpur, Jamshedpur 831014, India  
e-mail: [kksudhamsu@gmail.com](mailto:kksudhamsu@gmail.com)

A. Pandey · L. R. Chebolu  
Indian Institute of Technology Madras, Chennai 600036, India

by a “damage parameter” that evolves according to a separate damage evolution relation, e.g., Kachanov-Rabotnov [12] damage model uses Eq. (1a) to determine the creep strain rate at different creep stresses, time and states of damage. Equation (1b) provides the rate of change in damage parameter.

$$\dot{\varepsilon}_{cr} = A \left( \frac{\sigma}{1 - \omega} \right)^n t^m \quad (1a)$$

$$\dot{\omega} = B \left( \frac{\sigma^\chi}{(1 - \omega)^\phi} \right) \quad (1b)$$

where

$\varepsilon_{cr}$  is the creep strain,  $\sigma$  is the creep stress,  $\omega$  is the creep damage parameter and  $A$ ,  $B$ ,  $n$ ,  $m$ ,  $\chi$  and  $\phi$  are model parameters.

Similarly, CDM-based models such as Liu-Murakami creep model [7] introduces separate equations for constitutive relation and creep damage evolution. These creep damage models, especially the Kachanov-Rabotnov model and the Liu-Murakami model are widely used and are known for their accurate estimation and representation of creep behaviour in various ductile alloys. In spite of this apparent success of CDM models, the approach has also attracted criticism majorly due to two reasons.

Firstly, most CDM models are phenomenological models and they provide little insight into the damage mechanisms that are in play at micrometre length scale. In addition, the evolution of microstructure, the interaction of different damage mechanisms are not considered/explained by these models [6]. This limitation can be tolerable or intolerable based on the school of thought of the individual researchers. Researchers from a metallurgical or physics-based background are trained to understand materials based on their microstructure and they may find it unacceptable to use a phenomenological model that has no regard to the microstructure of the material [6]. On the other hand, researchers from mechanics background prepare models that are directly useful to engineers in development of products. Due to this, they are more interested in models that can accurately describe the material behaviour with smallest possible computational cost. Hence, this criticism may be dismissed with a note that different kinds of models appeal to researchers with different interests.

The second criticism is regarding the performance of CDM models that is when competing damage mechanisms are in action. In CDM models, a damage parameter is usually defined to qualitatively/empirically track damage based on patterns in the changes observed in the continuum material behaviour. When multiple damage mechanisms are involved, these patterns are more complex and it is often difficult to identify one parameter that can consolidate damage due to all mechanisms into one number. This is again due to the phenomenological nature of most CDM models.

One approach to overcome this limitation is to introduce multiple damage parameters to track each mechanism separately, e.g., Othman-Hayhurst-Dyson creep model [9] uses two damage parameters (each with a separate relation for their evolution).

While the first damage parameter tracks the softening due to dislocation multiplication, the second damage parameter tracks softening due to grain boundary cavity nucleation and growth. The ultimate failure is identified when any one of the damage parameter reaches its threshold value. In spite of the usefulness of such approach, multiple damage parameters are still challenging to define for every dominant damage mechanism that the material undergoes throughout its life. In addition, interpreting and consolidating the values of multiple damage parameters is also another challenge. Hence, in spite of the apparent limitations, single damage parameter models are still popular for their ease of use.

Another way to overcome the limitation of CDM models is to identify a single damage parameter that can universally track damage due to all the damage mechanisms. Entropy-based damage parameter introduced in unified mechanics theory (UMT) [2] is well-known for such universality. It has been successfully used to track damage due to mechanical and thermal low-cycle fatigue, thermo-migration, electromigration, high-cycle fatigue and high strain rate loading. The unified mechanics theory (UMT) asserts that the total specific entropy generated by a given material at a material point due to all kinds of thermal and mechanical damage processes will always be equal to a critical value at failure. Hence, in UMT, damage is defined as a function of total entropy generated in the material due to all failure mechanisms. This damage parameter, also known as thermodynamic state index (TSI), is given by Eq. (2) [2]:

$$\phi = 1 - e^{-\frac{m_s \Delta s}{R}} \quad (2)$$

Where

$\Delta s$  is the specific entropy generated at the material point of interest,

$m_s$  is specific mass (gram/mole),

$R$  is universal gas constant and

$\phi$  is the damage parameter or thermodynamic state index.

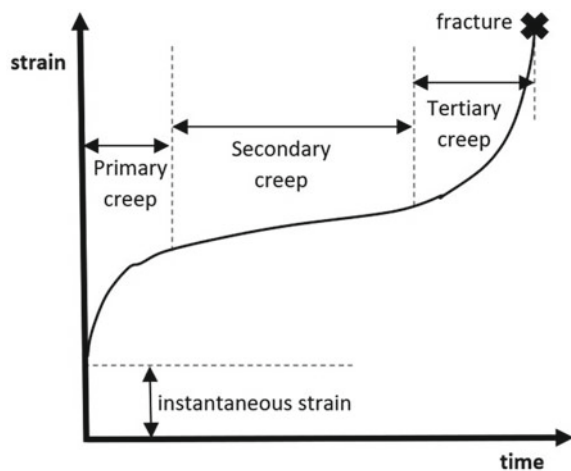
In spite of the universality of the entropy damage parameter, there have been very few attempts to implement entropy-based damage in creep [5, 13, 14]. In this paper, we attempt to implement this damage parameter along with a constitutive relation into a damage model to estimate creep behaviour in INCONEL-600 nickel-based superalloy. In the upcoming sections of this paper, we discuss this creep model and utilize it to describe available creep data.

## 2 Creep Model

Creep is generally defined as continued deformation of solids under the action of constant loads. Creep is known to occur at a very slow rate, even at stresses that are much less than the yield stress of the material. Figure 1 shows a general creep strain  $v/s$  time curve observed in a constant load condition. The creep curve shown in the figure can be categorized into three phases: primary creep, secondary creep and tertiary creep. Primary creep is known to occur due to dislocation movement in the material. The rate of increase in primary creep decreases as the dislocation movement saturates due to internal or grain boundary obstructions. The second phase is called secondary creep in which climb assisted dislocation and the diffusion of atoms through the lattice and through the grain boundary form the dominant mechanisms of creep. This creep occurs at a steady state and at a slowest possible pace. Hence, secondary creep is known for steady-state creep and minimum strain rate. The third phase of tertiary creep is characterized by rapid increase in creep strain rate followed by localization of stresses and ultimately fracture. This occurs due to intergranular or intragranular crack initiation and propagation. Creep-resistant super alloys are generally designed to obstruct dislocation movement [15]. Hence, very little primary creep is generally observed. For this reason, we only model secondary and tertiary creep in this paper.

As discussed, a CDM model consists of a constitutive relation and a damage evolution law. As a starting point, we consider Norton power law [8] that describes the steady-state secondary creep as shown by Eq. (3b). If there was no damage in the model, the creep rate would be constant as given by Eq. (3a). However, as the material generates entropy, the creep rate increases and is given by the second law of unified mechanics theory. This is given by Eq. (3b). When both these equations are clubbed with the damage evolution equation (given by Eq. (2) and rewritten as Eq. (3c)), the one dimensional creep model is complete.

**Fig. 1** Typical creep curve for a specimen subjected to uniaxial constant tensile load



$$\dot{\epsilon}_{cr^0} = A\sigma^n \quad (3a)$$

$$\dot{\epsilon}_{cr} = \frac{\dot{\epsilon}_{cr^0}}{1 - \phi} \quad (3b)$$

$$\phi = 1 - e^{-\frac{M_s \Delta s}{R}} \quad (3c)$$

Where

$\dot{\epsilon}_{cr^0}$  is steady-state creep strain rate at zero damage,

$\sigma$  is the magnitude of uniaxial creep stress,

$R$  is universal gas constant,

$\dot{\epsilon}_{cr}$  is the creep strain rate,

$\phi$  is the damage parameter or thermodynamic state index,

$\Delta s$  is the specific entropy generated at the material point of interest,

$m_s$  is specific mass (gram/mole) and

$A$  and  $n$  are model parameters.

The specific entropy,  $\Delta s$  in Eq. (3c) is obtained by integrating the entropy generation rate due to all energy dissipation processes [2].

$$\Delta s = \frac{1}{p} \int_{t_2=0}^{t_2} \gamma dt \quad (4a)$$

$$\gamma = \frac{1}{T} \boldsymbol{\sigma} : \mathbf{D} - \frac{\rho}{T} \frac{dWe}{dt} + \frac{k}{T^2} |\text{grad } T|^2 + \frac{\rho r}{T} \quad (4b)$$

Where

$\boldsymbol{\sigma}$  is the stress tensor

$\mathbf{D}$  is the deformation rate tensor

$T$  is the absolute temperature

$\rho$  is the density

$r$  is rate of heat generation

$t_1$  and  $t$  is time

$t_2$  are time at the beginning and time at failure, respectively

$w_e$  is the elastic strain energy

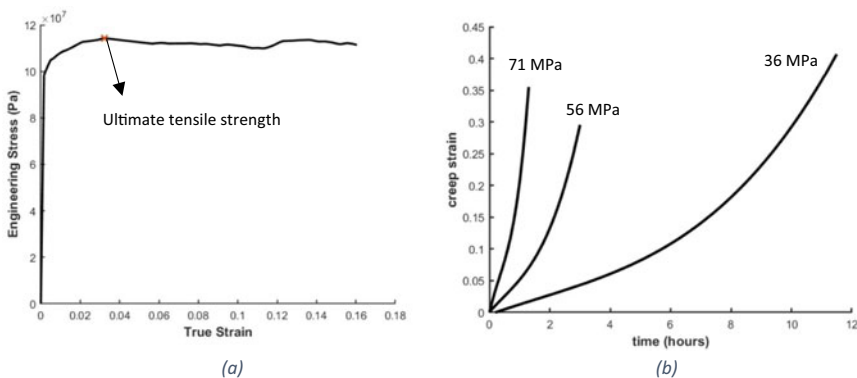
For the creep problem under consideration due to uniaxial loading, small deformation, uniform temperature distribution and due to absence of heat generation, Eq. (4b) turns into Eq. (4c).

$$\gamma = \frac{1}{T} \sigma \dot{\epsilon}_{cr} \quad (4c)$$

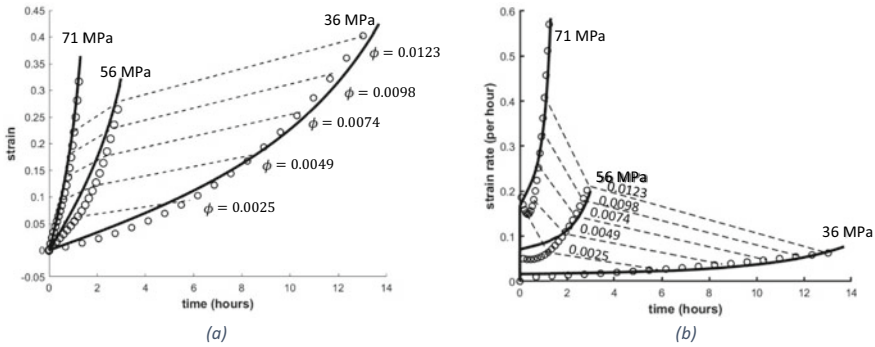
### 3 Experimental Data, Parameter Estimation and Results

Creep tests on Inconel-600 at different creep stresses and temperatures have been performed in [3]. In this paper, we use creep data from this paper for our analysis. Figure 2a and b show the uniaxial tensile test data for Inconel-600 at 1100oA under monotonic displacement-controlled loading and constant force creep loadings, respectively.

Creep model defined by Eq. (3a), (b) and (c) is now used to describe the experimentally observed creep data. The parameters  $A$  and  $n$  of Eq. (3a) are fit using the creep data at 76 and 55 MPa. This data is later used to predict creep at 36 MPa. The estimated strain and strain rates are compared with the experimentally observed values in Fig. 3a and b. It can be observed that the strain and strain rate data are well-predicted by the model. It can be observed, however, that the decrease in strain rate during the primary creep is seen in the experiment, but is not predicted by the model. This is due to the inability of the steady-state creep rate constitutive relation given by Eq. 3(a) in describing primary creep. The secondary and tertiary creep, however, are well-estimated due to the nature of Eq. (3a) and due to the introduced damage parameter defined by Eq. (3b) and (c).



**Fig. 2** Uniaxial tensile **a** Monotonic strain data **b** Creep test data. Data obtained from [3]



**Fig. 3** Uniaxial tensile **a** Monotonic strain data **b** Creep test data. Dashed lines represent iso-damage lines drawn for  $\phi$  values 0.0025, 0.0049, 0.0074, 0.0098, 0.0123. The scattered points shown by “o” are experimental data and the solid lines are the predictions from the model

Figure 3a and b also show iso-damage dashed lines. The thermodynamic state index of all the points is on any given iso-damage line. The value of thermodynamic state index corresponding to each of the lines is also shown in the figure. The iso-damage line corresponding to  $\phi = 0.0025$  represents damage corresponding to ultimate tensile strength in Fig. 1a. Localization of stresses due to necking occurs post ultimate tensile strength in Fig. 2a. It is only logical to expect necking in creep tests to occur soon after  $\phi = 0.0025$ . It can be further noticed from Fig. 3a and b that this damage at  $\phi = 0.0025$  also represents the beginning of tertiary phase at all stresses as the creep rates can be seen to increase more and more rapidly after this point. This is not a coincidence as it is widely accepted that necking starts at the beginning of tertiary phase. However, this can be conclusively only verified by further experimentation on necking in creep. Another end use of estimating damage is to predict fracture/rupture. In practice, rupture can occur over a range of strains for a given creep load. This is because necking and consequent rupture are due to sample specific defects that vary from sample to sample. One accepted way of predicting rupture is to predict the average rupture strain (i.e. the average of all rupture strains obtained by repeating each experiment multiple times). However, since such data is not available at this point, rupture prediction is not possible.

## 4 Conclusions

In this paper, an entropy-based damage parameter, known as thermodynamic state index is used along with Norton’s power law to predict secondary and tertiary creep in Inconel-600 nickel-based superalloy. Iso-damage regions in specimen subjected to different creep loads are identified. Creep times corresponding to onset of stress localization and necking for different creep loads are predicted by calculating the thermodynamic state index corresponding to ultimate tensile stress in monotonic

displacement-controlled uniaxial tensile test. It has been observed that the damage model describes the experimentally observed secondary and tertiary creep strain rates accurately. The model is hoped to predict rupture strains as well when exhaustive experimental data with repeated creep tests are available.

## References

1. Azadi M, Azadi M (2017) Evaluation of high-temperature creep behavior in Inconel713C nickel-based superalloy considering effects of stress levels. *Mater Sci Eng, A* 689:298–305
2. Basaran C (2021) Introduction to unified mechanics theory with applications. Springer Nature
3. Chavez SA, Korth GE, Harper DM, Walker TJ (1994) High-temperature tensile and creep data for Inconel 600, 304 stainless steel and SA106B carbon steel. *Nucl Eng Des* 148(2–3):351–363
4. Kachanov L (1986) Introduction to continuum damage mechanics, vol 10. Springer Science & Business Media
5. Lee Y, Basaran C (2011) A creep model for solder alloys
6. Li K-S, Wang R-Z, Yuan G-J, Zhu S-P, Zhang X-C, Tu S-T, Miura H (2021) A crystal plasticity-based approach for creep-fatigue life prediction and damage evaluation in a nickel-based superalloy. *Int J Fatigue* 143:106031
7. Liu Y, Murakami S (1998) Damage localization of conventional creep damage models and proposition of a new model for creep damage analysis. *JSME Int J Ser Solid Mech Mater Eng* 41(1):57–65
8. Norton FH (1929) The creep of steel at high temperatures. The University of Wisconsin
9. Othman AM, Hayhurst DR, Dyson BF (1993) Skeletal point stresses in circumferentially notched tension bars undergoing tertiary creep modelled with physically based constitutive equations. *Proc R Soc London Ser A: Math Phys Sci*, 441(1912):343–358.
10. Pollock TM, Tin S (2006) Nickel-based superalloys for advanced turbine engines: chemistry, microstructure and properties. *J Propuls Power* 22(2):361–374
12. Rabotnov YN (1969) Creep rupture. In: *Applied mechanics*. Springer, pp 342–349
13. Sri Krishna Sudhamsu K, Lakshmana Rao C (2022) Creep failure estimation of nickel-based superalloys using unified mechanics theory (UMT). In: *Recent advances in applied mechanics*. Springer, pp 737–743
14. Wang J, Yao Y (2019) An entropy-based failure prediction model for the creep and fatigue of metallic materials. *Entropy* 21(11):1104
15. Zhao P, Mills MJ, Wang Y, Niezgoda SR (2018) A homogenized primary creep model of nickel-base superalloys and its application to determining micro-mechanistic characteristics. *Int J Plast* 110:202–219



# Influence of Porosity and Temperature Load on Buckling Characteristics of Functionally Graded Material Plates



K. Swaminathan, H. Sachin, and T. Rajanna

**Abstract** Functionally graded material (FGM) plate is usually exposed to a thermal environment, and their mechanical behaviour under temperature loads is of great importance to the research community. Therefore, the objective of the current investigation is to study the impact of porosity and temperature loads on the buckling characteristics of FGM plates. The effective material properties of porous FGM plates are found using modified power law distributions, and the porosity defects are accounted for in this study as criteria of stiffness reduction. The buckling responses of porous FGM plates are investigated by incorporating four types of different porosity distributions. The analysis is carried out using the Finite Element (FE) technique. The accuracy of the current formulation is authenticated by comparing the present results obtained with analytical results existing in the literature. After the validation, the influence of several significant parameters such as the porosity, the volume fraction exponent, side-thickness ratio, support conditions and aspect ratio on buckling responses of the porous FGM plate under temperature loads is evaluated. Results showed that the buckling response of the FGM plate is substantially affected by porosity and temperature loads.

**Keywords** FGMs · Porosity · Thermal buckling · Neutral surface

## 1 Introduction

FGMs are an advanced set of composite materials obtained by continuous gradation of ceramic and metal constituents in a particular direction. The ceramic material in constituent possesses high compressive strength and heat resistance with low fracture toughness, but metal has better mechanical strength whilst unable to withstand

---

K. Swaminathan

Department of Civil Engineering, National Institute of Technology Karnataka,  
Mangaluru 575025, India

H. Sachin (✉) · T. Rajanna

Department of Civil Engineering, B.M.S College of Engineering, Bangalore 560019, India  
e-mail: [177cv011.sachinh@nitk.edu.in](mailto:177cv011.sachinh@nitk.edu.in)

a high thermal environment. Therefore, FGM has the advantage of chemical and physical properties of both materials resulting in thermal resistance, bond strength, and toughness. The roles of FGMs in numerous technical domains such as aerospace, automobile, defense, and nuclear fusion reactor industry have grown as a result of these alluring characteristics. Due to the substantial disparity in solidification temperatures between the constituent materials, it has been shown that during the FGM manufacturing process, micro-voids or porosities can accumulate in the materials [1, 2]. Porosity in the material, along with the temperature environment, significantly affects the mechanical properties of the FGMs. In this context, the impact of porosity and thermal loads on buckling response of porous FGMs plates are studied in recent times [3, 4]. Patil et al. [5] examined the buckling and free vibration characteristics of porous FGM beams exposed to mechanical and thermal loads using FE technique. The flexure and vibration characteristics of FGM plate are analysed by Gupta and Thala [6] in the framework of FE technique.

Due to the lack of symmetry in the material properties in the thickness direction, the neutral surface of FGM plates might not coincide with its middle surface. Therefore, in recent years, many researchers have employed a neutral surface as a reference plane for structural equilibrium. Mota et al. [1] and Singha et al. [2] analysed the static response of porous FGM plates considering the consequence of a neutral surface. Zhong and Zhou [3] performed theoretical analysis to study bending, free vibration, and buckling response of FGM plate based on physical neutral surface concept. Farzam-Rad et al. [4] presented static and free vibration study of FGM plate incorporating the effect of the neutral surface using isogeometric analysis. Lee et al. [5] and Do et al. [6] investigated the thermal buckling characteristics of FGM plates incorporating a neutral surface plane. Arefi et al. [7] incorporated the concept of neutral surface to study the vibration characteristics of sandwich nano plate resting on Pasternak foundation. Recently, Mohamed Saad and Hadji [8] performed thermal buckling analysis of thick porous FGM plate using higher-order theories and neglecting neutral surface. These studies demonstrated that formulation incorporating a neutral surface could bring a significant difference in the results.

From literature review, the studies pertaining to the influence of porosity and temperature loads on the buckling response of porous FGM plates are vastly covered so far. The novelty of the present study in comparison to other references is attributed to consideration of combined effect of different types of porosity distributions, temperature, and neutral surface shift to study buckling behaviour of porous FGM plate. The study is important as porosity and temperature adversely affects the stiffness of the plate. Therefore, in the current study, the effect of porosity and temperature on buckling response of FGM plate considering neutral surface is carried out using FE technique. The modified power law rule is incorporated to estimate the material properties of porous FGMs. The formulation incorporates FSDT and the neutral surface of FGM plates. The comprehensive study is accomplished considering the consequence of several porosity distributions, thickness ratio, plate aspect ratio, and support conditions on the thermal buckling behaviour of porous FGM plate.

## 2 Modelling of FGM Plates with Porosity

The FGM can be modelled by using modified power law homogenization technique [9] as in Eqs. (1)–(3) in the form of:

$$P(z_{ms}) = P_m + (P_c - P_m)\left(\frac{z_{ms}}{h} + \frac{1}{2}\right) - \frac{\beta}{2}(P_c + P_m)V_p \tag{1}$$

With respect to the neutral surface [10], Eq. (3) can be rewritten as follows

$$P(z_{ns}) = P_m + (P_c - P_m)\left(\frac{z_{ns} + d}{h} + \frac{1}{2}\right) - \frac{\beta}{2}(P_c + P_m)V_p \tag{2}$$

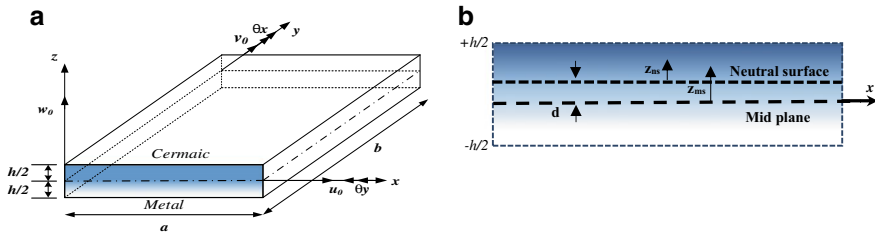
$$d = \frac{\int_{-h/2}^{h/2} E(z_{ms})z_{ms}dz}{\int_{-h/2}^{h/2} E(z_{ms})dz} \tag{3}$$

where, P(z) is a general term to represent material properties such as E(z) and  $\alpha(z)$ . The subscripts c and m refer to material properties of ceramic and metal, respectively. The term *n* is the volume fraction exponent, and  $p_i$  is the porosity coefficient. The expression  $V_p$  is the general function to represent the several kinds of porosity, and  $V_p$  can be either one of  $\{V_{UD}/V_{CD}/V_{XD}/V_{VD}\}$ . The porosity imperfection may occur during the manufacturing procedure of FGM plates in the form of micro-voids and can be modelled using mathematical equations as given in [11]. The variation of Young’s modulus along the thickness for several porosity distributions is shown in Fig. 2a. Further Fig. 2b represents neutral surface shift for various porosity distribution and *n*.

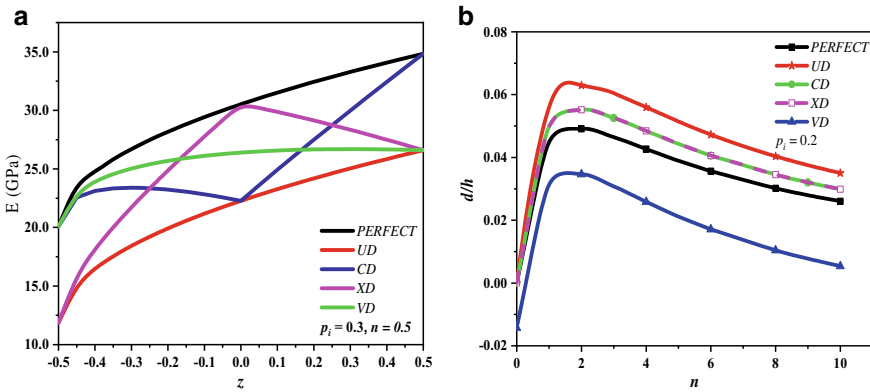
## 3 Theoretical Formulation

### 3.1 Geometry of Plate

FGM with plate length ‘*a*’, plate width ‘*b*’, and plate thickness ‘*h*’ along with a positive set of the coordinate system with respect to *x*, *y*, and *z* directions are as exemplified in Fig. 1. The terms  $u_0, v_0, w_0$  are the components of displacements along the coordinate’s directions *x*, *y*, and *z* respectively of an arbitrary point on the planes  $z = 0$  (mid-surface-MS). Further, the rotations of the normal to the mid planes about *y*- and *x*-axes are represented by  $\theta_x$  and  $\theta_y$  respectively.



**Fig. 1** **a** Geometry and coordinate system of FGM plate with a positive set of reference axis; **b** FGM plate cross-section with neutral surface



**Fig. 2** **a** Effective Young's modulus versus dimensionless thickness of FGM plate with several porosity distribution models; **b** Neutral surface shift due to different porosity distribution models

### 3.2 Kinematic Relations

FSDT is incorporated for current study to investigate the kinematics of the plate member [12]. The displacement field is given as below (Eq. (4)).

$$\begin{aligned}
 u(x, y, z) &= u_0(x, y) + z\theta_x(x, y), \quad v(x, y, z) \\
 &= v_0(x, y) + z\theta_y(x, y), \quad w(x, y, z) = w_0(x, y).
 \end{aligned}
 \tag{4}$$

### 3.3 Constitutive Relationship

The FGM plate linear constitutive relation can be stated as,

$$\begin{Bmatrix} \sigma_x \\ \sigma_y \\ \tau_{xy} \end{Bmatrix} = \frac{E(z)}{(1-\nu^2)} \begin{bmatrix} 1 & \nu & 0 \\ \nu & 1 & 0 \\ 0 & 0 & \frac{1-\nu}{2} \end{bmatrix} \begin{Bmatrix} \varepsilon_x - \alpha \Delta T \\ \varepsilon_y - \alpha \Delta T \\ \gamma_{xy} \end{Bmatrix}; \begin{Bmatrix} \tau_{yz} \\ \tau_{xz} \end{Bmatrix} = \frac{E(z)}{2(1+\nu)} \begin{bmatrix} 1 & 0 \\ 0 & 1 \end{bmatrix} \begin{Bmatrix} \gamma_{yz} \\ \gamma_{xz} \end{Bmatrix} \tag{5}$$

where  $(\sigma_x, \sigma_y, \tau_{xy}, \tau_{yz}, \tau_{xz})$  are stresses and  $(\varepsilon_x, \varepsilon_y, \gamma_{xy}, \gamma_{yz}, \gamma_{xz})$  are strains with respect to plate reference axes. Where  $E(z)$  signifies the Young’s modulus at any point along the  $z$ - direction. The total in-plane force resultants and moment resulting owing to temperature rise are expressed as in Eq. (6).

$$\begin{bmatrix} N_x^T & M_x^T \\ N_y^T & M_y^T \\ N_{xy}^T & M_{xy}^T \end{bmatrix} = \int_{-h/2}^{+h/2} \begin{Bmatrix} \sigma_x \\ \sigma_y \\ \tau_{xy} \end{Bmatrix} (1, z) \alpha \Delta T dz, \tag{6}$$

### 3.4 Strain–displacement Relation

In the current analysis, Green–Lagrange’s strain–displacement relations are applied in the formulation. The linear portion of strains is taken into consideration to form the elastic’s stiffness matrix, and the nonlinear portion of the strains is considered to arrive at the geometric stiffness matrix. By substitution of the displacement field given by Eq. (4) in strain terms, strain–displacement relations are obtained [13, 14].

### 3.5 FE Modelling

In the current works, the FG plates are discretized with the aid of 8 noded isoparametric elements with 5 degree of freedom per node. At any point of the model, the generalized displacement vectors and elements geometry can be signified in terms of shape functions as expressed in Eq. (7).

$$\{q\} = \bar{N}_i \{q_i\} \quad x = \sum_{i=1}^8 \bar{N}_i x_i \quad y = \sum_{i=1}^8 \bar{N}_i y_i \tag{7}$$

where  $\{q\} = \{u_i, v_i, w_i, \theta_{xi}, \theta_{yi}\}$  is displacement vector and  $u_i, v_i, w_i, \theta_{xi}$ , and  $\theta_{yi}$  are the particular values at node  $i$ . Further,  $x_i$  and  $y_i$  are the cartesian coordinates of the  $i$ th nodes. Then,  $\bar{N}_i$  is an interpolation shape function for  $i$ th node.  $\bar{N}_i$  for various nodes is given in [13]. Further, element stiffness  $[k_e]$ , geometric stiffness  $[k_G]$ , and consistent mass matrices  $[m]$ , as in Eq. (8) are obtained in FE domain by employing Gauss quadrature rule. The elemental matrices are assembled [13] to obtain global level matrices and incorporated in the governing equation in Sect. 3.6.

$$[\mathbf{k}_e] = \int_{-1}^{+1} \int_{-1}^{+1} [\mathbf{B}]^T [\mathbf{D}] [\mathbf{B}] |J| d\xi d\eta \quad (8)$$

$$[\mathbf{k}_G] = \int_{-1}^{+1} \int_{-1}^{+1} [\mathbf{B}_G]^T [\mathbf{S}] [\mathbf{B}_G] |J| d\xi d\eta \quad (9)$$

$$[\mathbf{m}] = \int_{-1}^{+1} \int_{-1}^{+1} [\overline{\mathbf{N}}]^T [\mathbf{I}] [\overline{\mathbf{N}}] |J| d\xi d\eta \quad (10)$$

where  $[\mathbf{B}]$  is the linear strain–displacement matrix,  $[\mathbf{B}_G]$  is the nonlinear strain–displacement matrix obtained by means of Green–Lagrange’s strain–displacement relation Bathe [13]. Further,  $[\mathbf{S}]$  represents the resultant stress matrix,  $[\overline{\mathbf{N}}]$  is the shape functions matrix, and  $[\mathbf{I}]$  is the inertial matrix obtained as in Swaminathan et al. [11].

### 3.6 Governing Equation

In the initial part of the solution, initial or pre-buckling displacement due to temperature loading is found from Eq. (11). Using the pre-buckling displacements, residual stresses induced due to temperature loading are found.

$$([\mathbf{K}])\{q\} = P^T \quad (11)$$

where  $[\mathbf{K}]$  is the global stiffness matrix and  $\{q\}$  is the pre-buckling displacement matrix.  $P^T$  is a load vector due to temperature. The geometric stiffness matrix  $[\mathbf{K}_G]$  is obtained from the pre-buckling displacements. The second part of the solution involves the determination of critical buckling temperature from the condition.

$$([\mathbf{K}] - \lambda[\mathbf{K}_G])\{q\} = 0 \quad (12)$$

By solving the above eigenvalue problem in Eq. (12), the value of critical buckling temperatures ( $T_{cr}$ ) at which the plate will buckle is obtained. The product of  $\lambda$  and the initial guessed value is the  $T_{cr}$ .

## 4 Results and Discussions

In the current investigations, both square and rectangular porous FGM plates are considered. Several cases of porosity distribution models are considered to understand the buckling behaviour of FGM plate. The aspect ratio and thickness ratio of a plate are represented by  $b/a$  and  $b/h$ , respectively. The material properties of constituent materials ( $\text{Si}_3\text{N}_4/\text{SUS304}$ ) considered in the current study are  $E_m = 201.04 \text{ GPa}$ ,  $E_c = 348.43 \text{ GPa}$ ,  $\alpha_m = 12.33 \times 10^{-6} \text{ } 1^\circ \text{ C}$ ,  $\alpha_c = 5.8723 \times 10^{-6} \text{ } 1^\circ \text{ C}$ , and Poisson’s ratio  $\mu = 0.3$ . In a string used to describe various support conditions, the letters ‘S’, ‘C’, and ‘F’ designate simply support, clamped, and free end conditions, respectively. The first two terms in the support condition string represent the right and left side support condition, whilst the last two terms denote the top and bottom support conditions of the plate. The displacements-based boundary conditions adopted in this study are obtained from [16]. The temperature is presumed to be constant through the thickness of the plate.

### 4.1 Convergence and Validation

To check the correctness and accuracy of the developed formulation, several example problems regarding the buckling characteristics of FGM plate are solved. The outcomes obtained are compared to the results existing in the literature.

- **Example 1:** In this example, convergence studies are performed by considering the  $T_{cr}$  of the square isotropic plate ( $E = 1.0 \text{ N/m}^2$ ,  $\nu = 0.3$ , and  $\alpha_0 = 1.0 \times 10^{-6}$ ). The convergence study is carried out by selecting different mesh sizes, and critical buckling temperature are mentioned in Table 1. It is noticed that accuracy in  $T_{cr}$  is achieved by mesh refinement. The results are well converged at  $10 \times 10$  mesh. Hence subsequent analysis is carried out using  $10 \times 10$  mesh.
- **Example 2:** In the second example, the FGM ( $\text{Al}/\text{Al}_2\text{O}_3$ ) simply supported square plate subjected to uniform temperature is considered to obtain  $T_{cr}$ .  $T_{cr}$  is obtained and compared to those given by Javaheri and Eslami [18], as tabulated in Table 2.

**Table 1** The convergence of  $T_{cr}$  for a simply supported square plate subjected to a uniform temperature

Mesh size	$b/h = 100$	$b/h = 20$
$2 \times 2$	3.1786E-04	3.7185E-03
$4 \times 4$	1.2835E-04	3.1129E-03
$6 \times 6$	1.2654E-04	3.1078E-03
$8 \times 8$	1.2646E-04	3.1072E-03
$10 \times 10$	1.2645E-04	3.1070E-03
Matsunaga [17]	$1.2640 \times \text{E-04}$	$3.1090 \times 10^{-3}$

**Table 2** Comparison of  $T_{cr}$  for square SSSS Aluminum/Alumina FGM square plate

Source	$n$	$b/h = 10$	$b/h = 20$	$b/h = 40$	$b/h_s = 60$	$b/h = 80$	$b/h = 100$
Javaheri and Eslami [18]	1	757.891	196.257	49.5	22.037	12.402	7.939
Present with MS		757.5699	198.671	50.293	22.405	12.613	8.076
Present with NS		747.189	195.487	49.453	22.028	12.400	7.939
Javaheri and Eslami [18]	10	692.519	183.141	46.455	20.703	11.657	7.462
Present with MS		697.16	185.064	47.002	20.952	11.798	7.554
Present with NS		691.078	183.005	46.447	20.702	11.656	7.463

The material properties of the constituent material are  $E_m = 70$  GPa;  $\alpha_m = 23 \times 10^{-6}/^\circ\text{C}$  for Aluminum (Al) and  $E_c = 380$  GPa;  $\alpha_c = 7.4 \times 10^{-6}/^\circ\text{C}$  for Alumina ( $\text{Al}_2\text{O}_3$ ). The solution obtained from the current formulation is in decent agreement with the results in the literature.

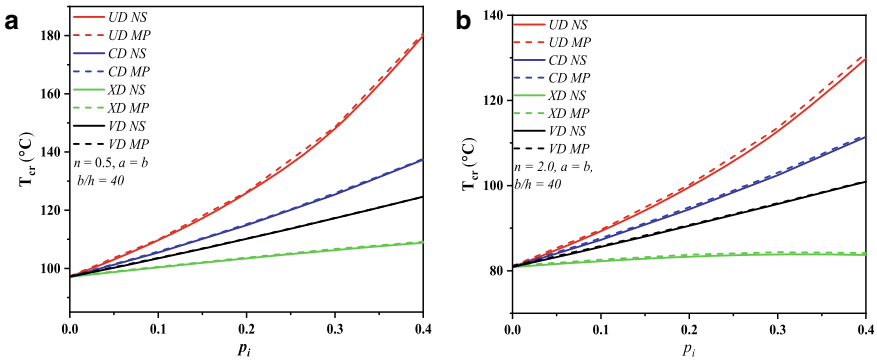
### 4.2 Parametric Investigations

In the previous section, it is noticed that the current results using FE formulation are in decent concurrence with the results existing in the literature. Thus, in the subsequent subsections, buckling responses of the FGM plates are examined by considering numerous parameters such as porosity distribution,  $n$ ,  $b/a$ ,  $b/h$ , and support condition. The parametric studies related to buckling characteristics are discussed in the successive subsections.

- Effect of porosity and volume fraction exponent

Figure 3 depicts the variation of  $T_{cr}$  with porosity coefficient and several porosity distribution models of porous FGM plate exposed to uniform temperature rise. The  $T_{cr}$  variation is plotted considering middle surface and neutral surface in the formulation and noticeable difference is observed showing the importance of neutral surface. It is detected from Fig. 3 that  $T_{cr}$  increases with an increase in porosity coefficient in the case of the plate with  $n = 0.5$ , irrespective of the porosity distribution. The reason for such behaviour can be because of the reduction in thermal conductivity due to the increase in porosity coefficient and increase in the moment of inertia of the FGM plate due to the occurrence of pores in the material. Whilst at a higher volume fraction exponent, it can be observed from Fig. 3b that a slight decrease in  $T_{cr}$  with an increase in the  $p_i$  is noticed in the case of VD kind of porosity. The porosity





**Fig. 3** Variation of  $T_{cr}$  with porosity coefficient for FGM plate with **a**  $n = 0.5$  **b**  $n = 2.0$  ( $b/a = 1$ ,  $b/h = 40$ )

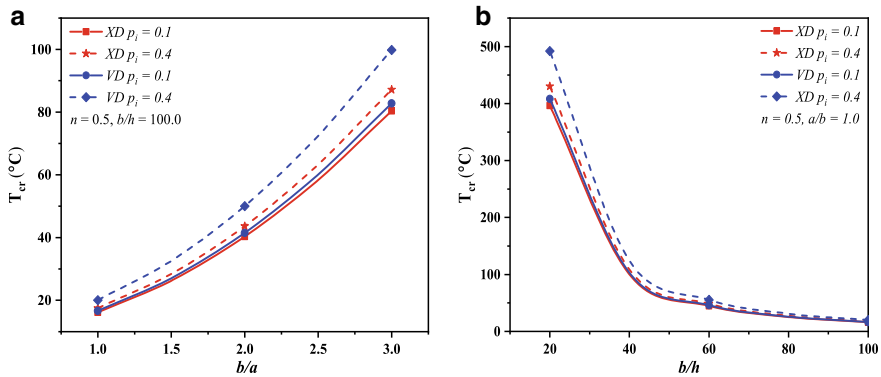
distribution model too significantly influences the critical buckling temperature as observed in the case of UD type porosity having maximum  $T_{cr}$  followed by CD, VD, and XD. Also, critical buckling temperature decreases with an increase in the  $n$ , irrespective of porosity distribution due to the increase in the metal component in the FGM plate. Significant variation in  $T_{cr}$  with porosity coefficient is observed for UD porosity distribution.

- Effect of aspect ratio and thickness ratio

The outcome of  $b/a$  and  $b/h$  on  $T_{cr}$  of porous FGM plate with XD and VD type of porosity is investigated in this segment by plotting the variation in Fig. 4a and b. The  $T_{cr}$  is noticed to increase with the increase in the  $bla$  of the porous FGM plate, irrespective of the porosity distribution. The  $T_{cr}$  increases with the increase in the porosity coefficient. The variation is significant in plates with higher  $bla$ . Further, it is observed that, for both the porosity distribution considered,  $T_{cr}$  decreases with an increase in  $b/h$ . This behaviour is due to the reduction in stiffness of the plates as the thickness of the plate decreases.

- Effect of support condition

Table 3 presented the variation of the  $T_{cr}$  for porous FGM plates with various porosity distribution and supported on different support conditions. Four different types of support conditions (SSSS, CCCC, SSCC, CCFF) and porosity distribution (UD, CD, VD, XD) are considered. For this study, the porosity coefficient is chosen as 0.1 and 0.4. It is noticed that the  $T_{cr}$  increases with the increase in porosity coefficient, regardless of porosity distribution and support condition. In addition, the  $T_{cr}$  increases with the increase in the number of edge restraints of the FGM plate in the order of SSSS < CCFF < CCSS < CCCC. The CCCC plates show a noteworthy increase in the  $T_{cr}$  with a rise in the  $p_i$  regardless of the porosity distribution. Conversely, the increase in the  $T_{cr}$  with an increase in the  $p_i$  is minimal in the case of SSSS porous FGM plates.



**Fig. 4** Variation of  $T_{cr}$  with porosity coefficient for FGM plate with **a** aspect ratio **b** thickness ratio  $T_{cr}$

**Table 3**  $T_{cr}$  for various support conditions of FGM plate with porosity in a thermal environment

Support conditions	UD		CD		XD		VD	
	$p_i = 0.1$	$p_i = 0.4$	$p_i = 0.1$	$p_i = 0.4$	$p_i = 0.1$	$p_i = 0.4$	$p_i = 0.1$	$p_i = 0.4$
SSSS	109.645	179.936	105.439	137.332	100.380	108.845	103.390	124.627
CCCC	288.429	473.422	277.309	360.978	264.099	286.576	271.957	327.806
CCSS	208.805	342.706	200.767	261.390	191.181	207.403	196.884	237.318
CCFF	147.656	242.391	141.944	184.701	135.215	146.798	139.218	167.803

## 5 Conclusion

The aim of the existing investigation is to study the consequence of porosity and temperature on the buckling response of FGM plate member considering neutral surface is carried out using FE technique. To simulate the porosity occurring during the manufacturing process, four different types of porosity distribution models are explored. Porosity-dependent material properties of FGMs are evaluated using modified power law. Thermal loads are presumed to be uniformly distributed along the thickness direction. The Influences of various parameters such as porosity distribution,  $b/a$ ,  $n$ ,  $b/h$ , and support conditions on the buckling response of porous FGM plates in thermal environment have been investigated considering a neutral surface. The main findings of the work are listed as follows:

1. It is observed that UD porosity exhibits the highest  $T_{cr}$  in comparison to other porosity distributions in the order of  $UD > CD > VD > XD$ .
2. In comparison to other porosity distributions, the maximum variation in the  $T_{cr}$  with porosity coefficient is noticed for the FGM plate with UD porosity. Conversely, plates with XD porosity show the least variation.

3. The neutral surface shift takes place due to changes in porosity distribution, porosity coefficient, and volume fraction exponent. This shift significantly affects the  $T_{cr}$ .
4. The  $T_{cr}$  of porous FGM plates increases with an increase in the number of edge restraints. The CCC plates show a significant increase in the  $T_{cr}$  with an increase in the  $p_i$ .
5. The  $T_{cr}$  increases with an increase in the aspect ratio and decreases with an increase in the thickness ratio of the porous FGM plate.

## References

1. Mota AF, Loja MAR, Barbosa JI, Rodrigues JA (2020) Porous functionally graded plates: An assessment of the influence of shear correction factor on static behavior. *Math Comput Appl* 25:25. <https://doi.org/10.3390/mca25020025>
2. Singha MK, Prakash T, Ganapathi M (2011) Finite element analysis of functionally graded plates under transverse load. *Finite Elem Anal Des* 47:453–460. <https://doi.org/10.1016/j.finel.2010.12.001>
3. Zhang DG, Zhou YH (2008) A theoretical analysis of FGM thin plates based on physical neutral surface. *Comput Mater Sci* 44:716–720. <https://doi.org/10.1016/j.commatsci.2008.05.016>
4. Farzam-Rad SA, Hassani B, Karamodin A (2017) Isogeometric analysis of functionally graded plates using a new quasi-3D shear deformation theory based on physical neutral surface. *Compos Part B Eng* 108:174–189. <https://doi.org/10.1016/j.compositesb.2016.09.029>
5. Lee Y, Bae S, Kim J (2016) Thermal buckling behavior of functionally graded plates based on neutral surface. *Compos Struct* 137:208–214. <https://doi.org/10.1016/j.compstruct.2015.11.023>
6. Van Do T, Doan DH, Duc ND, Bui TQ (2017) Phase-field thermal buckling analysis for cracked functionally graded composite plates considering neutral surface. *Compos Struct* 182:542–548. <https://doi.org/10.1016/j.compstruct.2017.09.059>
7. Arefi M, Mohammad-Rezaei Bidgoli E, Zenkour AM (2019) Free vibration analysis of a sandwich nano-plate including FG core and piezoelectric face-sheets by considering neutral surface. *Mech Adv Mater Struct* 26:741–752. <https://doi.org/10.1080/15376494.2018.1455939>
8. Saad M, Hadji L (2022) Thermal buckling analysis of porous FGM plates. *Mater Today Proc* 53:196–201. <https://doi.org/10.1016/j.matpr.2021.12.550>
9. Kiran MC, Kattimani SC, Vinyas M (2018) Porosity influence on structural behaviour of skew functionally graded magneto-electro-elastic plate. *Compos Struct* 191:36–77. <https://doi.org/10.1016/j.compstruct.2018.02.023>
10. Ebrahimi F, Jafari A, Barati MR (2017) Free vibration analysis of smart porous plates subjected to various physical fields considering neutral surface position. *Arab J Sci Eng* 42:1865–1881. <https://doi.org/10.1007/s13369-016-2348-3>
11. Swaminathan K, Hirannaiah S, Rajanna T (2022) Vibration and stability characteristics of functionally graded sandwich plates with/without porosity subjected to localized edge loadings. *Mech Based Des Struct Mach* 0:1–39. <https://doi.org/10.1080/15397734.2022.2038619>
12. Whitney JM, Pagano NJ (1972) Shear deformation in heterogeneous anisotropic plates. *J Compos Mater* 6:316–319. <https://doi.org/10.1177/002199837200600214>
13. Bathe KJ (2014) *Finite element procedures*, 2nd ed
14. Chandra SKS, Rajanna T, Rao KV (2020) A parametric study on the effect of elliptical cutouts for buckling behavior of composite plates under non-uniform edge loads. *Lat Am J Solids Struct* 17:1–15

15. Rajanna T, Banerjee S, Desai YM, Prabhakara DL (2016) Effects of partial edge loading and fibre configuration on vibration and buckling characteristics of stiffened composite plates. *Lat Am J Solids Struct* 13:854–879. <https://doi.org/10.1590/1679-78252239>
16. Swaminathan K, Sachin H, Rajanna T (2020) Buckling analysis of functionally graded materials by dynamic approach. *Mater Today Proc* 45:172–178. <https://doi.org/10.1016/j.matpr.2020.10.412>
17. Matsunaga H (2005) Thermal buckling of cross-ply laminated composite and sandwich plates according to a global higher-order deformation theory. *Compos Struct* 68:439–454. <https://doi.org/10.1016/j.compstruct.2004.04.010>
18. Najafizadeh MM, Heydari HR (2004) Thermal buckling of functionally graded circular plates based on higher order shear deformation plate theory. *Eur J Mech A/Solids*. 23:1085–1100. <https://doi.org/10.1016/j.euromechsol.2004.08.004>

# Experimental Investigation of the Behavior of Tubular T-Joint of Jacket Structures



N. Murugan, Vadivuchezhian Kaliveeran, and Subrahmanya Kundapura

**Abstract** This study deals with a preliminary experimental study to examine the behavior of tubular T-joint of Jacket structures under compressive load, which is helpful for further study of reinforcement in T-joints for strengthening. A specimen of T-joint with geometric dimensions of chord length = 494 mm, chord diameter = 141 mm, chord thickness = 5 mm, and brace length = 237 mm, brace diameter = 90 mm, brace thickness = 4.5 mm was considered for this study. The specimen is subjected to axial compressive load which is applied from the top end of the brace member. The ends of the chord member are in simply supported condition. The experiment is conducted in a 40 T UTM machine. The loads are applied with an interval of 50 kgf starting from zero to the yield load of 9,600 kgf. The experimental setup, specimen details, and the relevant results (load-deformation relationship and failure mechanism) are presented. The findings of the study, i.e., local joint deformation behavior under compressive load, are presented graphically.

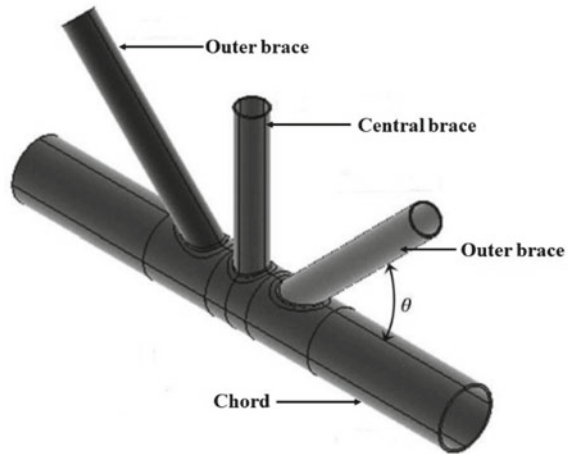
**Keywords** Offshore jacket platforms · Tubular T-joints · Compressive load · Experimental study · Strength

## 1 Introduction

Offshore platforms support drilling, production, storage, and distribution facilities in the sea. The most common offshore platform, the jacket platform, is used for shallow water depths up to 200 m [9]. The tubular sections made of steel are commonly used in offshore installations and the tubular sections are capable of resisting the hydrodynamic forces, and possess higher strength for the given weight of the section compared to conventional steel sections [4]. In general, cylindrical steel tubular sections are more commonly used due to their advantage in the construction of offshore structures [2], and numerous large tubular structures have been built for

---

N. Murugan · V. Kaliveeran (✉) · S. Kundapura  
Water Resources and Ocean Engineering, National Institute of Technology Karnataka,  
Mangalore 575025, India  
e-mail: [vadivuchezhian\\_k@yahoo.co.in](mailto:vadivuchezhian_k@yahoo.co.in)

**Fig. 1** Tubular KT-joint [6]

offshore oil exploration in the past six decades. Over 7000 offshore platforms have been installed around the world [3].

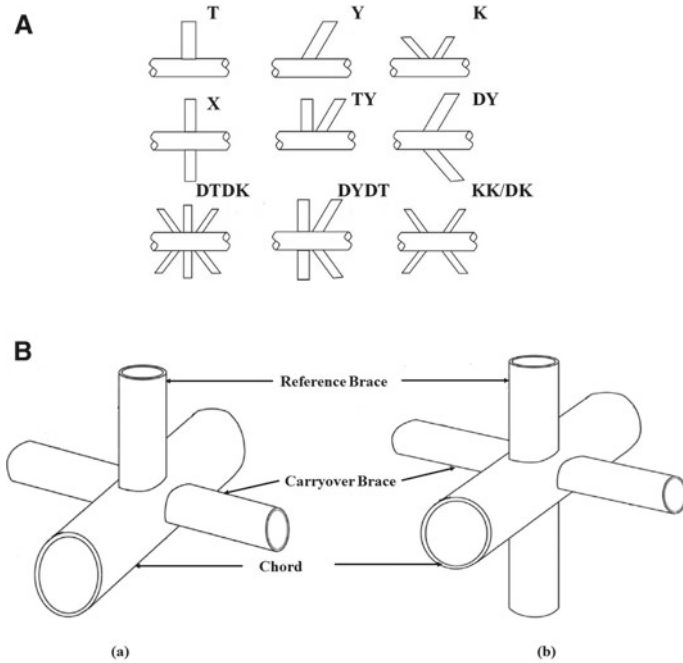
A joining of two or more tubular members, between vertical member, i.e., chord and horizontal/inclined members, i.e., brace is referred to a tubular joint (Fig. 1). The tubular member which has a large diameter is known as the chord, whereas the smaller diameter is called the brace [6].

Saini et al. [4] presented uniplanar (Fig. 2a) and multi-planar (Fig. 2b) joint types that are commonly utilized in offshore platforms. Qu et al. [5] reported that the tubular joints are critical structural members playing a crucial role in transferring the loads in an offshore platform structure. Fung et al. [8] documented that joints are an important part of the offshore structure and require greater attention because of their geometric discontinuity.

Figure 3 shows the possible failure types of unreinforced tubular T and X joints. The failure can be due to tensile forces and it can also be due to compressive forces. The tensile failure has both ductile and brittle nature and is characterized by fracture of the material.

Among the six failure types, first five are subjected to axial tensile load and in the last case, an axial compressive load is applied. The different types of failure mechanisms shown in Fig. 3 are explained in detail here.

The extension of the branch member is depicted in Failure Type 1 in Fig. 3. A branch's full strength is developed, and failure occurs at the branch adjacent to the weld toe, which is ductile. The fracture occurs closer to the weld toe, where localized stresses increase and defects are more easily to happen. Failure Type 2 is also experiencing the same phenomenon as Type 1 except that the weld metal is exposed to fracture. Here, the main concern is about designing of the weld which has to be taken enough care to arrest this kind of failure and maintain the full design load condition of the member. When the length of the chord is long with an unsupported length, the failure mechanism that occurs is Failure Type 3. The main reason for



**Fig. 2** a Types of uniplanar tubular joints [4]. b Example of multi-planar joints. **A** Multi-planar XT joint and **B** Multi-planar XX joint [4]

this failure is the chord wall experiences bending compressive stress and it cannot be considered as a true joint failure. The large plastic deformation of the chord wall is normal in Failure Type 4. The fracturing of chord wall occurs at the weld toe and happens at the latter stages of plastic deformation. In this mode of failure, the load-carrying capacity of both the branch and the chord is lost, so this failure mode should be avoided while designing joints.

Failure Type 5 is a metallurgical issue that gets very serious as the thickness of the wall exceeds 1–2 inches. Due to substantial local thermal strains and probable weak planes in the chord wall, lamellar tearing commonly occurs near to the welds. A T-joint compression failure is seen in Type 6 which is characterized by local buckling or failure of chord wall near branch intersection. In the present study, compressive loading is considered to understand the behavior of the joint deformation and its failure pattern which can be further useful in incorporating the stiffeners to enhance the strength of the joint.

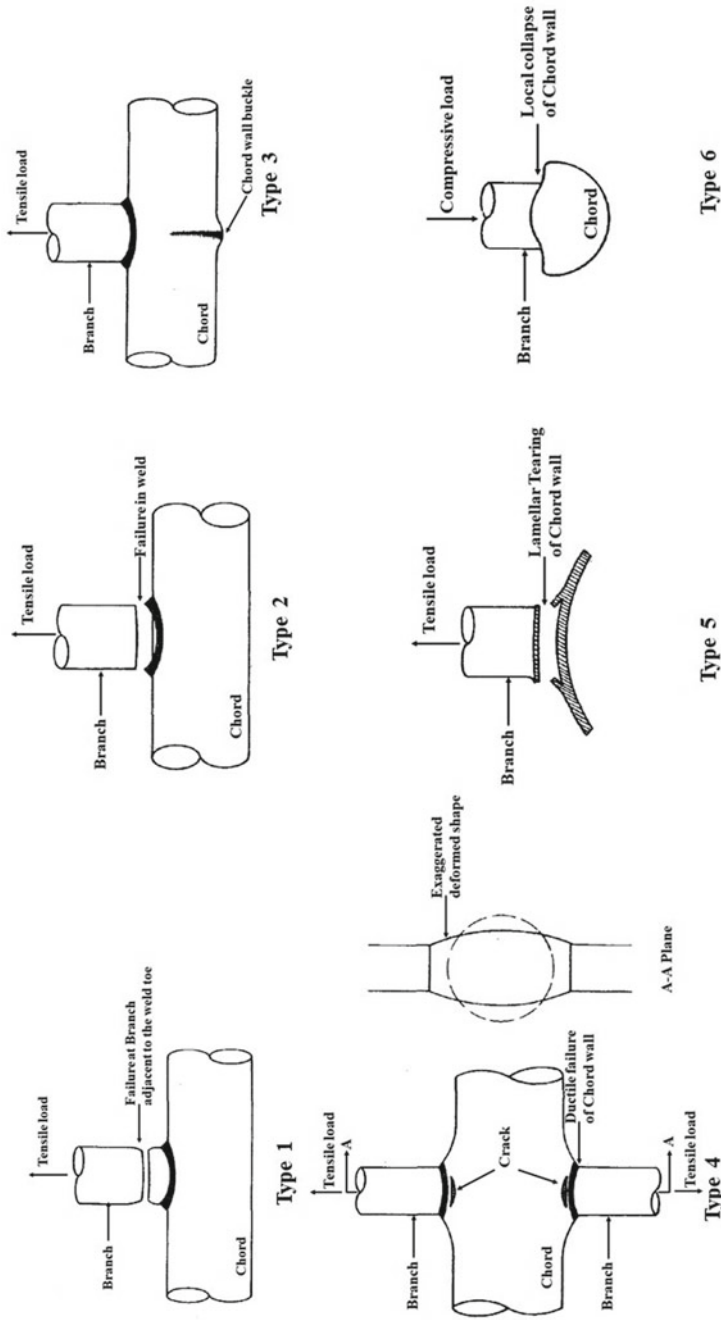


Fig. 3 Failure modes for tubular joints [7]



## 2 Experimental Study

The behavior of tubular joints under axial compressive load is studied by using an experimental setup. The tubular T-joint model is having dimensions of chord length = 494 mm, brace length = 237 mm, chord diameter = 141 mm, brace diameter = 90 mm, chord thickness = 5 mm, brace thickness = 4.5 mm and the corresponding dimensionless parameters are Brace to chord diameter ratio ( $\beta = d/D$ ) = 0.64, Chord wall slenderness ratio ( $\gamma = D/2T$ ) = 14.1, and Brace to chord wall thickness ratio ( $\tau = t/T$ ) = 0.9. The typical ranges for the parameter values are shown in Table 1. In total, three specimens are prepared for the experimental study.

### 2.1 Material Composition

The tubular T-joint used for experimental study is made of the material which has the following elements shown in Table 2. The chemical analysis by using spectrometric analysis test method is done at GWASF Quality Castings (P) Ltd.

### 2.2 Model Preparation

The specimens as per the dimensions are prepared for the present study. Initially, the raw long pipe was cut into the specimens by using grinder cutting machine as shown in Fig. 4a. The cutting machine is an industrial power tool that uses an abrasive wheel for cutting the material. The pipes are hold tightly by using clamp mechanism at the grinding machine, then the cutting process is done. The chord and brace members prepared after the cutting process are displayed in Fig. 4b. The edge of these members is non-uniform.

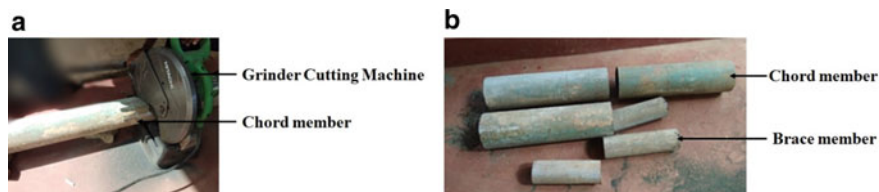
The non-uniformity of members' edges is made uniform by means of facing operation in the lathe. In this process, workpiece (specimen) is placed on the machine; a cutting tool is pressed against it at the end (Fig. 5). The material removal is done by the rotation of cutting tool over the workpiece.

**Table 1** Typical values of tubular joint parameters. Reference: API RP 2A [1]

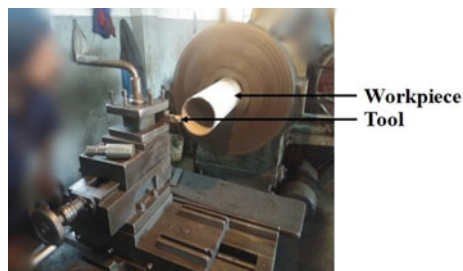
Parameter	Typical range	Limitations	
		Minimum	Maximum
$\beta = d/D$	0.4–0.8	0.2	1
$\gamma = D/2T$	12–20	10	50
$\tau = t/T$	0.3–0.7	0.2	1
$\theta$	40°–90°	30°	90°

**Table 2** Spectrometric analysis of material

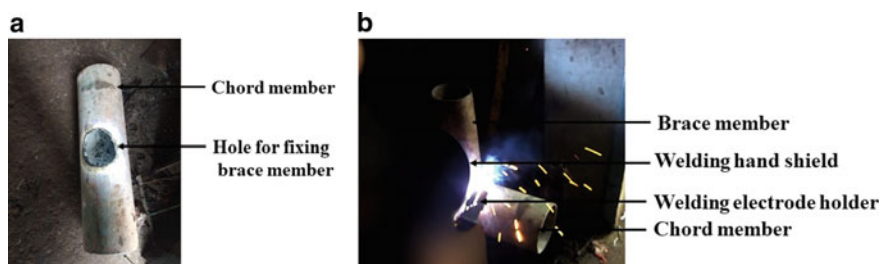
Element %	C	Si	Mn	S	P	Cr	Mo	Ni	Cu	V	W	Co	Nb	Fe
1	0.18	0.052	0.99	0.013	0.017	0.010	0.001	0.005	0.009	0.002	0.003	0.003	0.002	98.71
2	0.078	0.15	0.47	0.017	0.024	0.006	0.001	0.004	0.008	0.001	0.002	0.002	0.001	99.23



**Fig. 4** a Pipe cutting using grinder cutting machine. b Chord and brace members



**Fig. 5** Edge preparation

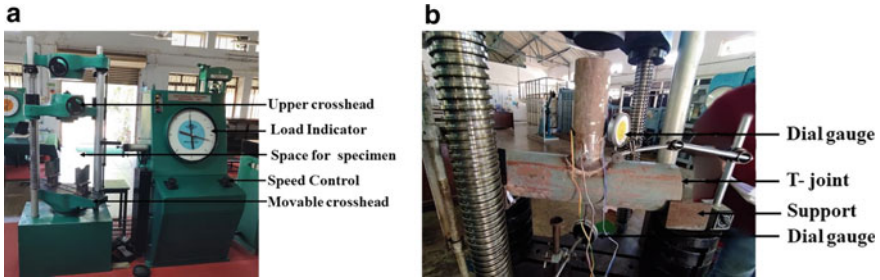


**Fig. 6** a Hole preparation for joining brace member. b Welding of chord and brace member

To join the brace member with the chord member, a circular hole with a diameter of 9 cm is made on the chord member by welding process depicted in Fig. 6a. Then the members are connected through welding process and yields in final tubular T-joint specimen as shown in Fig. 6b.

### 2.3 Experimental Details

The experimental setup used for the present study is shown in Fig. 7a. The dial gauges are placed to measure the chord ovalization of the tubular joint. The model is simply supported at the ends of the chord by means of saddle supports.



**Fig. 7** a Experimental setup. b Experimental setup with dial gauges

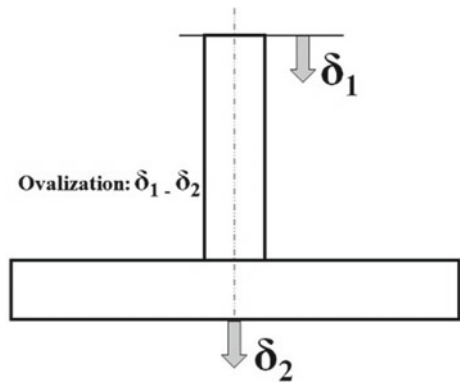
Strain gauges are used around the brace member to measure the strain variations at the crucial spots and dial gauges are used to measure the displacements at the designated places for each specimen (Fig. 7b). The load-controlled actuator can handle up to 40 tonnes of force. The brace load is applied on each specimen starting at 0 kg and steadily increasing with a load interval of 50 kg until the specimen fails.

### 3 Results and Discussion

This section presents and evaluates the load-deformation data obtained from the studies. The chord ovalization at the center of the T-joint is determined by measuring the difference between the value of the dial gauge reading near the chord-brace intersection and the dial gauge value measured at the center of the joint, as illustrated in Fig. 8. Displacements generated by overall chord bending are not taken into account.

From the ovalization curve, it is observed that the ovalization starts at 8000 kgf. The reason behind was the failure started at the supports initially. The supports were failing till the failure starts at the joint. After that, the ovalization was taking place

**Fig. 8** Definition of ovalization



**Fig. 9** Failure at support

in the joints in the usual way. Figure 9 depicts the failure of the specimen at the supports.

By observing the above ovalization curve, we can judge that there is a negative ovalization up to 8000 kg after that positive ovalization. During the experiment, we observed that the load was initially transferred to the support but the applied load should be transferred to the joint. So, this may be the reason for the negative ovalization up to 8000 kg. The corresponding load-deformation information is depicted in Fig. 10.

Figure 11 shows the ovalized specimen after the experiment. Till the elastic limit, the load and deformation vary linearly as it depicted in Fig. 12. The welded joint was transferring the load from the brace member to chord member effectively. Once the load is crossing the elastic–plastic transition and entering into the plastic limit, the chord wall starts to local buckling which results in ovalized shape of the specimen.

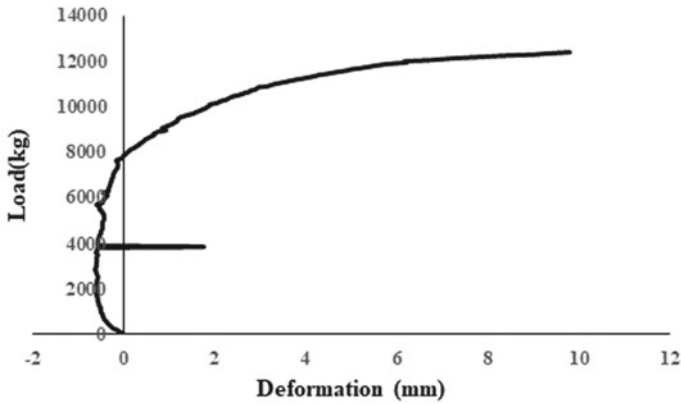


Fig. 10 Ovalization curve (case 1)

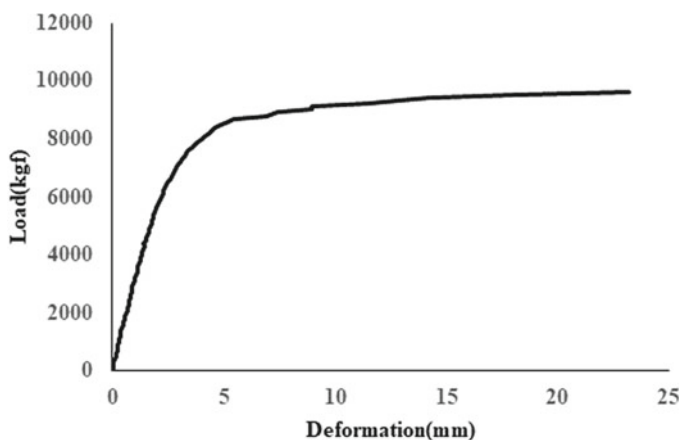
Fig. 11 Ovalized specimen



## 4 Conclusions

Three experiments on uniplanar tubular T-joints subjected to axial brace compressive load were performed. Based on the experimental results, the conclusions and recommendations arrived are the followings.

- From the deformed shape of the specimens, it is observed that T-joints under axial compressive loading failed by plastification of the chord around the joint intersection.
- By introducing reinforcements (further study), the joint strength enhancement can be done effectively.



**Fig. 12** Ovalization curve (case 2)

**Acknowledgements** We are very grateful to the funding agency, AR & DB, Ministry of defence, file number ARDB/01/2031964/MI for providing financial assistance for conducting our research work.

## References

1. API-RP American Petroleum Institute Recommended practice for planning, designing and constructing fixed offshore Platforms, 22nd edition (2014)
2. Chen WJ, Han DJ (1985) Tubular members in offshore structures. Pitman Advanced Publishing Program, Boston, MA
3. Digre KA, Krieger W, Wisch DJ, Petrauskas C (1994) API RP 2A draft section 17 assessment of existing platforms. In: Chrysostomidis C et al (eds) Behavior of offshore structures, BOSS '94. Pergamon, Oxford, pp 467–478
4. Saini DS, Karmakar D, Ray-Chaudhuri S (2016) A review of stress concentration factors in tubular and non-tubular joints for the design of offshore installations. *J Ocean Eng Sci* 1:186–202
5. Qu H, Huo J, Xu C, Fu F (2014) Numerical studies on dynamic behavior of tubular T-joint subjected to impact loading. *Int J Impact Eng* 67:12–26
6. Ahmadi H, Lotfollahi-Yaghin MA, Yong-Bo S (2013) Chord-side SCF distribution of central brace in internally ring-stiffened tubular KT-joints: a geometrically parametric study. *J Thin-Walled Struct* 70:93–105
7. Pan RB, Plummer FB, Kuang JG (1977) Ultimate strength of tubular joints. *J Petrol Technol* 29(04):449–460
8. Fung TC, Chan TK, Soh CK (1999) Ultimate capacity of Doubler plate-reinforced tubular joints. *J Struct Eng* 125(8)
9. Thandavamoorthy TS (2000) Investigations on internally ring-stiffened joints of offshore platforms. *J Offshore Mech Artic Eng (OMAE)* 122:233–242

# Numerical Investigation of Transient Heat Conduction Analysis in Functionally Graded Material (FGMs) Using MATLAB Partial Differential Equation (PDE) Toolbox



Mansingh Yadav and Divyansh Krishana

**Abstract** MATLAB partial differential equation (PDE) toolbox is used to evaluate the general partial differential equation of different problems like heat transfer, structural mechanics, and electromagnetics. It can find the heat flow rates, heat flux, and temperature distribution over the surfaces by modeling conduction-dominant heat transfer problems. Here, this chapter has solved the previous research problems of two-dimensional transient heat conduction by using MATLAB partial differential equations (PDE) toolbox simulation. Previously, it was solved by using the Numerical Manifold Method (NMM). Here, firstly, 2D or 3D geometry is imported from mesh data or STL files. Automatically, the PDEs toolbox creates meshes using tetrahedral and triangular elements through which solved the PDEs by using finite element methods, and post-processing is done to analyze the results. The findings indicate that the use of the MATLAB PDE toolbox as a solution technique is highly efficient, with closely matched results to the solution.

**Keywords** Functionally graded material · MATLAB PDE toolbox · Finite element method · Transient heat conduction

## 1 Introduction

Functionally graded materials (FGMs) were developed by Japan in 1984 as an advanced composite material with the aim of achieving specific material properties [1]. A composite material consists of two or more constituent materials with dissimilar properties that merge to produce the advantages of each constituent material. Generally, some problem occurs in the composite, like delamination or fiber

---

M. Yadav (✉)

Indian Institute of Technology Bombay, Mumbai, Maharashtra 400076, India  
e-mail: [mansinghyadav8418@gmail.com](mailto:mansinghyadav8418@gmail.com)

D. Krishana

Indian Institute of Technology Delhi, Hauz Khas, New Delhi 110016, India



cracking, due to discontinuity of composite material properties that could be overcome by using functionally graded material. FGMs generally continuously consist of multiphase material with required volume fraction change in the spatial direction, tailoring the required material properties and morphologies. The application of FGMs is extensive in numerous advanced technology domains, such as the automotive, aerospace, nuclear, and bioengineering industries [1, 2].

Compared to homogeneously reinforced composite materials, functionally graded materials are developed to increase the durability and working performance of the composite materials, generally to avoid the sharp area of the composite by an effective convergence of it. The single-phase/constituent is non-homogeneously distributed within the matrix in the mono-reinforced FGM, while in double FGM, more than one constituent/phase is involved. Both cases are produced in continuous gradient because of the matrix's continuous distribution variation of constituents/phases. Normally, designers categorize the FGMs on the basis of different combinations of matrices and constituent materials like metal/ceramic, polymer/ceramic, ceramic/ceramic, polymer/polymer, and metal/metal. The use of FG material enhances inter-phase bonding, boosts fracture resistance and toughness within the graded volume, and reduces thermal stresses in the final product [3].

It is observed that the temperature parameters like specific heat and thermal conductivity may vary spatially. The analytical problem to solve the FGMs requires, numerical approaches like boundary element method (BEM), finite element method (FEM), meshless methods, and PDE solver to solve unsteady state heat conduction problems [4]. Chen et al. [5], graded finite element methods and an adaptive time integration scheme are used for the investigation of the unsteady heat conduction problems in the FGMs. Charoensuk and Vessakosol [6] investigated the transient heat transfer in the FGMs through the high-order control volume FEM. Burlayenko et al. [7] studied thermal stresses and transient temperatures using graded FEM in the FGMs.

Sutradhar and Paulino [8] studied 3D unsteady heat conduction using the simple boundary element method (BEM) with the boundary-only formulation in the FGMs. Yang and Gao [9] used radial observation-based BEM in the FGMs for transient heat conduction. Cao et al. [10] investigated the unsteady/unstable state thermal regions in FGMs by using the hybrid-graded FEM. Recently, the numerical manifold method (NMM) has been used to investigate discontinuous/continuous problems and also used to solve the transition from continuous to discontinuous problems. NMM has bi-cover systems such as physical cover (PC) and mathematical cover (MC).

As a result, the evaluated portion of the NMM can be summed up as follows: (1) Not all constraints are compatible with the MC, which can considerably complicate the finite difference process, particularly when dealing with complex geometries. (2) To accurately represent inherent physical characteristics, unique terms may need to be incorporated into the sequence. (3) It is possible to obtain higher-order estimators [4].

In this chapter, the MATLAB PDEs toolbox is being explored to analyze 2D transient heat transfer problems in FGMs due to its benefits and the significance of FGMs thermal behavior studies. The chapter is structured as follows: Sect. 2 lists

the governing equation, boundary conditions, and initial condition. In Sect. 3, the discrete formulations of the problems using the MATLAB PDEs tool are derived, along with details about the solving procedures. To validate the proposed method, numerical examples are tested in Sect. 4. The chapter concludes with a summary in Sect. 5.

## 2 Governing Equation

Figure 1 shows the transient heat conduction issue in a two-dimensional body constructed of isotropic FGMs. The contour characterizes the practical domain of  $\Gamma_1$  and  $\Gamma_2$ , where  $\Gamma_1$  and  $\Gamma_2$  are the thermal and heat transfer boundaries, respectively. This situation's governing equation is:

$$\frac{\partial}{\partial x_1} \left( k(x) \frac{\partial T(x, t)}{\partial x_1} \right) + \frac{\partial}{\partial x_2} \left( k(x) \frac{\partial T(x, t)}{\partial x_2} \right) + Q = \rho(x)c(x) \frac{\partial T(x, t)}{\partial t} \quad (1)$$

where the partial derivative is denoted by  $k$ ,  $\rho$ , and  $c$  are the conductivity, density, and specific heat of the FGMs material at constant pressure, respectively. It may change with distance  $[x = (x_1, x_2)]$ . The temperature, time, and heat source are denoted by  $T$ ,  $t$ , and  $Q$ , respectively. The necessary and natural barrier conditions are as follows:

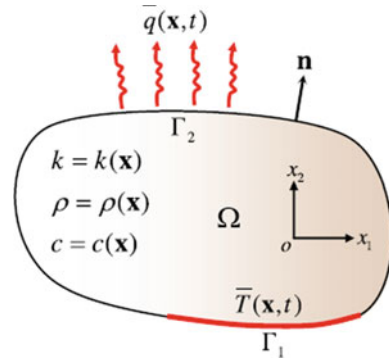
$$T(x, t) = \bar{T}(x, t) \text{ on } \Gamma_1 \quad (2)$$

$$-k(x) \frac{\partial T(x, t)}{\partial x_1} n_1 - k(x) \frac{\partial T(x, t)}{\partial x_2} n_2 = \bar{q}(x, t) \text{ on } \Gamma_2 \quad (3)$$

where  $\bar{q}$  and  $\bar{T}$  are the heat flux on  $\Gamma_2$  and temperature on  $\Gamma_1$ , respectively ( $n_1, n_2$ ) =  $n$  is the outward unit normal of the domain shown in Fig. 1. The starting condition is specified as

$$T(x, t)|_{t=0} = T_0(x) \quad (4)$$

**Fig. 1** Isotropic FGM body with transient heat conduction [4]



### 3 Analysis of Transient Heat Conduction Through MATLAB PDE Toolbox

#### 3.1 Introduction of the MATLAB PDE Tool

Nowadays, millions of scientists and engineers use MATLAB to analyze data, develop algorithms, and build models. The Partial Differential Equation Toolbox contains functions for using finite element analysis to solve heat transfer, structural mechanics, and general partial differential equations (PDEs) in MATLAB. Deformation, stress, and strain can all be calculated using linear static analysis. The toolkit includes a direct time integration solution for modeling structural dynamics and vibration. Modal analysis can be used to determine the structural properties of a component by determining natural frequencies and mode shapes.

Heat fluxes, temperature distributions, and heat flow rates by the surface can all be calculated using conduction-dominant heat transfer models. You can use bespoke PDEs to do magnetostatic and electrostatic evaluations, as well as tackle other common problems. The Partial Differential Equation Toolbox allowed the addition of 2D and 3D models from STL or mesh data. Meshes with triangular and tetrahedral elements can be generated automatically. Then PDEs are solved using the finite element method, which is then post-processed to study and interpret the results.” This study addresses the transient heat conduction problem to provide temperature distributions under time-varying conditions, and other thermal parameters are monitored [6–8].

In this study, we used MATLAB partial differential equation toolbox simulation to tackle the prior research difficulties of two-dimensional transient heat conduction, which were initially solved using the Numerical Manifold Method (NMM) [4]. To begin, import 2D or 3D geometry from mesh data or STL. The PDEs toolbox could create meshes automatically using tetrahedral and triangle elements, then solve PDEs utilizing finite element methods and analyze results through post-processing (Fig. 2).

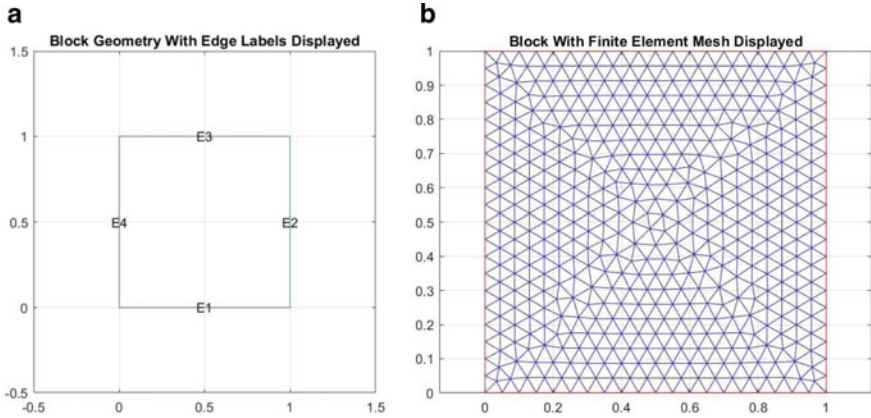


Fig. 2 Showing the block geometry (a) and finite element meshing (b)

### 3.2 Solving Processor for the Transient Heat Conduction Solutions

Three numerical instances of growing difficulty are studied in this part to verify the proposed strategy. Transient heat transport effects are investigated in the square region, the L-shaped region, and the multi-connected region made up of FGMs materials. These problems are solved by MATLAB PDE Tool using the following procedure given in the flow chart. The analytical solution for temperature variation is derived from Sutradhar and Paulino’s work [8].

$$T(x, t) = \frac{T_1 x_1}{\sqrt{kL}} + \frac{2T_1}{\sqrt{k}} \sum_{n=1}^{\infty} \frac{\cos(n\pi)}{n\pi} \sin\left(\frac{n\pi x_1}{L}\right) \exp\left(-\frac{n^2 \pi^2}{L^2} k_o t\right) \quad (5)$$

where

$$T_1 = \sqrt{k_0}(1 + \gamma L)T_r \text{ and } k_0 = \frac{k(x)}{\rho c(x)} \quad (6)$$

## 4 Numerical Analysis

### 4.1 In the Square Region, Unsteady State Heat Conduction

The effect of the material gradient is investigated. The discretization with step size  $\Delta t = 0.001$  and graded parameter  $\gamma = 2$  is used. Here in the  $x_1$  direction, transient heat conduction occurs in which temperature is the function of time and space. However, in the  $x_2$  direction, the surface is assumed to be adiabatic, where no heat transfer occurs. So, this problem is solved by using MATLAB PDE Tool from the above-given processor in the flow chart.

Figure 3 depicts the investigation of transient heat transfer in a square FGM plate with dimension. The density is constant, while specific heat and thermal conductivity are quadratic functions along the  $x_1$  -axis.

$$k(x) = k_o(1 + \gamma x_1)^2 \tag{7}$$

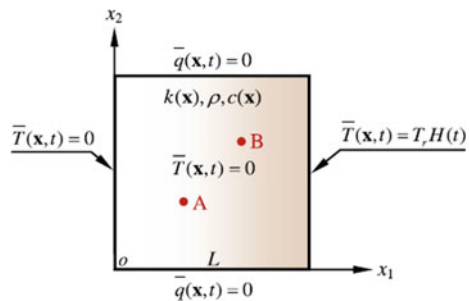
$$c(x) = c_o(1 + \gamma x_1)^2 \tag{8}$$

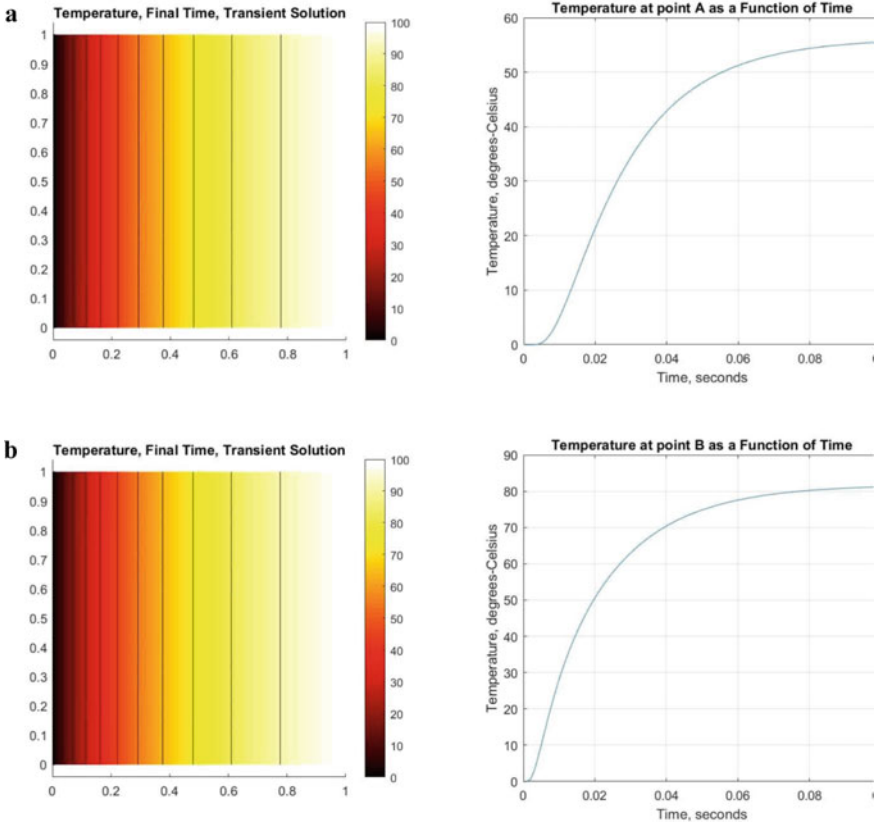
$$\rho(x) = \rho_o \tag{9}$$

The temperatures on the left side are held constant, while the temperatures on the right are altered  $\text{Tr } H(t)$ , with  $H(t)$  signifying the Heaviside step function. However, the other sides are isolated, and the temperatures are initially set to zero. The numerical analysis of temperature variation from points A and B, which is shown in Fig. 3, was investigated (Fig. 4, Tables 1 and 2).

When comparing the result of unsteady heat conduction in the square region problem by solving with MATLAB partial differential simulation results to the exact solution, it was found that as we increase the heat transfer time duration, results come very close, and the error percentage decreases.

**Fig. 3** Thermal conduction in a squared FGM domain during transients [4]





**Fig. 4** Temperatures of data points computed at various time steps: **a** point A and **b** point B

**Table 1** Comparison in computed simulation temperatures by MATLAB PDE tool with the exact solution at point A in the square plate

Time (s)	MATLAB PDE tool temperatures (°C)	Exact [4] temperatures (°C)	Error (%)
0.05	48.274	48.063	0.439
0.06	51.461	51.251	0.409
0.07	53.318	53.198	0.225
0.08	54.436	54.387	0.090
0.09	55.122	55.112	0.0181
0.1	55.561	55.555	0.0108

**Table 2** Comparison in computed simulation temperatures by MATLAB PDE tool with the exact solution at point B in the square plate

Time (s)	MATLAB PDE tool temperatures (°C)	Exact [4] temperatures (°C)	Error (%)
0.05	75.014	74.815	0.265
0.06	77.728	77.543	0.238
0.07	79.315	79.209	0.0133
0.08	80.275	80.225	0.0623
0.09	80.863	80.846	0.0210
0.1	81.234	81.224	0.0123

## 4.2 In the L-Shaped Region, Unsteady State Heat Conduction

As illustrated in Fig. 7, The material parameter is used to analyze heat conduction in the L-shape plate under the transient condition in the FGM material.

$$k(x) = k_o e^{(2\gamma x_2)} \quad (10)$$

$$c(x) = c_o e^{(2\gamma x_2)} \quad (11)$$

$$\rho(x) = \rho_o \quad (12)$$

The necessary boundary conditions are imposed in such a way that temperatures on the top and bottom edges are  $T_t H(t)$  and  $T_b H(t)$ , respectively. All of the remaining edges are adiabatic. Furthermore, across the domain, zero starting temperatures are taken, and the square plate is modeled using the given values  $L = 1.0$ ,  $k_0 = 5.0$ ,  $c_0 = 1.0$ ,  $\rho_0 = 1.0$ , and  $T_r = 100$  (Fig. 5).

The temperatures at the bottom and top edges are  $T_b$  and  $T_t$ , respectively. The remaining edges are all adiabatic. The following values are used in the modeling of L-shape plate,  $L = 0.02$ ,  $k_0 = 17$ ,  $c_0 = 1000$ ,  $i = 1000$ ,  $T_b = 1.0$ ,  $T_t = 0$ , and  $\gamma = 25$ . And independent boundary is defined using a mathematical cover (MC) of size  $h = 0.025$  [4] (Figs. 6 and 7).

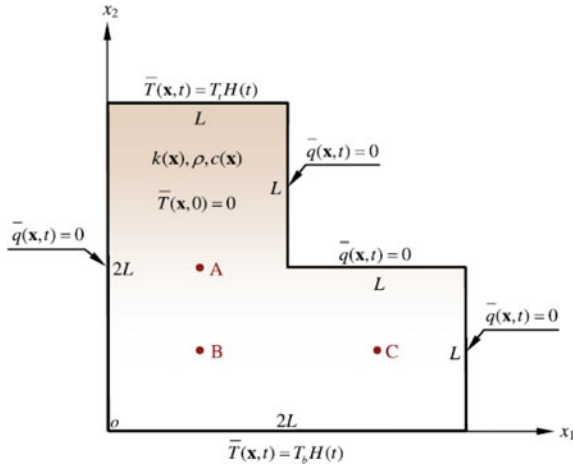


Fig. 5 Thermal conduction in an L-shaped FGM region under transients [4]

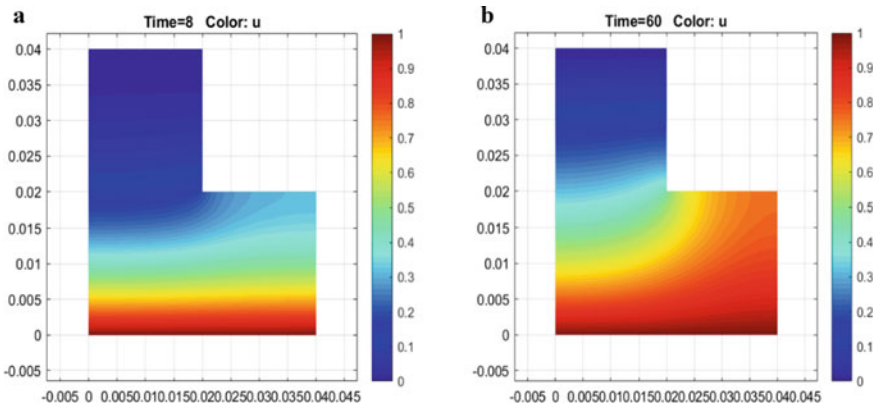


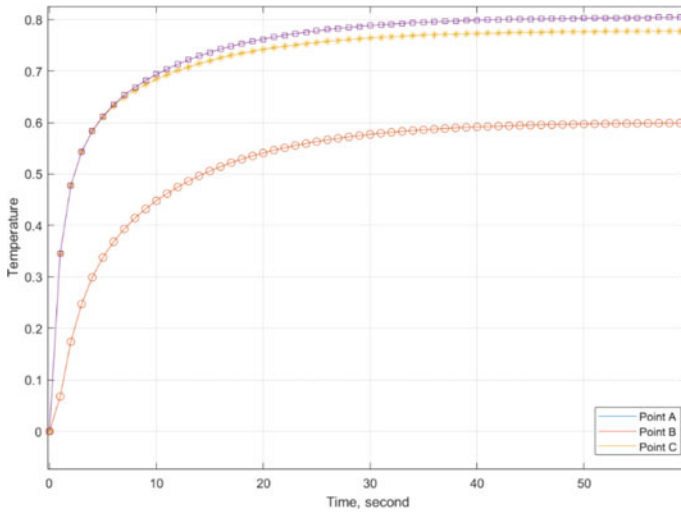
Fig. 6 The contour draws of temperature variation by using the MATLAB PDE simulation in the whole domain at a  $t = 8$  and b  $t = 60$

### 4.3 In a Multi-connected Domain, Unsteady Heat Conduction

A square plate has four circular holes of equal size, through which transient heat conduction occurs, as shown in Fig. 8. The thermal conductivity variation occurs vertically, whereas the specific heat and density are kept constant, as indicated by the formulae.

$$k(x) = k_0 e^{(\gamma x_2)} \tag{13}$$



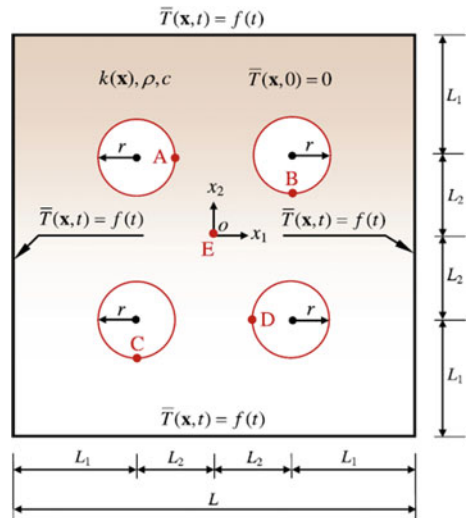


**Fig. 7** Combined temperature distribution graph using MATLAB PDE simulation at locations A, B, & C

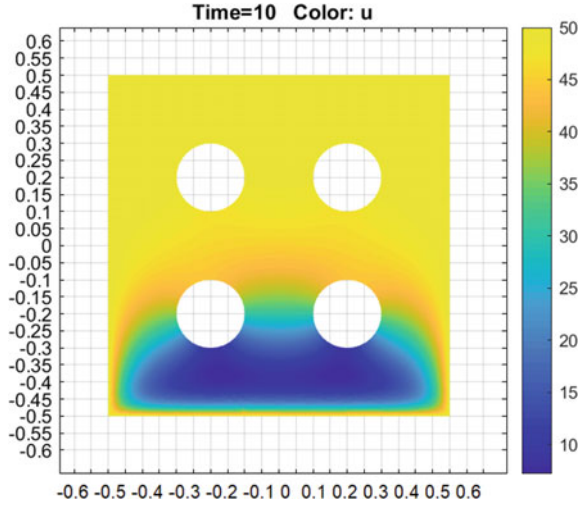
$$c(x) = c_o \tag{14}$$

$$\rho(x) = \rho_o \tag{15}$$

**Fig. 8** Transient heat conduction in a multi-connected region of FGM material [4]



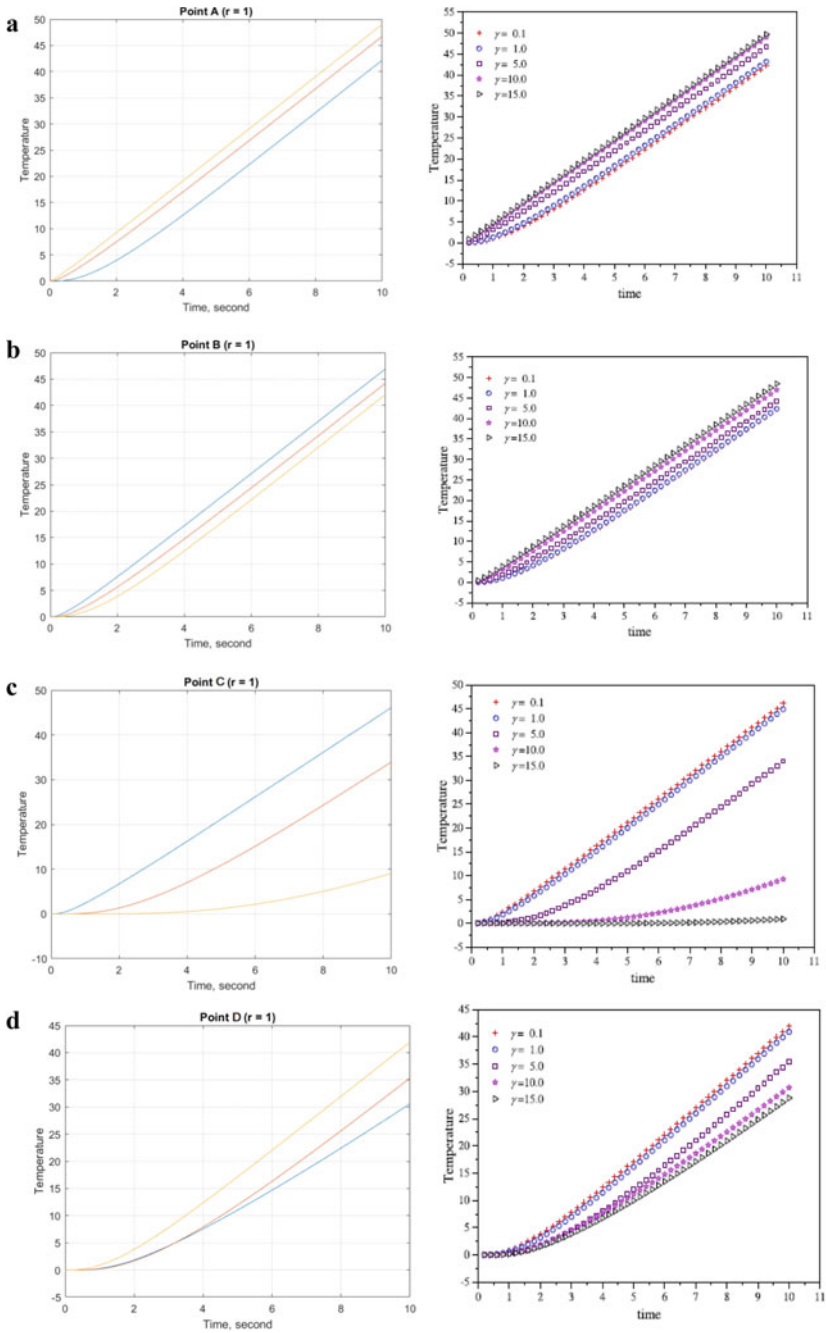
**Fig. 9** Contour draws of temperature variation by using the MATLAB PDE simulation in the whole region at  $t = 10$



The size of the hole radius is  $r$ , and the side length of the plate is  $L$ . Temperature  $f(t)$  of the outer space boundaries varies with time, whereas the temperature of the inside space boundaries is constant. In addition, zero beginning temperatures are used.

The other associated parameters are taken as:  $L = 1.0$ ,  $L_1 = 0.3$ ,  $L_2 = 0.2$ ,  $r = 0$ ,  $k_o = 100$ ,  $c_o = 2500$ ,  $\rho_o = 1.0$ ,  $f(t) = 5t$ , and  $\gamma = 1$ . The location of the centers of the circles is at  $(-0.2, 0.2)$ ,  $(-0.2, -0.2)$ ,  $(0.2, -0.2)$ , and  $(0.2, 0.2)$  (Figs. 9 and 10, Table 3).

Here, we compared the MATLAB partial differential equation simulation results to the numerical manifold methods whose results were first solved by Zhang et al. [4]. It was found that there was very little deviation in their results. And the simulation results that we found by using MATLAB were close to that of the exact solution. It is a very easy and effective tool to solve the transient heat conduction problems of material.



**Fig. 10** a Point A, b point B, c point C, d point D, and e point E: computed temperatures of sample points at various instants and material gradients

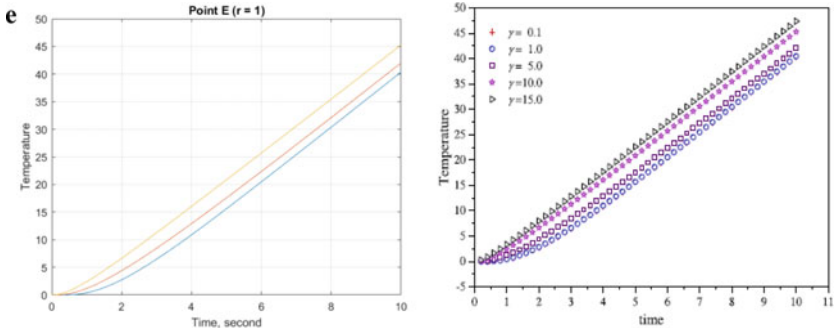


Fig. 10 (continued)

Table 3 Comparison in computed simulation temperatures by MATLAB PDE toolbox with the NMM at points A, B, C, D, and E in the square plate

Time	Method	Point A	Point B	Point C	Point D	Point E
2	PDE toolbox	3.9481	3.8857	6.7026	3.7915	2.7432
	NMM	3.9745	3.9100	6.6936	3.8043	2.7548
	Error (%)	0.66	0.62	0.134	0.336	0.421
4	PDE toolbox	12.565	12.481	16.253	12.3530	10.886
	NMM	12.5962	12.5091	16.2434	12.3648	10.8931
	Error (%)	0.247	0.224	0.0591	0.0954	0.0651
6	PDE toolbox	22.267	22.178	26.158	22.043	20.485
	NMM	22.2908	22.1988	26.1441	22.0459	20.4803
	Error (%)	0.106	0.0936	0.0531	0.0131	0.0229
8	PDE toolbox	32.189	32.099	36.133	31.962	30.380
	NMM	32.2231	32.1300	36.1221	31.9753	30.3889
	Error (%)	0.105	0.0964	0.0301	0.0415	0.0292
10	PDE toolbox	42.170	42.080	46.127	41.943	40.355
	NMM	42.2081	42.1148	46.1172	41.9596	40.3686
	Error (%)	0.0902	0.0826	0.0212	0.0395	0.0368

## 5 Conclusion

In this study, MATLAB, the partial differential equation simulation, was used to investigate issues related to 2D transient heat conduction problems in FGMs. We used MATLAB partial differential equation toolbox simulation to tackle the prior research difficulties of two-dimensional transient heat conduction, which were prior solved using the Numerical Manifold Method by Zhang. All three research problems are solved by using the MATLAB PDE toolbox. We solved the problems with the following above processors to begin importing 2D or 3D geometry from mesh data

or STL. PDEs toolkit generates meshes by using tetrahedral and triangular elements and solves PDEs using finite element methods. Then analyzed, the results were using post-processing. Firstly, we solved the square plate problem and compared its results to the exact solution that was available in the research paper. It was found that as we increase the time duration of heat transfer, results come very close, and the error percentage decreases. In the second problem with different complexity of L-shaped plates, simulation results were computed at A, B, and C locations. The third problem was solved with MATLAB, and the results were compared to numerical manifold methods available in the prior research paper. It was found that there was very little deviation in their results. And the simulation results we found by using MATLAB were close to that of the exact solution. It was a very easy and effective tool to resolve the transient heat conduction issues of FGMs materials.

## References

1. Wang LF, Zhou XP (2021) Fracture analysis of functionally graded materials by the field-enriched finite element method. *Eng Fract Mech* 253:107875
2. Sam M, Jojith R, Radhika N (2021) Progression in manufacturing of functionally graded materials and impact of thermal treatment—A critical review. *J Manuf Process* 68:1339–1377
3. Sam M, Radhika N (2021) Influence of carbide ceramic reinforcements in improving tribological properties of A333 graded hybrid composites. *Defence Technol*
4. Zhang HH, Han SY, Fan LF, Huang D (2018) The numerical manifold method for 2D transient heat conduction problems in functionally graded materials. *Eng Anal Bound Elem* 88:145–155
5. Chen BS, Tong LY, Gu YX, Zhang HW, Ochoa O (2004) Transient heat transfer analysis of functionally graded materials using adaptive precise time integration and graded finite elements. *Numer Heat Transf Part B Fundam* 45(2):181–200
6. Burlayenko VN, Altenbach H, Sadowski T, Dimitrova SD, Bhaskar A (2017) Modelling functionally graded materials in heat transfer and thermal stress analysis by means of graded finite elements. *Appl Math Model* 45:422–438
7. Charoensuk J, Vessakosol P (2010) A high order control volume finite element procedure for transient heat conduction analysis of functionally graded materials. *Heat Mass Transf* 46(11–12):1261–1276
8. Sutradhar A, Paulino GH (2004) The simple boundary element method for transient heat conduction in functionally graded materials. *Comput Methods Appl Mech Eng* 193(42–44):4511–4539
9. Yu B, Zhou HL, Yan J, Meng Z (2016) A differential transformation boundary element method for solving transient heat conduction problems in functionally graded materials. *Numer Heat Trans A Appl* 70(3):293–309
10. Cao LL, Qin QH, Zhao N (2012) Hybrid graded element model for transient heat conduction in functionally graded materials. *Acta Mech Sin* 28(1):128–139

# Numerical Analysis of Structural and Thermal Characteristics of Automotive Disc Brake Rotor



G. S. Abhiram, Aafis Aslam, K. Bhagavath Kumar, V. S. Amal Krishnan, and R. Kamal Krishna

**Abstract** Brake discs are components that are subjected to both structural and thermal deformations simultaneously. The pressure exerted by the brake pad on the disc leads to strains, whilst the heat generated due to friction results in thermal stresses. The problems dealing with the numerical analysis and the strength prediction of the brake disc are generally a complex problem that involves coupled structural and thermal analysis. The application of composite materials in the brake rotor improves the braking torque to weight ratio, but the system fails due to overheating. Whilst designing a brake rotor, it is important to develop the model with enough strength, lesser inertia and better thermal conductivity and heat dissipation properties. The heat dissipation can be increased by providing more area for conduction or increased airflow for enough forced convection. But the increase in holes may sometimes lead to increased stress concentration or reduced strength for the brake discs. Hence the design of brake rotor generally involves a proper selection of material for enough strength, an optimum number of holes for proper convection and lower deformations due to the combined action of pressure and temperature. The current work involves developing a numerical model of brake disc, static structural and dynamic/transient analysis, combined structural and thermal analysis. The literature dealing with the numerical analysis of brake discs with the coupled structural and thermal conditions is very rare. The numerical model is validated with the help of experimental modal analysis.

---

G. S. Abhiram · A. Aslam · K. B. Kumar · V. S. A. Krishnan · R. K. Krishna (✉)  
Department of Mechanical Engineering, Sree Chitra Thirunal College of Engineering,  
Pappanamcode, Thiruvananthapuram 695018, India  
e-mail: [kamal@scetce.ac.in](mailto:kamal@scetce.ac.in)

© The Author(s), under exclusive license to Springer Nature Singapore Pte Ltd. 2024  
R. Velmurugan et al. (eds.), *Dynamic Behavior of Soft and Hard Materials, Volume 3*,  
Springer Proceedings in Materials 36, [https://doi.org/10.1007/978-981-99-6259-4\\_15](https://doi.org/10.1007/978-981-99-6259-4_15)

**Keywords** Disc brake · Von mises stress · Dynamic analysis · Al–SiC

## Nomenclature

$Q^*$	Heat Flux
$K.E$	Kinetic energy of vehicle = $\frac{1}{2} * m * v_1^2$ .
$A_f$	Area of friction faces.
$t$	Stopping time.
$h_r$	Convective heat transfer coefficient.
$k_{air}$	Thermal conductivity of air.
$D_{outer}$	Outer diameter.
$R_e$	Reynold's number
$M_t$	Braking torque
$\mu$	Coefficient of friction
$P$	Actuating force
$R_f$	Friction radius = $\frac{2}{3} * \frac{(R_o^3 - R_i^3)}{(R_o^2 - R_i^2)}$ [1]
$R_o$	Outer radius of pad
$R_i$	Inner radius of the pad
$P_{bau}$	Average braking power
$m$	Mass of the vehicle
$a$	Deceleration of the vehicle
$v_1$	Velocity of the vehicle

## 1 Introduction

Brake system is an important primary safety system in a vehicle. The properties that are desired for a brake rotor material are stable frictional properties under varying loads and different velocities. It should also possess good wear properties at high temperatures. During braking, temperatures in the range of 300–800 °C are generated. The material should be able to withstand this temperature and have good resistance to abrasive wear [2]. Stainless steel and Gray cast iron are two materials that are used commercially as rotor materials. Finding or discovering better materials to replace existing materials has been an ongoing-research in the automotive industry for years. Composite materials are being studied as alternatives for rotor material. The advantages of composites over conventional materials are lightweight, good strength to weight ratio, good corrosion and wear resistance, enhanced mechanical and physical properties, enhanced thermal properties. The properties of the composite can be controlled by controlling the composition of reinforcement. But the cost of producing a composite is high which limits the application of composites in the automobile industry to racing applications and luxury vehicles.

The boundary conditions and loads are applied to the component and the corresponding stress, strain and deformation are estimated numerically. Numerical analysis on disc brake is done to calculate the thermal stress developed and temperature rise. Balaji et al. [3] analysed the stress, deformation, fatigue, temperature of various brake disc materials and observed that Al- and Carbon ceramic composites have good material characteristics and showed similar outcomes. Analysis of disc brake rotor with different materials helps to compare the behaviour of various materials and to find a material that exhibits desirable properties under different conditions. There are various causes of disc brake failure. It may be due to overheating of the pads. When this occurs, at higher temperatures, the coefficient of friction changes and due to this, braking cannot be done efficiently. Failure can also occur due to resonance. This occurs when the frequency of rotation due to external excitation of the rotor matches its natural frequency. The amplitude increases without an increase in frequency and, due to this, damage can occur. Modal analysis is conducted on the rotor under the free-free boundary condition to identify the natural frequency of the component. Another factor that decides the lifespan of a brake rotor is geometry. Daanvir Karan Dhir [4] studied the effect of the geometrical variation (holes and vents) on the lifespan and cooling of a brake rotor using numerical analysis. It was observed that the model with holes and vents had a lesser lifespan when compared to a solid disc under similar loading conditions. Sadagopan et al. [2] fabricated an Al-SiC composite brake disc using stir-casting method. Wear characteristics of the commercial and composite rotor were studied using pin on disc tribometer. It was observed that the composite rotor showed better wear characteristics. From the brake dynamometer test, it was found that the composite rotor showed a better cooling rate than the commercial rotor.

## 2 Theory

### 2.1 Assumptions

The assumptions made for the numerical analysis are as follows—The gross weight of the vehicle is assumed as 300 kg. The vehicle is brought to rest from a speed of 30.55 m/s. The braking load is distributed in the ratio of 60:40 between the front and rear axles [2]. It is assumed that the K.E of the vehicle is completely converted to heat energy during braking [2]. The braking efficiency is taken in the range between 60 and 80%. The structural analysis and thermal analysis of the brake disc are executed for three cases. Case 1 shows the analysis with 60% braking efficiency whilst case 2 and case 3 represent the numerical analysis with 70% and 80% braking efficiency, respectively.



## 2.2 Governing Equations

During braking, friction between brake pad and rotor causes the K.E of the vehicle to be converted to heat energy. For the thermal analysis, heat flux is given to the brake rotor as the thermal load. This heat flux [2] is given by the equation

$$Q^* = \frac{K.E}{A_f * t} \quad (1)$$

In the rotor, the generated heat is dissipated by (i) Conduction between the pad rotor interface. (ii) Convection between the rotor and surrounding air. The convective heat transfer coefficient [5] is given by the equation

$$h_r = 0.70 \left( \frac{k_{\text{air}}}{D_{\text{outer}}} \right) R_e^{0.55} - \text{laminar flow} (R_e < 2.4 * 10^5) \quad (2)$$

$$h_r = 0.40 \left( \frac{k_{\text{air}}}{D_{\text{outer}}} \right) R_e^{0.8} - \text{turbulent flow} (R_e > 2.4 * 10^5)$$

Braking torque is the force applied at the wheels to stop the motion of the vehicle and it is given by [1]

$$M_t = \mu * P * R_f \quad (3)$$

Braking power is defined as the ability of the braking system to bring the vehicle to a halt. It is the power output which is measured at the crankshaft. The braking power [1] can be calculated

$$P_{bav} = \frac{k * m * a * V_1}{2} \quad (4)$$

Power can also be expressed in terms of the force acting on the brake rotor using the relation [6]

$$\text{Power} = P * v_1 \quad (5)$$

The stopping time of the vehicle is calculated using the third equation of motion. The stopping time for different braking efficiencies is given in Table 1. Table 2 represents the structural and thermal loads that are acting on the brake discs.

**Table 1** Stopping time for various braking efficiencies

Case	Brake efficiency (%)	Deceleration (m/s <sup>2</sup> )	Stopping time (s)
Case 1	60	0.6g = 5.88	5.19
Case 2	70	0.7g = 6.86	4.45
Case 3	80	0.8g = 7.84	3.89

**Table 2** Calculated values of structural and thermal loads

Case	Braking power (W)	Force (N)	Pressure (Pa)	Heat flow (W)	Heat flux (W/m <sup>2</sup> )
Case 1	26945.1	882	287109.375	16184	8780618.715
Case 2	31435.95	1029	334960.937	18502	10240766.55
Case 3	35926.8	1176	382812.3	21593	11715015.72

### 2.3 Sampling Theorem

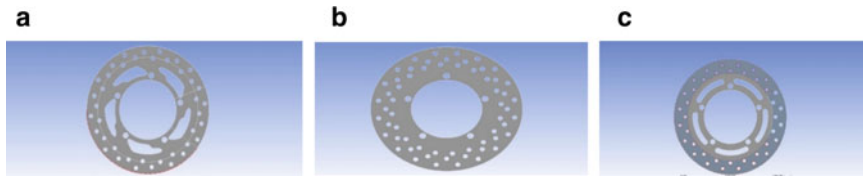
According to Nyquist-Shannon sampling theorem, the sampling frequency should be equal to or greater than twice the maximum signal frequency. In this experiment, sampling frequency is set as 1500 Hz which is 15 times the signal frequency. 4096 samples were considered per average [7].

### 2.4 Frequency Response Function (FRF) [7]

FRF is one of the prime factors controlling the quality of modal parameters. In this study, Discrete Fourier Transform (DFT) technique is used. In this method, the sampling signal should be periodic during the time interval. The input ( $m(t)$ ) and output signals ( $n(t)$ ) are measured and transformed into frequency domain ( $M(f)$  and  $N(f)$  respectively).

### 2.5 Coherence Function [7]

The correlation between input signal and output signal is given by this function. Its value lies between 0 and 1. A function of value 0 indicates no correlation exists between the input and output signal. It is a dimensionless function.



**Fig. 1** a Model A. b Model B. c Model C

### 3 Numerical Analysis of Brake Rotor

#### 3.1 Brake Rotor Models

**Model A**—Figure 1a shows a model of brake rotor generally used in two wheelers. The dimensions of the rotor are *Outer diameter*—240 mm; *Inner diameter*—112 mm; *Bolt hole diameter*—10.5 mm; *Drilled hole diameter*—7.8 mm; *Disc thickness*—3.5 mm. The disc consists of 2 rows of drilled holes and a set of splines around the bolt holes for better heat dissipation.

**Model B**—Figure 1b shows the proposed model. The dimensions of the rotor are the same as that of model-A. The spline is removed in this model and an extra row of holes are added to the rotor.

**Model C**—Figure 1c shows the 2nd proposed model. The dimensions of the model are the same as that of model-A. This model is composed of 2 materials. The inner section is of Stainless steel and the outer section is of Al–SiC matrix composite. The spline around the bolt holes has been modified. The number and design of holes in the outer section are the same as that of model-A.

#### 3.2 Materials

Stainless steel is the commercial material used and the composite material taken for this study is 20% SiC reinforced Aluminium matrix composite. Balaji et al. [3] observed that the performance of aluminium and carbon ceramic composites are better than alloy steel.

Al SiC as a rotor material has greater strength, improved stiffness, wear and abrasion resistance and controllable coefficient of thermal expansion. Sadagopan et al. [2] studied the performance of Al–SiC brake rotor compared to a commercial brake rotor and found that it had better wear resistance and heat dissipation. It was also reported that up to 25% of SiC by volume of SiC in AMC increased the hardness and impact strength increases and beyond that the hardness of the material decreases and above 30% shows crack initiation at the interface. 20% SiC reinforced Al SiC shows a reduction in wear compared to other volume fractions [2]. The properties of stainless steel were obtained from ANSYS Engineering data sources. The properties

**Table 3** Properties of materials

Property	Stainless steel	20% SiC reinforced aluminium matrix composite
Density (kg/m <sup>3</sup> )	7750	3700
Young's modulus (GPa)	193	103
Poisson's ratio	0.31	0.13
Bulk modulus (MPa)	16930	4636
Shear modulus (MPa)	73664	45575
Coefficient of thermal expansion (K <sup>-1</sup> )	1.70E-05	1.48E-05
Compressive yield strength (MPa)	207	761
Tensile ultimate strength (MPa)	586	370
Thermal conductivity (W/m K)	15.1	5
Specific heat (J/kg K)	480	920

of Stainless steel and 20% SiC reinforced aluminium matrix composite [2, 8, 9] are given in Table 3.

### 3.3 Mesh Convergence for Numerical Analysis

A modal analysis is done to analyse the influence of fundamental frequency on the number of elements of the brake rotor. The mesh convergence was conducted by changing the mesh element size and observing the variation in the fundamental frequency of the disc.

The element size was selected as 13 mm. The coarse mesh was further refined around the holes and splines in order to reduce execution time and obtain more accurate results. The mesh was modelled using the element Solid 186. After refinement, the number of nodes and elements are 31585 and 4050 respectively (Table 4).

**Table 4** Mesh specifications

S. no.	Element size (mm)	No. of elements	No. of nodes	Frequency (Hz)
1	6	3788	29746	227.54
2	7	3289	26748	227.58
3	8	3139	25038	227.62
4	9	3141	24912	227.66
5	10	2933	23356	227.7
6	11	2758	22281	227.75
7	12	2609	21103	227.8

### 3.4 Structural Analysis

The structural analysis is done to find the deformation, stress and strain in the brake rotor under loads. Static and transient structural analysis are conducted on the rotor.

**Static structural analysis**—This analysis is conducted for 3 cases of acceleration. The disc is fixed on the 5 bolt holes and the force is applied as shown below and pressure throughout the face on both faces of the rotor.

**Transient structural analysis**—This analysis is also being conducted for 3 cases of acceleration. It is conducted for a time period of 5 seconds with time step of 0.5 seconds. The force is applied at a linearly increasing rate. The values and method of application of force and pressure applied are the same as that in the case of static structural analysis. In addition to these parameters, a rotational velocity  $\dot{\omega} = 141.5$  rad/s is applied at time  $t = 0.5$  s. It then linearly decreases to zero at time  $t = 5$  s.

### 3.5 Thermal Analysis

**Steady-state thermal analysis**—In this analysis, a heat flow rate is applied to the disc as shown in Fig. 2. The Reynold's number is  $4.87 \times 10^5$  ( $>2.4 \times 10^5$ ), hence the analysis is conducted for turbulent flow of air. The value of convective heat transfer coefficient is  $h_r = 1.53e-003$ . Convective heat transfer is applied similar to the application of heat flow and radiation condition to the whole face of rotor on both faces.

**Transient thermal analysis**—The analysis is conducted for 12 s with time step of 0.5 s. The heat flow is replaced by heat flux. The brake load is distributed as 60:40. Hence 60% of the total heat flux is applied. The disc surface is divided into 6 faces and heat flux is applied to each face in successive order. The convection and radiation conditions are also applied similar to steady-state analysis.

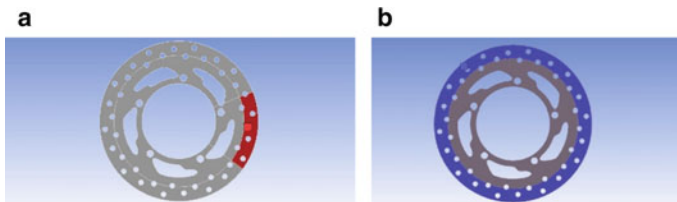


Fig. 2 Application of **a** Force. **b** Heat flow

**Fig. 3** Brake disc suspended using inextensible string



### 3.6 Thermal-Stress Analysis

This analysis is conducted using the **Thermal Stress** module in ANSYS Workbench. The temperature obtained by conducting the transient thermal analysis is imported as an additional load to the transient structural module. Thus, the structural analysis is conducted on the rotor which is at higher temperatures.

### 3.7 Modal Analysis

**Numerical Analysis**—The numerical analysis is conducted using ANSYS. The analysis is conducted in free-free boundary condition.

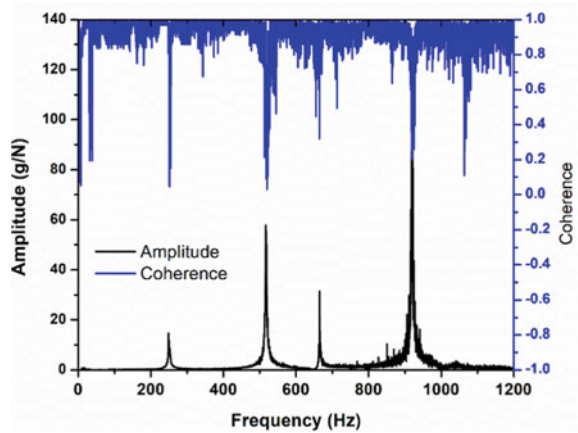
**Experiment Setup**—The brake disc was suspended using an inextensible string (shown in Fig. 3) and the disc was excited using an impact hammer (PCB 086C03) hard rubber tip. The response is captured by triaxial accelerometer (PCB 356A16). The accelerometer and impact hammer are connected to DAQ (NI USB 4431). The Frequency response function (FRF) and the coherence were generated using MEScope VES software [7] (Fig. 4).

## 4 Results and Discussion

### 4.1 Model Validation

The results of numerical analysis are compared to that of experimental analysis. It is observed that the results of the numerical analysis agreed with the results of the experimental analysis.

**Fig. 4** Frequency response function and coherence of the brake disc under free-free boundary condition



**Table 5** Modal analysis results

Sl no.	Frequency (Hz)	
	Experimental analysis	Numerical analysis
1	245	227.95
2	510	469.22

The figure shows the frequency response function and coherence measured for the brake disc under free-free boundary condition. The free-free boundary condition is achieved with the help of an extensible string attached to the brake disc. The first and second fundamental frequencies are found to be 245 Hz and 510 Hz respectively. Table 5 shows the results of experimental and numerical modal analysis of the brake disc.

## 4.2 Structural Analysis

### 4.2.1 Static Structural Analysis

The deformation, equivalent stress, strain of the model were calculated. It was observed that model A showed maximum values of deformation, stress and strain. The Al-SiC rotors have lesser values of deformation and stress but the strain is higher for Al-SiC. The deformation values are of the order  $10^{-5}$  (Table 6).

It is observed that the deformation is maximum around the periphery and decreases as we move to the inner regions. The stress and strain are found to be maximum at the area of application of force.

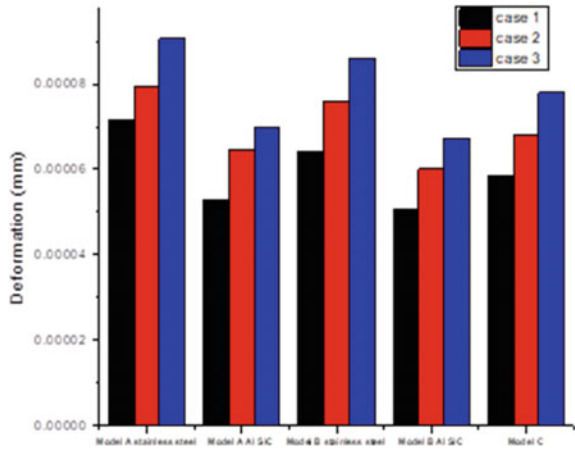
Figure 5 shows the deformation of all the models in the static structural analysis. It is observed that model A stainless steel rotor exhibits maximum value deformation.

**Table 6** Static structural analysis results

Model	Material	Case	Total deformation (mm)	Von Mises stress (MPa)	Von Mises strain
Model A	Stainless steel	Case 1	7.17E-05	0.80106	4.15E-06
		Case 2	7.92E-05	0.92272	4.81E-06
		Case 3	9.07E-05	1.0897	5.67E-06
	Al-SiC	Case 1	5.29E-05	0.84331	8.21E-06
		Case 2	6.48E-05	0.9795	9.52E-06
		Case 3	6.97E-05	1.0881	1.06E-05
Model B	Stainless steel	Case 1	6.43E-05	0.78328	4.07E-06
		Case 2	7.58E-05	0.86284	4.51E-06
		Case 3	8.60E-05	1.0271	2.56E-06
	Al-SiC	Case 1	5.07E-05	0.74988	7.29E-06
		Case 2	6.01E-05	0.93198	9.09E-06
		Case 3	6.71E-05	1.0064	9.86E-06
Model C	Stainless steel & Al-SiC	Case 1	5.85E-05	0.66193	6.49E-06
		Case 2	6.82E-05	0.77139	7.52E-06
		Case 3	7.80E-05	0.88159	7.59E-06

It is observed that deformation is lesser for Al-SiC rotors than stainless steel rotors. Al-SiC is a harder material and has better compressive strength than stainless steel.

**Fig. 5** Static structural analysis graph-deformation (mm)





**Table 7** Transient structural analysis results

Model	Material	Case	Total deformation (mm)	Von Mises stress (MPa)	Von Mises strain
Model A	Stainless steel	Case 1	1.04E-03	11.009	5.71E-05
		Case 2	1.05E-03	11.427	5.94E-05
		Case 3	1.06E-03	9.005	4.74E-05
	Al-SiC	Case 1	9.23E-04	4.6181	4.51E-05
		Case 2	9.21E-04	4.5623	4.50E-05
		Case 3	9.52E-04	5.2685	5.12E-05
Model B	Stainless steel	Case 1	5.53E-04	4.8582	2.59E-05
		Case 2	5.57E-04	4.7849	2.56E-05
		Case 3	5.63E-04	4.9391	2.69E-05
	Al-SiC	Case 1	4.81E-04	2.6082	2.60E-05
		Case 2	4.85E-04	2.5703	2.62E-05
		Case 3	4.90E-04	2.6995	2.72E-05
Model C	Stainless steel & Al-SiC	Case 1	3.89E-04	2.6574	1.45E-05
		Case 2	3.96E-04	2.7037	1.47E-05
		Case 3	4.02E-04	2.7516	1.49E-05

#### 4.2.2 Transient Structural Analysis

The values of stress, strain and deformation were found to increase compared to that of the static structural analysis. Deformation was of the order  $10^{-4}$  ( $10^{-3}$  for stainless steel rotor) and strain to the order  $10^{-5}$  from  $10^{-6}$ . Model A showed the maximum values of stress, strain and deformation. The maximum values of deformation, strain and stress were obtained at time  $t = 0.5$  s, then decreases as the analysis continues. This trend was observed in all the models (Table 7).

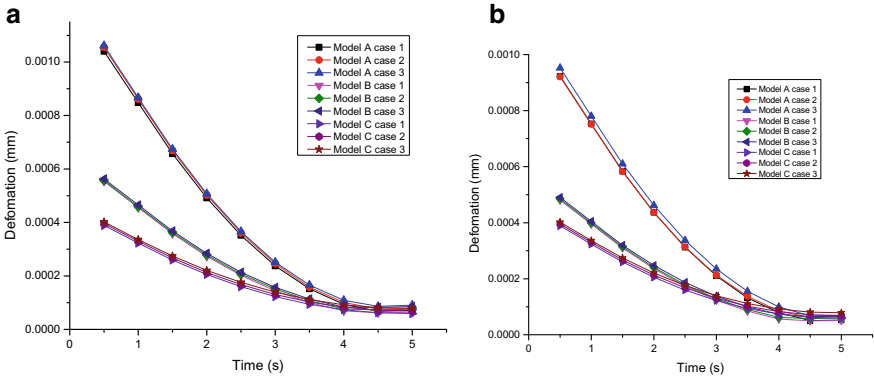
Figure 6 shows the variation of deformation with time. It is observed that the values decrease as the analysis progresses.

### 4.3 Thermal Analysis

#### 4.3.1 Steady-State Thermal Analysis

The heat flux and temperature of the rotor were calculated. The temperature of Al-SiC rotor is slightly higher than the temperature of stainless steel rotor. The heat flux is greater for the stainless steel rotor. Model A shows the maximum temperature and model C has the minimum temperature amongst the 3 models (Table 8).

The maximum temperature was recorded at the outer region where the thermal load was applied. The temperature decreased towards the inner regions of the disc.



**Fig. 6** Transient structural graph-deformation versus time. **a** Stainless steel. **b** Al-SiC

**Table 8** Steady-state thermal analysis results

Model	Material	Case	Temperature (°C)	Total heat flux (W/mm <sup>2</sup> )
Model A	Stainless steel	Case 1	800.06	0.58274
		Case 2	897.82	0.72292
		Case 3	1020.9	0.9142
	Al-SiC	Case 1	805.85	0.41653
		Case 2	903.99	0.50494
		Case 3	943.47	0.51193
Model B	Stainless steel	Case 1	742.08	0.51323
		Case 2	834.24	0.6266
		Case 3	951.3	0.78244
	Al-SiC	Case 1	735.48	0.32978
		Case 2	827.08	0.40513
		Case 3	943.47	0.51193
Model C	Stainless steel & Al-SiC	Case 1	603.83	0.22155
		Case 2	680.82	0.25301
		Case 3	780.74	0.32042

Figure 7 shows the results of steady-state thermal analysis. It is observed that Model A showed the highest values of heat flux and temperature. The design of models B and C has been changed by adding more holes and redesigning the spline. As a result, the area for convective heat transfer increased and hence the heat flux and temperature is lesser than that of model A.

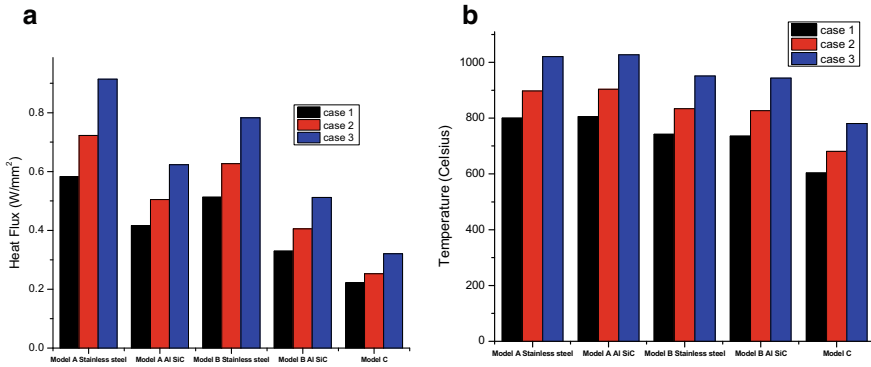


Fig. 7 Steady-state thermal analysis graphs. **a** Heat flux ( $\text{W/mm}^2$ ). **b** Temperature ( $^{\circ}\text{C}$ )

### 4.3.2 Transient Thermal Analysis

The values of temperature and heat flux are higher than the values from the steady-state analysis. The temperature gradually increases as the analysis continues. The variation in heat flux is irregular. This might be because of the change in contact area of the pad with the brake disc as the disc rotates. The maximum temperature is obtained at time  $t = 10$  s and maximum heat flux is obtained at time  $t = 3$  s. The temperature of the Al–SiC rotor is higher than the stainless steel rotor. Model C has the highest temperature and model B has the lowest value of temperature amongst the 3 models (Table 9).

The maximum temperature and heat flux are observed at the sector at which thermal load is applied at time  $t = 12$  s. The values of temperature and heat flux are observed to be decreasing as we move from the periphery to the inner steel regions of the disc.

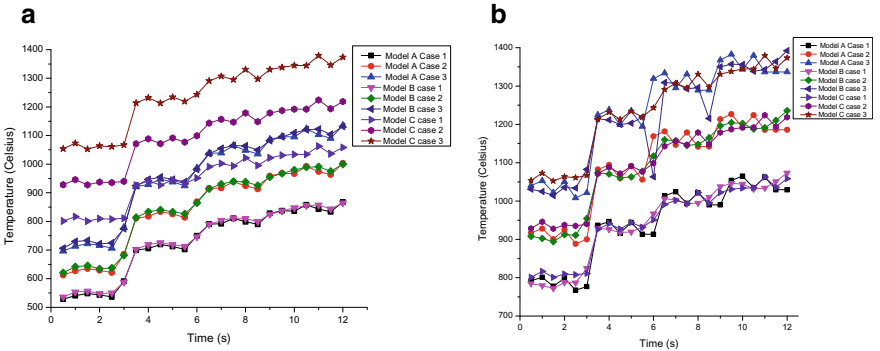
Figure 8 shows the variation of temperature with time for stainless steel and Al–SiC rotors. It is observed that the temperature gradually rises as the analysis progresses.

## 4.4 Thermal-Stress Analysis

The analysis was conducted to analyse the deformation of the rotor at higher temperatures. There is a significant rise in deformation compared to the structural analysis. The deformation is of the order  $10^{-4}$  ( $10^{-3}$  in stainless steel rotor) in the structural analysis. It has increased to the order of  $10^{-2}$  in the thermal-stress analysis. The deformation and stress concentration is observed to be maximum around the periphery of the disc whilst it is observed to be minimum at the inner regions of the disc. From Fig. 6, it is observed that in the transient structural analysis, the deformation decreases as the analysis progresses. From Fig. 9, it is observed that in the

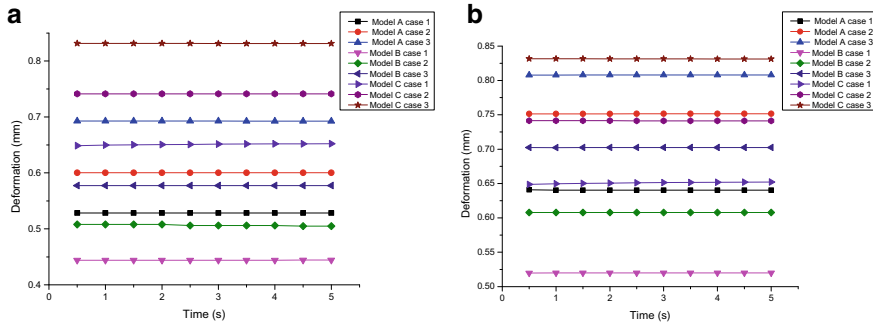
**Table 9** Transient thermal analysis results

Model	Material	Case	Temperature (°C)	Total heat flux (W/mm <sup>2</sup> )
Model A	Stainless steel	Case 1	867.53	5.4866
		Case 2	1002.7	6.4009
		Case 3	1135	7.3134
	Al-SiC	Case 1	1064.9	3.5555
		Case 2	1226.7	4.1325
		Case 3	1382.6	4.7007
Model B	Stainless steel	Case 1	864.91	4.979
		Case 2	999.75	5.8084
		Case 3	1131.7	6.636
	Al-SiC	Case 1	1073.3	4.0002
		Case 2	1235.7	4.6614
		Case 3	1392	5.3185
Model C	Stainless steel & Al-SiC	Case 1	1062.6	3.9296
		Case 2	1223.8	4.5846
		Case 3	1379.2	5.2386



**Fig. 8** Transient thermal analysis graphs-temperature versus time. **a** Stainless steel. **b** Al-SiC

thermal-stress analysis, the deformation remains constant throughout the analysis. The highest value of deformation is observed in Model C. Model B shows the lowest value of deformation amongst the 3 models (Table 10).



**Fig. 9** Total deformation versus time graph. **a** Al–SiC. **b** Stainless steel

**Table 10** Thermal-stress analysis

Model	Material	Case	Total deformation (mm)
Model A	Stainless steel	Case 1	0.64
		Case 2	0.751
		Case 3	0.808
	Al–SiC	Case 1	0.5284
		Case 2	0.60023
		Case 3	0.6927
Model B	Stainless steel	Case 1	0.51981
		Case 2	0.607
		Case 3	0.702
	Al–SiC	Case 1	0.444
		Case 2	0.508
		Case 3	0.5775
Model C	Stainless steel & Al–SiC	Case 1	0.65213
		Case 2	0.74148
		Case 3	0.83168

## 5 Conclusions

The numerical analysis of the disc brake rotor was conducted and the model was validated using the results of the modal analysis. The numerical analysis was conducted for stainless steel and Al–SiC rotors. From the structural analysis, it was observed that the stress, strain and deformation of models B & C are less than that of model A. The Al–SiC rotor has lesser values of stress and deformation and a higher value of strain compared to the stainless steel rotor in the static structural analysis.

It was observed from the results of the thermal analysis that the temperature of Al–SiC rotor is higher than the temperature of the stainless steel rotor. Model C

showed the highest value of temperature amongst the 3 models. The Al–SiC rotors are to be used in applications where there is provision for better cooling such as in racing applications where features such as brake ducts are provided for cooling the brake rotor.

The Thermal-Stress analysis was conducted to find the deformation of the rotor at higher temperatures and it was observed that the deformation remains constant throughout the analysis.

Out of the two proposed models, Model B showed better performance than model A and model C. Model C showed better performance in the structural analysis but from the thermal analysis and thermal-stress analysis, it showed the maximum value of temperature and deformation. Hence at higher temperatures, Model B exhibits better performance than others.

## References

1. Bhandari VB. Design of machine elements, Fourth edn. ISBN 978-93-392-2112-6
2. Sadagopan P, Natarajan HK, Praveen Kumar J (2018) Study of silicon carbide-reinforced aluminum matrix composite brake rotor for motorcycle application. *Int J Manuf Technol* 94:1461–1475
3. Balaji R, Nadarajan M, Selokar A, Kumar SS, Sivakumar S (2019) Modelling and analysis of disk brake under tribological behaviour of Al–Al<sub>2</sub>O<sub>3</sub> ceramic matrix composites/Kevlar® 119 composite/C/SiC-carbon matrix composite/Cr–Ni–Mo–V steel. *Mater Today: Proc* 18:3415–3427
4. Dhir DK (2018) Thermo-mechanical performance of automotive disc brakes. *Mater Today: Proc* 5:1864–1871
5. Limpert R (2011) Brake design and safety, Third edn. SAE International, U.S.A. ISBN:978-0-7680-3438-7
6. Wilson M (2020) Mechanics: force, mass, acceleration, energy, work, power. *Anaesth Intensive Care Med* 21:256–260
7. Krishna RK, Mahesh MR, Unnikrishnan M, Kochupillai J (2020) Effect of sagging on dynamic characteristics of silicone tube conveying fluid. *J Inst Eng (India): Series C* 101:241–56
8. Zare R, Sharifi H, Saeri MR, Tayebi M (2019) Investigating the effect of SiC particles on the physical and thermal properties of Al6061/SiCp composite. *J Alloys Compd* 801:520–528
9. Jiang L, Jiang Y-L, Liang YU, Nan SU, Ding Y-D (2012) Thermal analysis for brake disks of SiC/6061 Al alloy co-continuous composite for CRH3 during emergency braking considering airflow cooling. *Trans Nonferrous Metals Soc China* 22:2783–2791

# Stress Analysis of Thin Rectangular Sections Subjected to Twisting Moment



Saiarpan V. Joshi and Vadivuchezhian Kaliveeran

**Abstract** The major issue in the stress analysis of thin sections is the stress concentration on the edges, especially the sharp edges. Whilst analysing thin sections for any analysis, be it flexural, torsional, axial etc., the phenomenon of sharp edge stress concentration reduces the quality of results of the analysis. Thus, it becomes necessary to determine the particular loading orientations in order to study the analysis in its purest form without the interventions of other unnecessary behaviours. The present study is about the stress analysis of thin rectangular section, when it is subjected to a twisting moment. A thin rectangular member of dimensions, length = 100 mm, depth = 40 mm, and width = 1 mm is considered with one end of the length as fixed and the other end as free. A torque of magnitude 0.1 Nmm is applied at the free end. Initially, a theoretical analysis is done and the point of maximum shear stress is determined. Then numerical analysis of the same is done on an FEM modelling software with different combinations of loadings in the form of a twisting moment. The determination of the exact load orientation which simulates the pure torsional moment behaviour for a thin rectangular section is the main objective of this study. The results obtained by FEM modelling on the software are validated theoretically and experimentally.

**Keywords** Offshore structures · Finite element analysis · Torsion · Thin rectangular sections · Stress concentration · Experimental study

## 1 Introduction

Thin-walled structural members with open or closed cross-sections are extensively utilized in various engineering disciplines, such as mechanical, civil, aerospace, and offshore structures [1–4]. In offshore structures [5], circular structural elements dominate in the sub-structure part which forms majority of structure. The non-circular

---

S. V. Joshi · V. Kaliveeran (✉)

Water Resources and Ocean Engineering, National Institute of Technology Karnataka,  
Mangalore 575025, India

e-mail: [vadivuchezhian\\_k@yahoo.co.in](mailto:vadivuchezhian_k@yahoo.co.in)

sections are limited to super structure part or the deck part. The offshore structures always being subjected to a dynamic environment of loading [6], the non-circular sections in the deck part are always subjected to impact loads due to the freeboard available between the deck and the sea surface [7]. Not only in the offshore structures, most of the aircraft structural components are made of non-circular members such as wings, fuselage, and spars. These components are subjected mainly to bending and torsion due to aerodynamic loads [8].

Torsional effects on non-circular sections induce warping [9] which needs detailed study. Such kind of out of plane deformations are critical. These deformations occur in the direction perpendicular to the cross-section which are not normal in case of torsion study which is generally done on circular cross-sections and such deformations need complex analysis [10].

Preventing warping in a structural member can have a significant impact on shear stress and also produce the normal stress within the member. When a member is subjected to pure torsion, shear stress is generated within the member. However, if the member is subjected to non-uniform torsion, in addition to shear stress, it also generates longitudinal stress within the member [11]. These additional stresses are must not be avoided for thin-walled cross-sectional members [12].

The behaviour of thin sections in any loading cases is a bit irregular as the presence of sharp ends or edges cause steep stress gradient and the original behaviour of the considered analysis won't happen. Practically, when the loads are applied, if the loading conditions for a normal section are similarly applied on thin sections, the true behaviour won't be existing.

This is because, though the shape of both normal and thin sections is same, but in thin sections, one of the dimensions being way smaller than the other, the stress variation along that direction is negligible, and the stresses tend to get concentrated at the edges [13]. Analysing stress and deformation in a non-circular cross-section of a member through analytical methods can be challenging and complex [14]. However, when it comes to practical implementation, torsion must not be ignored, and analysing the stress distribution of a structural member under torsion is vital in ensuring the member's efficient design [15].

In order to simulate the torsional behaviour on very thin rectangular sections, a cantilever member of thickness 1 mm, depth 20 mm, and length 100 mm was considered.

A torque of magnitude 0.1 Nmm was considered to be acting at the free end of the member. This member was analysed theoretically using the equations for torque and maximum shear stress for very thin rectangular sections. Using membrane analogy [16], the maximum shear stress point has been determined which, for thin rectangular sections or any rectangular sections for that matter lies along the line joining the midpoints of cross-sections from the fixed end to free end.

The same member was analysed numerically using FEM software *ANSYS APDL* [18]. The torque was applied on the bar in the form of a couple. The position of the couple was varied when the stress concentration at the edges was seen. The required loading position was decided and the results were compared and validated that the theoretical and numerical results can be considered for the study.



Experimental study of the problem was done by fabricating the possible specimen. Specimen of thickness 2.2 mm, depth 140 mm, and length 800 mm was considered for experiment. To ensure end fixture, the necessary support was fabricated and in order to have an end loading, small loading arms were welded to the existing specimen as a part of the loading setup which was made to be manual as the loading to be applied was very small. A torque of magnitude 303.356 Nmm was applied manually. Then, the specimen of the same dimensions was analysed theoretically and numerically.

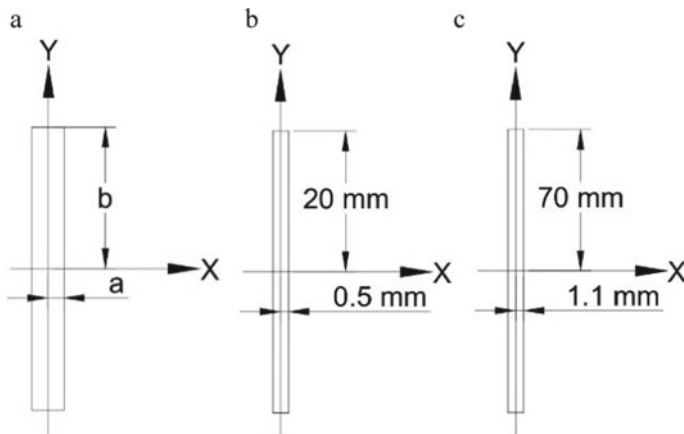
## 2 Analysis

For thin rectangular sections, the torque equation can be written as,  $T = \frac{16}{3} \mu \alpha a^3 b$ , where,  $T \rightarrow$  Torque applied;  $\mu \rightarrow$  Modulus of Rigidity;  $\alpha \rightarrow$  Twist per unit length;  $a, b \rightarrow$  As mentioned in the Fig. 1a. The maximum shear stress,  $\tau_{max} = 2 \mu \alpha a$  [17].

### 2.1 Problem 1

#### 2.1.1 Theoretical Analysis

In this problem, the specimen considered possesses thickness,  $2a = 1 \text{ mm} \Rightarrow a = 0.5 \text{ mm}$  and depth,  $2b = 40 \text{ mm} \Rightarrow b = 20 \text{ mm}$  and length,  $L = 100 \text{ mm}$  as shown in the Fig. 1b. The considered thin rectangular section is fixed at one end and a torque of magnitude 0.1 Nmm is applied at the free end of the member. Considered material



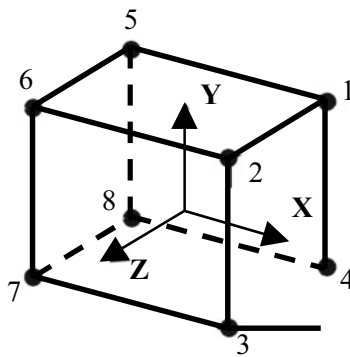
**Fig. 1** a General rectangular section; b cross-section of specimen in problem 1; c cross-section of specimen in problem 2

is steel with Modulus of elasticity,  $E = 210$  GPa, Poisson's ratio,  $\nu = 0.29$ , and Modulus of Rigidity,  $\mu = 79$  GPa. Substituting the given values in the equations of torque and maximum shear stress, we get  $\alpha = 9.493671 \times 10^{-8}$  rad/mm and  $\tau_{\max} = 7.5 \times 10^{-3}$  N/mm<sup>2</sup> or MPa.

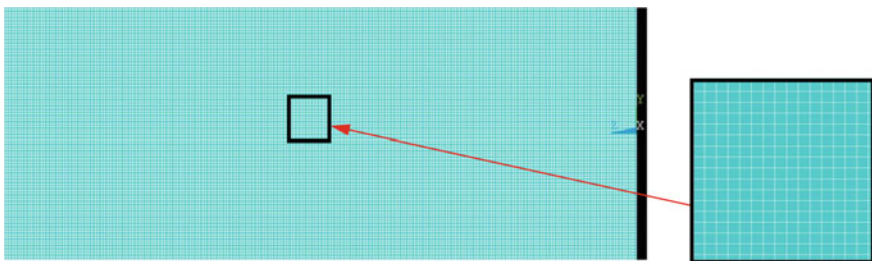
### 2.1.2 Numerical Analysis

The element type chosen is 'Solid 8 Node 185 (SOLID185)'. This element has 8 nodes with 3 degrees of freedom each node, therefore the element has a total of 24 degrees of freedom (Fig. 2). The meshing is done uniformly throughout the member as there are no discontinuities in the member and the cross-section is uniform throughout the member (Fig. 3).

The element type has been selected to be a brick element because, (a) the variation of the shear stress in the transverse direction in the cross-section had to be studied which was determined theoretically to be varying from positive to negative in magnitude which wouldn't have been attained if a 2D plane element or a shell element had been selected and (b) as the considered specimen was a cuboid, without



**Fig. 2** Solid 8 Node 185 (SOLID185) element type



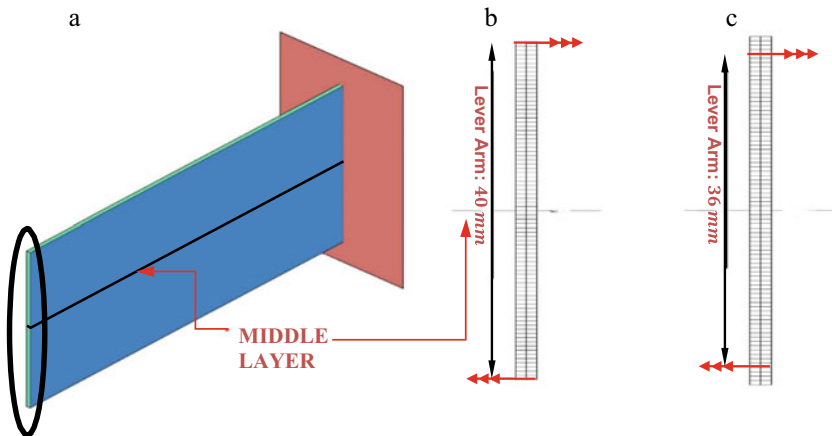
**Fig. 3** Uniform meshing of the member in problem 1

any type of discontinuity in the lattice, the brick element helped a lot in the analysis by providing the required data at required points. The element size is 0.5 mm and the total number of elements is 32000, and the total number of nodes is 48843.

The load was applied in the form of a torsional couple with one load on top nodes and the other load on the bottom nodes. Initially, the loading of the couple was applied on the nodes at the extreme ends of the cross-section. The load is divided into 3 parts to be applied on the 3 nodes, for both top and bottom loads as shown in Fig. 4b. Applied torque,  $T = 0.1 \text{ Nmm} = 0.1 \times 10^{-3} \text{ Nm}$  and the lever arm between the loads is,  $LA = 40 \text{ mm} = 0.04 \text{ m}$ . Thus, the load per side can be obtained by dividing the torque to be applied by the lever arm available. This gives a load of,  $F = 2.5 \times 10^{-3} \text{ N}$  on each side.

Dividing the load by 3 for application on the 3 nodes each side, we get load per node as,  $P = 8.3 \times 10^{-4} \text{ N}$ . For this loading, the required maximum shear stress concentrated at the edges of the member at the free end as shown in the Fig. 5.

This stress concentration led to the idea of changing the load location by shifting the loads inwards or towards the middle layer. This iteration was continued till the stress concentration at the edges vanishes and the maximum shear stress point is obtained on the middle layer. This convergence happened at the 5th iteration, wherein the forces were applied on the nodes of 5th layer from the extreme ends as shown in Fig. 4c. The force applied on the nodes can be calculated as  $P = 0.1 \times 10^{-3} / 0.036 \times 3 = 9.259 \times 10^{-4} \text{ N}$ .



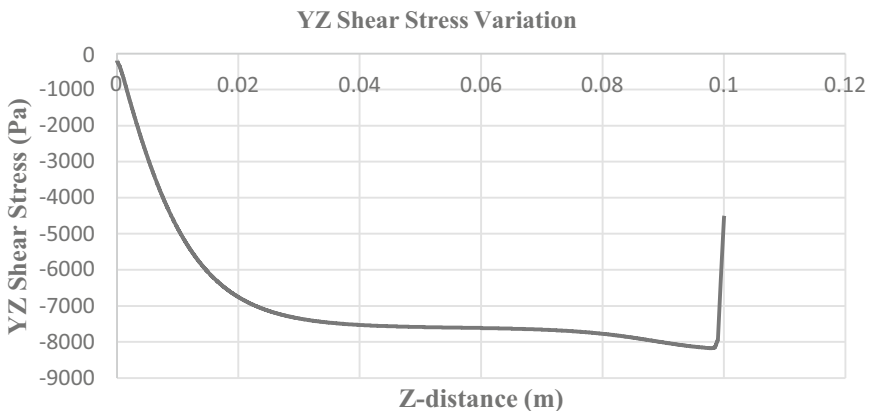
**Fig. 4** a Isometric view of the member in problem 1, wherein loading is done on the end face; b 1st iteration of loading with uniform mesh visible on the face; c 5th iteration of loading with uniform mesh visible on the face



**Fig. 5** Stress pattern in the member of problem 1 for the first iteration showing stress concentration at the corners

### 2.1.3 Inference

The theoretical analysis gives that the magnitude of maximum shear stress for the considered problem is 7500 Pa and it is assumed in it that the variation of stresses in ‘z’ direction is zero which means the maximum shear stress which is found to be appearing at the midpoint of the longest side of the cross-section, is constant along the line joining the midpoints of the longest side of the cross-section. In numerical analysis, the element type is a 3D brick type and there are no restrictions or assumptions for that matter. This is the reason, a variation of YZ Shear Stress can be clearly seen along the same line as mentioned above (Fig. 6). The maximum value that numerical analysis gives is, 8167.7 Pa. The percentage error between both the values is, 8.9%. But looking at the variation, the graph stays almost constant for a considerable length at a value nearing to the theoretical value i.e., 7500 Pa.



**Fig. 6** The YZ Shear stress variation along the line of middle layer from the fixed end to the free end where loading is done

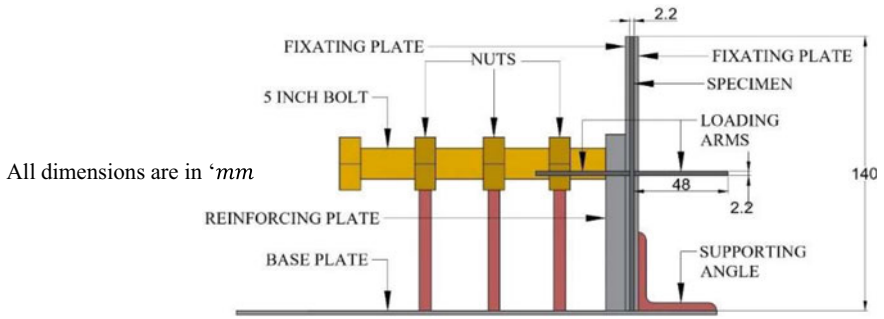


Fig. 7 Front view of the setup

Thus, the inference can be derived that numerical and theoretical analysis give considerably nearing values. Now, experimental validation for the same is necessary for final conclusion.

## 2.2 Problem 2

For experimentation, the specimen considered in problem 1 was not feasible to be fabricated. Thus, a galvanized steel sheet of thickness 2.2 mm was taken and a specimen with suitable dimensions was cut out and used to experiment. The dimensions of the specimen considered were, length as 800 mm, depth as 140 mm, and thickness as 2.2 mm. Two loading arms of length 48 mm, width 15 mm, and thickness 2.2 mm were considered for loading. Both theoretical and numerical analysis were repeated on the specimen with same dimensions and material.

### 2.2.1 Experimental Study

#### *Schematic Diagram of Experimental Setup*

The schematic diagram of the experimental setup design for the experimental study is as follows (Figs. 7, 8 and 9).

#### Specimen Preparation

The specimen considered in the problem 2 was made into a real-life model. In order to represent a very thin rectangular section, a thin sheet of galvanized steel was considered as the raw material. A rectangular sheet of dimensions, 800 mm × 140 mm × 2.2 mm are cut out of the bigger sheet. Then 2 small loading arms for loading

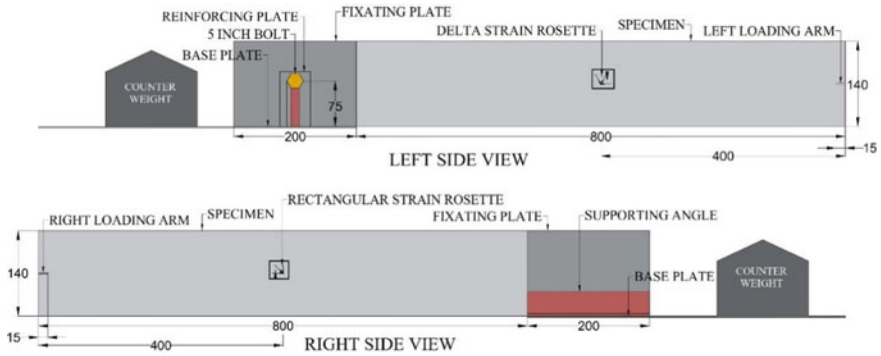


Fig. 8 Side views of the setup

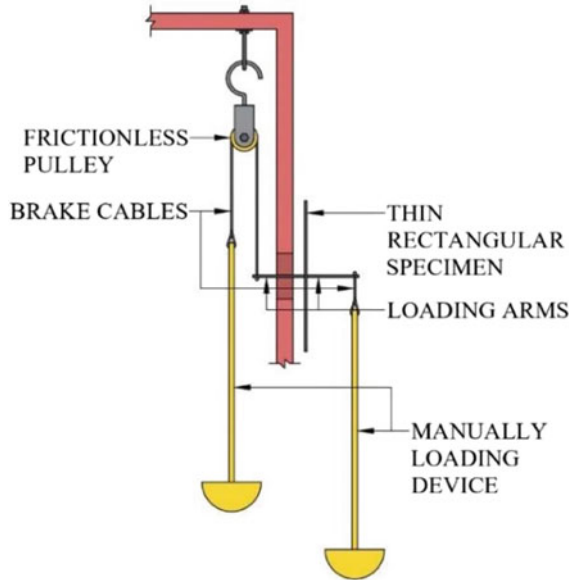
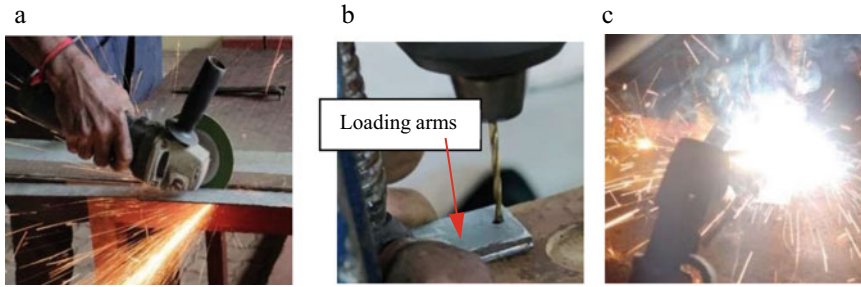
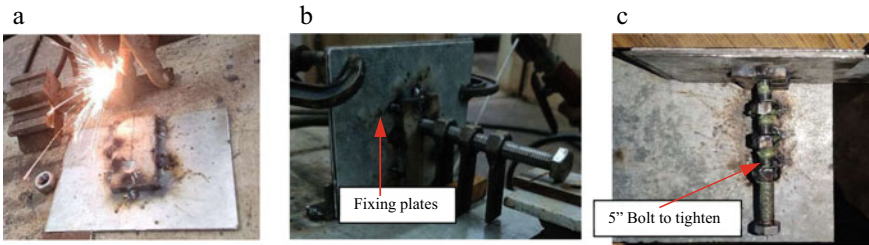


Fig. 9 Loading setup at the free end to induce couple for torsion

on either sides, of dimensions  $4.8 \text{ mm} \times 1.5 \text{ mm}$  were cut from the main sheet. The setup used for loading included usage of cycle brake cables of diameter 1.5 mm. Thus, holes of diameter 2 mm were drilled on the loading arms. The arms were welded onto the main model (Fig. 10).



**Fig. 10** a Cutting the galvanized steel for specimen and loading arm; b drilling hole for the brake cables; c welding of loading arms to the specimen



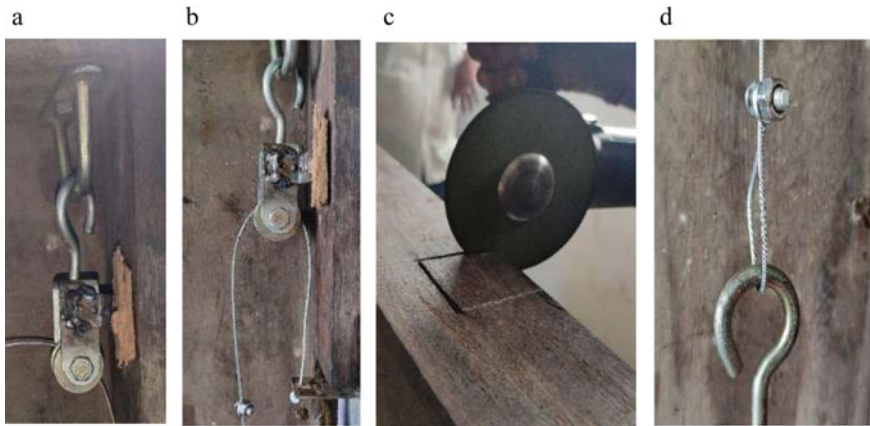
**Fig. 11** a One of the plates being welded to the base; b preparation of the 3 nuts and a bolt assembly for fixation of the specimen; c fixture ready with greased bolt for free movement

*Fixture Preparation*

In order to make a fixed end, 2 flat sheets of dimensions, 200 mm × 140 mm were cut out. One side was welded on to a flat base plate at the edge of one of the sides so that the specimen considered be suspended freely beyond that. Other plate was made to freely move. In order to fix both the plates with the specimen between them, an assembly of 3 nuts and a 5 inches long bolt was used (Fig. 11).

*Loading Assembly Preparation*

As the loading being applied is very small considering the capacity of the UTMs (Universal Testing Machines) in the laboratory, the loading had to be done manually. Loading was planned to be given on the loading arms welded to the specimen. As it was a twisting couple, one side was to be pulled upwards and the other side to be pulled downwards. Thus, one side was loaded using a frictionless pulley setup. To make the pulley setup, a wooden box was considered and the pulley was fixed at the top corner. To make the loading arm reach the position of pulley, a groove was cut on the side of the corner pulley was near to. The loading cable used were normal cycle brake cables as these are quite good in tension and would transfer the load applied



**Fig. 12** **a** Pulley fixed to the wooden box; **b** groove cut on the side of the box; **c** pulley with the brake cable over it and one end of cable fixed at the loading arm; **d** loop at one end of the brake cable with the loading hook

completely without any considerable deformation. One end of brake cables has knob type thing which would lock itself at the loading arm after the whole cable is passed through the hole made onto it. A loop was made at the other end of the cables making it able to accommodate the hook of the manual loading device (Fig. 12).

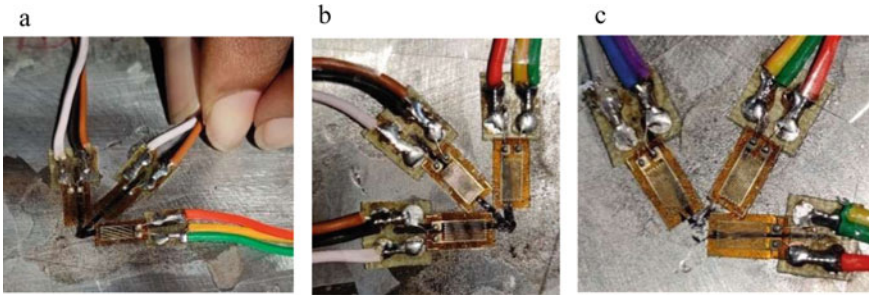
### Strain Rosette Mounting

In order to analyse the shear stresses generated in the specimen, strain rosettes have been used. Position of the strain rosette was decided to be the centroid of the side face on both the sides as the maximum shear stress is expected to be occurring at the midpoint of the cross-section and observing the graph of shear stress variation for problem 1 Fig. 8, it can be seen that the graph is almost constant on one value midway in 'z' direction. One side, rectangular rosette and the other side, delta rosette was formed using the available strain gauges (Fig. 13).

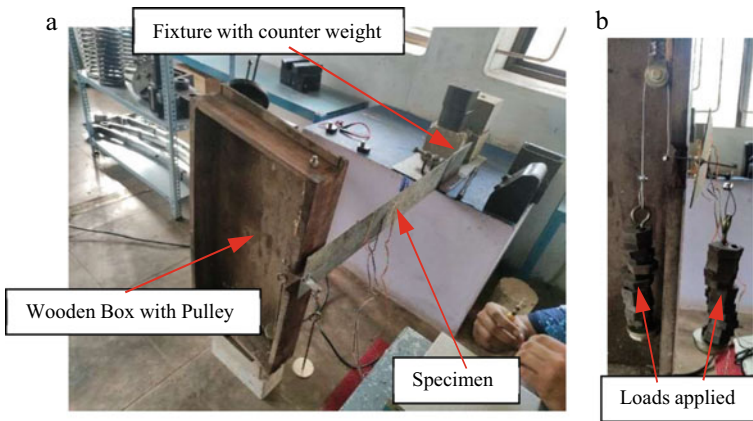
### Experiment

Loading was given equally on both the loading devices. The wires coming from the strain gauges were connected to the DAS (Data Acquisition System). The strain values for the applied constant load were noted down and the further calculations necessary for the determination of the maximum shear stress were done (Fig. 14).





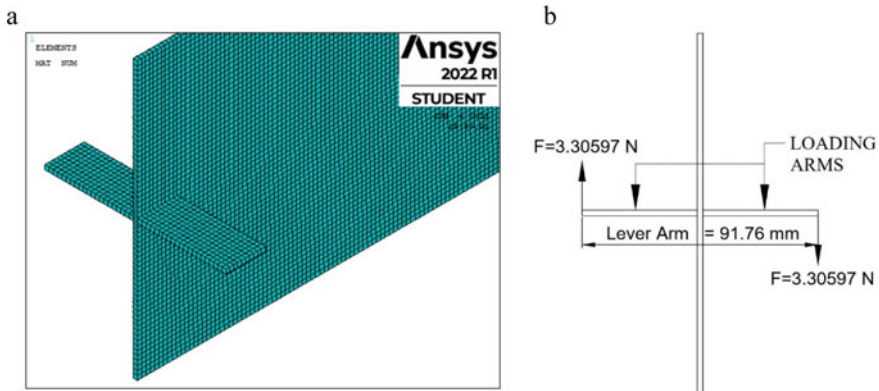
**Fig. 13** a Mounting strain gauges in the formation of rosette; b rectangular rosette; c delta rosette



**Fig. 14** a Whole setup including the fixture, specimen, strain rosettes and loading setup; b loading devices loaded with the weights inducing the twist required in the beam

**2.2.2 Theoretical Analysis**

In this problem, the specimen considered possesses width,  $2a = 2.2 \text{ mm} \Rightarrow a = 1.1 \text{ mm}$  and depth,  $2b = 140 \text{ mm} \Rightarrow b = 70 \text{ mm}$ , and length,  $L = 800 \text{ mm}$  as shown in the Fig. 1c. The considered thin rectangular section is fixed at one end and a torque of magnitude  $303.356 \text{ Nmm}$  is applied at the free end of the member. Considered material is galvanized steel with Modulus of elasticity,  $E = 200 \text{ GPa}$ , Poisson’s ratio,  $\nu = 0.29$  and Modulus of Rigidity,  $\mu = 80 \text{ GPa}$ . Substituting the given values in the equations of torque and maximum shear stress, we get  $\alpha = 7.6311 \times 10^{-6} \text{ rad/mm}$  and  $\tau_{\text{max}} = 1.343 \text{ N/mm}^2$  or MPa



**Fig. 15** **a** Uniform meshing of the member and the loading arms mentioned in problem 2. **b** Loading on the arms

### 2.2.3 Numerical Analysis

The element type chosen is ‘Solid 8 Node 185 (SOLID185)’. This element has 8 nodes with 3 degrees of freedom each node, therefore the element has a total of 24 degrees of freedom (Fig. 2). The small loading arms are modelled separately and glued to the main specimen using Glue operation under Boolean operations. The meshing is done uniformly throughout the member as there are no discontinuities in the member and the cross-section is uniform throughout the member (Fig. 15a).

Similar to problem 1, the member is cuboidal without any lattice discontinuity, therefore the type of element is a brick element and the stress variation along the transverse direction in the cross-section can be well determined by a 3D brick element rather than a 2D plane element. The size of element is 2.2 mm. This leads to formation of a total of 23590 elements and a total of 48122 nodes. Here, the loading is applied at the ends of the loading arms. The applied torque is of magnitude 303.356 Nmm. The lever arm between the loads being applied on the load arms is, 91.76 mm. Thus, the force to be applied on each loading arm is obtained by dividing the torque by the lever arm which is, 3.30597 N. The front view of free body diagram of the member under loading is shown in Fig. 15b. There are 2 nodes at the point of application of the load thus the obtained force value is divided by 2 and the value of force to be applied on the nodes is,  $3.30597/2 = 1.652985$  N.

## 3 Results and Discussion

As per the inference mentioned in the Sect. 2.1.3, which included the inference derived from the problem 1, the theoretical and numerical analysis of the member in problem 1 gave an affirmation to go forward with the validation of torsion study by

**Table 1** The values obtained from the rectangular strain rosette

$\epsilon_A$	$\epsilon_B$	$\epsilon_C$	$\epsilon_1$	$\epsilon_2$	$\sigma_1$ (MPa)	$\sigma_2$ (MPa)	$\tau_{\max}$ (MPa)
$-3.5 \times 10^{-5}$	$2.8 \times 10^{-5}$	$-1 \times 10^{-6}$	$5.31 \times 10^{-5}$	$-3.51 \times 10^{-5}$	13.8	-11.0	1.40

**Table 2** The values obtained from delta strain rosette

$\epsilon_A$	$\epsilon_B$	$\epsilon_C$	$\epsilon_1$	$\epsilon_2$	$\sigma_1$ (MPa)	$\sigma_2$ (MPa)	$\tau_{\max}$ (MPa)
$-2.6 \times 10^{-5}$	$3 \times 10^{-5}$	$8 \times 10^{-6}$	$3.35 \times 10^{-5}$	$-5.15 \times 10^{-5}$	10.6	-13.4	-1.40

**Table 3** Percentage errors seen in the results

Experimental results (MPa)	Theoretical results (MPa)	Numerical results (MPa)	Percentage error between theoretical and experimental results	Percentage error between theoretical and numerical results	Percentage error between experimental and numerical results
$\pm 1.40$	$\pm 1.343$	$\pm 1.239$	4.24%	7.74%	11.5%

experimentation. The percentage error between the theoretical and numerical values was 8.9%.

For experimentation, a new specimen of problem 2 of the said dimensions was fabricated and tested. The results of the experiment were obtained in the form of the strain data of the strain rosettes. This data was used and using the relevant formulas, the maximum shear stress was calculated. The final calculation results are mentioned in the Tables 1 and 2.

The theoretical analysis of this specimen gave the maximum shear stress value to be, 1.343 MPa. The numerical analysis of the same gave the value to be 1.239 MPa. Now the percentage errors are as shown in Table 3.

## 4 Conclusion

In problem 1, the convergence of the loading was done to determine the load orientation in order to get the maximum shear stress on the middle layer and it converged in 5th iteration. This was done to avoid sharp edge stress concentration. The percentage error obtained from the problem 1 between the theoretical and numerical results was 8.9%. Using the numerical results of problem 1, the location for best suiting for mounting of strain rosettes in experimentation was decided. The experiment was done on the suitable specimen. The specimen was analysed theoretically and numerically again. The percentage error between theoretical and experimental value is,

4.24%. The percentage error between theoretical and numerical values is, 7.74%. The percentage error between experimental and numerical results is, 11.5%. In torsion, YZ shear stress plays a very critical role. This stress analysis study concludes the location of the maximum shear stress and the correct orientation for loading for torsion in thin rectangular sections.

**Acknowledgements** We are very grateful to the funding agency, AR & DB, Ministry of defence, file number ARDB/01/2031964/M/I for providing financial assistance for conducting our research work.

## References

1. Obst M, Kurpisz D, Paczos P (2016) The experimental and analytical investigations of torsion phenomenon of thin-walled cold formed channel beams subjected to four-point bending. *Thin-Walled Struct* 106(2016):179–186
2. Grenda M, Paczos P (2019) Experimental and numerical study of local stability of non-standard thin-walled channel beams. *J Theor Appl Mech* 57(3):549–562
3. Chen Z, Huang Z, Guo Y, Li G (2022) Prediction of mechanical properties of thin-walled bar with open cross-section under restrained torsion. *Coatings* 2022(12):562
4. Carrera E, Zappino E, Petrolo M (2013) Analysis of thin-walled structures with longitudinal and transversal stiffeners. *J Appl Mech* 80:011006-1
5. Jo CH, Kim KS, Lee SH (2002) Parametric study on offshore jacket launching. *J Ocean Eng* 29:1959–1979
6. Elshafey AA, Haddara MR, Marzouk H (2009) Dynamic response of offshore jacket structures under random loads. *J Marine Struct* 22:504–521
7. Sekhar GR, Nallayarasu S (2013) Experimental investigation of the wave slam and slap coefficients for array of non-circular section of offshore platforms. *J Ships Offshore Struct* 8(1):15–28
8. Abdelkader K, Toufik Z, Mohamed BJ (2015) Torsional stress in non-circular cross sections by the finite element method. *Adv Mech Eng* 7(5):1–20
9. Mascarenhas ML, Poliševski D (1994) The warping, the torsion and the Neumann problems in a quasi-periodically perforated domain. *RAIRO—Modélisation mathématique et analyse numérique*, 37–57
10. Brabie G (2005) An analysis of the state of stresses generated by torsion in twisted non-circular bars. *J Mater Process Technol* 169:401–408
11. Galishnikova VV, Gebre TH (2022) The behaviour of thin-walled beam with restrained torsion. *Mag Civil Eng* 110(2). Article No. 11009
12. Nguyen T-C, Tang V-L, Nguyen T-S, Nguyen Q-T (2019) Analysis of thin-walled bars stress state with an open section. *IOP Conf Ser: Mater Sci Eng* 661:012011
13. Marcello Celi (2020) Stress concentration factors in loaded strips and bars
14. Chattopadhyay S (2013) A study of warping of non-circular shafts in torsion. In: 120th annual conference 2013. American Society for Engineering Education
15. Andelic NM (2012) Torsional analysis of open section thin-walled beams. *FME Trans* 40:93–98
16. Heinrich SM, Associate Member ASCE (1996) Membrane analogy for saint-venant torsion: new results. *J Eng Mech* 122(11):1110–1112
17. Chen H (2019) Saint-Venant's torsion by finite-volume method
18. Thompson MK, Thompson JM (2017) ANSYS mechanical APDL for finite element analysis

# Stress Analysis of a Member of Jacket Structure with Different Types of Stiffeners



T. S. Sreejith and Vadivuchezhian Kaliveeran

**Abstract** Jacket structures are subjected to very challenging environmental conditions and thus require certain reinforcements to ensure the resistance against the challenging conditions. The present study deals with the stress analysis of a member of a jacket structure with triangular type stiffener and another with second order curved stiffener. The specimen considered is of steel with dimensions 800 mm × 100 mm × 10 mm. The member is considered as a fixed bar subjected to a concentrated load of 500 N at the mid-span. The idea is to reinforce the member to strengthen up which in turn increases the life of the structure. The configuration of the stiffeners is such that the stress concentration is avoided. The triangular stiffener has a length of 200 mm and height of 20 mm and thickness of 10 mm. The second order curved stiffener has the same length, height and thickness and follows the variation  $y = 20 - \frac{x}{5} + \frac{x^2}{2000}$ . Four stiffeners are provided, one at the top and one at the bottom of each end. The structure is simulated and analyzed in a Finite Element Modelling (FEM) software and the necessary results are obtained. The results from this analysis are validated using the experimental results.

**Keywords** Offshore jacket structure · Finite element analysis · Stress concentration · Experimental stud · Strength

## 1 Introduction

Offshore oil reserves are explored and exploited using offshore structures. The need for exploring the extensive hydrocarbon reserves in the offshore regions and the oil industries is the main driving force for the installation of offshore platforms. The offshore platforms are also key for military and navigation purposes.

A jacket structure is a welded tubular frame used primarily to support rigs in the offshore region [1]. They are formed of steel vertical and battered legs and

---

T. S. Sreejith · V. Kaliveeran (✉)  
Water Resources and Ocean Engineering, National Institute of Technology Karnataka,  
Mangalore 575025, India  
e-mail: [vadivuchezhian\\_k@yahoo.co.in](mailto:vadivuchezhian_k@yahoo.co.in)

supported by horizontal bracings. They consist of working platforms, corrosion protection systems, cables, ladders, etc. [2]. Reinforcing refers to the up-gradation of the jacket structure with the desired properties. A jacket structure may be improved in the following fields: Strength, Fire resistance, Corrosion resistance, Weight reduction, Transportation easiness, Lifespan, Floatability, Production, etc. [3]. The study deals with reinforcing the jacket structure to improve the strength characteristics and thereby the lifespan. Stress concentration is a major factor that affects the design of a structure [4].

The study deals with the study of stress distribution in a member of the jacket structure [5] subjected to a particular loading [6, 7] and aims to reduce or avoid the stress concentration by reinforcing or modifying [8] the structure with different types of stiffeners. Finite Element Method is the main tool used for the study. The Finite Element Method is an approximate but very effective technique that converts a complex scenario into finer/smaller parts and solves for the smaller parts and combines the results to provide the solution for the complex problem. Finite element modelling is done for the jacket structures to determine the essential parameters required for the design of the jacket structures [9]. Various computer softwares are available for finite element modelling which makes the finite element modelling relatively easy widely [10]. The study also involves experiment using Universal Testing Machine (UTM) of 400 kN capacity. Strain gauges are used to determine the stresses evolved at the required points which are made into use with the help of strain indicators.

## 2 Methodology

The jacket structures are very gigantic and complex structures subjected to different types of environmental loads and mechanical loads. In the present study, a member of the jacket structure is idealized as a thin rectangular bar subjected to central concentrated load. This idealization is done to obtain a particular solution for the problem taken up. This particular solution can be used to arrive at a general solution for the problems of this nature which can be used to solve the problems having difference in the type of cross-section, material used, dimensions and so on. Consider a rectangular bar of length 800 mm, height 100 mm and thickness 10 mm. The bar was designed as a fixed bar subjected to a concentrated load of 500 N at the mid-span. The bar was of mild steel with modulus of elasticity and Poisson's ratio  $2 \times 10^5$  N/mm<sup>2</sup> and 0.29 respectively. The problem was first solved using finite element software and the results were validated by conducting an experiment in the laboratory.

First, the ordinary fixed bar was analyzed, and it was subjected to stress concentration at the corners. Since the idea is to reduce the stress concentration along with the improvement in the strength of the bar, the stiffeners used were of such configuration that their volume reduces gradually rather than abruptly. From the *ANSYS* simulation of the cantilever bar with rectangular stiffeners, it was inferred that although the rectangular stiffeners were successful in improving the strength of the bar as well

**Table 1** Convergence study

Element size (mm)	Number of elements	Normal stress (N/mm <sup>2</sup> )	Percentage error between theoretical value and numerical value
25	128	2.5629	14.57
20	200	2.7062	9.7933
15	378	2.91197	2.9343
10	800	3.12985	4.3283
5	6400	3.52296	17.432

as reducing the stress concentration in the bar, there were still some stress concentrations. This resulted in coming up with a gradually varying configuration for the stiffeners. The study deals with the attachment of the bar with two different types of stiffeners, triangular type and second order curved type. The triangular stiffener had a length of 200 mm, height 100 mm and thickness 10 mm. The second order curved stiffener has the same length, height and thickness and follows the variation,  $y = 20 - \frac{x}{5} + \frac{x^2}{2000}$ . The volume of each triangular and second order curved stiffener was 20,000 mm<sup>3</sup> and 13,333.333 mm<sup>3</sup> respectively. Four stiffeners were provided, one at the top and one at the bottom of each end of the bar as the modification.

### 3 Convergence Study

Before fixing the size of the element to be used for the numerical study, certain different sizes of the elements were trialed, and the results were compared with the theoretical value. The different sizes (edge length) of elements tried were 25 mm, 20 mm, 15 mm, 10 mm and 5 mm. From the theoretical analysis, the maximum normal stress acting in the member was obtained as 3 N/mm<sup>2</sup>. A comparison is made between the different element numbers obtained corresponding to the element sizes and the respective normal stress values (Table 1). From the study, the edge length for the element was obtained as 15 mm (Fig. 1).

### 4 Numerical Study

The simulation of the problem was accomplished in a finite element software. The element type considered was ‘Solid Brick 185’ which is a 3D 8-noded structural solid element with three degrees of freedom at each node i.e.; translations in x, y and z directions (Fig. 2). Since the geometry was not complex and accurate results could be obtained using this linear element, this element was chosen for the analysis.

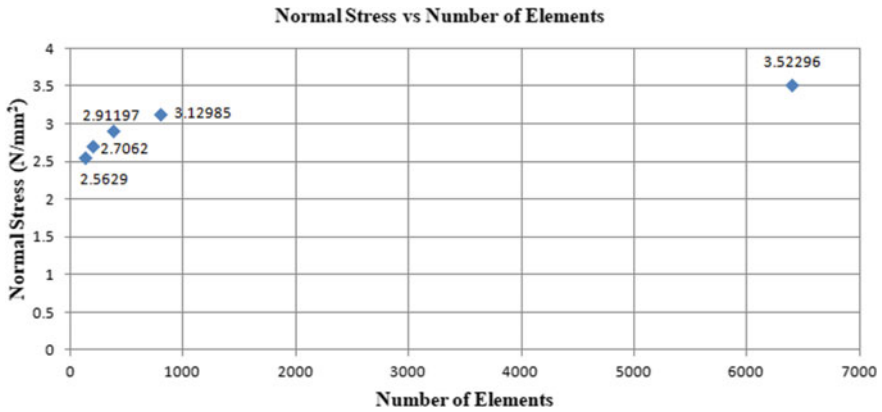
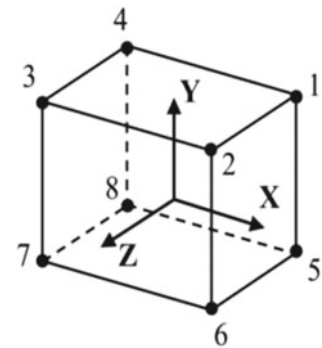


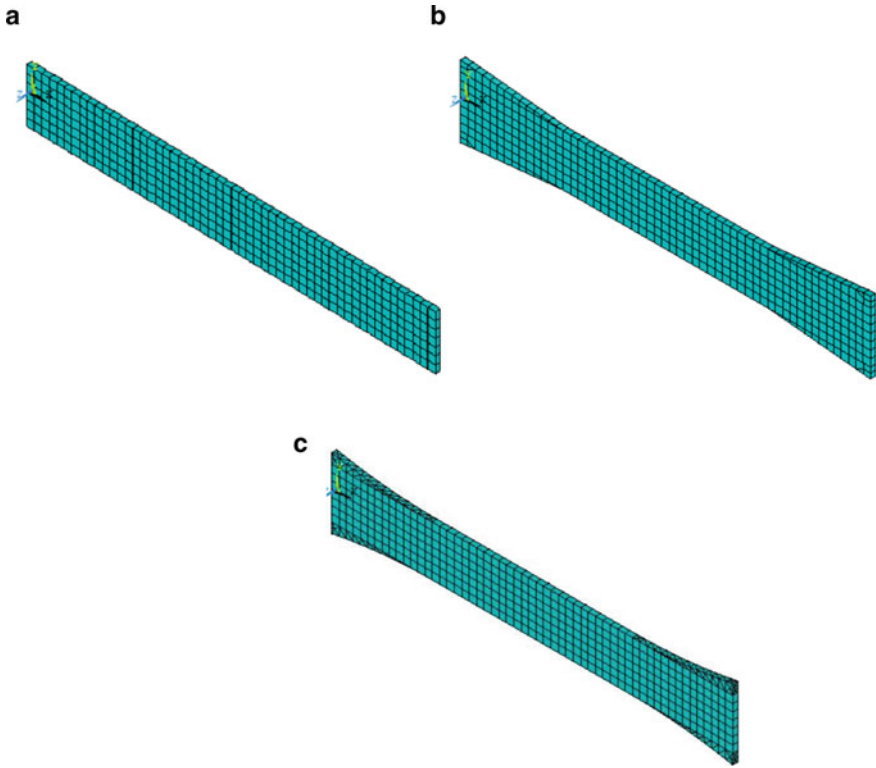
Fig. 1 Convergence study

Fig. 2 Solid brick (185) element (Courtesy ANSYS manual)



The material properties (modulus of elasticity and Poisson’s ratio as  $2 \times 10^5$  N/mm<sup>2</sup> and 0.29 respectively) were provided. The geometry of the bar was then created and meshed (Fig. 3). The bar was divided into elements with size 15 mm constituting a total number of 378 elements. The bar had 8 nodes in the Y-direction and 55 nodes in the X-direction in a single plane accounting to 440 nodes. The boundary conditions and the load were then provided and the problem was solved. The boundary conditions provided were at  $x = 0$  mm,  $y = 0$ ,  $\frac{dy}{dx} = \theta_x = 0$  and at  $x = 800$  mm,  $y = 0$ ,  $\frac{dy}{dx} = \theta_x = 0$ . For the stiffeners, at  $x = 0$ ,  $y_s = 20$  mm and at  $x = 200$  mm,  $y_s = 0$ . Particularly for a second order curved stiffener, at  $x = 200$  mm,  $\frac{dy_s}{dx} = \theta_x = 0$ .



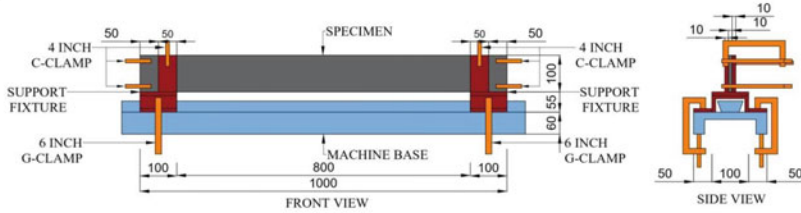


**Fig. 3** Meshed images of **a** ordinary bar element, **b** bar element reinforced with triangular stiffener, **c** bar element reinforced with second order curved stiffener

## 5 Experimental Study

For the experiment to be conducted in the laboratory, it was necessary to design a fixture for providing fixed end condition for the bar. The making of the fixture included cutting and welding of mild steel planks and channel section. The fixity was mainly achieved using 4 inch-C-clamps, six in numbers, and the fixture was fixed to the base of the Universal Testing Machine with the help of four no.s, 6 inch-G-clamps. The schematic diagram of the designed set-up is provided below (Fig. 4).

a



b

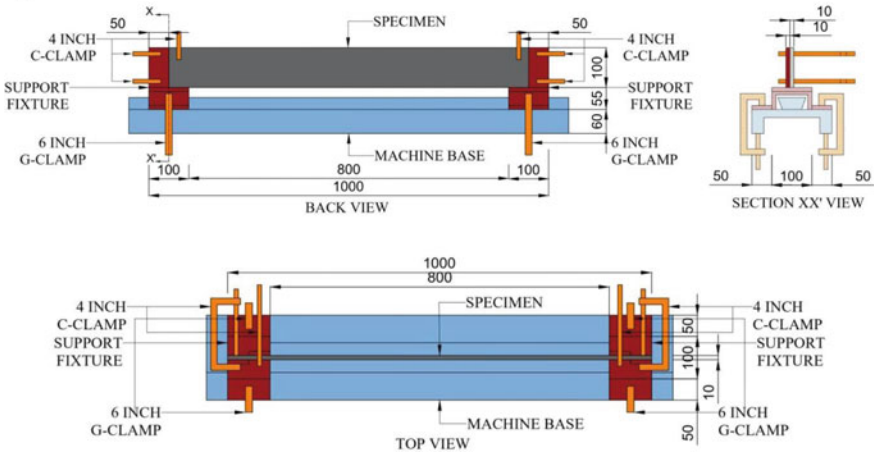


Fig. 4 Experimental set-up a Front and side view. b Back, section and top view

## 5.1 Preparation of the Set-Up

### 5.1.1 Fixture

Four pieces of rectangular plate of height 70 mm, width 50 mm and thickness 10 mm were cut. Two square plates of side 100 mm and thickness 10 mm were cut and welded on all four sides over a channel section of web length 100 mm, flange length 45 mm and thickness 8 mm. The four rectangular plates were welded on the outer side over the square plate, with two rectangular plates provided over each square plate. The rectangular plates were positioned in a staggered manner with a gap of 10 mm in between the plates. This was done to ensure firm hold of the specimen in between the plates, prevent the specimen from slipping in the other direction if the plates were welded on the same side and to act as fixtures for clamping the specimen. To the bottom of the channel section on each side, one plate of size 100 mm × 50 mm × 10 mm was welded. This plate was used for clamping the fixture to the machine base. Only one set of fixtures (Fig. 5) was made with the idea of reusing the same for the different cases.



**Fig. 5** Support fixture

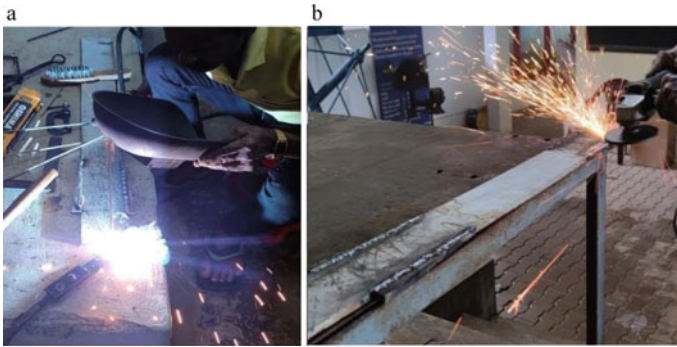
### 5.1.2 Specimen

The ordinary rectangular specimen was easily made as it required only cutting out a rectangular plate of length 800 mm, height 100 mm and thickness 10 mm. Two more rectangular plates of the same dimensions as of the ordinary rectangular specimen were cut out; one for attaching triangular stiffeners and the other for attaching second order curved stiffener. The task was creating the specimen with stiffeners, especially the stiffeners itself. The stiffener shapes were drawn in Autocad software, and their printouts were taken. These printouts were pasted over the required material and the material was cut into the shape of the stiffeners, both triangular and second order curved stiffeners, with the help of hand cutter. The thinner end was cut with the help of shear cutter. The finishing touch and small grinding works were taken up with the hand cutter. For welding the stiffeners to the rectangular plate, the top stiffener and the bottom stiffener of one end were clamped with c-clamp to the plate and were welded along the length. Similarly, the stiffeners at the top and the bottom of the other end were welded along the length.

After the welding process on one side, the plate was turned over for welding the stiffeners to the plate on the opposite side, completing two side welding of each stiffener to the plate. Succeeding the whole welding process, it was required to provide finishing touch to remove the uneven surfaces created and it was attained with the usage of hand cutting machine (Fig. 6).

### 5.1.3 Mounting the Strain Gauges

The strain gauges were mounted at the points where the stress was required to be examined. Before mounting the strain gauges, the required points were made almost smooth by rubbing thoroughly with sandpaper and cleaned with acetone. The strain gauges were tested using multi-metre to ensure the specification of the gauges. The strain gauges ordered were of 120 ohms with a gauge factor of 2.1 and the same was ensured with the aid of multi-metre. Two strain gauges per specimen were mounted accumulating to a total number of 6 strain gauges for the project. The stress distribution was symmetric as obtained from ANSYS as the loading was symmetric. One strain gauge was mounted at the point of maximum stress and the other at a



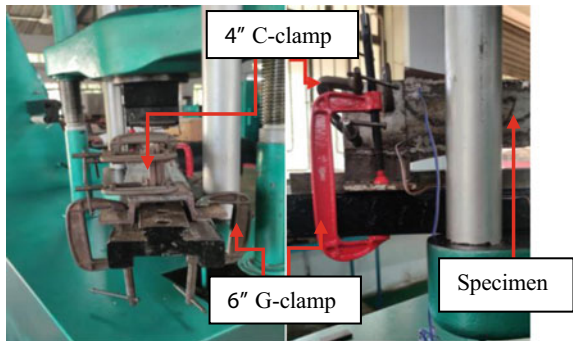
**Fig. 6** a Welding of the stiffeners to the rectangular bar element. b Grinding the irregular surfaces on the specimen

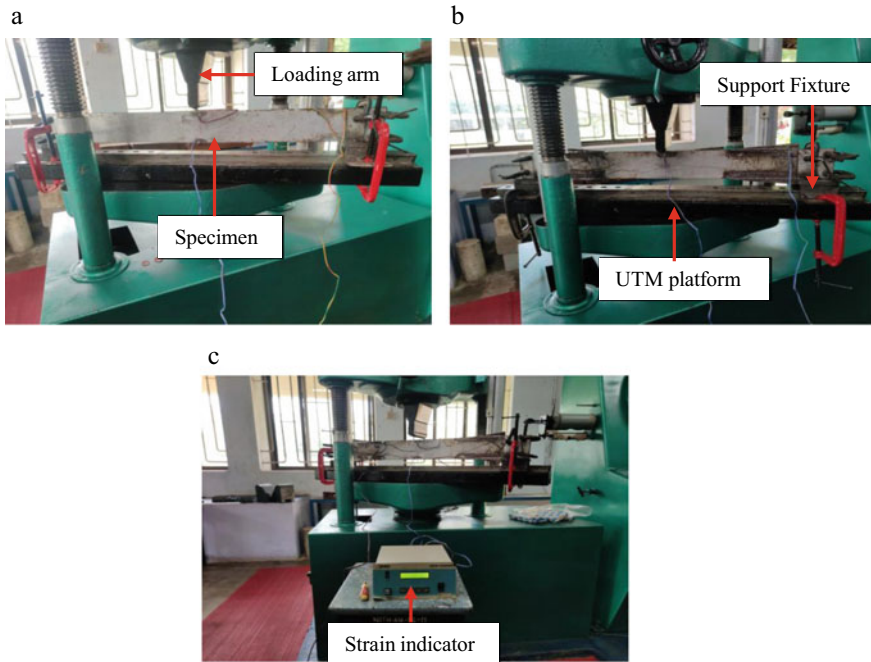
distance of 25 mm from one end at the joint of the stiffener and the original bar for the reinforced bar and for the ordinary bar; it was mounted at 25 mm from the end at the top end. The point at the distance of 25 mm from the end was noted as ‘Point 1’ and the other at the point of maximum stress as ‘Point 2’.

The experiment was conducted using the Universal Testing Machine of capacity 400 kN at the Strength of Materials lab of Water Resources and Ocean Engineering Department of National Institute of Technology Karnataka, Surathkal. The support fixtures were placed on the platform provided on the UTM and the first specimen, ordinary bar, was placed over the fixture. Using the six no.s, 4 inch-C-clamps, the specimen was fixed to the staggered plates of the support fixture. Once it was ensured that the load would be imposed at the centre of the specimen, the support fixtures were clamped to the platform of the UTM using the four no.s, 6 inch clamps, one each at the four end faces (Fig. 7).

The strain gauges were connected to the strain indicator with the connection being 1–4–5. The channels were checked to ensure zero reading, and the standard factors were set. The UTM imposed load on the specimen at an interval of 100 N till 600 N and the strain in the strain gauges was noted from the strain indicator (Fig. 8). After

**Fig. 7** Fixing the specimen on the UTM platform





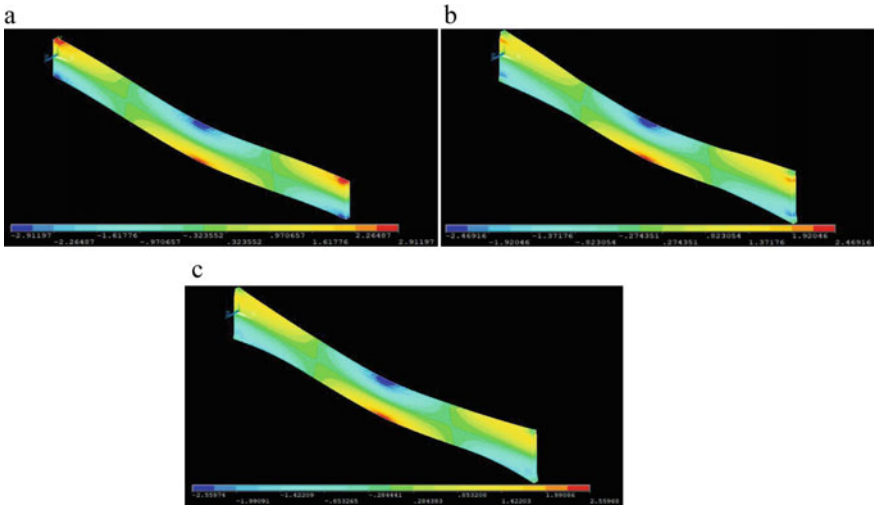
**Fig. 8** Experimental set-up for **a** ordinary bar element, **b** bar element reinforced with triangular stiffener, **c** bar element reinforced with second order curved stiffener

conducting the test on the first specimen, it was removed and the next specimen, bar reinforced with triangular stiffener was fixed in the same manner and tested. After the bar reinforced with triangular stiffeners, the bar reinforced with second order curved stiffeners was tested and the results were recorded.

## 6 Results and Discussion

The results from the simulation of the ordinary bar element and the bar elements reinforced with triangular and second order curved stiffener are given below (Fig. 9).

In the case of the ordinary fixed bar, there was stress concentration near the edges at support region and it was the maximum normal stress acting in the bar with a value of  $2.91197 \text{ N/mm}^2$ . The normal stress at the edges at the mid-span region was slightly lesser than that at the support region with a value of  $2.8816 \text{ N/mm}^2$ . With the triangular stiffener incorporated to the bar, the stress concentration was avoided, and the maximum normal stress acted at the mid-span region at the edges with a value of  $2.46916 \text{ N/mm}^2$ . Similar was the situation with the bar with second order curved stiffener, as the stress concentration was avoided, and the maximum normal stress acted at the edges of the mid-span with a slightly different value of  $2.55968 \text{ N/}$



**Fig. 9** ANSYS result of **a** ordinary bar element, **b** bar element reinforced with triangular stiffener, **c** bar element reinforced with second order curved stiffener

mm<sup>2</sup>. The experimental results of the testing of the physical models of the ordinary bar element (Table 2) and the bar elements reinforced with triangular (Table 3) and second order curved (Table 4) stiffener using the UTM are tabulated below.

From the experiment on the physical model of the ordinary bar element, the normal stress at the point at the edge of the mid-span was obtained as 2.8 N/mm<sup>2</sup> and that at the point 25 mm from the support region at the edge was 2.4 N/mm<sup>2</sup>. For the bar reinforced with triangular stiffener, the normal stress at the same points was 2.4 N/mm<sup>2</sup> and 1.4 N/mm<sup>2</sup> respectively. For the bar reinforced with second order curved stiffener, it was 2.6 N/mm<sup>2</sup> and 1.6 N/mm<sup>2</sup> respectively. Table 5 shows the comparison between the numerical and experimental results.

**Table 2** Experimental result of ordinary bar element

Load (N)	Strain in (micro strains)		Modulus of Elasticity (N/mm <sup>2</sup> )	Stress at (N/mm <sup>2</sup> )	
	Strain Gauge 1	Strain Gauge 2		Point 1	Point 2
0	0	1	200,000	0	0.2
100	2	2	200,000	0.4	0.4
200	3	4	200,000	0.6	0.8
300	6	8	200,000	1.2	1.6
400	9	11	200,000	1.8	2.2
500	12	14	200,000	2.4	2.8
600	16	18	200,000	3.2	3.6

**Table 3** Experimental result of bar element reinforced with triangular stiffener

Load (N)	Strain in (micro strains)		Modulus of Elasticity (N/mm <sup>2</sup> )	Stress at (N/mm <sup>2</sup> )	
	Strain Gauge 1	Strain Gauge 2		Point 1	Point 2
0	0	2	200,000	0	0.4
100	2	6	200,000	0.4	1.2
200	3	8	200,000	0.6	1.6
300	5	10	200,000	1	2
400	6	11	200,000	1.2	2.2
500	7	12	200,000	1.4	2.4
600	9	13	200,000	1.8	2.6

**Table 4** Experimental result of bar element reinforced with second order curved stiffener

Load (N)	Strain in (micro strains)		Modulus of elasticity (N/mm <sup>2</sup> )	Stress at (N/mm <sup>2</sup> )	
	Strain Gauge 1	Strain Gauge 2		Point 1	Point 2
0	0	1	200,000	0	0.2
100	1	2	200,000	0.2	0.4
200	3	4	200,000	0.6	0.8
300	5	7	200,000	1	1.4
400	6	10	200,000	1.2	2
500	8	13	200,000	1.6	2.6
600	10	15	200,000	2	3

**Table 5** Comparison of Numerical and experimental results

Model	Stress at Point1 (N/mm <sup>2</sup> )		Stress at Point2 (N/mm <sup>2</sup> )		Percentage error (%)	
	Numerical value	Experimental value	Numerical value	Experimental value	At point 1	At point 2
Ordinary bar element	2.2898	2.4	2.91197	2.8	4.5916	3.9989
Bar element reinforced with triangular stiffener	1.2756	1.4	2.46916	2.4	8.8857	2.8817
Bar element reinforced with second order curved stiffener	1.3991	1.6	2.55968	2.6	12.5563	1.5508

## 7 Conclusions

The numerical results from the ANSYS were almost coinciding with the experimental results obtained by testing the physical models of the specimens with the maximum percentage error obtained as 12.5563%. This error may be due to the difference in the environmental conditions like temperature and wind between the numerical study and the experimental study. In the software, it is rather a constant condition achieved compared to a fluctuating condition in the reality. Also in the real case, it is difficult to achieve perfect homogeneity of the material and also there was minute difference in the dimensions of the real specimen with respect to the virtual specimen. This concluded that with the reinforcements provided to the ordinary bar element in the form of triangular stiffeners and second order curved stiffeners, the stress concentration in the bar was reduced which resulted in the improvement of the strength of the bar thereby increased the lifespan of the bar. This also conveyed that the use of gradually varying profile for stiffeners is very effective in reducing the stress concentration.

**Acknowledgements** We are very grateful to the funding agency, AR & DB, Ministry of defence, file number ARDB/01/2031964/M/I for providing financial assistance for conducting our research work.

## References

1. Jo CH, Kim KS, Lee SH (2002) Parametric study on offshore jacket launching. *J Ocean Eng* 29:1959–1979
2. Bai Y, Wei-Liang J (2016) ‘Offshore structural analysis’ chapter in textbook on “Marine Structural Design (Second Edition)”
3. Lotfollahi-Yaghin MA, Tarinejad R, Shahverdi S, Asgarian B (2011) Structural health monitoring (SHM) of offshore jacket platforms. In: Proceedings of the ASME 2011 30th international conference on ocean, offshore and arctic engineering, OMAE2011, June 19–24, 2011, Rotterdam, The Netherlands
4. Saini DS, Karmakar D, Ray-Chaudhuri S (2016) A review of stress concentration factors in tubular and nontubular joints for the design of offshore installations. *J Ocean Eng Sci* 1:186–202
5. Sekhar GR, Nallayarasu S (2012) Experimental investigation of wave slam and slap coefficients for array of non-circular section of offshore platforms. *Ships Offshore Struct* 8(1):15–28
6. Mendes AC, Kolodziej JA, Correia HJD (2004) Numerical modelling of wave-current loading on offshore jacket structures. *Trans Built Environ* 71. ISSN 1743-3509
7. Elshafey AA, Haddara MR, Marzouk H (2009) Dynamic response of offshore jacket structures under random loads. *J Mar Struct* 22:504–521
8. Ju S-H (2022) Increasing the fatigue life of offshore wind turbine jacket structures using yaw stiffness and damping. *Renew Sustain Energy Rev* 162:112458
9. Harish N (2010) Analysis of offshore jacket platform. In: National conference on sustainable water resources management, SWaRM 20, NITK, Surathkal, India, Jan7–9, 2010
10. Thompson MK, Thompson JM (2017) ANSYS mechanical APDL for finite element analysis



# Structural Analysis of Non-prismatic Column Using Finite Element Approach



Gautam Kumar and Vadivuchezhian Kaliveeran

**Abstract** Offshore pipelines are subjected to various types of loading, depending upon the sub-sea conditions during their design life. Buckling is a major structural instability problem in the offshore pipelines operating at high pressure and high temperature, along with other causes. Various kinds of non-prismatic sections are generally used in special areas of the pipeline system. The present research work focuses on estimating the structural response (buckling strength, in particular) of the non-prismatic offshore pipelines. Eigenvalue buckling analysis using the Finite Element (FE) method was conducted to find the buckling strength and mode shape of the pipeline model. The non-prismatic pipeline was modeled as 1-D and 3-D FE models; the 1-D model was analyzed using the *MATLAB* program, and the complete 3-D model was analyzed using the *ANSYS* workbench. Both the 1-D and 3-D numerical analysis results were compared and verified experimentally. The results of the analysis and their convergence pattern were also discussed.

**Keywords** Offshore pipelines · Eigenvalue buckling analysis · Finite element method · Mode shape

## 1 Introduction

In the present scenario, where energy is our day-to-day need, apart from coal, we rely mainly on crude oil and natural gas to fulfill those needs. The offshore region is a powerhouse of these resources, and offshore pipelines play an important role in offshore crude oil and natural gas extraction projects. Pipelines are the proven, most economical means of transportation of water, crude oil, and natural gas in large quantities regularly on competing routes. Pipelines have shown robust adaptability to

---

G. Kumar · V. Kaliveeran (✉)

Department of Water Resources and Ocean Engineering, National Institute of Technology  
Karnataka, Surathkal 575025, India

e-mail: [vadivuchezhian\\_k@yahoo.co.in](mailto:vadivuchezhian_k@yahoo.co.in)

various environments, including remote areas and hostile environments. Due to their adaptability to alternatives, pipelines are widely used in the petrochemical industry [1].

An offshore pipeline generally withstands loading like external loads induced by waves, current, uneven seabed, pullover, trawl-board impact, expansion due to pressure and temperature, and installation and operational loads. Experience shows that the significant load response of the offshore pipeline during installation (subjected to external hydrostatic pressure) and during operation (subjected to internal pressure) is bending combined with longitudinal force. A critical concern in the design of pipelines is the phenomenon of global buckling, which is one of the consequences of the high temperature and high pressure combined with other factors. Global buckling can be catastrophic if not properly analyzed and contained within a required limit. The pipeline failure in Guanabara Bay, Brazil, in January 2000 is a notable example of global buckling failure. It unexpectedly buckled about 13 feet laterally and exploded, releasing 7,000 barrels of oil into the sea. The pipeline failed due to lateral displacement caused by high temperature and pressure during pipeline operation, according to the assessment [2].

Pipelines are generally subjected to higher temperature and pressure conditions during the operational phase compared to the installation phase, which leads to their expansion. It produces an effective axial compressive force if the pipe is not free to deform. In the pipelines with free ends, soil friction generally provides resistance to expansion. A “fully restrained” pipeline section is developed between two points in the pipeline section when the expansion force is equal to the resistance force [3, 9].

Achieving pipeline installation in precise straight paths is impossible due to an uneven seabed, deep water, and other factors. This imperfection in the pipeline, combined with effective axial compressive force, produces a global buckling in the offshore pipeline to relieve the excess axial compression. The buckling in pipelines occurs at the locations where effective axial force and forces developed due to imperfection in the pipe becoming more than the resistive (soil friction, pipe weight, and flexural stiffness) forces. Generally, there are two ways global buckling in the pipeline takes place: first, in the horizontal plane (lateral buckling), and second, in the vertical plane (upheaval buckling) [3, 8].

The present paper is intended to estimate the critical buckling load of a non-prismatic pipe section numerically and experimentally. A numerical buckling analysis using the finite element method [4] was performed on the pipeline model, considering 1-D modeling in *MATLAB* and 3-D modeling in *ANSYS*. Experiments were conducted on a mild steel pipeline model of  $L = 600$  mm,  $d_o = 21.58$  mm,  $d_i = 14.14$  mm, and  $t = 3.72$  mm with a longitudinal variation in thickness. The experimental critical buckling load for the pipeline model was calculated using the double tangent method [5, 7] which was used to validate the critical buckling load values obtained from numerical analysis.

## 2 Material Modeling

### 2.1 Material Modeling

The current study uses mild steel conforming to IS: 1239 (part-1) 2004 as a pipe material for both numerical and experimental modeling. The material properties of the mild steel pipe model provided by the manufacturer are given below in Table 1.

The non-prismatic pipe model used for FE modeling is a seamless mild steel pipe of 600 mm length, 21.58 mm outer diameter, 14.14 mm inner diameter, and 3.72 mm thickness with a longitudinal variation in thickness at specific sections as shown in Fig. 1.

## 3 1-D Finite Element Modeling Using MATLAB

In the present study, the non-prismatic pipeline given in Fig. 1. is modeled as a pinned–pinned column subjected to axial compressive loading (P), as shown in Fig. 2. The governing differential equation (GDE) with boundary conditions for the problem is given below in Eq. (1) [4].

$$EI \frac{d^4 y}{dx^4} + P \left( \frac{d^2 y}{dx^2} \right) = 0 \tag{1}$$

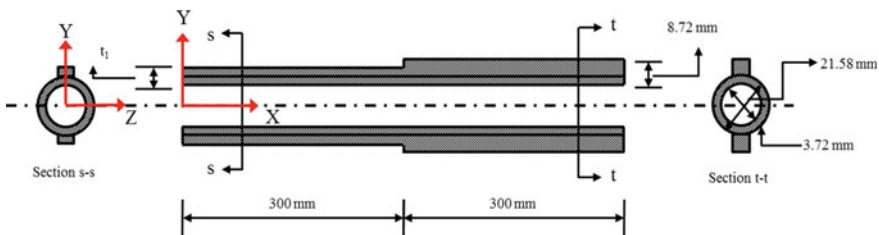
Essential boundary conditions: at  $x = 0, y(0) = 0$ ;  $x = L, y(L) = 0$ .

Non-essential boundary conditions: at  $x = 0, EI \frac{d^2 y(0)}{dx^2} = 0$ ;  $x = L,$

Using the Euler–Bernoulli bending equation, Eq. (1) can be rearranged as a bending moment-based governing differential equation. The moment-based

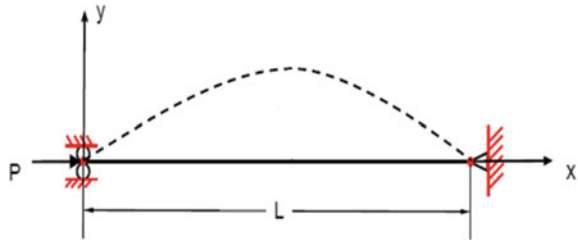
**Table 1** Material properties of non-prismatic pipe model

Young’s modulus of elasticity	Poisson’s ratio	Density
210 GPa	0.3	7850 kg/m <sup>3</sup>



**Fig. 1** Schematic diagram of non-prismatic pipeline model

**Fig. 2** Non-prismatic pipeline modeled as a pinned-pinned column



governing differential equation given below in Eq. (2) is in the form of a general boundary value problem, which can be modeled as a 1-D finite element model easily to estimate the critical buckling load [4].

$$EI \frac{d^2 M(x)}{dx^2} + PM(x) = 0 \tag{2}$$

at  $x = 0, M_0 = 0; x = L, M_L = 0$ .

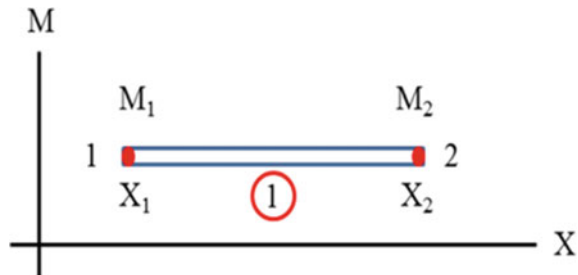
### 3.1 Finite Element Analysis and Results

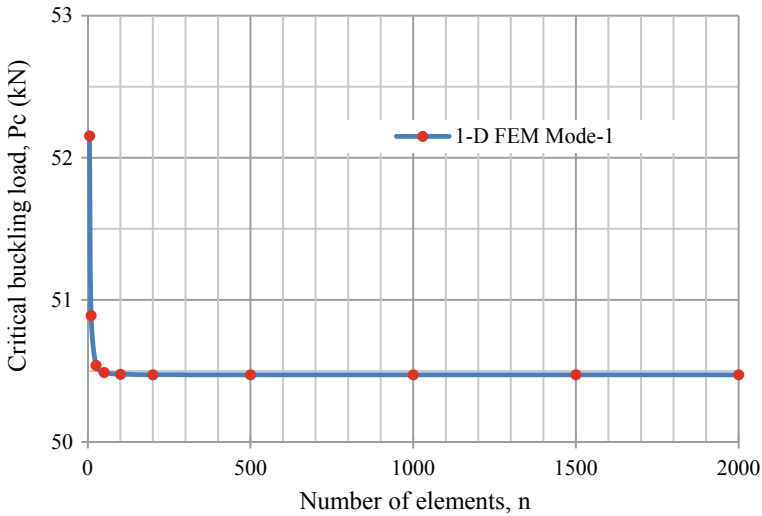
In the FE modeling, the problem domain was discretized into n number of elements, each having an equal length l and two nodes at its end. Each node got one degree of freedom in the x direction, so that each element has two degrees of freedom. The linear element used is shown below in Fig. 3.

Assuming  $M(x)$ , which varies linearly over the element, as a solution of Eq. (2), an element equation, was developed using the Galerkin weighted residual method [4]. The element equation obtained using linear first-order shape functions is given below in Eq. (3).

$$\begin{bmatrix} 1 & -1 \\ -1 & 1 \end{bmatrix} \begin{Bmatrix} M_1 \\ M_2 \end{Bmatrix} = P \begin{bmatrix} \frac{l^2}{3EI} & \frac{l^2}{6EI} \\ \frac{l^2}{6EI} & \frac{l^2}{3EI} \end{bmatrix} \begin{Bmatrix} M_1 \\ M_2 \end{Bmatrix} \tag{3}$$

**Fig. 3** Schematic diagram of linear element used in 1-D FE modeling





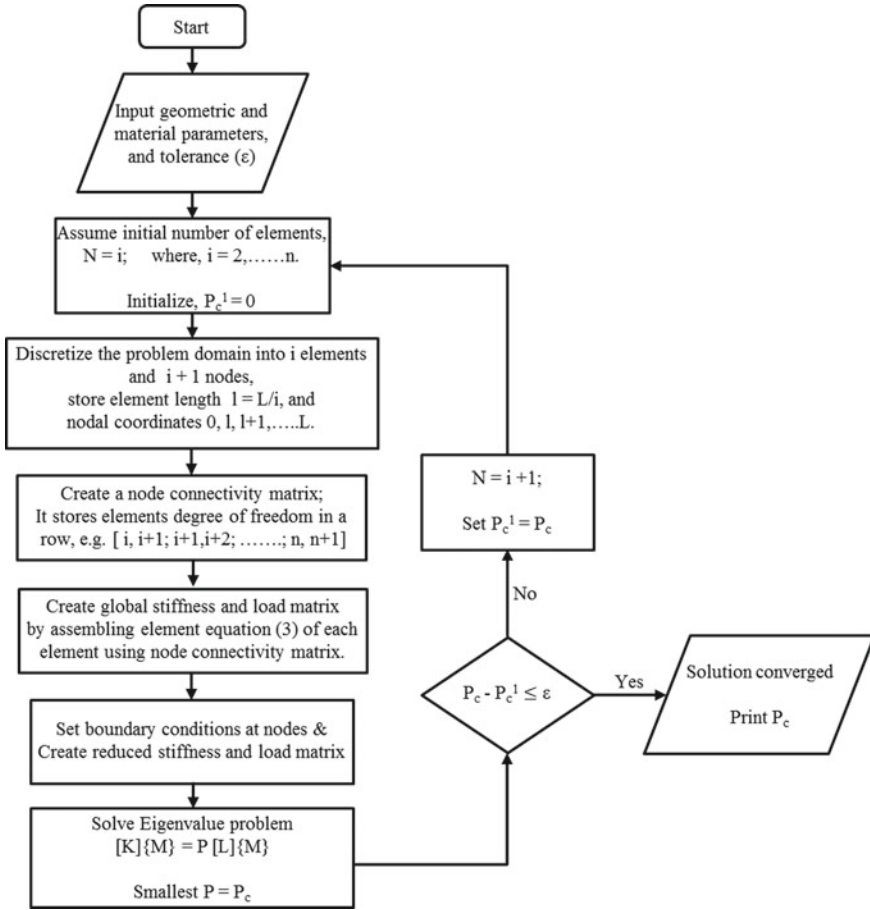
**Fig. 4** Flowchart for 1-D finite element buckling analysis

The value of second moment area ( $I$ ) for an element was considered as an average of the second moment area ( $I$ ) values at element nodes. Where,  $M_1$  and  $M_2$  are respective bending moment values at node 1 and node 2 of the line element having a length equal to  $l$ . Element equations for all the elements were written using Eq. 3 and were combined using node connectivity to obtain a global matrix equation. A reduced global matrix equation was obtained by applying relevant boundary conditions at the given nodes. Considering  $P$  as unknown, the reduced global matrix equation in the eigenvalue problem form was solved to obtain the critical buckling load. A *MATLAB* program was used to implement these steps. The steps followed in *MATLAB* for 1-D finite element-based eigenvalue buckling analysis of pipeline are given in Fig. 4.

After conducting the buckling analysis, it was observed that the pipeline buckles about the Y-axis in the X–Z plane at the critical buckling load of 50.472 kN. The critical buckling occurs about the Y-axis due to the fact that the maximum  $I$  value of the pipe section about the Y-axis [ $I_Y = 8787.6 \text{ mm}^4$ ] is less than the  $I$  value of the pipe section about the X-axis [ $I_X = 17,618.8 \text{ mm}^4$ ]. The solution converges to critical buckling load as the number of elements increases for mode 1 is shown below in Fig. 5.

### 4 3-D Finite Element Modeling Using ANSYS

The 3-D finite element model of pipe was modeled and analyzed with aid of *ANSYS workbench*. First, the static structural module was used to analyze the pipeline model, then linked with the Eigen buckling analysis module. The Eigen buckling module



**Fig. 5** Convergence pattern of the critical buckling load with increment in number of elements

solves the eigenvalue problem using perturbation techniques to give a load multiplier (Eigen value) and different possible buckling modes. The critical buckling load equals the load multiplier times the loading used in static structural analysis.

The 3-D geometry of the non-prismatic model used in 3-D simulation using ANSYS is shown in Fig. 6. It was drawn using Space-claim, CAD software integrated with ANSYS. Solid 187 elements (Fig. 7a) were used for modeling and meshing of pipeline model. Solid 187 is a 10-noded higher order 3-D element, with each node having 3 degrees of freedom (displacements in the x, y, and z directions) [6].

A total of 12,829 elements and 24,914 nodes were generated in the pipeline model using automatic and program-controlled meshing (Fig. 7b). The element size used for pipeline meshing is 5 mm. Boundary conditions considered in simulations were displacement and loading boundary conditions on the left (loading end) and right faces (far end) of the pipeline model (reference Fig. 3).

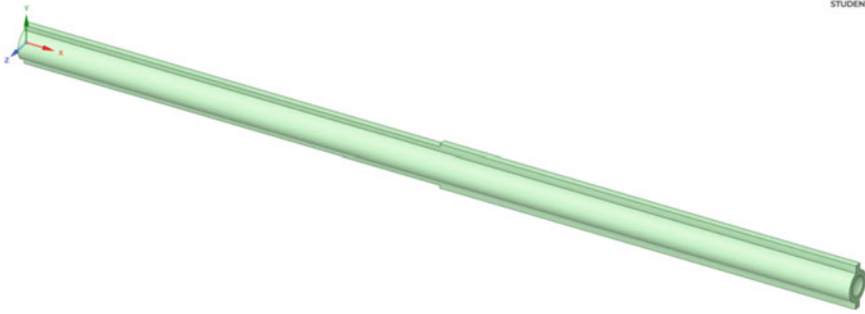


Fig. 6 Geometry of non-prismatic pipeline model used in ANSYS simulation

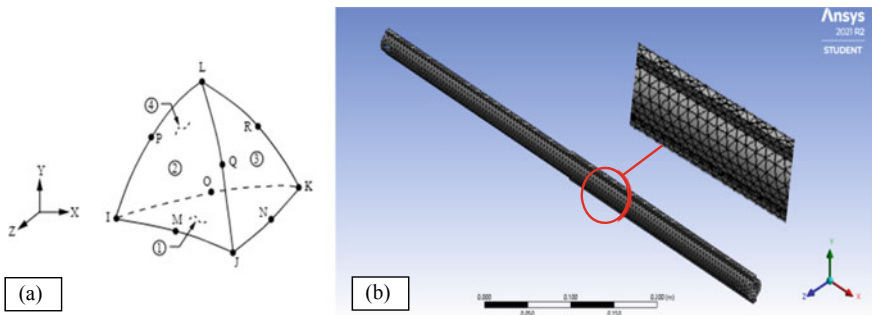


Fig. 7 a Solid 187 element; b solid meshing of 3-D pipeline model in ANSYS

The left face displacement boundary condition considers  $u \neq 0, v = 0, w = 0$ , and a remote displacement boundary condition considers  $u = 0, v = 0, w = 0, \theta_x \neq 0, \theta_y \neq 0, \theta_z \neq 0$  at right face. Where,  $u, v$ , and  $w$  are translations in the  $x, y$ , and  $z$  directions, and  $\theta_x, \theta_y$ , and  $\theta_z$  are rotations about  $x, y$ , and  $z$  directions, respectively. On the left face, a compressive loading of 1 N was applied as loading boundary condition. After the eigenvalue buckling analysis, two modes of buckling were observed (Fig. 8).

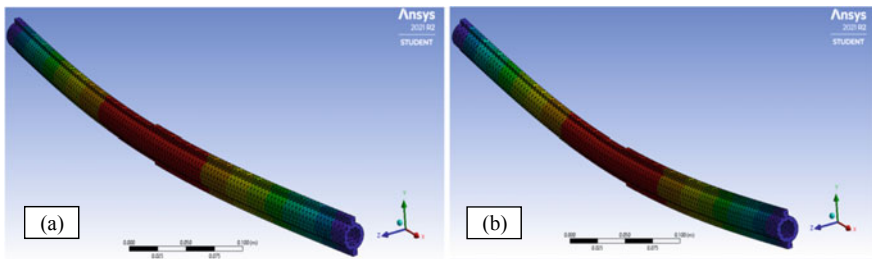


Fig. 8 Buckling of pipeline model. a Mode 1; b Mode 2

In the first mode, the pipeline buckles about the Y-axis at a critical buckling load of 50.211 kN, and in the second mode, it buckles about the Z-axis at a buckling load of about 86.326 kN. It shows that the given non-prismatic pipelines are more prone to buckle in the lateral direction ( $X-Z$  plane) due to the least  $I$  value about Y-axis.

## 5 Buckling Experiment on Pipeline Model

### 5.1 Buckling Experiment and Results

The non-prismatic pipe specimen fabricated for the buckling experiment is given below in Fig. 9a. It was fabricated using mild steel metal strips (dimensions:  $l = 300$  mm,  $b = 5$  mm,  $d = 5$  mm and  $l = 300$  mm,  $b = 5$  mm,  $d = 3$  mm) and a pipe section (outer diameter: 21.58 mm, internal diameter: 14.14 mm) of 300 mm length. The buckling test was conducted on the pipe specimen using the buckling set-up shown in Fig. 10. The buckling set-up comprises of *UTM* machine of 400 kN capacity for compressive load application, a specimen holder, and dial gauges of 0.01 mm accuracy for deflection measurement in the lateral direction. The pipe specimen was held straight in the compression space of the *UTM* machine between the holders fixed with upper and lower end blocks. The experiment started with the movement of the lower end block, which physically simulates a pinned–pinned column subjected to compressive loading, and by measuring the lateral deflection using dial gauges for each load step of 0.5 kN. During the experiment, when the deformation in the specimen reaches the plastic stage, after a point in time, a sudden decrease in load with large deformation was observed at 56 kN load.

The Double tangent method was used to obtain the critical buckling load from experimental load versus lateral deflection data. In double tangent method, two tangents are drawn, one tangent to elastic part of the load–deflection curve and other to the plastic part of the curve [5, 7]. The ordinate of the point at which these tangents intersect is equal to the value of critical buckling load. The double tangent method provided a critical buckling load of 50.02 kN (Fig. 11).

The critical buckling load obtained from the double tangent method is the experimental critical buckling load and was used for error calculation.



**Fig. 9** Non-prismatic pipe specimen. **a** before buckling experiment; **b** after buckling experiment



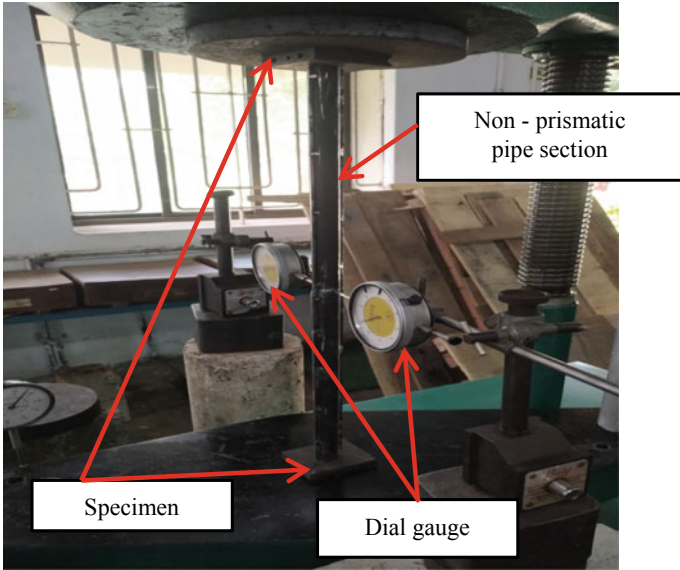


Fig. 10 Experimental arrangement used for buckling experiment

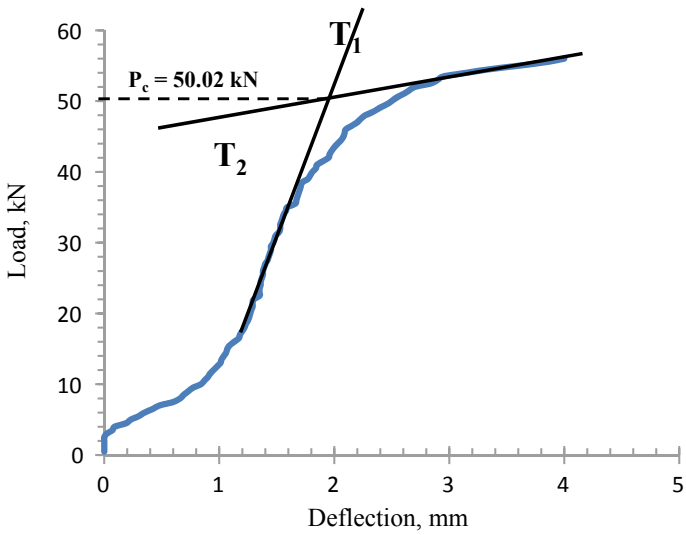


Fig. 11 Load versus deflection curve and double tangent method

**Table 2** Experimentally and numerically estimated critical buckling load

S.No	Models	Critical buckling load P <sub>c</sub> (kN)	Absolute error (%)
1	Double tangent method	50.02	–
2	1-D finite element model	50.47	0.90
3	3-D finite element model	50.21	0.34

## 5.2 Comparisons of 1-D, 3-D Finite Element Analysis Results with Experimental Results

The experimentally obtained critical buckling load (ECB) and numerically obtained critical buckling load (NCB) for the given pipeline model are presented in Table 2. Equation 4 was used to calculate the absolute error in used in Table 2.

$$\text{Absolute error} = \left| \frac{ECB - NCB}{ECB} \right| \times 100. \quad (4)$$

## 6 Conclusions

The buckling behavior of non-prismatic pipeline model was studied numerically and experimentally. 1-D and 3-D finite element model was validated by conducting experimental work on the pipeline model. Buckling results obtained from 1-D and 3-D numerical models comparatively showed a negligible error. The numerically and experimentally obtained critical buckling load shows a similar trend showing an error of about 1%. The present analysis shows that a finite element-based 1-D and 3-D can be a reliable and economical tool for accurately accessing the critical buckling load of non-prismatic pipeline components subjected to axial compressive load.

**Acknowledgements** We are very grateful to the funding agency, AR & DB, Ministry of Defense, file number ARDB/01/2031964/MI for providing financial assistance for conducting our research work.

## References

1. Guo B, song S, Ghalambor A, Lin TR (2014) Offshore pipelines, 2nd edn. Elsevier Inc.
2. Bai Q, Bai Y (2014) Subsea pipeline design, analysis, and installation. Elsevier Inc.
3. Hobbs RE (1984) In-service buckling of heated pipes. J Trans Eng 110:175–188

4. Bhatti MA (2005) *Fundamental finite element analysis and applications: with Mathematica and Matlab computations*. Wiley, New Jersey
5. Tuttle M, Singhatanadgid P, Hinds G (1999) Buckling of composite panels subjected to biaxial loading. *J Exp Mech* 39(3):191–201
6. ANSYS Help System (2009) *Analysis guide and theory reference Ver 12:0*
7. Rao NR, Kaliveeran V (2020) Finite element modeling and experimental validation of rectangular pin buckle arrestors for offshore pipelines. *Mech Based Des Struct Mach*
8. Karampour H, Albermani F, Gross J (2013) On lateral and upheaval buckling of subsea pipelines. *J Eng Struct* 52:317–330
9. Vazouras P, Tsatsis A, Dakoulas P (2021) Thermal upheaval buckling of buried pipelines: experimental behaviour and numerical modelling. *J Pipe Syst Eng Prac ASCE* 12(1):04020057(1–20)

# 2D and 3D Numerical Investigation of Delrin Spur Gear



A. P. Sugunesh and A. Johnney Mertens

**Abstract** Delrin gears are used in light and medium-duty engineering applications. Such gears are subjected to Hertzian contact stress due to the non-conformal contact nature. The contact stress is majorly influenced by the directional stresses ( $\sigma_x$ ,  $\sigma_y$ , and  $\tau_{xy}$ ) during their engagement and also significantly affected by the face width of the gear. ANSYS is one of the widely used Finite Element Analysis (FEA) tool to determine the behaviour of contact stress of those gears. Even though numerous 2D and 3D FEA investigations were performed to determine the gear contact stress behaviour, the occurrence of surface and subsurface stresses was not explored especially for Delrin gears. Thus, the work attempted to study the surface and subsurface contact stress of the 2D (plane stress with 1 mm thickness condition) and 3D gear pair using ANSYS APDL. The optimum mesh sizes were selected from the convergence study, and further simulations were performed. From the analysis, the maximum stress was observed at the contact surface for 2D analysis, whereas, 3D analysis showed the maximum stress at a depth of 0.12 mm below the contact surface (subsurface stress). Almost similar trend was observed for the X-directional normalized stresses, whereas Y and XY-directional normalized stresses showed a deviation of 27 and 45% respectively during the 2D and 3D gear pair analysis. The variation in contact stresses along the different consecutive face-width planes causes the Y and XY-directional stress deviations.

**Keywords** Contact stress · FEA · DELRIN gear · Surface stress · Subsurface stress

---

A. P. Sugunesh · A. J. Mertens (✉)

Department of Mechanical Engineering, National Institute of Technology Puducherry, Karaikal, India

e-mail: [johnney.m@nitpy.ac.in](mailto:johnney.m@nitpy.ac.in)

## 1 Introduction

Polymer gears are significantly used in power transmission applications owing to the facts of self-lubricating properties; noiseless operation; high strength-to-weight ratio; and cost-effectiveness [1]. Among the available polymer groups, Delrin is the most widely utilized gear materials in many engineering applications such as the automotive industry, office machines, food and textile machinery [2]. But low mechanical and thermal characteristics limit its usage in light and medium-duty applications.

Delrin gears are undergone major failures such as pitting [3], tooth root crack [4], excessive wear [5], and, plastic deformation [6]. During the engagement, the repetitive cyclic tooth contact stress plays a vital role in determining the durability of Delrin gears and is responsible for the above-mentioned failures. The contact stress behaviour of the polymer gears was affected by the face width of the gear [7]. Finite Element Analysis (FEA) has been effectively used to determine the contact stress behaviour of polymer gear pair for different face widths where the analytical or experimentation cannot be performed [8]. Wang and Howard [9] investigated the contact stress behaviour of 2D and 3D gear models using finite element analysis. Contact stresses were obtained for various face widths of gear under plane stress, plane strain, and 3D analysis. Wang and Howard [10] also explored the contact stress of a high contact ratio spur gears under 2D plane stress condition by using FEA (ANSYS APDL) and the stress was observed maximum at the contact surface. Hwang [11] also analyzed the contact stress of spur gears using 2D FEA and found the maximum stress at the contact pitch point. Zorko et al. [12] numerically investigated a polyether ether ketone (PEEK) against steel spur gear pair using the ANSYS 17.2. All 2D simulations were performed on the middle teeth under plane stress condition with five-teeth gear geometry. Karimpour et al. [13] analyzed the performance of Delrin spur gear by utilizing ABAQUS FEA tool and maximum stress was obtained on the surface of the gear profile. Vijayarangan and Ganesan [14] examined the contact stress analysis of a spur gear by means of 2D FEA under plane stress condition, in which the contact stress was observed maximum at the contact surface.

Very fewer investigations were carried out on 3D gear contact stress analysis due to high computational time and lower efficiency. Qin and Guan [15] numerically investigated the three-dimensional distribution of contact stress. Maximum stress was observed on the spur gears beneath the contact (subsurface stress). Patil et al. [16] calculated the contact stresses of 3D spur gear using finite element method (FEM). A variation in the maximum contact stress was observed along the consecutive face-width planes of the gear model. Mapper et al. [17] analyzed the influence of tip relief on the stress behaviour on a spur gear pair using 3D FEA (SOLID 185 element) software ANSYS. The maximum contact stress distribution was detected beneath the contact area at subsurface.

From the literature survey, it was understood that a notable number of numerical investigations were performed to interpret the contact stress behaviour of polymer gear under 2D (plane stress) and 3D FEA conditions. For all the 2D FE analysis, the

maximum contact stress occurred at the contact point. Contrarily, subsurface stress (a depth beneath the contact point) was observed during the 3D FE analysis. The occurrence of such phenomena (surface and subsurface stress) was not extensively explored for Delrin gear. Thus, the current work attempts to explore the contact stress behaviour of a Delrin gear pair under 2D (plane stress) and 3D FEA analysis. The occurrence of maximum contact stress for different planes along the face width was explored using a 3D FE analysis and compared with a 2D FE analysis.

## 2 Methodology

Finite element analysis (FEA) is performed in this work using ANSYS 2019 R1, to explore the contact stress behaviour of polymer gear pair. Delrin was chosen as a polymer material for both gear and pinion and the material properties were mentioned in Table 1.

For both 2D and 3D FE analysis, a single tooth gear profile geometry was used in order to reduce the computational time. The gear profile was designed as per the parameters given in Table 2 and imported to ANSYS through IGES format. During FEM modelling, the following assumptions were assumed:

- Static condition was assumed for all the analysis.
- The material properties were presumed as linearly elastic, homogenous, and isotropic.
- Analysis was performed within the elastic limit.
- The load distribution was assumed to be uniform along the gear and pinion hub.
- The friction coefficient of the gear contact was assumed to be zero.

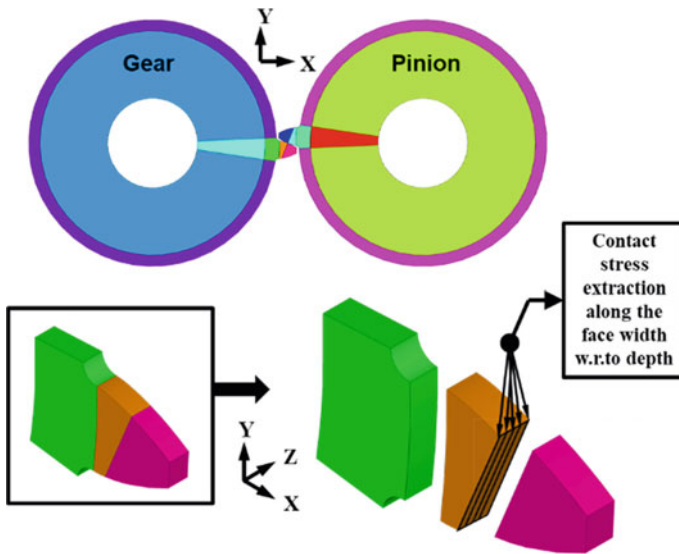
For a 2D FEA analysis, PLANE 183 was selected and line-to-line contact was generated between the gear pair. Surface-to-surface contact was formed between the gear pair. To create the mapped mesh on the gear profile, the gear was partitioned into number of divisions as shown in Fig. 1. The contact and fillet regions were finely

**Table 1** Gear and pinion material properties [13]

Material	Elastic modulus	Poisson’s ratio	Elastic limit
Delrin	3100 MPa	0.35	50 MPa

**Table 2** Parameters of Gear and Pinion

Parameters	Gear and Pinion
Pressure angle	20 <sup>0</sup>
Module	2 mm
Pitch circle diameter	60 mm
Face width	1 mm



**Fig. 1** Gear area partition and slicing of gear tooth for data extraction

meshed whereas, the other regions of the gear were coarsely meshed, and the gear parameters were listed in Table 2.

To obtain an optimum mesh size, convergence study was carried out and a number of trials were performed out for both 2D (plane stress) and 3D. The obtained contact stress values were compared with theoretically calculated values. The optimum mesh size was selected from the convergence study and used for further analysis.

During the 2D FE analysis, the element size was differed from 0.5–0.01 mm at contact, 0.1 mm at fillet, and 0.5 mm at other regions. Whereas, 3D FE analysis consists of the following mesh sizes: 0.25–0.02 mm at contact; 0.1 mm at fillet region; 0.5 mm at other regions; 2–100 divisions along face width. All DOF were constrained on the hub of the gear for both 2D and 3D. Only UX was constrained for 2D and UX, UZ were constrained for 3D on the pinion hub to avoid the movements in their respective directions. As shown in Fig. 2, a 50 N load was applied on the pinion hub along the rotational ( $\theta$ ) direction. After implementing the above boundary conditions, the solution was obtained and a convergence graph was plotted for the obtained maximum contact stress with respect to number of elements. The Corresponding 2D and 3D convergence study for Delrin gear pair as shown in Fig. 3.

An optimal element size of 0.02 mm at contact, 0.1 mm at fillet, and 0.5 mm at other regions for 2D FEA analysis was obtained from the convergence study. Similarly, 0.05 mm at contact, 0.1 mm at fillet, 0.5 mm at other regions, and 17 divisions along the face width of the gear were selected for 3D FEA analysis. A similar convergence study trend was also reported by Sugunesh and AJ Mertens [18].

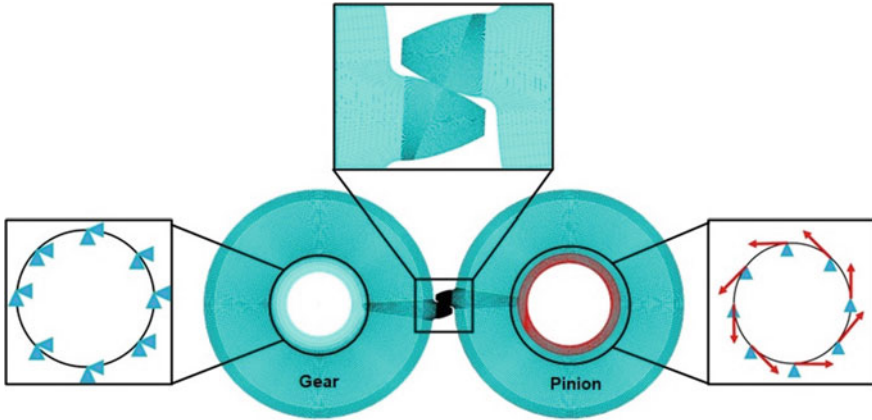
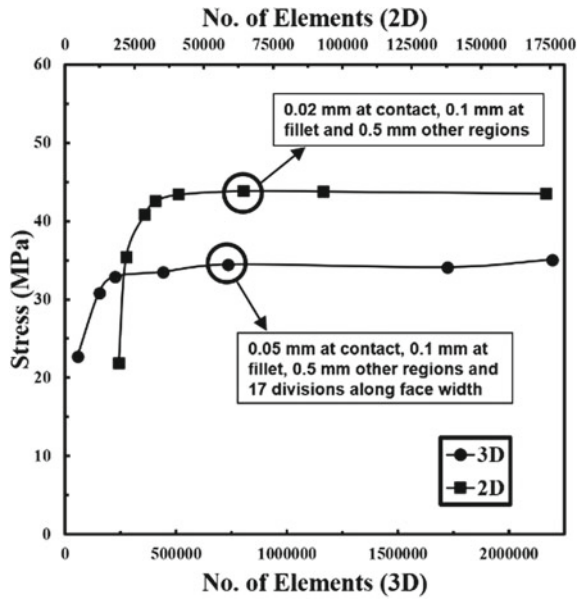


Fig. 2 FE model with mesh and boundary condition

Fig. 3 2D and 3D FEA convergence plot



### 3 Results and Discussion

#### 3.1 Theoretical Contact Stress Calculation

$$\sigma_c = \frac{4F}{\pi BL} \tag{1}$$



$$B = \sqrt{\frac{8F}{\pi L} \times \left[ \frac{\left(\frac{1-\nu_1^2}{E_1}\right) + \left(\frac{1-\nu_2^2}{E_2}\right)}{\left(\frac{1}{D_1}\right) + \left(\frac{1}{D_2}\right)} \right]} \tag{2}$$

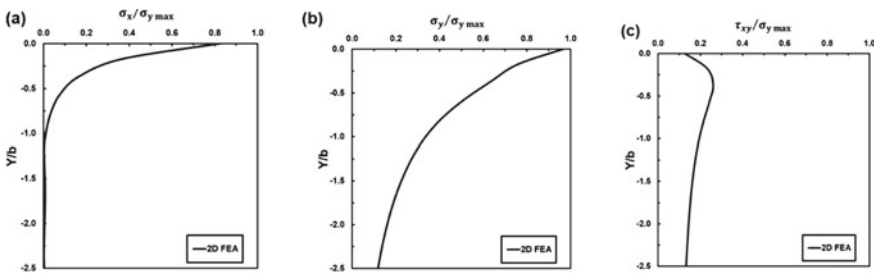
The contact stress ( $\sigma_c$ ) was determined using the Hertzian contact stress Eq. (1). Where F is the force applied in Newton (50 N); L is the gear face width in mm (1 mm); B denotes the width of contact (mm), which is predicted from Eq. (2);  $E_1, E_2$  are the Elastic modulus in N/mm<sup>2</sup> (3100 N/mm<sup>2</sup>);  $\nu_1, \nu_2$  denotes the Poisson’s ratios (0.35);  $D_1, D_2$  are the diameter of the equivalent cylinder of meshing gear tooth in mm (20.52 mm). The maximum contact stress of 44.1174 MPa was obtained for the applied 50 N load.

### 3.2 2D Gear Contact Stresses

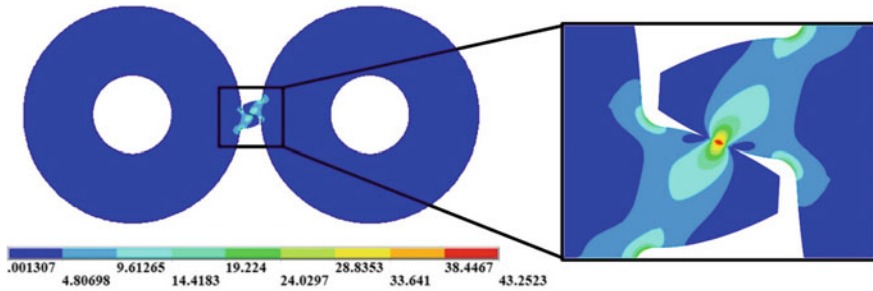
Gear teeth are subjected to normal and shear stresses along X, Y, and Z directions during their engagements. Stress analysis along the respective directions reveals the contact stress behaviour of Delrin gears. The obtained directional stresses were normalized and shown in Fig. 4.

The maximum normalized X-directional stress (Fig. 4a) of 0.8976 was observed at the contact surface followed by a gradual stress decrement up to 0.0012 with a slope rate of 1.9042. And then a steep drop in the stress was observed along the vertical direction. The maximum normalized Y-direction stress was reduced to 0.1250 from 1.0 with respect to tooth depth at a mean slope rate of 7.277. An increase in normalized shear stress (Fig. 4c) was observed from 0.1081 (contact stress) to 0.2607 (0.36 mm depth) with respect to tooth depth and then decreased gradually to 0.1345 with an average slope rate of 31.685.

Figure 5 shows the stress contour of Delrin gear pair for 2D plane stress with 1 mm thickness condition. The stress of 43.2523 MPa was detected maximum at the contact surface and has a good agreement (1.96% error) with the theoretical value.



**Fig. 4** Normalized stress plot for 2D FEA with 1 mm thickness. **a** X-Direction, **b** Y-Direction, and **c** XY-Direction



**Fig. 5.** 2D FEA contour stress plot of Delrin gear with plane stress condition

Karimpour et al. [13] also obtained a similar contact stress pattern at the surface of the gear tooth contact.

### 3.3 3D Gear Contact Stresses

The X, Y, and XY-directional stresses were plotted for different consecutive face-width planes (0, 0.2, 0.4, 0.6, 0.8, and 1 mm) of 1 mm thickness Delrin gear under 3D FE analysis. During the analysis, the variation in the directional stresses was observed for different consecutive face-width planes.

The maximum normalized X-direction average stress (Fig. 6a, b) of 0.8808 was observed at the contact surface followed by a gradual stress decrement up to 0.0087 with an average slope rate of 1.0683. And then a sharp stress decrement was observed along the vertical direction for all the consecutive face-width planes (0, 0.2, 0.4, 0.6, 0.8, and 1 mm). The maximum normalized Y-direction stress (Fig. 6c) was decreased to 0.1802 about the tooth depth with an average slope rate of 6.3928. An increase in normalized shear stress (Fig. 6d) was observed from 0.2917 (contact surface) to 0.5336 (0.22 mm depth) and then decreased slowly with an average slope rate of 15.328. A similar trend along X, Y, and XY-directional stresses was attained by Santos et al. [19] for the railroad wheels application.

The 3D stress contour for 1 mm thickness gear is shown in Fig. 7. The maximum stress of 34.0945 MPa was detected at a depth of 0.12 mm below the contact point. An error percentage of 22.72% was observed for 3D analysis with respect to theoretical contact stress. A similar trend was observed by Qin and Guan [15].

### 3.4 Comparison of 2D Versus 3D Gear Contact Stress

The comparison of gear contact stress behaviour for both 2D and 3D FE analysis is shown in Fig. 8. The 2D FE analysis possessed the maximum stress at the contact

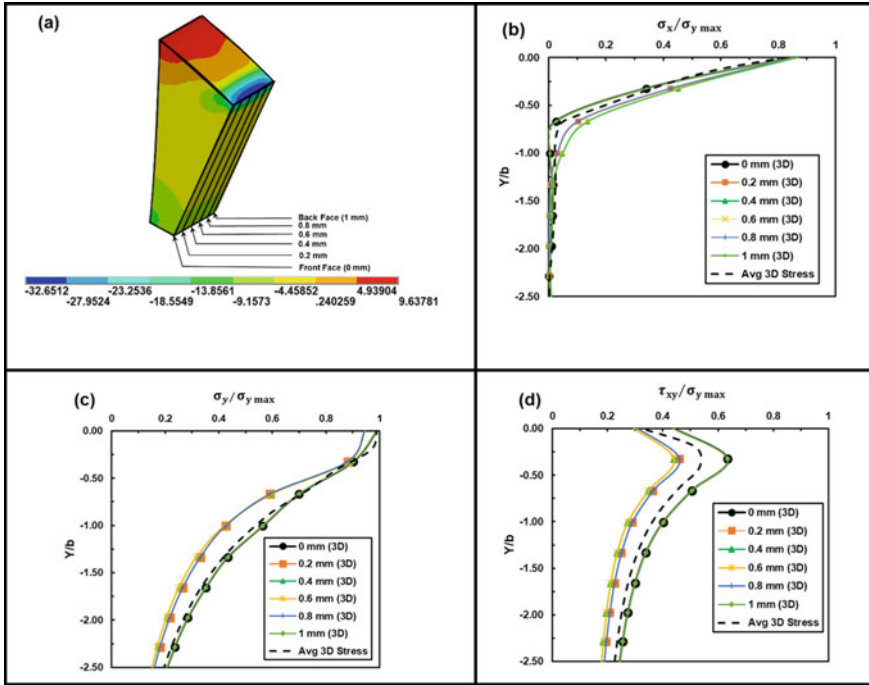


Fig. 6 Normalized stress plot for 3D FEA with 1 mm thickness. a stress contour along X-direction, b X-Direction, c Y-Direction, and d XY-Direction

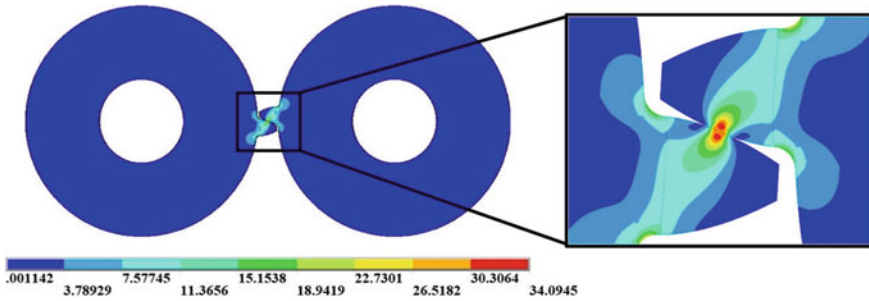
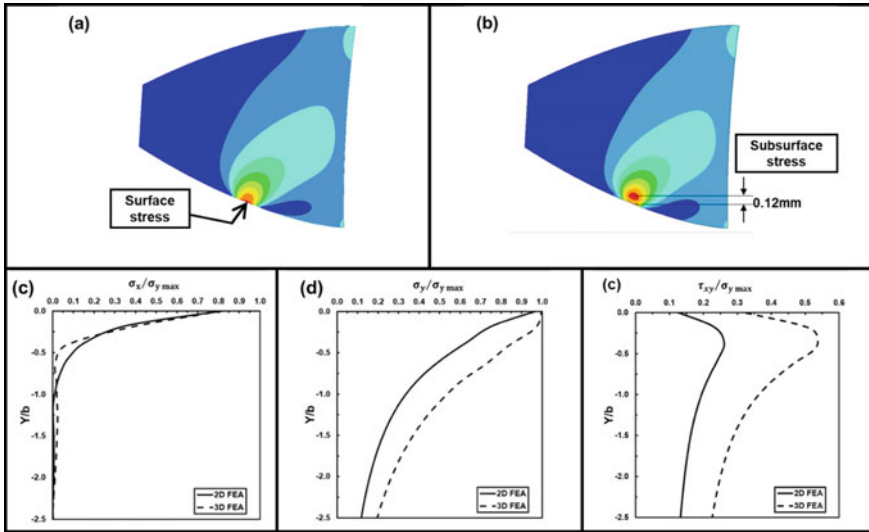


Fig. 7. 3D FEA contour stress plot of Delrin gear with 1 mm thickness

point as shown in Fig. 8a, whereas, 3D FE analysis showed the maximum stress at a depth of 0.12 mm below the contact point (subsurface stress) as shown in Fig. 8b.

The normalized X-direction stress values and trend are almost similar for both 2D and 3D analysis. However, the Y and XY-direction stresses followed a similar trend, but the values are deviated at a percentage of 27 and 45% (Fig. 8c–e).



**Fig. 8** Contact stress contour of **a** 2D Delrin gear, **b** 3D Delrin gear, 2D and average 3D normalized stress plot along, **c** X-direction, **d** Y-direction and **e** XY-direction

### 4 Conclusion

In this present work, both 2D and 3D FE analysis were used to explore the contact stress behaviour of Delrin gear for the tooth thickness of 1 mm and based on the analysis, conclusions were made as follows:

- The stress of 43.2523 MPa was obtained maximum for 2D analysis whereas, 34.0945 MPa was obtained for 3D analysis.
- Surface stress was detected in the 2D FEA analysis, whereas subsurface stress was found in the 3D analysis.
- An almost similar trend was observed between the normalized stress plot of both 2D and 3D FEA along the X-Direction. But a deviation of 27 and 45% normalized stresses along Y and XY-Direction were observed for both 2D and 3D analysis.
- Variation in the maximum contact stress was observed for different consecutive face-width planes of 3D Delrin gear and needs further exploration for other polymer gears.

## References

1. Mao K, Li W, Hooke CJ, Walton D (2009) Friction and wear behaviour of acetal and nylon gears. *Wear* 267(1–4):639–645. <https://doi.org/10.1016/j.wear.2008.10.005>
2. Mehat NM, Kamaruddin S, Othman AR (2012) A study of hybrid optimization of injection moulding process parameters for plastic gear. *Adv Mater Res* 591–593:2135–2138. <https://doi.org/10.4028/www.scientific.net/AMR.591-593.2135>
3. Bharti S, Selvaraj S (2019) Effects of lubricant on the surface durability of an injection molded polyamide 66 spur gear paired with a steel gear. *Tribol Int.* <https://doi.org/10.1016/j.triboint.2019.02.050>
4. Pandian AK, Gautam SS, Senthilvelan S (2020) Experimental and numerical investigation of the bending fatigue performance of symmetric and asymmetric polymer gears. *Proc Inst Mech Eng Part L J Mater Des Appl* 234(6):819–834. <https://doi.org/10.1177/1464420720909486>
5. Mertens AJ, Kodeeswaran M, Senthilvelan S (2016) Injection molded asymmetric spur gear tooth deflection: Numerical and Experimental investigation. In: *Proceedings of SPE ANTEC™ plastic technologies conferences Indianap*, pp 23–25
6. Senthilvelan S, Gnanamoorthy R (2004) Damage mechanisms in injection molded unreinforced, glass and carbon reinforced nylon 66 spur gears. *Appl Compos Mater* 11(6):377–397. <https://doi.org/10.1023/B:ACMA.0000045313.47841.4e>
7. Imrek H, Düzcükoğlu H (2007) Relation between wear and tooth width modification in spur gears. *Wear* 262(3–4):390–394. <https://doi.org/10.1016/j.wear.2006.06.004>
8. Mao K (2006) An approach for powertrain gear transmission error prediction using the non-linear finite element method. *Proc Inst Mech Eng Part D J Automob Eng* 220(10):1455–1463. <https://doi.org/10.1243/09544070JAUTO251>
9. Wang JD, Howard IM (2006) Error analysis on finite element modeling of involute spur gears. *J Mech Des Trans ASME* 128(1):90–97. <https://doi.org/10.1115/1.2114891>
10. Wang J, Howard I (2005) Finite element analysis of High Contact Ratio spur gears in mesh. *J Tribol* 127(3):469–483. <https://doi.org/10.1115/1.1843154>
11. Hwang SC, Lee JH, Lee DH, Han SH, Lee KH (2013) Contact stress analysis for a pair of mating gears. *Math Comput Model* 57(1–2):40–49. <https://doi.org/10.1016/j.mcm.2011.06.055>
12. Zorko D, Kulovec S, Duhovnik J, Tavčar J (2019) Durability and design parameters of a Steel/PEEK gear pair. *Mech Mach Theory* 140:825–846. <https://doi.org/10.1016/j.mechmachtheory.2019.07.001>
13. Karimpour M, Dearn KD, Walton D (2010) A kinematic analysis of meshing polymer gear teeth. *Proc Inst Mech Eng Part L J Mater Des Appl* 224(3):101–115. <https://doi.org/10.1243/14644207JMDA315>
14. Vijayarangan S, Ganesan N (1994) Static contact stress analysis of a spur gear tooth using the finite element method, including frictional effects. *Comput Struct* 51(6):765–770. [https://doi.org/10.1016/S0045-7949\(05\)80016-1](https://doi.org/10.1016/S0045-7949(05)80016-1)
15. Qin WJ, Guan CY (2014) An investigation of contact stresses and crack initiation in spur gears based on finite element dynamics analysis. *Int J Mech Sci* 83:96–103. <https://doi.org/10.1016/j.ijmecsci.2014.03.035>
16. Patil SS, Karuppanan S, Atanasovska I (2015) Contact stress evaluation of involute gear pairs, including the effects of friction and helix angle. *J Tribol* 137(4):1–5. <https://doi.org/10.1115/1.4030242>
17. Maper A, Karuppanan S, Patil SS (2019) Analysis and formulation of spur gear stresses with different tip modifications. *J Cent South Univ* 26(9):2368–2378. <https://doi.org/10.1007/s11771-019-4180-x>
18. Sugunesh AP, Mertens AJ (2020) 2D FEA study of Hertzian contact stress between two cylindrical bodies. *Mater Today Proc* 44:4474–4478. <https://doi.org/10.1016/j.matpr.2020.10.721>
19. Santos FDC, Dos Santos AA, Bruni F, Santos LT (2004) Evaluation of subsurface contact stresses in railroad wheels using an elastic half-space model. *J Brazilian Soc Mech Sci Eng* 26(4):420–429. <https://doi.org/10.1590/S1678-58782004000400007>

# Study of Solid Particle Erosion Behaviour of Uncoated Superalloys of Turbine Application



M. S. Vinod Kumar, R. Suresh, N. Jagadeeswaran, and BSKeerthi gowda

**Abstract** Superalloys such as Ti-31 and Superalloy-605 are extensively used material for gas-turbine component. Most of these gas-turbine components such as compressors, blades and vanes work under very high temperature condition. The residue results after combustion of fuel consists of solid particles such as coal ash and unburned carbon particle. These solid particles travelling at very high speed when hit the component lead to the erosion wear. The damage caused to the component due to erosion wear has significant effect on the service life of the component. Thus, in present investigation effort has been made to conduct solid particle erosion wear test on Ti-31 and Superalloy-605 superalloys. The test was conducted as per ASTM G76 standard with the help of Air jet Erosion test rig. The test was performed at an air pressure of 1 Bar at different impact angles of 30°, 60°, and 90°. Steady state volumetric rate of erosion is calculated to analyse the erosion under different impact angles. Further, micrograph of eroded surface was taken using scanning electron microscope to analyse the mechanism of material removal. From the result, it was observed that loss of material is higher in Superalloy-605 in comparison to Ti-31 superalloy. Micrograph reveals that in case of Superalloy-605, the material removal takes place mainly through brittle fracture whereas ductile mode of erosion was observed in case of Ti-31 superalloy.

**Keywords** Superalloy-605 · Ti-31 · Superalloy · Erosion · Scanning electron microscope · XRD

---

M. S. Vinod Kumar (✉) · R. Suresh · B. gowda  
VTU Centre for PG Studies, Mysore, Karnataka, India  
e-mail: [vinodms@vtu.ac.in](mailto:vinodms@vtu.ac.in)

N. Jagadeeswaran  
REVA University, Bangalore, Karnataka, India

## 1 Introduction

Solid particle erosion has been reported as the cause of material degradation in many mechanical systems, such as aircraft gas turbines, thermal power plants, industrial waste incinerators, and many others [1], and superalloys have been found to be a better option for the components of mechanical systems that will be exposed to severe material degradation conditions, as it has been a major concern in recent research topics. From the observations made in the literature, there are mainly two categories of erosion mechanisms, namely brittle and ductile erosion, and they are further classified as deformation mechanisms and cutting mechanisms [2–4]. Under oblique impact conditions, the cutting mechanism is the most effective mode of erosion, whereas, under normal impact conditions, the deformation mechanism is the major cause of the erosion [5]. The effectiveness of each of the mechanisms is directly proportional to the tangential and normal components of the impact energy of the erodent, which also depends on the angle of impact [6]. Many parts of the turbine are likely to be subjected to intense mechanical and thermal loads; they will also be exposed to erosion. Hence, for a single material, it would be tough to cope with the desired properties. Hence, composite material is the best solution for satisfying demanding requirements [7–10]. Prashanth Kumar Singh et al. used a detonation gun spray technique to coat SAE213-T1<sub>2</sub> boiler steel with WC-12CO, Stellite 21, and Stellite 6 coatings, and then tested them for solid particle erosion. The cobalt component of the coating was revealed to play a significant influence in erosion resistance, with Stellite 21 and Stellite 6 coatings exhibiting 50 to 60% greater erosion resistance than WC-Co [1].

Aravind Nagaraj et al. [11] reported studies on solid particle erosion of the nickel-based superalloy CY5SnBiM at particle velocities of 59, 92, and 124 m/s and at four different angles of impact, namely 30°, 45°, 60°, and 90°. The results show that the mode of erosion is ductile, with deep pits and craters formed by rebounding erodent particles at higher angles of impact. Mustafa Kaplan et al. [12] in an investigation reported the erosion behaviour of Inconel718 superalloy using two different coatings: CoNiCrAlY and ZrO<sub>2</sub> + 8% Y<sub>2</sub>O<sub>3</sub>. Following the air jet erosion test, it was discovered that the largest erosion rate occurred at a 60° impact angle, indicating a semi-ductile/semi-brittle mode of erosion. Mayank Patel et al. [13] reported solid particle erosion investigations of boiler tube steel SS304 at room temperature with alumina of size 50 m, impact velocity of 40 m/s, and impact angles of 30° and 90°. And results indicate the erosion rate is higher at 30° angle of impact than at 90° confirming the ductile mode of erosion. SB Mishra et al. [14] in a study employed three types of coatings on Nickel based superalloys in their study: NiCrAlY, Ni-20Cr, and Ni3Al, and subjected them to solid particle erosion tests. The results showed that the coating Ni3Al had the lowest rate of erosion at 30° and 90° angles of impact. The coating Ni-20Cr has the highest rate of erosion.

Shibe et al. [15] investigated the erosion properties of three distinct coating types, including WC-12%CO, Cr<sub>3</sub>C<sub>2</sub>-25%NiCr, and Al<sub>2</sub>O<sub>3</sub>-13%TiO<sub>2</sub>, on ASTM36 steel and uncoated ASTM36 steel, and found that all three types of coatings were effective

**Table 1** Chemical composition of material

Material	% Composition										
	Ni	Fe	C	Ti	Cr	V	Al	Sn	Co	Si	Mn
Superco -605	10	3	0.08	–	20	–	–	–	Bal	0.3	1.5
Ti-31	0.3	–	–	Bal	0.1	4.5	6.75	0.1	–	–	–

in protecting the base metal from solid particle erosion at 45° impact angles, while WC-12%CO, Cr<sub>3</sub>C<sub>2</sub>-25%NiCr coatings were effective in protecting the substrate. Sidhu et al. [16] investigated the erosion behaviour of bare and HVOF spray coated boiler tube steel (GrA1) at 250 °C and results indicate that the coating's hardness is better than bare steel, and that the coating's material loss is greater than uncoated boiler tube steel. Pauzi et al. [17] reported the wear effects in hot-gas-path components and different hard face coatings are discussed in depth. Wear is identified as a major issue in gas-turbine hot-gas-path components. Erosion-resistant coatings, especially on turbine blades, may extend the life of hot-gas-path components. In the present work, an attempt has been made to compare and evaluate the solid particle erosion behaviour of special alloy Ti-31 and Superco-605 superalloy.

## 2 Experimental Details

### 2.1 Superalloy Materials

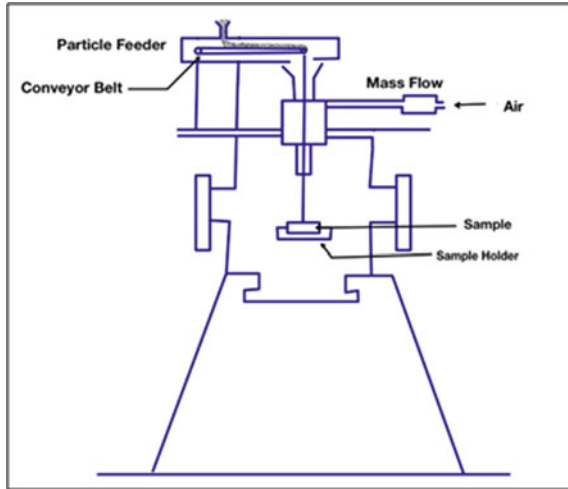
In present experimental work, Superco-605 (a cobalt based superalloy, ASTM B338 grade 5) and Ti-31 (ASTM 9009) superalloy are chosen as the workpiece material. The material was procured from Mishra Dhatu Nigam Limited (MIDHANI), Hyderabad, India. The material is selected due to its extensive application in the manufacturing of turbine components which demands a very high resistance to erosion wear. The chemical composition of the material is given in Table 1. The material was cut in the dimension of 25mmW × 5mmH × 25 mmL to perform the experiment.

### 2.2 Solid Particle Erosion Test

The erosion test is carried out as per ASTM G76 standard with the help of Air jet Erosion rig shown in Fig. 1. The process parameter used to perform the test is listed in Table 2. To start, the sample is first cleaned using acetone to remove any dirt and dust. Using an electronic weight balance (accuracy: 0.001gm), the sample's initial weight is recorded. The sample is then located in the test rig's sample holder. The erosion test is performed at different impact angles 30°, 60°, and 90° with constant particle velocity of 40 m/s. The pressure of air jet was maintained to 1 bar throughout



**Fig. 1** Schematic diagram of air jet erosion test setup



**Table 2** Process parameter for erosion test

Erodent	Particle size ( $\mu\text{m}$ )	Temperature (in $^{\circ}\text{C}$ )	feed rate of sand (g/min)	angle of impingement (in $^{\circ}\text{C}$ )	Nozzle diameter (mm)	Velocity of sand particles (m/s)	SOD (mm)
Silica sand	150	30	5	$30^{\circ}$ , $60^{\circ}$ , and $90^{\circ}$	4.5	40	10

the test. After each cycle of operation, the weight loss and cumulative weight are recorded. This procedure is repeated until the erosion rate reaches to a steady state. From the recorded data, the following formulas are used to compute erosion rate and steady state volumetric erosion rate.

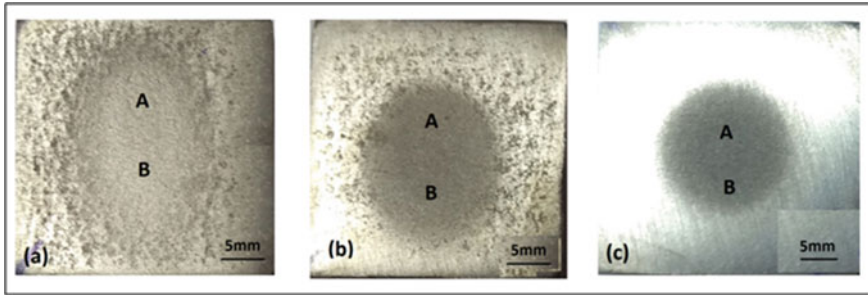
$$\text{Erosion rate (g/g)} = \frac{\text{Cumulative weight loss of sample}}{\text{Mass of erodent}}$$

$$\text{Steady state volumetric rate of erosion (cm}^3\text{/g)} = \frac{\text{Average of erosion rate}}{\text{Density}}$$

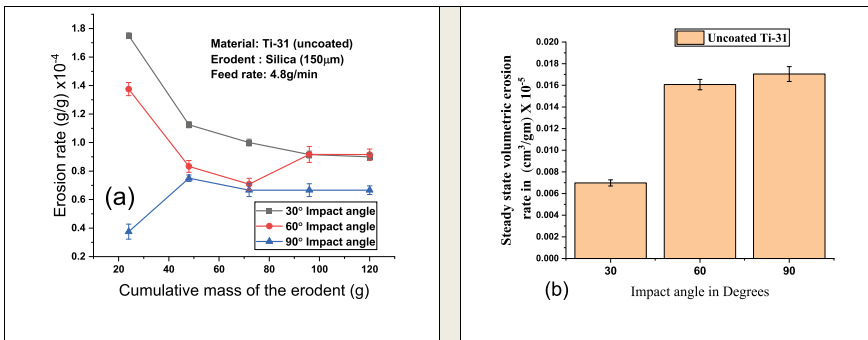
### 3 Results and Discussion

#### 3.1 Studies of Erosion Mechanism of Ti-31

Figure 2 shows an optical micrograph of the scar formed by erosion of a Ti-31 sample at various impact angles. The enclosed region of the micrograph depicts the material loss on account of erosion which is immediately followed by elastically loaded material zone. Figure 2 shows the erosion rate and steady state volumetric erosion rate graphs. Figure 2a shows an increasing erosion rate at a  $30^{\circ}$  impact angle



**Fig. 2** Images of scar developed due to erosion on Ti-31 sample at **a** 30° angle of impact, **b** 60° angle of impact, **c** 90° angle of Impact

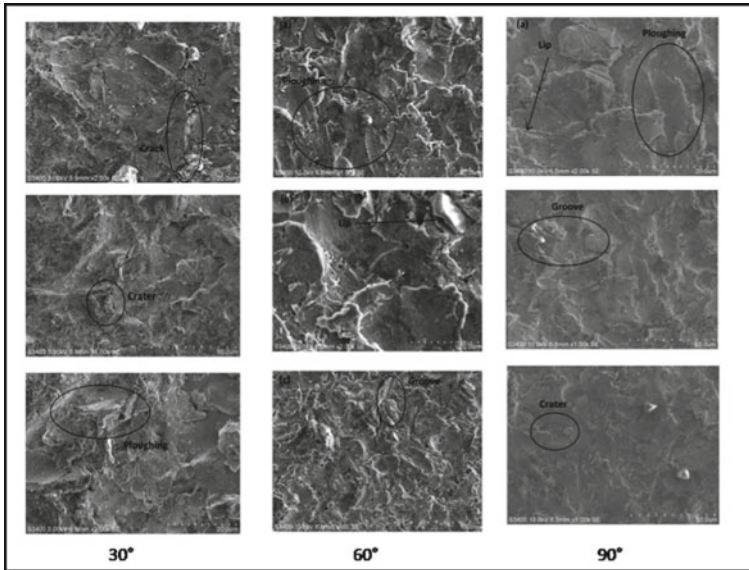


**Fig. 3** Plots for Ti-31 special alloy exposed to erosion at three different angles of impact, **a** erosion rate curves; **b** bar chart of steady state volumetric erosion rate

and a minimum at a 90° impact angle, Similarly, as demonstrated in Fig. 2b, steady state volumetric erosion rate is highest at 30° and lowest at 90° angle of impact, which is the trend generally observed in materials that exhibit ductile mode of erosion. The variation in erosion rate with cumulative mass of erodent is shown in Fig. 3a. Also, the variation in steady state volumetric rate of erosion at different impact angles is shown in Fig. 3.

### 3.2 SEM/EDS Analysis

The SEM micrograph of the encircled region is taken to depict the mechanism of material removal involved in the erosion process and is shown in Fig. 4. SEM micrographs of scars developed on Ti-31 samples due to erosion at a 30° impingement angle are shown in Fig. 4a, and material removal is seen as actions like ploughing, formation of loose debris, and grooves. SEM images of the erosion scar obtained



**Fig. 4** SEM image of scar developed due to erosion on superalloy Ti-31 at 30°, 60°, and 90° angle of impingement

on special alloy Ti-31 for a 60° impingement angle are shown in Fig. 4b, and material removal is seen as ploughing and crater formation, and the crater is formed when embedded sand particles are dropped from the surfaces. When the samples are subjected to erosion at a 90° angle of impact, the micro structural features are as shown in Fig. 4c. It is obvious from the micro graph that ploughing action, erodent entrapment, and groove development occur. EDS examination (ref Fig. 5) on the erosion scar developed on a sample subjected to erosion at 30° impact angle reveals that on the surface there is 46.01 wt % Ti as the major phase and 10.45% of C, 4.85% Al as minor constituents, and the presence of 7.59% Si confirms the entrapment of sand particles in the substrate.

### 3.3 Erosion Behaviour of Superco-605 Superalloy

Figure 6a–c shows photographs of the erosion scar generated on the Superco-605 sample at 30°, 60°, and 90° impedance angles, respectively. The eroded scar's middle (A) symbolises a limited zone of material deterioration that is surrounded by an elastic loading area B). The erosion rate and steady state volumetric erosion rate are calculated; Fig. 7 shows the erosion rate curves as well as the steady state volumetric erosion rate bar chart. The steady state volume erosion rate is found to be greatest

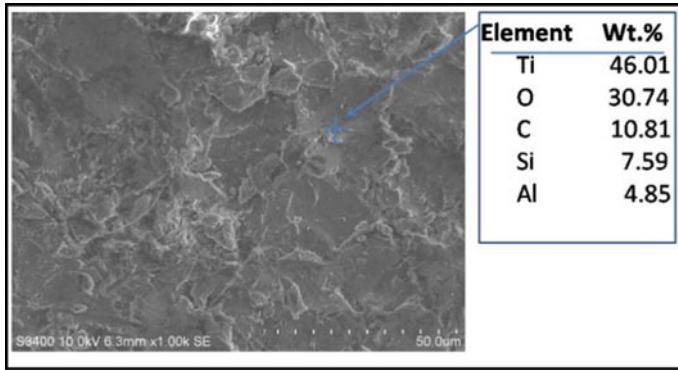


Fig. 5 EDS analysis of Ti-31 sample eroded at 30° impact angle

at 90° impact angles and lowest at 30° impact angles (Fig. 6b). This is the typical behaviour of materials that have a brittle mode of erosion.

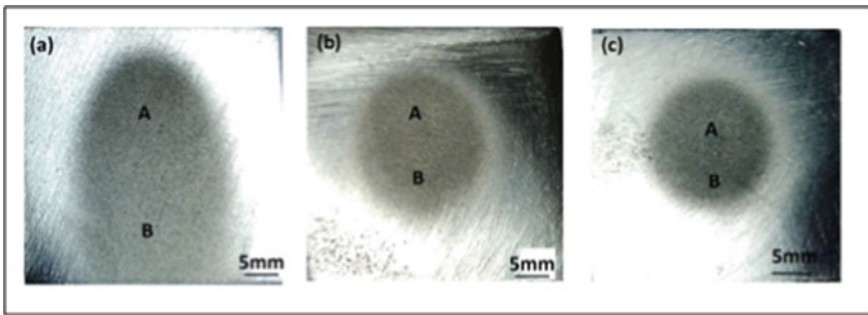


Fig. 6 Macrographs of uncoated Superc0-605 being eroded at different angles of impact. a 30°, b 60°, c 90°

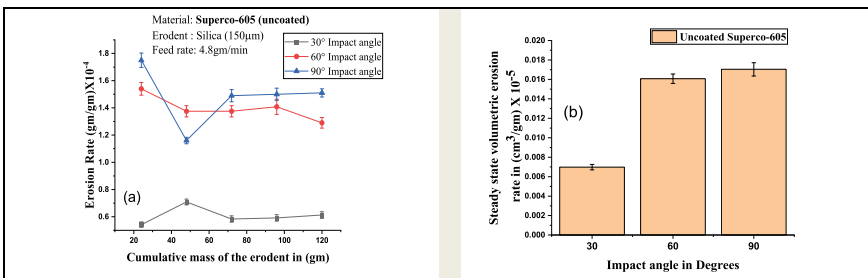
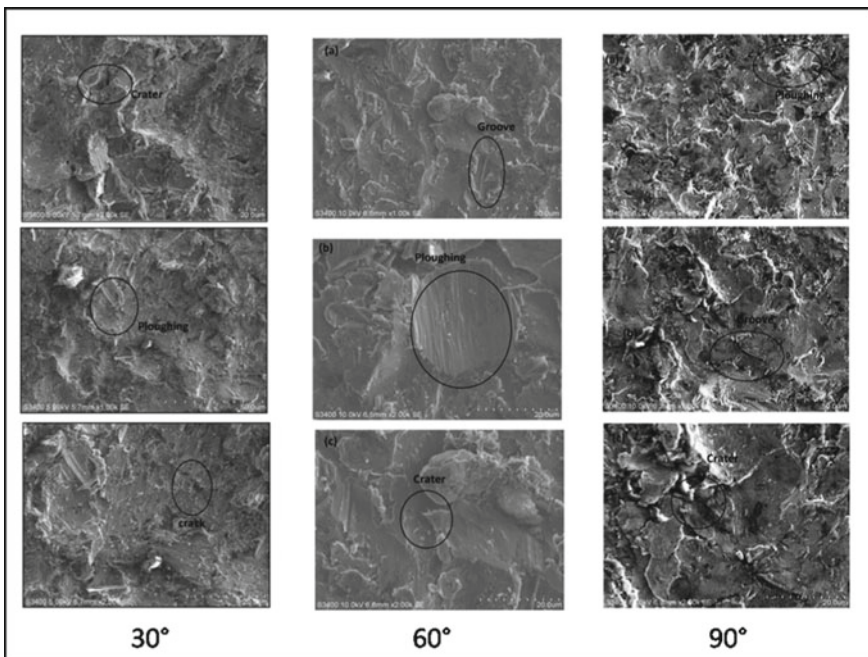


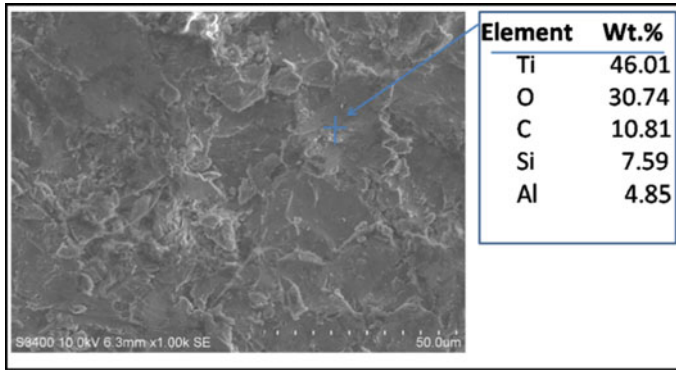
Fig. 7 a Plot of erosion rate and; b steady state volumetric erosion rate of Superc0-605 superalloy for all three angles of impact

### 3.4 SEM with EDS Analysis

The scar generated on uncoated Superco-605 at a 30° impact angle is shown in micro structural detail in Fig. 8a. Ploughing, debris trapping, and groove creation are all visible damage in the microstructure. Similarly, Fig. 8b depicts microstructure features in a scar created by a 60° impact angle, which reveals material degradation in the form of ploughing, groove creation, and craters. Craters may occur when erodent particles are dislodged from their entrapment. Micrographs of material damage at a 90° erodent impact angle are shown in Fig. 8c. Ploughing causes material degradation, crater creation, and erodent particle trapping. EDS analysis (refer to Fig. 9) of the erosion scar on a sample that was eroded at a 30° impact angle shows that the surface contains 50.96 wt.% Co as the major phase, 19.45 wt.% C, 17.79 wt.% Cr as minor constituents, and 10.45wt.% Si, which shows that sand particles have been trapped in the substrate.



**Fig. 8** SEM images of erosion scar developed on Superco-605 at impact angles of 30°, 60°, and 90°



**Fig. 9** EDS analysis of Superco- 605 sample eroded at 30° impact angle

## 4 Conclusions

1. In the instance of Ti-31, erosion is higher at 30 degrees and less at 90 degrees. This is the typical behaviour of material that erodes in a ductile mode.
2. The erosion rate of Superco-605 is greater at 90° and lower at 30° angle of contact, indicating that the mechanism of erosion is brittle.
3. Material loss in the form of ploughing, groove, and crater development can be seen in SEM micrographs of eroded samples of Ti-31 and Superco-605.
4. EDS analysis reveals silica sand particle penetration into the substrate, followed by crater formation as a result of entrapped sand particle drop-off from the substrate.

**Acknowledgements** The authors would like to thank NIE Mysore for providing an Air Jet Erosion Test rig for conducting solid particle erosion investigations, as well as Vignyana Bhavan University of Mysore for providing SEM/EDS.

## References

1. Singh PK, Mishra SB (2020) Erosion performance of detonation gun deposited WC–12Co, Stellite 6 and Stellite 21 coatings on SAE213-T12 steel. *Tribol-Mater Surf Interfaces* 14(4):229–239
2. Kablov EN, Muboyadzhyan SA (2017) Erosion-resistant coatings for gas turbine engine compressor blades. *Russian Metallurgy (Metally)* 6:494–504
3. Anand Babu, K, N Jagadeeswaran, Kapilan N, Ramesh MR (2020) Improved erosion resistance by HVOF sprayed 10% Al<sub>2</sub>O<sub>3</sub>-COCrAlTaY coating on Ti-31. *IJRTE* 8:1605–1610
4. Vinod Kumar MS, Suresh R, Jegadeeswaran N (2021) Study of solid particle erosion behavior of HVOF spray coated superco-605 superalloy. *Mater Today: Proc* 45:10–14
5. Thirugnanasambantham KG, Natarajan S (2015) Degradation through erosion: mechanistic studies on IN-718 superalloy under hot air jet conditions. *J Mater Eng Perform* 24(7):2605–2613

6. Zhao J-R, Hung F-Y, Lui T-S (2019) Erosion resistance and particle erosion-induced tensile embrittlement of 3d-selective laser melting inconel 718 superalloy. *Metals* 10(1):21
7. Bircan B, Fidan S, Çimenoğlu H (2014) Solid particle erosion behavior of Inconel 718 super alloys under elevated temperatures. *J Achieve Mater Manuf Eng* 66(1):5–12
8. Jappes JTW et al (2022) Numerical analysis of 3D printed Inconel 718 superalloy for mechanical properties and solid particle erosion studies. *Mater Today: Proc* 52:239–245
9. Levin BF, Dupont JN, Marder AR (1998) Solid particle erosion resistance of ductile wrought superalloys and their weld overlay coatings. *J Mater Sci* 33(8):2153–2163
10. Kumar D, Npandey K (2021) A comparative study of erosion wear rate of conventional and nonconventional thermal barrier coatings on IN800 superalloys. *Sādhanā* 46(3):1–17
11. Aravind Nagaraj T, Kumaresh Babu SP, Vallimanalan A, Srinivasan SA, Mahendran R (2019) Solid particle erosion behavior of cast CY5SnBiM at room temperature. *J Inst Eng-India* 100:91–96
12. Kaplan M, Uyaner M, Avcu E, Yildiran Avcu Y, Karaoglanli AC (2019) Solid particle erosion behavior of thermal barrier coatings produced by atmospheric plasma spray technique. *Mech Adv Mater Struct* 261:606–1612
13. Patel M, Patel D, Sekar S, Tailor PB, Ramana PV (2016) Study of solid particle erosion behaviour of SS 304 at room temperature. *Procedia Technol* 23:288–295
14. Mishra SB, Prakash S, Chandra K (2006) Studies on erosion behaviour of plasma sprayed coatings on a Ni-based superalloy. *Wear* 260(4–5):422–432
15. Shibe V, Chawla V (2019) Erosion studies of D-Gun-Sprayed WC-12% Co, Cr<sub>3</sub>C<sub>2</sub>-25% NiCr and Al<sub>2</sub>O<sub>3</sub>-13% TiO<sub>2</sub> coatings on ASTM A36 steel. *J Therm Spray Technol* 28(8):2015–2028
16. Sidhu HS, Sidhu BS, Prakash S (2007) Solid particle erosion of HVOF sprayed NiCr and Stellite-6 coatings. *Surf Coat Technol* 202:232–238
17. Pauzi AA et al (2020) Wear characteristics of superalloy and hard face coatings in gas turbine applications—a review. *Metals* 10(9):1171

# Evaluation of the Compression Properties of 3D Printed ePA-GF TPMS Structures



S. Jeyanthi, R. Prabhu, R. Arunkumar, Nivedhitha Ramesh,  
S. Vinoth Kumar, and L. Prince Jeya Lal

**Abstract** 3D printed minimal surface structures have received considerable research interest in the past decade and are proposed for many multidisciplinary applications. The mechanical performance of these structures is significantly affected by their structural configuration, materials, and 3D printing parameters. To explore the behavior of structural profiles, four different designs were developed and 3D printed from ePA-GF materials using a fusing filament fabrication and evaluated by axial compression experiments at a quasi-static staining rate. The experimental results provide insight into the compression properties, plastic deformation, and failure mechanism of short fiber reinforced structures. The results of axial compression experiments revealed that unit cell topology plays an important role in unit cell selection and design. It has been found that the Diamond structure has the highest compressive modulus and energy absorption capacity, while the Primitive structure has the lowest range of compressive modulus and energy absorption capacity. However, the Primitive structure recorded the lowest induced stress and highest efficiency among all other designs. Fiber pull-out and fracture was observed on induced cracks in the structure, which confirms uniform stress transfer to successive layers.

**Keywords** Composite 3D printing · ePA-GF · TPMS · Compression properties · Energy absorption

---

S. Jeyanthi · S. V. Kumar  
School of Mechanical Engineering, VIT Chennai Campus, Chennai 600127, India

R. Prabhu  
Department of Mechanical Engineering, Mahendra Engineering College, Namakkal 637503, India

R. Arunkumar  
Department of Mechanical Engineering, Sri Sairam Institute of Technology, Chennai 600044, India

N. Ramesh  
Tamil Nadu Government Dental College, Chennai 600003, India

L. P. J. Lal (✉)  
Department of Mechanical Engineering, Rajalakshmi Institute of Technology, Chennai 600124, India  
e-mail: [princejeyalal.1@ritchennai.edu.in](mailto:princejeyalal.1@ritchennai.edu.in)



# 1 Introduction

Additive manufacturing offers researchers the ability to fabricate complex structural configurations that cannot be achieved through conventional manufacturing. Because of their remarkable properties such as the specific strength and energy absorption properties of [1], minimal surface structures have attracted the attention of researchers over the past decade. It has been found that the mechanical properties of the lattice structure are directly related to the size and cellular topology of the structure [2]. Fused deposition modeling (FDM) [3], poly jet [4], selective laser sintering (SLS) [5], and adhesive injection [6] are widely used additive manufacturing processes to develop porous structures from polymers. Shape memory polymer [7], poly lactic acid (PLA) [8], acrylonitrile butadiene styrene (ABS) [9], PA [5], photosensitive resin [10], biopolymer [11], nylon PA 2200 [12], PEEK [13], PETG [14], TPU [15], etc. are widely used polymers to develop highly porous lattice structures.

This work focuses on the fabrication of short glass fiber reinforced polyamide composites through the FFF process to develop bio-inspired minimal surface area sheet-based lattice structures. Short fiber reinforcement in pristine printing filaments can significantly improve the mechanical properties of 3D printed composite structures. The research of [16] revealed that short carbon fiber reinforcement in ABS filaments enhanced the tensile strength and modulus by  $\sim 115\%$  and  $\sim 700\%$  respectively. In addition, the properties of the 3D printed composite structures can be tailored for specific applications [17].

## 1.1 Research Motivation

3D printed lattice structures are preferred for a number of applications such as lightweight aerodynamic structures [18] and protective structures against impact [19]. Similarly, highly porous 3D printed structures are used during bone integration [20] to develop bio-implants with human bone-like stiffness and in heat exchangers [21] to improve flow and heat transfer. To further expand the application areas of 3D printed lattice structures, it is essential to understand the relationship between cell configuration and the resulting properties. Much research is underway to explore the mechanical properties of sheet lattice structures made of various polymers using a variety of additive manufacturing techniques. However, no previous studies have focused on the compressive mechanical properties of short fiber reinforced polyamide (ePA-GF) composites produced by FFF. Therefore, this study focuses on evaluating the mechanical properties of the sheet-based lattice structure fabricated with FFF subjected to axial compression to help researchers develop a sheet-based lattice structure with tailorable stiffness and strength for engineering applications.

## 2 Methodology

### 2.1 Design of Sheet-Based Lattice Structures

Triply minimal surface (TPMS) is a type of network design that provides multifunctional capabilities [22]. This has attracted the attention of researchers in recent years to evaluate the properties of different types of network designs with different relative densities depending on the topology configuration. Lattice structures exhibit failure either in a bending dominated mode or in a stretching dominated mode [23]. Many researchers [24] have explored strut-based cell structures to design open-cell configurations with desirable mechanical properties because of achievable node connectivity, resulting in stretch-dominated failure [25]. The strut-based cell profiles exhibit bands of shear strain typically formed by the rapid failure of the struts in successive layers with a significant increase in the peak stress continuing to rapidly decrease [26]. This results in undulations in the load-carrying capacity of the structure due to alignment of the struts in the direction of the load resulting in a higher elastic modulus. Undulations in load-carrying capacity can be minimized and energy absorption can be enhanced with the use of sheet-based TPMS configurations. The power law relationship proposed by Gibson-Ashby is used to specify the exact volume fraction or relative density. The relative density of the lattice structure can only be controlled by assigning thickness to the surfaces for equivalent unit cell sizes, and thus the lowest relative density is limited based on the minimum thickness of the printable surface as it is difficult to print lattice structures with reduced unit cell sizes or relatively lower density [27]. In this work, four different configurations with design relative densities of 29.4% were designed with the following approximations presented in [28].

Schwarz Diamond

$$\begin{aligned} &\sin(x) \sin(y) \sin(z) + \sin(x) \cos(y) \cos(z) \\ &+ \cos(x) \sin(y) \cos(z) + \cos(x) \cos(y) \sin(z) = 0 \end{aligned} \quad (1)$$

Fisher-Koch

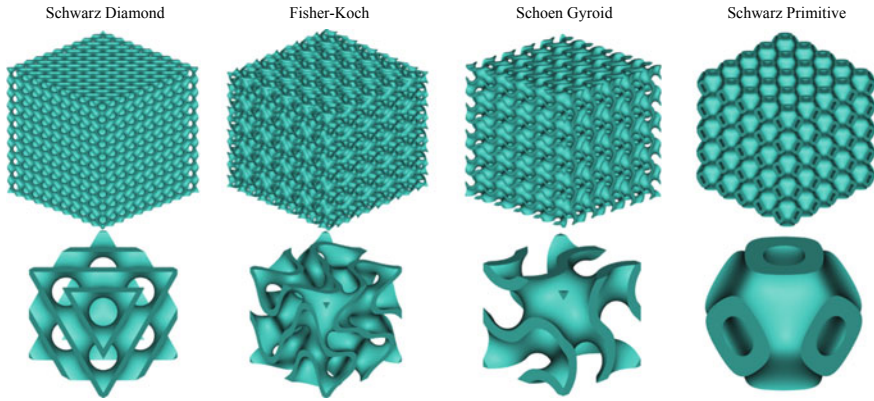
$$\cos(2x) \sin(y) \cos(z) + \cos(x) \cos(2y) \sin(z) + \sin(x) \cos(y) \cos(2z) = 0 \quad (2)$$

Schoen Gyroid

$$\cos(x) \sin(y) + \cos(y) \sin(z) + \cos(z) \sin(x) = 0 \quad (3)$$

Schwarz Primitive

$$\cos(x) + \cos(y) + \cos(z) = 0 \quad (4)$$



**Fig. 1** CAD model of a lattice structure with a unit cell representing the thickness value of the sheet in mm

CAD models of unit cells of different thicknesses to achieve a fixed relative density for different TPMS configurations are shown in Fig. 1.

## 2.2 3D Printing of the TPMS Lattice Structure

Fused filament fabrication was used to develop the sheet-based lattice structure for this study. FFF is the material extrusion process as defined by ASTM 52900 for selective layered deposition of molten polymers through a heating nozzle based on CAD data. The filament is ePA-GF (Manufacturer: Shenzhen Esun Industry Co., Ltd., China), short glass fiber reinforced nylon with a tough and strong, non-brittle formulation with improved mechanical properties compared to pure nylon filament is used to 3D print the structures (Table 1).

An in-house built 3D printer with dual-fan configuration with controllable wind speed for enhanced print quality and refined extruder sensors for more accurate

**Table 1** Mechanical properties of ePA-GF

Mechanical properties	ePA-GF
Density ( $\text{g/cm}^3$ )	1.24
Tensile strength at yield (MPa)	100.96
Tensile Modulus (MPa)	3953
Elongation at break (%)	16.72
Impact strength (Izod-notched) ( $\text{kJ/m}^2$ )	13.67
Flexural strength (MPa)	126.45
Flexural modulus (MPa)	3213.96

**Table 2** Recommended printing parameters of ePA-GF

Process parameter	Value
Nozzle diameter (mm)	0.4–0.6
Nozzle distance (mm)	0.2–0.3
Nozzle temperature (°C)	240–260
Bed temperature (°C)	60–90
Chamber temperature (°C)	80
Layer height (mm)	0.12
Infill density (%)	100
Infill pattern	Triangle
Infill speed (mm/s)	60–90
Print Speed (mm/s)	90–150
Cooling fan	Off

leveling for enhanced dimensional accuracy is used to print all the sheet-based structures. Reinforcing glass fiber additives intends to block the nozzle more frequently and hence the use of a stainless-steel nozzle with slow speed and reduced retraction significantly helps to get enhanced extrusion quality. It is recommended to oven dry the filaments at 90 °C for 3–4 h before initiating the printing process to mitigate the effects of humidity. An open source slicing application CURA by Ultimaker is used in this study during the pre-printing phase to prepare the model for FFF and the recommended printing parameters are presented in Table 2.

### 2.3 *Quasi-Static Compression Experiments*

The existing structure–property relationships in the structures based on the ePa-GF sheets developed by the FFF technique can be investigated through the compression behavior of the structures. The compressive properties of the sheet-based structures were evaluated by uniaxial compression tests using the Autograph AGS-X Series Universal Testing Machine (manufacturer: Shimadzu Corporation, Japan) in displacement-controlled mode with a strain rate of 0.001/s and equipped with a 50 kN load cell. The test parts are precisely placed in the center of the steel compression plates to eliminate misalignment. The compressive force applied to the samples was measured and the corresponding displacement was recorded until the sheet-based structures were fully compressed. The whole experiment was recorded with a high-resolution video camera, through which the gradual collapse behavior of sheet-based structures was further investigated from the extracted individual images.

## 2.4 Performance Metrics

Energy absorption ( $E_a$ ): A typical indicator to evaluate a porous structure is the energy absorption. It is in fact the energy dissipated by the lattice structure during the compression event through structural deformation and collapse that can be estimated by integrating the area covered the force–displacement curve generated during the compression event.  $E_a$  can be estimated through the following expression:

$$E_a = \int_0^{\delta_{max}} f(x)dx \quad (5)$$

where,  $\delta_{max}$  is the end crush length and  $f(x)$  is the applied compression force on the lattice structure as a function of displacement.

Specific energy absorption (SEA): An indicator used to compare the energy absorption in structures developed through different structural configurations and materials with reference to the weight of the structure. SEA can be calculated as:

$$SEA = \frac{E_a}{m} \quad (6)$$

Mean crushing force (MCF): MCF is the ratio of the total energy absorbed by the lattice structure till the onset of densification to the crushing length during the compression event. MCF can be quantified by:

$$MCF = \frac{E_a}{\delta_{max}} \quad (7)$$

Crushing force efficiency (CFE): CFE is a performance metric used to compare and evaluate the efficiency of a structure under compression loading. Since the primary objective of the structure is to bring down the initial peak force and to delay the onset of densification, a higher value of CFE is highly desirable.

$$CFE = \frac{P_{mean}}{P_{peak}} \times 100 \quad (8)$$

**Table 3** Technical information of 3D printed structures

Test order	Cell configuration	Sheet thickness (mm)	Relative density $\rho^*/\rho_s$	Deviation (%)	Mass (g)
1	Schwarz Diamond	1.025	29.68	0.95	24.84
2	Fisher-Koch	0.9	34.37	16.90	27.88
3	Schoen Gyroid	1.2	28.1	-4.42	22.5
4	Schwarz Primitive	0.7	28.1	-4.42	22.34

### 3 Results and Discussion

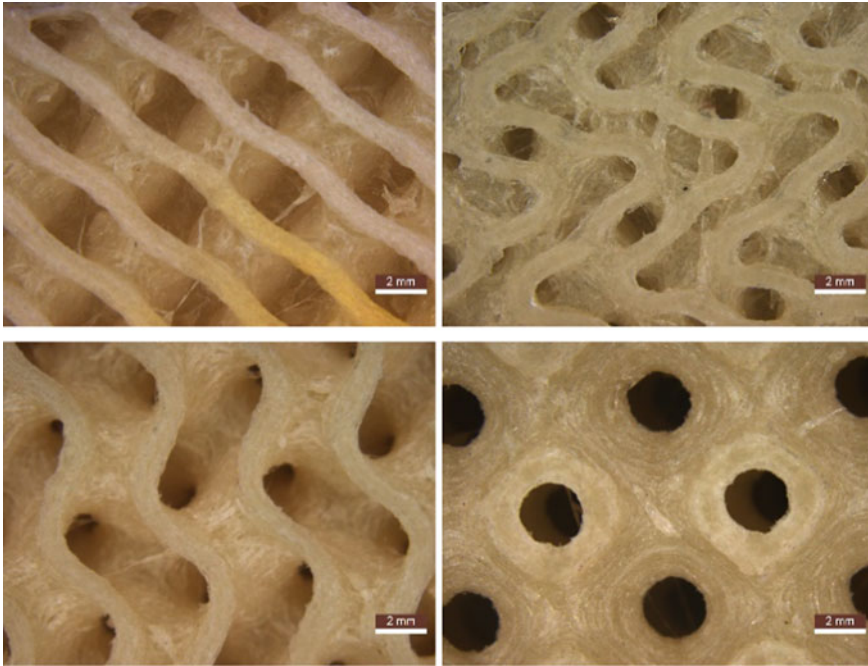
#### 3.1 Assessment of Print Quality

All the 3D printed TPMS structures were analyzed before experimental testing, for print quality and dimensional accuracy using a Leica M205C stereo microscope that can achieve optical resolution of 0.952  $\mu\text{m}$ . Furthermore, the internal quality of the print is analyzed using the GE LightSpeed VCT CT Scanner using the SnapShot Pulse™ operating from 200 to 500 mA. The relative densities of all TPMS structures were estimated and were found to be consistent with their 3D CAD model. A total of four samples were developed and measured data are presented in Table 3.

The print quality of the surfaces, observed defects and the internal morphologies of the sheet-based structures are presented in Fig. 2.

#### 3.2 Compression Properties of Structures

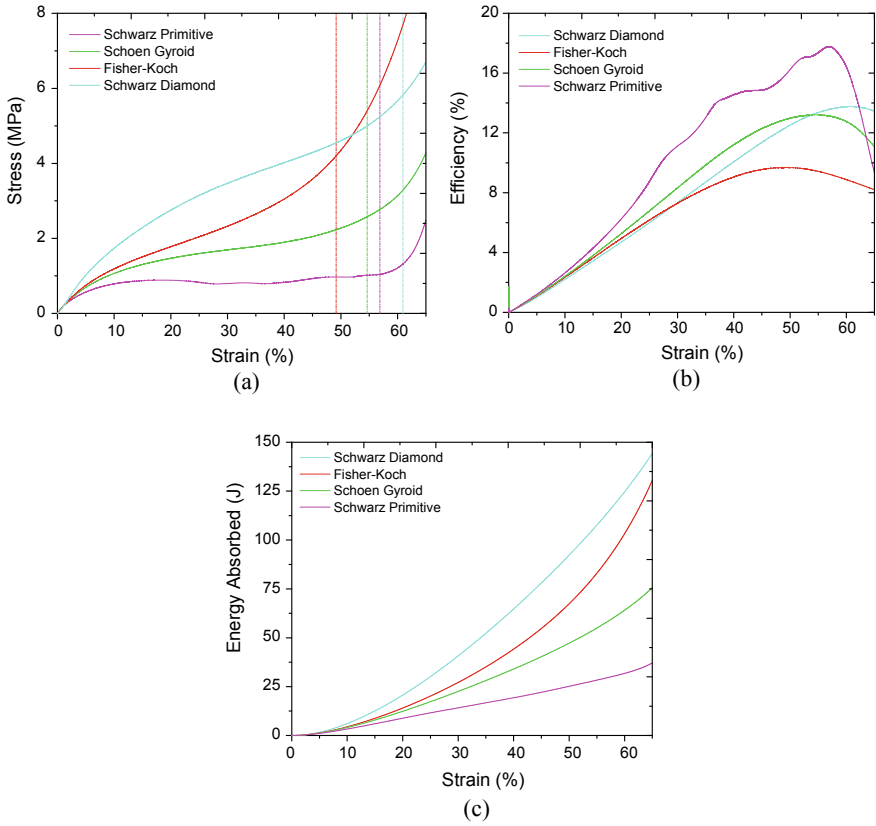
The axial compression response of TPMS structures is shown in Fig. 3. The stress–strain curves of all structures show an initial modulus followed by a plastic plateau phase and the end with the onset of densification with exponential increase of stress along with strain. The compression characteristics of all samples calculated from the stress–strain data are presented in Table 4. From Fig. 3a, it is observed that in the elastic phase, the induced stress increases linearly and after yielding, in the plastic phase, the induced stress increases non-linearly and hardening phenomenon is observed in the Schwarz Diamond, Fisher-Koch, and Schoen Gyroid structures. In addition, no peaks and valleys were observed due to gradual compression, meaning no cracks and smooth compression without any catastrophic failure modes, a typical feature of structures with thin sheet-based architecture. Whereas in Schwarz Primitive structures, after yielding, slight softening is observed at plastic phase and when the onset of densification point is reached (readers must match the color of the vertical line to the color of the curve) the resulting stress increases non-linearly because there is no negative space in the structure to allow for further compression. The



**Fig. 2** Surface quality of sheet-based structures observed by optical microscope. **a** Schwarz Diamond, **b** Fisher-Koch, **c** Schoen Gyroid, **d** Schwarz Primitive

small peaks in the plastic region represent cell cracking of the structure and the same can be visualized from the corresponding efficiency curve.

Figure 3b presents the efficiency of the structures under compression loading. It is observed that the efficiency curve of the Schwarz Primitive structure is appreciable compared to the other three structures and the efficiency curve of the Fisher-Koch structure offered least performance. The densification strain is estimated from the efficiency curve of the corresponding structure. Figure 3c reveals the energy absorbed by the structures under the compression loading. It is observed that the energy absorbed by the Schwarz Diamond structure is 333.44% higher than the Schwarz Primitive structure. But it is to be noted that this increase in energy absorption comes with the higher value of induced stress in the order of 465%. Similarly, though the relative density of Schoen Gyroid and Schwarz Primitive are identical, the performance of both the structures exhibits unique features under compression loading. For instance, the compression modulus of Schoen Gyroid is 27.37%, mean compressive force is 68.99%, and the energy absorption is 83.83% higher than the Schwarz Primitive structure. However, the efficiency of the latter is 34.58% higher than Schoen Gyroid.

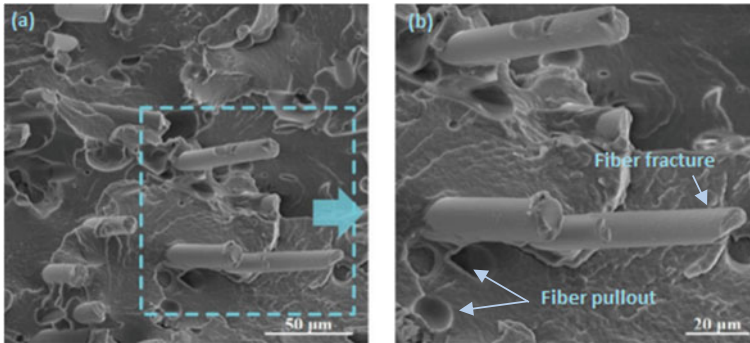


**Fig. 3** Results of sheet-based structures under quasi-static axial compression. **a** stress–strain curves with vertical lines to represent the onset of densification, **b** efficiency–strain curves from which the onset of densification is estimated, **c** energy absorption curves of sheet-based structures

**Table 4** Compression properties 3D printed sheet-based structures

Test order	Cell configuration	Relative density $\rho^*/\rho_s$	Compression modulus (MPa)	Mean compressive force (kN)	Energy absorbed (J)	Densification strain	Efficiency (%)
1	Schwarz Diamond	29.68	22.82	5.25	128.17	0.61	34.38
2	Fisher-Koch	34.37	15.76	3.31	65.16	0.49	24.21
3	Schoen Gyroid	28.1	14.10	2.48	54.36	0.55	33.02
4	Schwarz Primitive	28.1	11.07	1.29	29.57	0.57	44.44



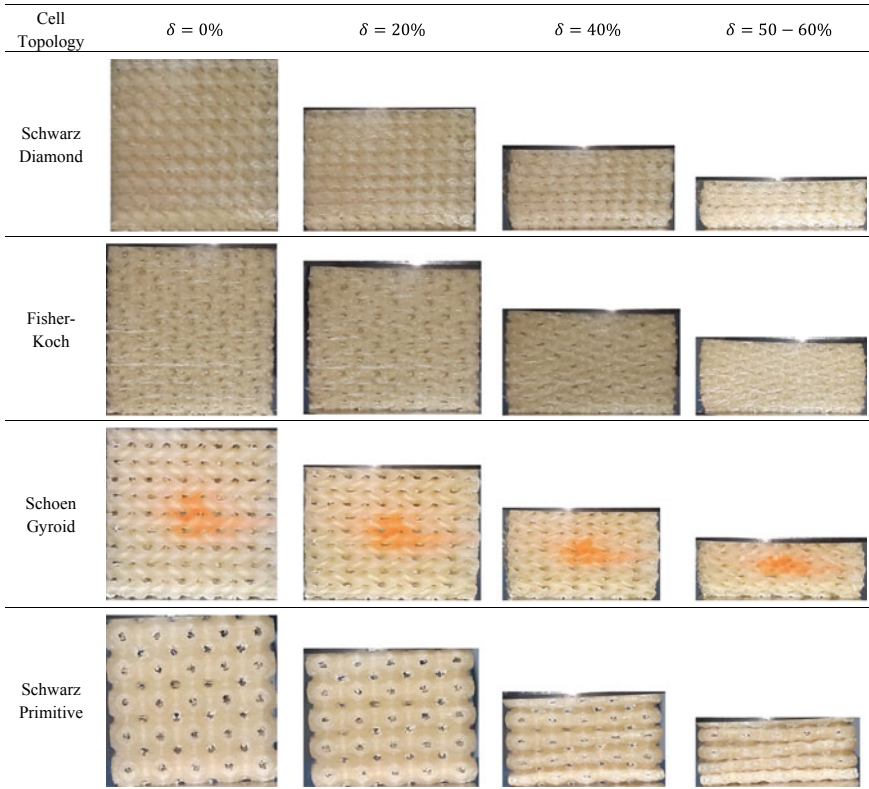


**Fig. 4** Failure analysis of Schwarz Primitive

### 3.3 Deformation Studies

The cracks were only observed in the Primitive structures ranging from one cell to the adjacent cell as presented in Fig. 4. Typical failure mechanisms observed in fiber reinforced composites such as fiber pull-out, fiber breakage were observed in 3D printed structures reinforced with short fibers. The Primitive structures had collapsed under the action of the tensile force and thus the reinforced short fibers had been pulled out their positions. Additionally, fiber breakage was observed, confirming that reinforced fibers do significantly transfer the compressive force to successive layers leading to a progressive failure mode.

The deformation patterns and failure modes of all four TPMS structures are presented in Fig. 5. For compression strain lesser than 3%, linear elastic deformation is observed in all structures. After the strain exceeds 10%, the structures began to fail due to horizontal layer wise plastic deformation. No typical shear bands or crack planes were observed as in strut-based structures. All TPMS structures have shown progressive collapse that occurs due to compression of all cells in consecutive layers. However, no decrease in stress was observed during the collapse. At the end of the plateau regime in the strain range of 50–60%, all structures were fully compressed and densification was observed. Localized barreling was observed in the central region of all structures except Schwarz Primitive. The compacted structures were visually examined and all structures were intact with no macro cracks or shear bands which is a typical failure mode in short fiber reinforced composite structures.



**Fig. 5** Collapse behavior of sheet-based structures. **a** Schwarz Diamond, **b** Fisher-Koch, **c** Schoen Gyroid, **d** Schwarz Primitive

## 4 Conclusion

This research focuses on the study of the compression properties of sheet-based FFF printed short fiber reinforced TPMS structures. The main results of this work are summarized in this section. The Gyroid and Schwarz Primitives have been identified as structures with high manufacturability. On the other hand, Fisher-Koch showed a higher deviation from design relative density. The results of the compression experiment show that the diamond structure has the highest stiffness and the Primitive structure has the lowest stiffness values. In terms of compression efficiency, the Primitive structure recorded higher efficiency than the other structures. Although the diamond structure recorded a very high energy absorption, the induced stress was also proportionally higher than any other structure. Therefore, from a design point of view, a structure with a lower value of induced stress with a higher energy absorption function is highly recommended for load-bearing applications.

## 5 Scope for Future Research

Advancements in 3D printing technologies have greatly aided product development in the development of Structures that cannot be made with conventional fabrication. Hence the research on composite porous structures for automotive, sports, aerospace, and biomedical applications has grown in popularity in recent years. However, research exploring the use of composite structures for such applications is very limited. The synergistic properties of the FFF process to manufacture composite structures based on bio-inspired TPMS structures could be exploited for applications such as the development of patient-specific body implants with customized stiffness, low weight, and high stiffness spatial structures and protective structures to mitigate explosions and impact loads.

## References

1. Lazar P, Jeyanthi S, Manickam M, Vinoth Kumar S (2023) Imperfections and computational modeling of lattice structures developed through powder bed fusion—A short review. *Mater Today: Proc.* <https://doi.org/10.1016/j.matpr.2023.02.269>
2. Leary M et al (2018) Inconel 625 lattice structures manufactured by selective laser melting (SLM): mechanical properties, deformation and failure modes. *Mater Des* 157:179–199. <https://doi.org/10.1016/j.matdes.2018.06.010>
3. Maconachie T et al (2020) The compressive behaviour of ABS gyroid lattice structures manufactured by fused deposition modelling, pp 4449–4467
4. Kadkhodapour J, Montazerian H, Raeisi S (2014) Investigating internal architecture effect in plastic deformation and failure for TPMS-based scaffolds using simulation methods and experimental procedure. *Mater Sci Eng C* 43:587–597. <https://doi.org/10.1016/j.msec.2014.07.047>
5. Maskery I et al (2018) Insights into the mechanical properties of several triply periodic minimal surface lattice structures made by polymer additive manufacturing. *Polymer (Guildf)* 152:62–71. <https://doi.org/10.1016/j.polymer.2017.11.049>
6. Liu J, Kannan R, Zhang D, Liu T, Nandwana P, Devaraj A (2022) *Journ Prproo. Addit Manuf* 102834. <https://doi.org/10.1016/j.addma.2022.102834>
7. Yuan C, Wang F, Qi B, Ding Z, Rosen DW, Ge Q (2020) 3D printing of multi-material composites with tunable shape memory behavior 193:1–10. <https://doi.org/10.1016/j.matdes.2020.108785>
8. Alizadeh-osgouei M, Li Y, Vahid A, Ataee A, Wen C (2021) Smart materials in medicine high strength porous PLA gyroid scaffolds manufactured via fused deposition modeling for tissue-engineering applications. *Smart Mater Med* 2(August 2020):15–25. <https://doi.org/10.1016/j.smaim.2020.10.003>
9. Al Rifaie M, Mian A (2018) Compression behavior of three-dimensional printed polymer lattice structures 1–11. <https://doi.org/10.1177/1464420718770475>
10. Cao X et al (2021) Mechanical performance and defect analysis of the imperfect micro smooth gyroid cylinder shell structure 273(June), 1–9. <https://doi.org/10.1016/j.compstruct.2021.114320>
11. Pecorini G, Braccini S, Parrini G, Chiellini F (2022) Additive manufacturing of Poly (3-Hydroxybutyrate-co-3-Hydroxyvalerate)/Poly (D, L-Lactide-co-Glycolide) Biphasic scaffolds for bone tissue regeneration

12. Abueidda DW, Elhebeary M, Shiang CA, Pang S, Al-rub RKA, Jasiuk IM (2019) Mechanical properties of 3D printed polymeric Gyroid cellular structures: experimental and finite element study. *Mater Des* 165:107597. <https://doi.org/10.1016/j.matdes.2019.107597>
13. Shanmugam V et al (2021) Fatigue behaviour of FDM-3D printed polymers, polymeric composites and architected cellular materials. *Int J Fatigue* 143(August 2020):106007. <https://doi.org/10.1016/j.ijfatigue.2020.106007>
14. Basurto-vázquez O, Sánchez-rodríguez EP, Meshane GJ, Medina DI (2021) Load distribution on PETG 3D prints of honeycomb cellular structures under compression load, pp 1–13
15. Bates SRG, Farrow IR, Trask RS (2016) 3D printed polyurethane honeycombs for repeated tailored energy absorption. *JMADE* 112:172–183. <https://doi.org/10.1016/j.matdes.2016.08.062>
16. Tekinalp HL et al (2014) Highly oriented carbon fiber—polymer composites via additive manufacturing. *Compos Sci Technol* 105:144–150. <https://doi.org/10.1016/j.compscitech.2014.10.009>
17. Wang K, Li S, Rao Y, Wu Y, Peng Y, Yao S. Flexure behaviors of ABS-based composites containing carbon and Kevlar fibers by material extrusion 3D printing, pp 1–12
18. Zhou H et al (2019) Lightweight structure of a phase-change thermal controller based on lattice cells manufactured by SLM. *Chin J Aeronaut* 32(7):1727–1732. <https://doi.org/10.1016/j.cja.2018.08.017>
19. Brennan-Craddock J, Brackett D, Wildman R, Hague R (2012) The design of impact absorbing structures for additive manufacture. *J Phys Conf Ser*, 382(1). <https://doi.org/10.1088/1742-6596/382/1/012042>
20. Zadpoor AA (2019) Mechanical performance of additively manufactured meta-biomaterials. *Acta Biomater* 85:41–59. <https://doi.org/10.1016/j.actbio.2018.12.038>
21. Fee C (2017) 3D-printed porous bed structures. *Curr Opin Chem Eng* 18:10–15. <https://doi.org/10.1016/j.coche.2017.07.003>
22. Lazar PJJ, Subramanian J, Natarajan E, Markandan K, Ramesh S (2023) Anisotropic structure-property relations of FDM printed short glass fiber reinforced polyamide TPMS structures under quasi-static compression. *J Mater Res Technol* 24:9562–9579. <https://doi.org/10.1016/j.jmrt.2023.05.167>
23. Khaderi SN, Deshpande VS, Fleck NA (2014) The stiffness and strength of the gyroid lattice. *Int J Solids Struct* 51(23–24):3866–3877. <https://doi.org/10.1016/j.ijsolstr.2014.06.024>
24. Lijun X, Weidong S (2018) Additively-manufactured functionally graded Ti-6Al-4V lattice structures with high strength under static and dynamic loading: experiments. *Int J Impact Eng* 111(October 2017):255–272. <https://doi.org/10.1016/j.ijimpeng.2017.09.018>
25. Deshpande VS, Fleck NA, Ashby MF (2001) Effective properties of the octet-truss lattice material 49:1747–1769
26. Mieszala M et al (2017) Micromechanics of amorphous metal/polymer hybrid structures with 3D cellular architectures: size effects, buckling behavior, and energy absorption capability, pp 1–13. <https://doi.org/10.1002/sml.201602514>
27. Abou-ali AM, Al-ketan O, Lee D, Rowshan R, Al-rub RKA (2020) Mechanical behavior of polymeric selective laser sintered ligament and sheet based lattices of triply periodic minimal surface architectures. *Mater Des* 196:109100. <https://doi.org/10.1016/j.matdes.2020.109100>
28. Hsieh M, Valdevit L (2020) Minisurf—A minimal surface generator for finite element modeling and additive manufacturing. *Softw Impacts* 6(July):100026. <https://doi.org/10.1016/j.simpa.2020.100026>

# Analysis and Design of Pre-engineered Building Structure Using SAP2000



Mrunali Surpam and Archana Tanawade

**Abstract** Nowadays, pre-engineered building (PEB) structures are getting very popular globally. These type of structures are manufactured in factory and erected on site. Also, these structures are economical, eco-friendly and recyclable. PEB heavy structures need advanced software like SAP2000 for analysis and design. The objective of the current study is to check performance of PEB structures. The parameters used for analysis and design are bay spacing, frame spacing, wind analysis and earthquake analysis. The bay spacings 5 m, 8 m and 9 m and the frame spacings 20 m, 35 m and 50 m are considered. Basic wind speed from 33 m/s to 50 m/s is selected for wind analysis and zone III is selected for seismic analysis. The design is carried out by using Indian Standard Code 800:2007. The comparison of the PEB structures and conventional steel building (CSB) structures has been determined on the basis of weight of the frame sections, sway and deflection of the steel frames. The result shows that, percentage of weight reduction of PEB structure is about 30% to 40% compared with CSB structures. Result of sway analysis shows that the span length increased from 20 to 50 m gives less deflection, and also in earthquake analysis PEB structures shows less deflection compared with CSB structures. The study concludes that PEB structures are economical, light weight and safe than CSB structures.

**Keywords** Pre-engineered steel building · Conventional steel building · SAP2000 · Pre-fabricated steel building · Built-up section · Minimum weight

## Nomenclature

PEB Pre-engineered steel building  
CSB Conventional steel building

---

M. Surpam (✉) · A. Tanawade  
Civil Department, Vishwakarma Institute of Information and Technology, Pune 411048, India  
e-mail: [mrunali.220m0044@viit.ac.in](mailto:mrunali.220m0044@viit.ac.in)

# 1 Introduction

Nowadays, pre-engineered structures are getting very popular globally. These type of structures are concept of steel building system which are manufactured in factory and erected on site. Researchers are trying to make the steel structure economical as well as effective in terms of time, quality and cost. Steel is a very expensive building material among all but throughout the lifetime of a structure, steel is found to be very economical. Also, these structures are eco-friendly and recyclable.

Conventional steel building is the type of steel building which is mainly containing sections of simple I section, channel sections and hot-rolled sections, whereas, pre-engineered steel building contains cold-formed sections which contributes to minimum weight of the frames due to tapered sections and ultimately cost of the construction gets reduced. Pre-engineered building proves economical, saves time and is eco-friendly compared with the conventional steel building, which eventually leads to decrease of the danger of global warming and pollution by reducing demolition and construction waste.

## 1.1 Literature Review

In the steel structure, researchers have presented the comparison of PEB structure over CSB structure in terms of time limitation, advanced aesthetic view, weight reduction, economy and fast construction. For the designing and analysis part of the PEB structure the software mainly used was Bentley STAAD pro [1]. This research focuses on PEB structure construction system that approaches the best quality, best architectural view, less construction cost and time. In this study, aim of author was to study the concept of PEB structure and to reduce the cost and time of the construction. The conclusion was the amount of steel required for the construction of PEB structure is comparatively lower than the CSB structure. The percentage of cost reduction for PEB structure is 35% compared with CSB structure. Therefore, PEB structure is more economical than CSB structure [2]. This research work focuses on the design of PEB structure evaluating using built-up sections and cold-formed sections. This study goal was to minimise the weight and cost of the steel structure so that the effect of lateral forces is reduced. To achieve the objective a simple PEB structure was first analysed with standard hot-rolled steel sections and then with pre-engineered tapered built-up and cold-formed sections. The conclusion of the study was that secondary sections of PEB structure reduced the weight of the structure up to 60% compared with the conventional steel sections. For primary sections of PEB structure, the weight of the structure reduced up to 35% compared with CSB structure [3]. The research work reports on experimental evaluation of stiffness and strength for rod bracing in PEB structure. In this work, twelve rod bracings were used in primary

frame members with different detailing and anchorage and angle of the rod bracing were tested in tension until failure. Nonlinear stiffness of rod bracings was found. In rod bracing design, at 20% of peak load of tangent stiffness is recommended to use. The different types of limits stated were observed in rod bracing like brittle failure and ductile failure. The provided strength and stiffness values can be used to improve the design of rod bracings [4]. The study comments on experimental investigation on buckling analysis of high-strength stainless steel stiffened and unstiffened slender hollow section columns. The main objective of the study was to analyse the buckling behaviour of cold-formed high-strength stainless steel stiffened and unstiffened slender square and rectangular hollow section columns. The finite element model was developed to investigate the buckling behaviour of the column sections. The finite element software ABAQUS was used for the analysis. FEA models of 84 columns were analysed. For designing American Specification, Australian/New Zealand Standard and European Code were used for cold-formed stainless steel structures. The results of the parametric study had shown the high-strength stainless steel stiffened slender hollow section columns offer a considerable increase in the column strength over that of the unstiffened slender hollow section columns [5]. The research investigates more advanced computational techniques with higher level of complication and advancement to estimate structural damage and human injury. In this research work, a single pre-engineered metal building was selected for analysis and five different computational analytical methods were used and each method compared to demonstrate the benefit of each analytical method. The conclusion shows that the FEA method is most effective method [6]. The study comments on finite element computational technique to investigate buckling coefficients of tapered web plates. In this research, three boundary conditions were considered for steel web plates: uniform compression, pure bending and pure shear. The study concluded that the tapering of a web plate increases its resistance to buckle due to the stiffness provided by the “more-stiff zone” near the smaller plate width compared with the “less stiff zone” at the larger width [7].

In the past studies, all the mentioned research studies have given the weight reduction comparison for a single span of PEB structure. However, the weight reduction of frame section is influenced by many terms like bay spacing, frame spacing and structural responses. Furthermore, the research studies presented the comparison only in terms of weight and cost for single pre-engineered building and conventional steel building frames. The outcomes of wind analysis and seismic analysis are not presented in detail and the results related to structural forces like sway and deflection are not given. The current research work unfolds the effects of frame spacing, bay spacing, sway and deflection on the structure.

## 1.2 Objective

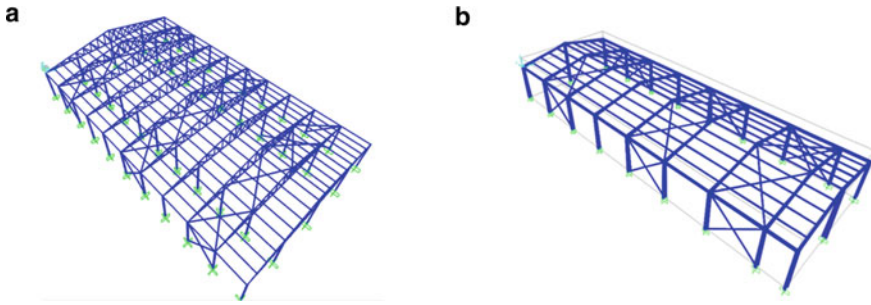
- To analyse and design the PEB and CSB steel structure using SAP2000.
- Analysis of PEB and CSB steel structure considering the parameters as bay spacing, frame spacing and sway and deflection.
- To compare percentage weight reduction and structural behaviour (sway and deflection) of PEB and CSB steel structure.

## 2 Methodology

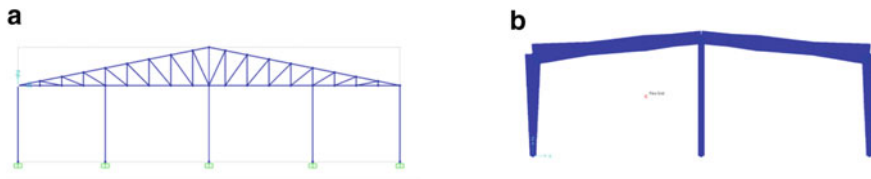
All the research works mentioned in the literature review mainly focused on PEB and CSB structures comparison in terms of weight reduction, sway and deflection. Percentage of weight reduction is mainly influenced by frame spacing, bay spacing and structural responses. The mentioned research works have given no information related to the structural response like sway and deflection. Hence, in this research, PEB and CSB structures are analysed and designed for bay spacing and frame spacing. Also, wind analysis and seismic analysis are presented in detail. SAP2000 software is used for analysis and designing of the CSB and PEB structures. This particular study mainly focuses on the performance comparison of CSB and PEB structure at various bay spacing, frame spacings, sway and deflection comparisons. This study evaluated the percentage of weight reduction in PEB structures compared with CSB structure. In this present work, 42 models of steel structure have been analysed and designed on SAP2000. The minimum yield strength of the steel sections used in both PEB and CSB structure is  $345 \text{ N/mm}^2$  conforming to ASTM.

In the first phase, a total of 14 different steel models are prepared, in which, 7 models for PEB structure and 7 models for CSB structure are analysed and designed having frame spacing varying from 20 m, 25 m, 30 m, 35 m, 40 m, 45 m and 50 m with 5 m of interval. The results of the variation are evaluated in terms of percentage of weight reduction and structural responses of the frame. In second phase, 10 models are prepared to analyse bay spacing of the frames that varies from 5 m, 6 m, 7 m, 8 m and 9 m. The frame spacing of 25 m has been kept constant for bay variation. The effects of the variation are presented in the form of weight reduction, sway and deflection. In the third phase, total 18 models are prepared for seismic and wind analysis. For seismic analysis, zone II, III, IV and V are considered. In wind analysis, wind forces gradually varied from 33 m/s, 39 m/s, 44 m/s, 50 m/s and 55 m/s. The results of all these wind speeds and seismic zones variations are compared in terms of percentage of weight reduction, deflection and sway (Figs. 1 and 2).





**Fig. 1** a CSB 3D model, b PEB 3D model



**Fig. 2** a Elevation of CSB steel structure, b Elevation of PEB steel structure

### 3 Results and Discussion

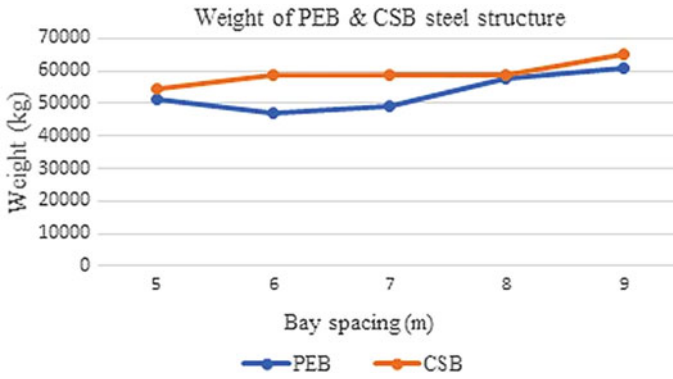
#### 3.1 Comparison of PEB and CSB Steel Structure for Different Bay Span

##### 3.1.1 Effects on Structural Weight

In this study, five different bay spacings ranging from 5 m, 6 m, 7 m, 8 m and 9 m are considered. Frame spacing for all models were kept constant at 20 m. In the PEB structures, most commonly used bay spacing are 6–8 m. Load is calculated on every bay spacing and applied on each frame. Figure 3 and Table 1 show the comparison of PEB and CSB structural weights with their percentage reduction from 1.5% to 19.95%. At every interval of bay spacing, PEB structures are lighter in weight than the CSB structures. It is observed that, PEB structure reduces weight by 19.95% compared with the CSB structure at a bay spacing of 6 m.

##### 3.1.2 Sway Comparison of the Frame

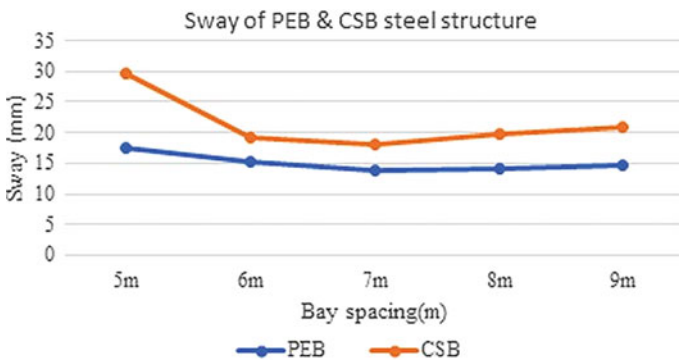
For sway analysis, bay spacing was considered from 5 to 9 m. As shown in Fig. 4 and Table 2, the sway reduction comparison is ranging from 21 to 41%. The bay spacing



**Fig. 3** Weight of PEB and CSB steel structure for different bay spacing

**Table 1** Weight of PEB and CSB steel structure for different bay spacing

Bay spacing (m)	PEB structure weight (Kg)	CSB structure weight (Kg)	% Weight reduction
5	51,300	54,625	6.08
6	47,187	58,935	19.95
7	49,027	58,497	16.18
8	57,703	58,563	1.5
9	60,968	65,035	6.25

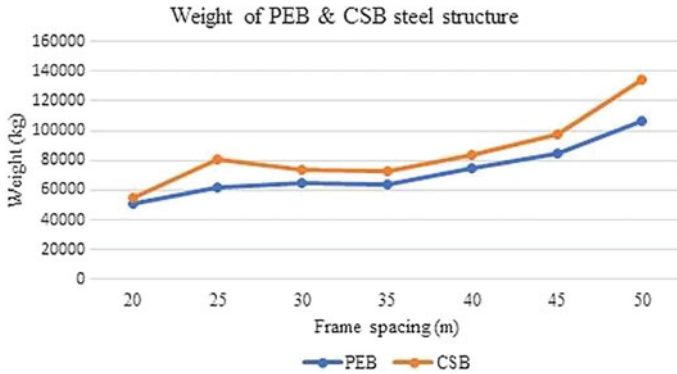


**Fig. 4** Sway of PEB and CSB steel structure for different bay spacing

of 5 m and 9 m gives maximum percentage of sway difference of 41% and 30% in PEB structure compared with CSB structure, respectively.

**Table 2** Sway of PEB and CSB steel structure for different bay spacing

Bay spacing (m)	PEB steel structure (mm)	CSB steel structure (mm)	% Sway reduction
5	17.6	29.54	41
6	15.3	19.24	21
7	13.84	18.04	23
8	14.03	19.74	29
9	14.74	20.94	30



**Fig. 5** Weight of PEB and CSB steel structure for different frame spacing

### 3.2 Comparison of PEB and CSB Structure for Different Frame Spacing

#### 3.2.1 Effects on Main Frame Weight

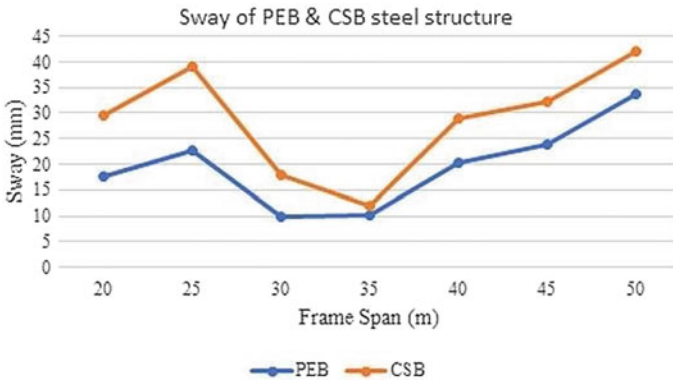
In the phase three, as shown in Fig. 5 and Table 3, it is observed that the PEB structure is approximately ranging from 6% to 23% lighter in weight compared with the CSB structure. However, 25 m span gives maximum percentage of weight reduction of 23%.

#### 3.2.2 Sway Comparison of the Frame

For the sway analysis, result gives the percentage difference of sway from 20.20% to 44.14% for PEB structure compared with CSB structure. It is found that, CSB structure shows comparatively larger lateral displacement than PEB structure. The maximum percentage difference in the displacement is 44.14% observed at 30 m span length (Fig. 6; Table 4).

**Table 3** Weight of PEB and CSB steel structure for different frame spacing

Frame spacing (m)	PEB steel structure (kg)	CSB steel structure (kg)	% Weight reduction
20	51,300	54,625	6.08
25	61,742	80,276	23.08
30	65,037	73,666	12
35	63,731	72,836	13
40	74,678	83,489	11
45	84,648	97,443	13
50	106,508	133,788	20



**Fig. 6** Sway of PEB and CSB steel structure for different frame spacing

**Table 4** Sway of PEB and CSB steel structure for different frame spacing

Frame spacing (m)	PEB steel structure (mm)	CSB steel structure (mm)	% Sway reduction
20	17.6	29.54	40.41
25	22.78	39.06	41.67
30	9.97	17.85	44.14
35	10.25	12.01	14.65
40	20.2	28.93	30.17
45	23.75	32.21	26.26
50	33.68	42.21	20.20

### 3.3 Seismic Analysis of CSB and PEB Structure

For seismic analysis, five different seismic zones are selected as per IS Code1893. For both CSB and PEB structure, the frame spacing and bay spacing were kept constant at 33 m and 6 m, respectively. As shown in Fig. 7, for all the seismic zones,

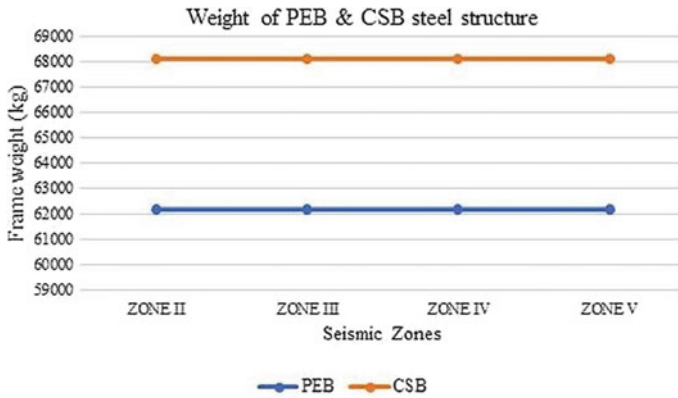


Fig. 7 Weight of PEB and CSB steel structure for different seismic zones

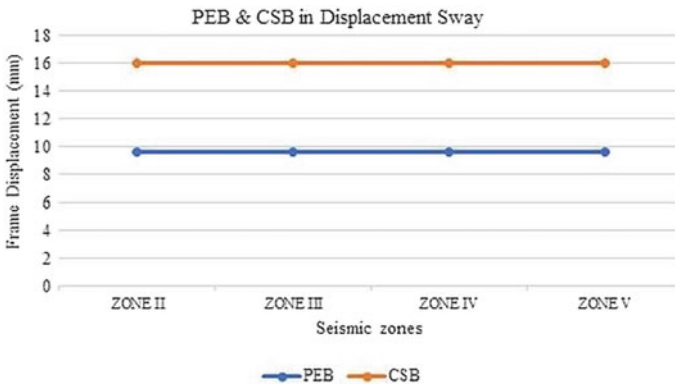
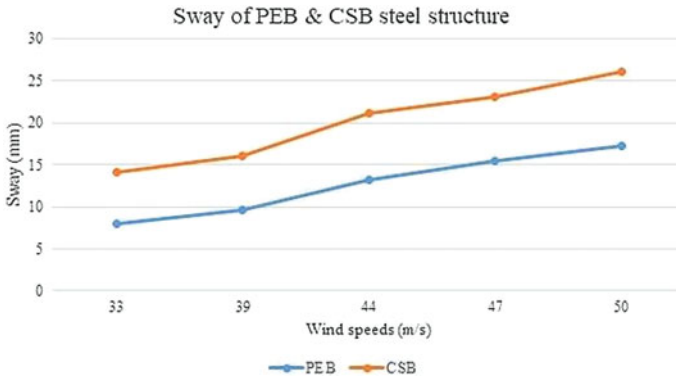


Fig. 8 Sway of PEB and CSB steel structure for different seismic zones

no structural weight difference is found. The sway of PEB structure is 9.66 mm that is found to be constant for all the seismic zones and similar behaviour is observed in case of CSB structure having sway of 15.97 mm (Fig. 8).

### 3.4 Wind Analysis of CSB and PEB Structure

In wind analysis, bay spacing and frame spacing were kept constant at values 6 m and 35 m, respectively. IS 875 (part 3) was used for the wind analysis. It is observed that 33 m/s wind speed gives maximum percentage of sway reduction of 43.71 % (Fig. 9; Table 5).



**Fig. 9** Sway of PEB and CSB steel structure for different wind speeds

**Table 5** Sway of PEB and CSB steel structure for different wind speed

Frame spacing (m)	Bay spacing (m)	Wind speed (m/s)	PEB (mm)	CSB (mm)	% Sway reduction
35	6	33	7.92	14.07	43.71
35	6	39	9.66	15.97	39.51
35	6	44	13.26	21.17	37.36
35	6	47	15.41	23.1	33.29
35	6	50	17.21	26.07	33.38

## 4 Conclusions

Following conclusions were drawn from the research as follows:

- In this PEB and CSB structural weight comparison, 6 m bay spacing gives maximum percentage of weight reduction of 19.95% for PEB structures compared with CSB structure.
- In PEB steel structure, bay spacing variation, 5 m and 9 m bay spacing give maximum percentage of sway difference of 41% and 30%, respectively compared with CSB structure.
- In this PEB and CSB structural weight comparison, percentage of weight reduction is ranging from 6 to 23%. PEB structure proves to be lighter in weight compared with the CSB structure. However, 25 m span gives maximum percentage of weight reduction of 23%.
- It is found that, CSB structure shows comparatively larger lateral displacement than PEB structure. The result gives the percentage difference of sway from 14.65% to 44.14% for PEB and CSB structures. The maximum difference in the displacement is 44.14% observed at 30 m span length.

- In seismic analysis, no structural weight difference is found for all the seismic zones. The sway of PEB structure is 9.66 mm which is found to be constant for all the seismic zones and similar behaviour is observed in case of CSB structure having sway of 15.97 mm.
- It is concluded that, the seismic forces do not play any significant role on both CSB and PEB structure due to minimum weight and lower roofing.
- In wind analysis, it is observed that 33 m/s wind speed gives maximum percentage of sway reduction of 43.71% for PEB structure compared with CSB structure.
- As wind speed increases, percentage of sway reduction decreases which shows that wind speeds play very important role in PEB and CSB structures.
- After analysing all the 42 models for PEB and CSB structure, the main frames of PEB structure have shown less lateral deflection (sway) compared with CSB structure.
- The study concludes that PEB structures are light weight and safe and gives better solutions than CSB structures.

**Acknowledgements** The authors are grateful to the industrial mentors for their thoughtful guidance and support. They are also indebted to Solstruct Consultancy LLP for offering all the required information regarding parameters, software and design specifications.

## References

1. Sharma L, Taak N, Mishra PK (2021) A comparative study between the pre-engineered structures and conventional structures using STAADPRO. *Mater Today: Proc* 45(2021):3469–3475
2. Kalesha S, Ratnamala Reddy BSS, Chaitanya Kumar Jagarapu D (2020) An analytical study on pre-engineered buildings using staad pro. *Mater Today: Proc* 5
3. Umair Saleem M, Ahmad Siddiqi Z, Qureshi H (2013) Minimum weight design of pre-engineered steel structures using built-up sections and cold formed sections. *Adv Mater Res* 684:125–129
4. Foroughi H, Moen CD, Schafer BW (2020) Experimental determination of stiffness and strength for metal building system rod bracing. *J Constr Steel Res* 171:106149
5. Ellobody E (2007) Buckling analysis of high strength stainless steel stiffened and unstiffened slender hollow section columns. *J Constr Steel Res* 63:145–155
6. Milner D, Wesevich J, Nikodym L, Nasri V, Lawver D, Mould J (2018) Improved blast capacity of pre-engineered metal buildings using coupled CFD and FEA modelling. *J Loss Prevent Process Ind*
7. Mohamed Ibrahim M, Mohamed El Aghoury I, Abdel-Basset Ibrahim S (2020) Finite element investigation on plate buckling coefficients of tapered steel members web plates. *Structures* 28:2321–2334

# Applicability of Meshfree Method in Computational Solid Mechanics



Kichu Paul and K. S. Babu Narayan

**Abstract** Meshfree methods are powerful computational tools that offer several advantages over conventional finite element methods. Based on a cloud of points, meshfree methods are easy to construct and provide great adaptivity. Among these methods, the element free Galerkin (EFG) method is widely used for solving solid mechanics problems. In this study, the influence of nodal density on accuracy and computational time is investigated using the EFG method for an axially loaded 1D bar. The method is also applied to a 2D cantilever beam that is subjected to a point load at the free end, and the essential boundary conditions are enforced using Lagrange multipliers. A MATLAB-based program is used to obtain displacement profiles along the length of the bar. The study evaluates the accuracy and computational cost of the EFG method and reports a good agreement between the obtained results and the exact analytical solution.

**Keywords** Meshfree method · Moving least square method · Lagrange multiplier · Element free Galerkin method

## Nomenclature

K	Global stiffness matrix
U	Global displacement vector
G	Global nodal vector
$\lambda$	Lagrange multiplier
F	Global force vector
x	Point in 1D
$x_i$	Point/node (whose weight is computed)
$u^h x$	Approximation of $u(x)$
$u(x)$	Field variable

---

K. Paul (✉) · K. S. Babu Narayan  
Department of Civil Engineering, National Institute of Technology Karnataka, Surathkal,  
Mangaluru 575025, India  
e-mail: [kp.197cv007@nitk.edu.in](mailto:kp.197cv007@nitk.edu.in)



$w_{iw}(x)$	Weight function of $i$ th node evaluated at a point $x$
$a(x)$	Coefficient vector
$p(x)$	Polynomial basis function
$q$	Nodal vector (essential boundary)
$\varnothing(x)$	Shape function

## 1 Introduction

Computational mechanics is used in the study of characteristics and behavior of engineering systems and physical phenomena that are governed by the laws of mechanics. Finite element method (FEM) has created a great impact on the ever-growing field of computational mechanics. Finite element method can be used for the design and development of physical systems. FEM fundamentally relies on discretization of problem domain using meshes which is not suited for the simulation of discontinuities and moving boundaries. For discontinuities, remeshing is to be done at each step so as to ensure that the meshes merges with the discontinuities. This will make the method quite burdensome by decreasing the accuracy and increasing the complexity of the simulation process. In meshfree methods, the representation of geometry and numerical discretization are primarily based on nodes and are used to resolve boundary/initial value partial differential equations (PDE) [5].

Many researches are going on in the area of meshfree methods due its versatility in solving mechanics problems. Meshfree methods are not based on elements, as in FEM, instead attempt to idealize the given geometry through approximations at nodes. Meshless approaches appear to be highly promising for a variety of problems including material and geometry discontinuities, composites, moving boundaries and so on [1, 11]. The meshfree methods, based on the Galerkin weak form, and finite element method has many similarities. Fixed and local interpolants are used in FEM, while moving least square (MLS) approximations are utilized in meshfree approaches such as the EFG [8]. MLS method approximates a set of points in single stretch, followed by another set of points in the succeeding stretch and the approximation goes on and finally minimizes the error.

The aim of this work is to demonstrate the applicability of the EFG method. The method is applied to an axially loaded 1D bar and a 2D cantilever beam subjected to a point load at the free end, as these structures represent common engineering problems that can be effectively analyzed using the EFG method. The accuracy, characteristics and computational effectiveness of EFG method are examined. A MATLAB program is used to formulate equations of EFG method.

### 1.1 Meshfree Method

A system of algebraic equations is developed using meshfree techniques to solve the problem domain [9]. A cloud of points known as field nodes are scattered within the problem domain and on its boundaries. The EFG method is one of the most widely used meshfree methods for solving boundary value problems, owing to its ability to handle complex geometries and its high accuracy in numerical approximations [4]. In contrast to FEM, just nodes were employed to discretize the problem, and the weak form of the equilibrium equations uses moving least square (MLS) shape functions [2]. The EFG method is a novel approach that is currently being used to a wide range of applied mechanics problems [4].

### 1.2 Need for Meshfree Method

Meshfree methods are robust, flexible and versatile methods that have widespread applications. The method is used to solve many kinds of linear and nonlinear problems. Meshfree methods have many advantages over FEM.

- The absence of mesh eliminates the difficulty in remeshing due to element distortion [9].
- Easily adaptable refinement schemes to improve the accuracy.
- In FEM, the displacement functions are piecewise continuous, so that the stresses obtained will be discontinuous at the interface. The stresses obtained from meshfree methods do not have discontinuity as the displacement functions are continuous over the whole domain [3].

### 1.3 Moving Least Squares Shape Functions

Due to the approximation functions at the nodes not being equal to unity, the moving least squares approach does not result in interpolants that pass through the data points [9]. Least square approximation minimizes the square of the residual over the whole set of points in the domain [10]. Moving least square (MLS) approximation uses localized weight function that limits the influence of its nodes locally to the corresponding domain of influence. Meshfree shape functions are built using the MLS approximations [8]. The accuracy of solutions in the MLS approach is influenced by the shape function and approximate values of the field variables. When interpolating scattered data in multiple dimensions, the MLS approach outperforms the non-interpolating conventional least squares (LS) method. Let  $u^h(x)$  is the approximation of  $u(x)$  at a point  $x$  in the problem domain  $\Omega$  [9], then,

$$u^h(x) = p^T(x)a(x), \tag{1}$$

where  $p(x)$  is a polynomial basis function and  $m$  is the number of monomials in the basis function. In two- and three-dimensional problems, the Pascal's triangle and pyramid are the building blocks from which the  $p(x)$  is constructed. By minimizing the weighted residual function, the coefficients of 'a' can be found [9].

$$J(x) = \sum_{i=1}^n w_i(x) [p^T(x_i)a(x) - u_i]^2 \tag{2}$$

The weight function  $w_i(x)$  is evaluated at a Gauss point  $x$  to determine the influence of each node  $i$  within the domain. The total number of nodes in the influence domain of  $x$  is denoted by  $n$ , and the nodal value of  $u$  when  $x = x_i$  is represented by  $u_i$  [9]. The weight function of  $i$ th node is defined as,

- $w_i(x) > 0$  within the support domain.
- $w_i(x) = 0$  outside the support domain.

The cubic spline, quartic spline and exponential functions are used as weight functions.

On minimizing Eq. (2), the Eq. (1) can be rewritten as [5, 6, 9] (Figs. 1 and 2),

$$u^h(x) = p^T(x)A^{-1}(x)B(x)u = \phi^T(x)u. \tag{3}$$

In order to impose fundamental boundary conditions such as essential boundary conditions, the EFG method often utilizes Lagrange multipliers. These multipliers

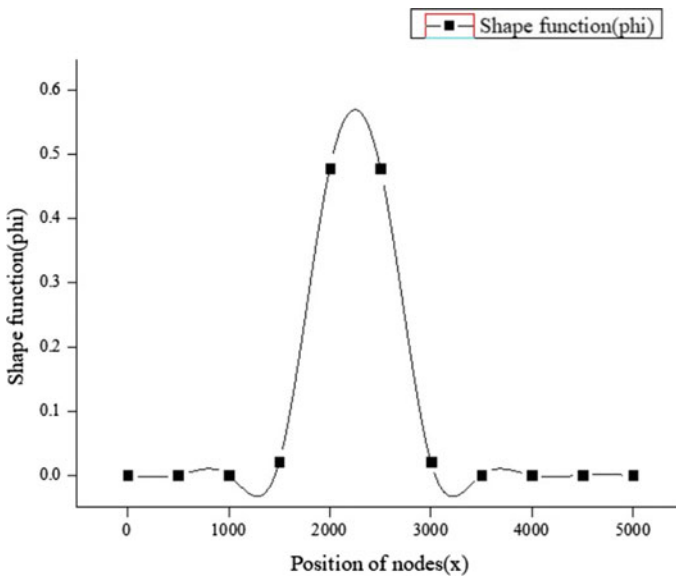
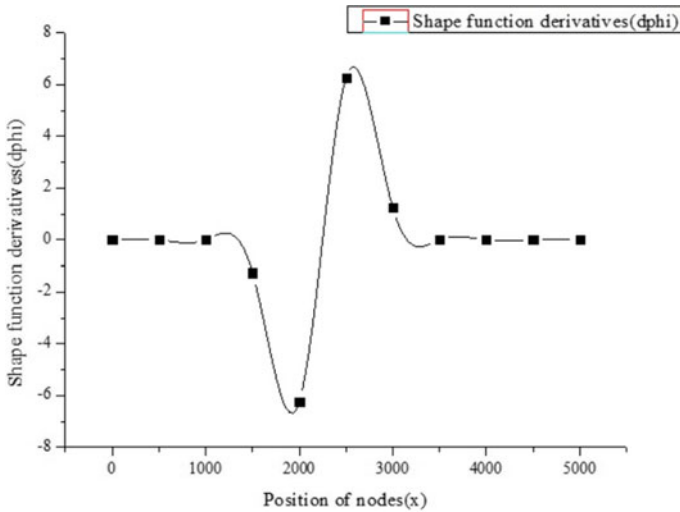


Fig. 1 EFG shape function in one dimension



**Fig. 2** Shape function derivatives in one dimension

provide a mechanism for enforcing the constraints of the boundary conditions within the solution [7, 8]. The discrete linear system of equations in EFG method using Lagrange multiplier is as follows [9],

$$KU - G\lambda - F = 0, \tag{4}$$

$$G^T\lambda - q = 0. \tag{5}$$

The final displacements of the problem can be evaluated from Eqs. (4) and (5). Although MLS shape functions are commonly used in meshfree methods for interpolation and approximation, they do not satisfy the Kronecker delta property. This property, which requires that shape functions evaluate to 1 at their respective node and 0 elsewhere is not satisfied by MLS shape functions due to the nature of the weighted least squares formulation. So the MLS shape functions are categorized as approximants rather than interpolants. Because of this, the values derived through the MLS approximation do not represent the nodal values, instead, they are referred to as nodal parameters or fictitious nodal values [5, 9].

## 2 Problem Definition

### 2.1 Problem 1

In linear elastostatics, the EFG method can be applied to analyze an axially loaded bar in one dimension. A bar of 1000 mm length ( $L$ ) is subjected to an axial force ( $P$ ) of 50 kN at the free end. One end of the bar is fixed. The material properties considered are Young's modulus ( $E$ ) =  $2.1 \times 10^5$  N/mm<sup>2</sup>, cross-sectional area ( $A$ ) = 10,000 mm<sup>2</sup>.

Exact solution: Deflection at free end of bar,  $u_{\text{exact}} = \frac{PL}{AE}$ .

### 2.2 Problem 2

The EFG method can be utilized for the two-dimensional analysis of a cantilever beam that is subjected to a point load at the free end. The beam is of unit thickness. The width of beam is  $D = 1$  m,  $L = 5$  m,  $\nu = 0.3$ ,  $P = 500$  N,  $E = 2.1 \times 10^5$  N/mm<sup>2</sup>. A cloud of points is used to discretize the domain of the beam. The Galerkin weak form is integrated using a background mesh, where the nodes are distributed regularly. In each integration cells,  $4 \times 4$  Gauss quadrature is used to evaluate the stiffness matrix. The deflection of beam is an important parameter that is used to assess the performance of the beam under different loading conditions.

Exact solution: Deflection at the free end of a cantilever beam,  $u_{\text{exact}} = \frac{PL^3}{3EI}$

## 3 Results and Discussions

In the EFG method, the bar's length is discretized into a cloud of nodes, with integration points selected between the nodes using Gauss's method to achieve the best possible accuracy with a given number of nodes. The governing differential equation is then transformed from its conventional weighted residual form into a local weak form. Trial functions or shape functions are constructed using MLS interpolation to approximate the solution. Lagrange multipliers are used to enforce essential boundary conditions. A system of algebraic equations is obtained by substituting the trial and test functions into the local weak form. This system of equations represent the discretized form of the governing differential equation, and it can be used to numerically solve for the unknowns of the problem such as displacement, stress, and strain. Gauss quadrature is used to integrate the Galerkin weak form [5, 6]. The choice is made to use test functions with clearly defined shapes and values that disappear within the support domain. After computing the shape functions, the global stiffness

matrix and force vector are evaluated, and essential boundary conditions are imposed. The global system of equations are then solved to determine the displacement field, stress and strain fields [3, 7].

### 3.1 Problem 1

The EFG meshfree method is used to describe the behavior of one-dimensional bar subjected to axial (tensile) load at the free end. The length of the bar is discretized into cloud of nodes, i.e., 11 uniformly spaced nodes. Galerkin weak form integration is carried out using one point gauss quadrature [5, 6]. The integration points are chosen exactly at the mid-point of the interval between the nodes. To determine the effectiveness of the EFG method, the solutions are compared with the exact theoretical values. The precision and effectiveness of the method depend on various parameters such as the nodal density and weight function [12]. The computational cost includes the time required to create the geometry, discretize the domain, generate the necessary matrices (especially the stiffness matrix) and solve the problem.

The displacement obtained from EFG method is compared with those of the analytical solution in order to validate it as a potential meshfree technique [13] (Fig. 3).

It is found that the displacement field calculated with EFG method matches with the analytical solution.

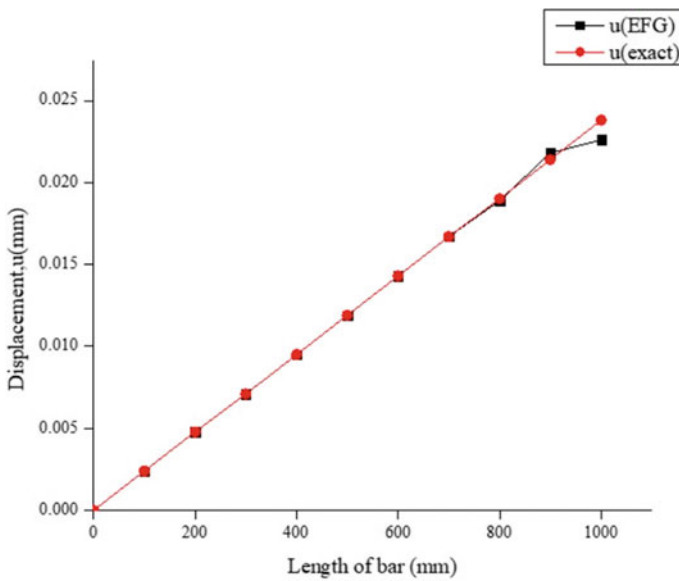


Fig. 3 Comparison of EFG and exact analytical results for displacement field

The EFG approach is investigated for convergence by discretizing the elastic bar domain initially with eleven nodes and subsequently with 21, 51, 81 and 101 nodes. The aim is to analyze the effect of nodal density on the accuracy and precision of the EFG method. The weight function is a cubic spline function for all node schemes [13] (Figs. 4 and 5).

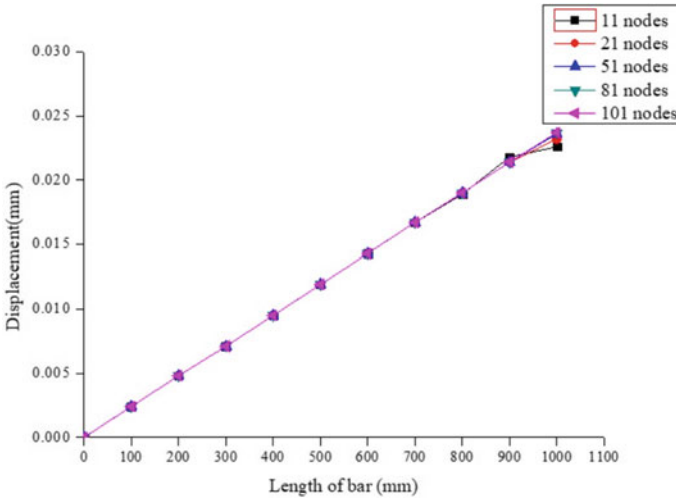


Fig. 4 Dependence of nodal density on displacement field

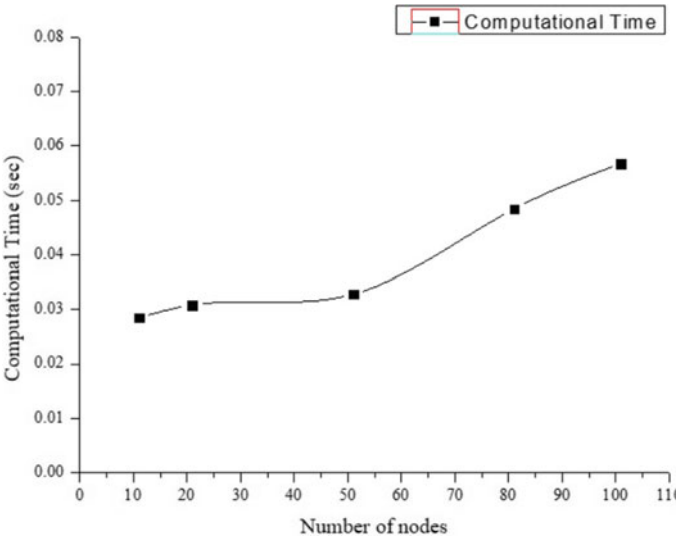


Fig. 5 Dependence of nodal density on computational time

The graph shows that nodal density has great influence on the computational cost. Dense nodes require more time to determine the solution of the problem. When compared with inverting the matrix, the stiffness matrix generation takes longer time [12]. In light of this, it can be said that one of the key factors in computing efficiency is the number of nodes.

### 3.2 Problem 2

The EFG method is used to analyze a cantilever beam in 2D subjected to point load at free end. The domain of beam is discretized with a set of points. A regular number of nodes is used and the Galerkin weak form is integrated using a background mesh. In each integration cell,  $4 \times 4$  Gauss quadrature is used to evaluate the stiffness matrix [5, 6]. A linear basis function is adopted with cubic spline weight function. A comparison of displacements obtained from EFG method and those obtained from analytical method (Fig. 6) is made and found the same.

The shear stresses across the beam are plotted, and the results obtained using the EFG method show good agreement with the exact solution (Fig. 7).

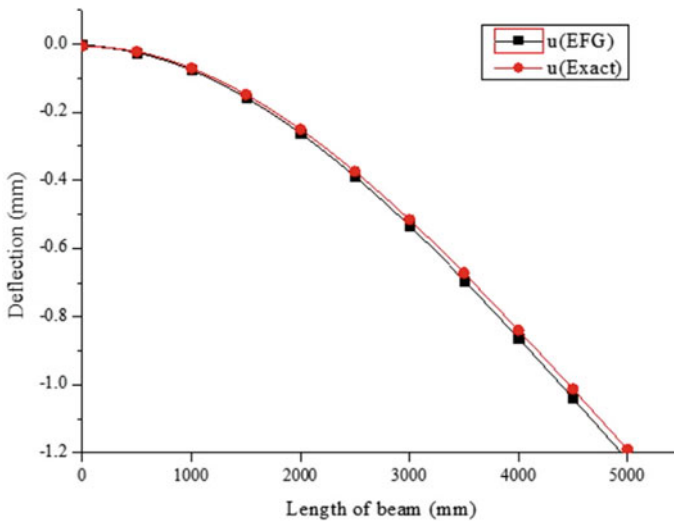


Fig. 6 Deflection along the length of beam



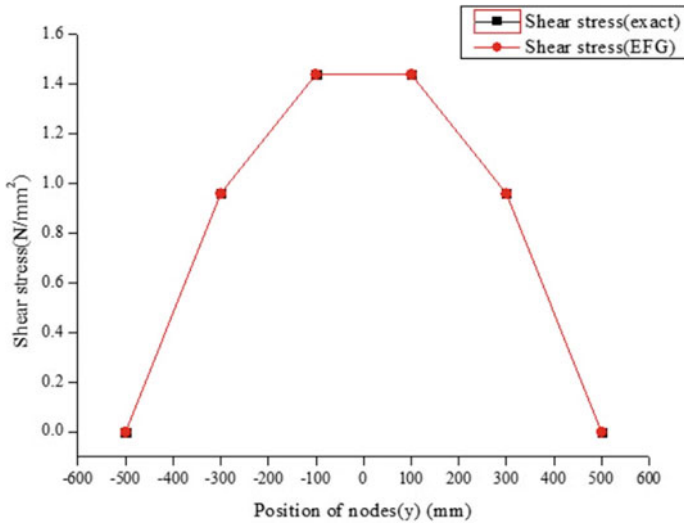


Fig. 7 Shear stress in beam

## 4 Conclusions

The study evaluates the suitability of the EFG method for solving computational solid mechanics problems and concludes that the method can effectively analyze 1D bars and 2D beams. Comparative studies demonstrate that the solutions obtained using the EFG method exhibit good agreement with the exact theoretical solutions, indicating the method's precision and adaptability. This is due to the smoothness of the moving least squares approximations. However, one of the main drawbacks of the EFG approach is its high computational cost.

## References

1. Atluri SN, Zhu T (2000) New concepts in meshless methods. *Int J Numer Methods Eng* 47(1–3):537–556. [https://doi.org/10.1002/\(SICI\)1097-0207\(20000110/30\)47:1/3<537::AID-NME783>3.0.CO;2-E](https://doi.org/10.1002/(SICI)1097-0207(20000110/30)47:1/3<537::AID-NME783>3.0.CO;2-E)
2. Belytschko T, Lu YY, Gu L (1994) Element-free galerkin methods. *Int J Numer Methods Eng* 37:229–256. <https://doi.org/10.1002/nme.1620370205>
3. Bhavana Patel SS, Babu Narayan KS, Venkataramana K (2014) Modeling high stress gradients in plates by meshfree method. *J Civ Eng Technol Res* 2(1):71–76
4. Brighenti R (2005) Application of the element-free Galerkin meshless method to 3-D fracture mechanics problems. *Eng Fract Mech* 72(18):2808–2820
5. Dolbow J, Belytschko T (1998) An introduction to programming the meshless element free Galerkin method. *Arch Comput Methods Eng* 5(3):207–241. <https://doi.org/10.1007/BF02897874>

6. Dolbow J, Belytschko T (1999) Numerical integration of the Galerkin weak form in meshfree methods. *Comput Mech* 23:219–230. <https://doi.org/10.1007/s004660050403>
7. Kishore NPM, Patel B, BabuNarayan K (2015) Potential applicability of Meshfree method using Lagrange multiplier. *Int J Res Eng Technol* 3(6):19–28. ISSN(E): 2321-8843; ISSN(P): 2347-4599
8. Liu GR, Gu YT (2005) An introduction to Meshfree methods and their programming. <https://doi.org/10.1007/1-4020-3468-7>
9. Liu GR (2009) Meshfree methods: moving beyond the finite element method (2nd ed). CRC Press. <https://doi.org/10.1201/9781420082104>
10. Lancaster P, Salkauskas K (1981) Surfaces generated by moving least squares methods. *Math Comput* 37(155):141. <https://doi.org/10.1090/S0025-5718-1981-0616367-1>
11. Nguyen VP, Rabczuk T, Bordas S, Duffot M (2008) Meshless methods: a review and computer implementation aspects. *Math Comput Simul* 79(3):763–813. <https://doi.org/10.1016/j.matcom.2008.01.003>
12. Valencia OF, Gomez-Escalonilla FJ, López Díez J (2008) Influence of selectable parameters in element-free Galerkin method: one-dimensional bar axially loaded problem. *Proc Inst Mech Eng Part C J Mech Eng Sci* 222(9):1621–1633
13. Vyas JN, Daxini S (2016) Meshless formulation and parameters study for an elastic bar problem. In: International conference on electrical, electronics, and optimization techniques (ICEEOT), Chennai, India, pp 1694–1699. <https://doi.org/10.1109/ICEEOT.2016.7754975>

# Thermal Degradation of Kinetics of PET, PTT and PBT Hybrid Nanocomposites



Abjesh Prasad Rath, P. Santhana Gopala Krishnan, and K. Kanny

**Abstract** Poly (ethylene terephthalate) (PET), Poly (trimethylene terephthalate) (PTT) and Poly (butylene terephthalate) (PBT) and its hybrid nanocomposites containing graphene oxide (GO) and functionalized multi-walled carbon nanotubes (f-MWCNT) were prepared by melt blending. Both pristine polyesters and the hybrid nanocomposites were studied for thermal degradation kinetics using thermogravimetric analyzer. The nanocomposites were studied from the temperature range of 100 to 800 °C at a heating rate of 10 °C/min in a nitrogen atmosphere. Activation energy ( $E_a$ ) and pre-exponential or frequency factor ( $A$ ) were determined for the thermal degradation of these nanocomposites using the Coats–Redfern equation and was found to follow first-order kinetics in nitrogen atmosphere. The effect of nanofiller content on the parameters of thermal degradation kinetics was discussed.

**Keywords** Polyesters · Thermal degradation · Non-isothermal kinetics · Coats–Redfern equation

---

A. P. Rath

Laboratory for Advanced Research in Polymeric Materials (LARPM), School for Advanced Research in Petrochemicals (SARP), Central Institute of Petrochemicals Engineering and Technology (CIPET), Patia, Bhubaneswar 751024, India

P. Santhana Gopala Krishnan (✉)

Advanced Polymer Design and Development Research Laboratory (APDDRL), School for Advanced Research in Petrochemicals (SARP), Central Institute of Petrochemicals Engineering and Technology (CIPET), Devanahalli, Bengaluru 562149, India  
e-mail: [psgkrishnan@hotmail.com](mailto:psgkrishnan@hotmail.com)

A. P. Rath · K. Kanny

Composites Research Group, Department of Mechanical Engineering, Durban University of Technology, Durban 4000, South Africa

P. Santhana Gopala Krishnan

Faculty of Engineering and the Built Environment, Durban University of Technology, P O Box 1334, Durban 4000, South Africa

## 1 Introduction

Recent years have seen a rise in the importance of PET, PTT and PBT as members of the aromatic polyesters made from diols such as ethylene glycol, 1,3-trimethylene diol and 1,4-butane diol. Most aspects of PET, PTT and PBT have been extensively researched, including synthetic technique, spinning technology, morphological structure and fibre properties and crystallization behaviour. Although the thermogravimetric analysis (TGA) plot of pristine aromatic polyesters under nitrogen has also been reported, the thermal decomposition kinetics of these aromatic polyester-based hybrid nanocomposites have received no attention. TGA was used in this study to examine the thermal degradation of three polyesters with various amounts of hybrid nanofillers in a nitrogen atmosphere. The many physical or chemical properties of polymers today are provided by nanoscale additives and fillers. Depending on the intended use, organic or inorganic additives enhance the desired polymer properties. Here the aromatic linear polyesters undergoes complex physiochemical transformations after reinforcement with GO and f-MWCNT by melt blending [1]. Such degradative processes may be induced by thermal or chemical interactions between the matrix and nanofiller during processing. Like those different mechanisms and kinetics of degradation of polyester nanocomposites have long been of interest. When a polyester nanocomposite is heated it undergoes decomposition, which is an important class of solid-state reaction. But compared with conventional isothermal methods, non-isothermal methods for determining kinetic parameters have lot of benefits. A single sample and less data are required and the kinetics can be calculated over an entire temperature range in a continuous manner [2]. Kinetics studies were generally carried out on similar compounds with a correctly chosen mechanical function  $f(\alpha)$  ( $\alpha$  is the weight fraction of material decomposed at temperature  $T$  and time  $t$ ) and show a linear relationship between the logarithm of pre-exponential factor and activation energy. There are different methods to study the thermal degradation and determination of the kinetic parameters which include Flynn Wall and Ozawa (FWO), Kissinger-Akahira-Sonuse (KAS), Kissinger and Coats Redfern method. The advantage of the Coats–Redfern method requires a single heating rate for the determination of thermal degradation kinetic parameters, whereas in other above-mentioned methods, TGA analysis has to be done in at least three different heating rates. Mathematical analysis was performed on the thermogravimetric data using the integral method of the Coats and Redfern which has been used successfully for studies on the kinetics of thermal degradation of solid substance. The activation energy ( $E_a$ ) and the logarithmic value of pre-exponential or frequency factor ( $A$ ) for the degradation of hybrid nanocomposites have been successfully calculated from the thermogravimetric curves [3].

Due to the reinforcement of GO and f-MWCNT in aromatic polyesters, both thermal and electrical conductivity is enhanced, making it ideal for many applications. However, to the best of our knowledge, thermal degradation kinetic study on these hybrid nanocomposites was not reported so far. This study will shed light to understand the effect of hybrid nanofillers on the thermal stability of the prepared nanocomposites.

## 2 Experimental

### 2.1 Materials

PET was purchased from Kalinga Gas Pvt. Ltd., Bhubaneswar of grade AS19C. PTT was supplied by Futura Polyesters Limited, Chennai, India. PBT was purchased from D.R Polymer Pvt. Ltd., Chennai, India. Graphite with a mean particle size of  $<20\ \mu\text{m}$ , sodium nitrate ( $\text{NaNO}_3$ ), and potassium permanganate ( $\text{KMnO}_4$ ) were purchased from United Scientific, SA. Conc. sulphuric acid ( $\text{H}_2\text{SO}_4$ ), conc. hydrochloric acid ( $\text{HCl}$ ), anhydrous tetrahydrofuran (anhydrous THF) and hydrogen peroxide ( $\text{H}_2\text{O}_2$ ) were purchased from local chemical suppliers. Multi-walled carbon nanotubes (MWCNT)s of a specific grade (Nanocyl NC 7000) were purchased from Platonic Nanotech Pvt. Ltd., Jharkhand. Conc. nitric acid ( $\text{HNO}_3$ ) was purchased from United Nanotech Innovation Pvt. Ltd., Bangalore used without further purification.

### 2.2 Nanocomposites Preparation

The GO was synthesized using a modified Hummer's method [4], which utilized graphite powder as a starting material. 0.5 g graphite powder was pre-oxidized using 23 mL concentrated  $\text{H}_2\text{SO}_4$  and 0.5 g  $\text{NaNO}_3$  in a conventional process. MWCNTs were dispersed in a mixture of  $\text{H}_2\text{SO}_4$  and  $\text{HNO}_3$  with volume ratio of 3:1. Carboxylic acid-functionalized MWCNTs (f-MWCNT)s were obtained by oxidation of pristine MWCNTs via ultrasonication in sulfuric-nitric acid mixture [5]. Polyester hybrid nanocomposites containing 0 wt.% to 2 wt.% GO and 2 wt.% to 0 wt.% of f-MWCNT were prepared by melt compounding, on a Haake Rheomix OS batch mixer with different melting conditions. The overall nanofiller content was kept constant at 2 wt.%. The formulations for different nanocomposites are mentioned in Table 1.

**Table 1** Samples code and formulation of hybrid polyester nanocomposites

Sample code	Polyesters	GO	f-MWCNT
	(wt.%)	(wt.%)	(wt.%)
PET/PTT/PBT	100	0	0
M2	98	0	2
G0.5M1.5	98	0.5	1.5
G1M1	98	1	1
G1.5M0.5	98	1.5	0.5
G2	98	2	0

### 2.3 Characterization

The densities of the nanocomposites were determined as per ASTM D729 using Mettler Toledo instrument (Mettler Toledo India Private Limited, Mumbai, India). The specimen is weighed in air then weighed when immersed in distilled water at 23 °C using a sinker and wire to hold the specimen completely submerged as required. Density and specific gravity are calculated by immersion method. Density of nanocomposites reflects the microstructure's tightness, which is governed by the specific volume ( $\nu$ ). The density of nanocomposites ( $\nu_{\text{mix}}$ ) can be computed using the equation below in an ideal state.

$$\rho_{\text{mix}} = \frac{m_{\text{mix}}}{\nu_{\text{mix}}} = \frac{m_{\text{mix}}}{\frac{m_1}{\rho_1} + \frac{m_2}{\rho_2} + \frac{m_3}{\rho_3}} = \frac{1}{\frac{m_1}{m_{\text{mix}}\rho_1} + \frac{m_2}{m_{\text{mix}}\rho_2} + \frac{m_3}{m_{\text{mix}}\rho_3}}. \quad (1)$$

Now simplify this equation as follows

$$\frac{1}{\rho_{\text{mix}}} = \frac{m_1}{m_{\text{mix}}\rho_1} + \frac{m_2}{m_{\text{mix}}\rho_2} + \frac{m_3}{m_{\text{mix}}\rho_3}. \quad (2)$$

The density and quantity of the nanofiller in the nanocomposites determine the specific volume of the nanocomposites ( $\nu_{\text{mix}}$ ).

$$\nu_{\text{mix}} = \frac{1}{\rho_{\text{mix}}} = \frac{w_1}{\rho_1} + \frac{w_2}{\rho_2} + \frac{w_3}{\rho_3}, \quad (3)$$

where  $\rho_1$  and  $w_1$  are density and weight fraction of polyesters, respectively,  $\rho_2$  and  $w_2$  that of GO and  $\rho_3$  and  $w_3$  that of f-MWCNT, respectively.

The following equation can be used to compute the densification of nanocomposites.

$$\Delta\nu = (\nu - \nu_{\text{mix}}) \quad (4)$$

### 2.4 Polymer Degradation

To determine the kinetic degradation parameters, all the polyesters and their hybrid nanocomposites were subjected to TGA. The decomposition temperatures for PET, PTT and PBT were measured using an STA 7300 simultaneous TGA instrument supplied by Hitachi, Japan. The heating rate chosen was 10 °C/min and the temperature range scanned was 100–800 °C. The weight loss of the polymer nanocomposites was determined by loading 11–12 mg into a platinum crucible and heating it under a

steady flow of nitrogen (50 mL/min). The output signals from the STA 7300 analyzer were fed to a computer interface, where the data was stored.

### 3 Result and Discussions

#### 3.1 Density Studies

The density of nanocomposites indicates the tightness between the matrix and filler. The density of composite material depends on the relative proportion of reinforcing and matrix material [6]. The void content only makes difference between theoretical and experimental densities. Larger the contents of the void lesser is the density and vice versa. The void content affects the mechanical properties and even the performance of nanocomposites in the workplace. Nanocomposites in comparison with the pristine polyesters have slightly higher experimental density due to the presence of nanofillers of higher density [7].

Both experimentally determined densities and specific volume of neat PET, PTT and PBT and their nanocomposites are given in the Table 2a–c, respectively. Theoretical density was determined using the Eq. 3. Theoretical density of amorphous PET is 1.37 g/cc which is comparable with the experimentally determined density of PET is 1.3757 g/cc [8]. Similarly the experimentally determined density of PTT and PBT are 1.3190 and 1.2982 g/cc which is comparable with the reported amorphous density of PTT and PBT 1.31 and 1.298 g/cc, respectively [8]. It is also reported that the true density of f-MWCNT is 2.1 g/cc [9] and GO is 3.6 g/cc [10]. These values were taken for calculation of  $v_{\text{mix}}$  of hybrid nanocomposites. The  $\Delta v$  is difference between the theoretical and experimental values of densities as given in Table 2.

For the PET and PTT nanocomposites, the  $\Delta v$  value exhibited positive number indicating a loose microstructure of the nanocomposites. Poly (urethane methacrylate) nanocomposites were shown to have a comparable effect [11]. Negative  $\Delta v$  value indicated that the structure of the M2 and G0.5M1.5 in PBT nanocomposites is in condensed form/tight form as given in Table 2c [12]. The reason behind the condensed structure of nanocomposites was credited to the nucleating effects of GO and f-MWCNT. A similar observation was reported for PLA nanocomposites [13].

#### 3.2 Thermogravimetric Studies

PET, PTT and PBT and their nanocomposites were analyzed using a thermogravimetric analysis (TGA) to determine the percentage of ash content. The polyesters PET, PTT and PBT have a notable stability, as the degradation process begins above 320 °C. It occurs in two steps up to a complete weight loss up to 800 °C as shown in Fig. 1a. The first process is caused by degradation of the polymer chain implying

**Table 2** (a) Specific volume of PET and its nanocomposites

Sample code	Density (g/cc)	$v$ (ml/g)	$v_{\text{mix}}$ (ml/g)	$\Delta v$ (ml/g)
PET	1.3757	0.7269	–	–
M2	1.3822	0.7235	0.7219	0.0016
G0.5M1.5	1.3818	0.7237	0.7209	0.0028
G1M1	1.3831	0.7230	0.7200	0.0030
G1.5M0.5	1.3847	0.7222	0.7190	0.0032
G2	1.3807	0.7243	0.7180	0.0063

(b) Specific volume of PTT and its nanocomposites

PTT	1.3190	0.7582	–	–
M2	1.3276	0.7532	0.7525	0.0007
G0.5M1.5	1.3246	0.7549	0.7515	0.0034
G1M1	1.3310	0.7513	0.7506	0.0007
G1.5M0.5	1.3284	0.7528	0.7496	0.0032
G2	1.3275	0.7533	0.7486	0.0047

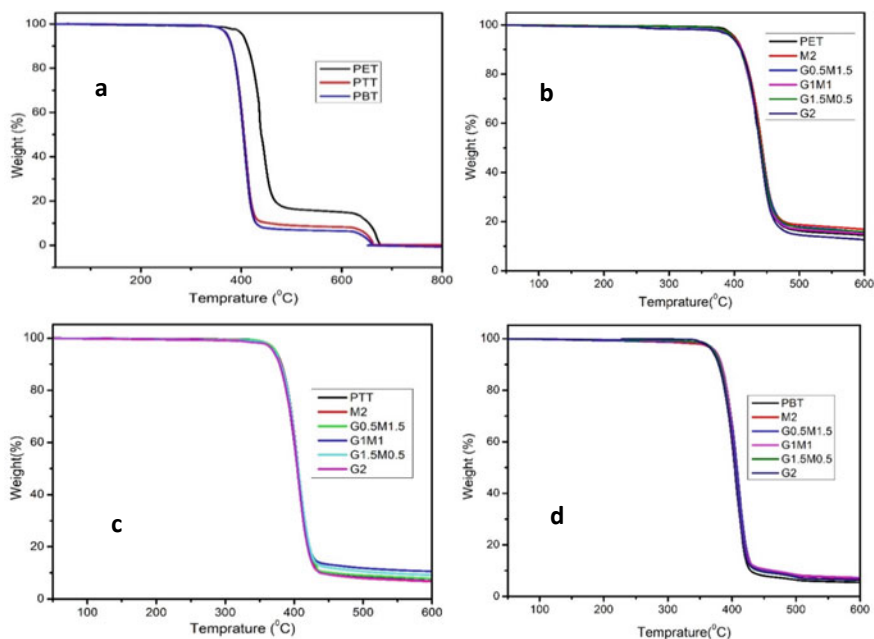
(c) Specific volume of PBT and its nanocomposites

PBT	1.2982	0.7730	–	–
M2	1.3143	0.7609	0.7649	-0.0035
G0.5M1.5	1.3154	0.7602	0.7634	-0.0032
G1M1	1.3071	0.7651	0.7625	0.0026
G1.5M0.5	1.3102	0.7632	0.7615	0.0017
G2	1.3014	0.7707	0.7605	0.0079

an end group initiation mechanism affected by the molecular weight of polyesters. The second degradation process is mainly caused by the thermal degradation of the products formed during the first decomposition process and it is not affected by the molecular weight (end groups) of polyesters [14].

The degradation reaction model was anticipated by Martin-Gullon [15] based on two independent portions of the mass loss curve: the first, when the initial PET, PTT and PBT sample thermally degraded (about 80%) fast into char and volatiles at around 347–527 °C. The char slowly disintegrated (6–7%) in the second part as the temperature increased. To lower the residual amount, the char (residue) can be combusted. The maximum decomposition temperature in second step of degradation for PET, PTT and PBT is 667, 656 and 657 °C, respectively, which confirm the thermal stability of PET is high when compared with PTT and PBT. In a comparative approach, during a thermal decomposition, it was also observed that both PTT and PBT underwent molecular weight degradation faster than PET which was assigned to the contribution of chain propagation reactions due to vinyl end groups [16]. It was also observed that for neat PET, PTT and PBT having no residue or 0% residue at 800 °C which authenticates those polyesters have fully degraded.





**Fig. 1** Weight loss curve as a function of temperature for **a** Neat PET, PTT and PBT up to 800 °C and **b, c, d** Their nanocomposites up to 600 °C

The 5% weight loss temperature, the maximum decomposition temperature ( $T_{max}$ ) and the charred residue at 600 °C and 800 °C are listed in Table 3. It can be seen that the thermal degradation temperature of 5wt.% weight loss of the PET nanocomposites increased substantially when compared with neat PET, whereas in the case of nanocomposites of PTT and PBT, the increase is marginal when compared with neat PTT and PBT. The maximum decomposition temperature of PET, PTT and PBT nanocomposites was higher than the corresponding neat polyesters which attributed to the increased thermal stability. It can also be seen from the Fig. 1b–d and Table 3 that the charred residue at 600 °C for polyesters nanocomposites increased when compared with the neat polyesters. The improved thermal stability was attributed to the higher barrier effect of the incorporated nanoparticles.

### 3.3 Kinetics of Thermal Degradation

TGA-based kinetic analysis using the Coats and Redfern technique to determine the variable activation energy of the polyester's degradation reaction revealed that the variable kinetic parameters are more likely to predict the degradation mechanism of plastics such as PET, PTT and PBT under simulated heating conditions.

**Table 3** (a) TGA data of PET nanocomposites under nitrogen atmosphere at 10 °C/ min

Code	Temp	T <sub>max1</sub> (°C)	T <sub>max2</sub> (°C)	Residue (%)	
	(5% wt. loss)			600 °C	800 °C
PET	390	427	667	14.4	0
M2	400	434	–	15.5	–
G0.5M1.5	397	435	–	15.7	–
G1M1	398	435	–	15.1	–
G1.5M0.5	398	436	–	15.8	–
G2	396	434	–	14.6	–

(b) TGA data of PTT nanocomposites under nitrogen atmosphere at 10 °C/min

PTT	371	427	656	6.0	0
M2	373	438	–	8.7	–
G0.5M1.5	373	433	–	7.7	–
G1M1	371	433	–	10.6	–
G1.5M0.5	371	436	–	11.2	–
G2	370	432	–	6.9	–

(c) TGA data of PBT nanocomposites under nitrogen atmosphere at 10 °C/min

PBT	370	435	657	5.4	0
M2	370	438	–	6.9	–
G0.5M1.5	374	441	–	7.1	–
G1M1	375	449	–	7.3	–
G1.5M0.5	373	445	–	6.1	–
G2	370	439	–	6.3	–

There are different types of kinetics methods available to characterize the thermal degradation of polymeric materials. From different methods, the Coats–Redfern method [17] is used here to calculate the thermal stability of PET, PTT and PBT and its nanocomposites. This formulation is used here because there are no significant changes seen in the mechanism throughout the reaction.

By assuming that only one reaction can happen at a time, we can express the product disappearance as following basic rate of change of equation,

$$\frac{d\alpha}{dt} = k(1 - \alpha)^n, \quad (5)$$

where  $\alpha$  = fraction of decomposed at time  $t$ ,  $n$  = order of reaction,  $k$  = rate of constant where it is equal to

$$k = Ae^{-E_a/RT}, \quad (6)$$

where  $A$  = frequency factor,  $E_a$  = activation energy,  $R$  = universal gas constant,  $T$  = Absolute temperature again, fraction decomposed ( $\alpha$ ) is defined as

$$\alpha = \frac{m_i - m}{m_i - m_f},$$

where  $m$  is the mass of the sample and subscripts,  $i$  and  $f$  denote initial and final states, respectively. For a linear heating rate of say, a deg./min.

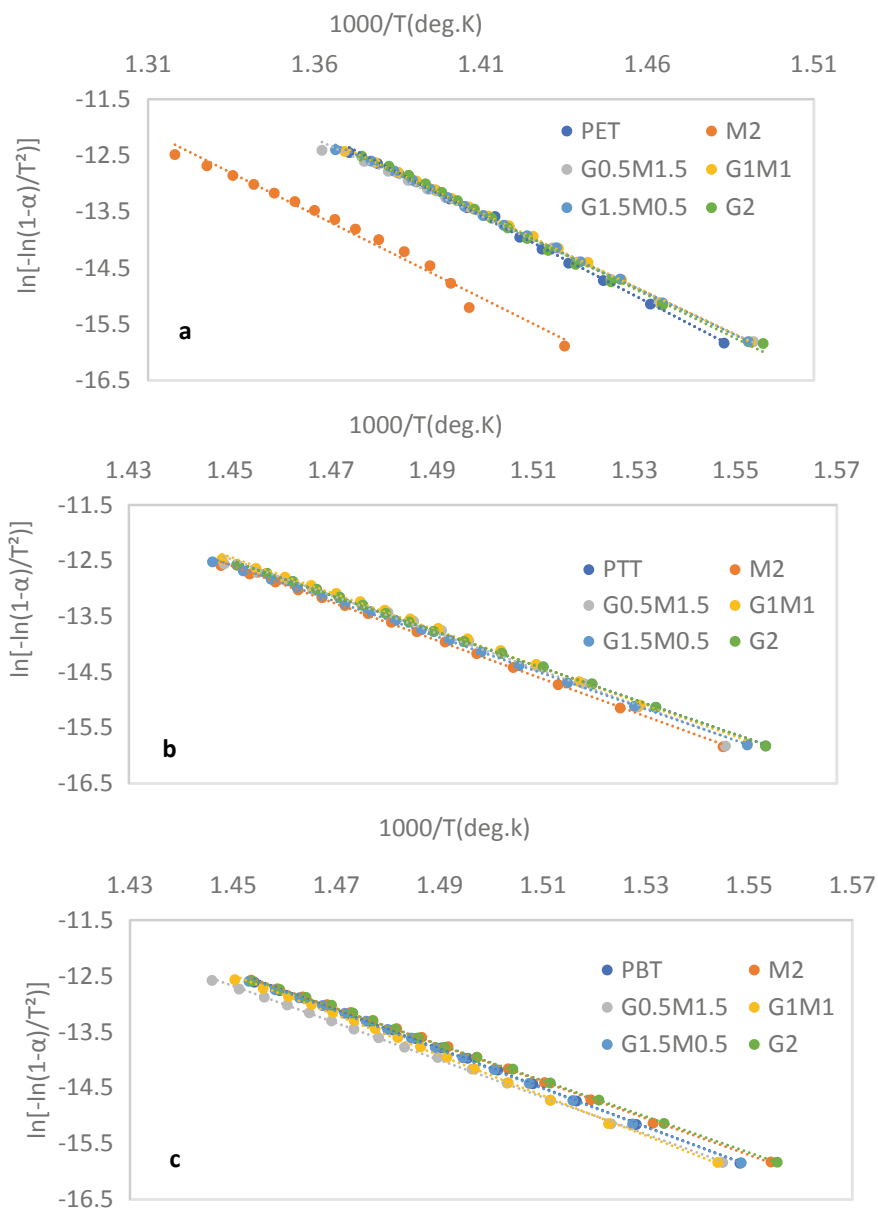
$$\varphi = \frac{dT}{dt}. \quad (7)$$

By combining and rearranging these above equations, assuming order of reaction one, Coats and Redfern got,

$$\ln \left[ -\frac{\ln(1-\alpha)}{T^2} \right] = \ln \left( \frac{AR}{\varphi E} \right) \left[ 1 - \left( \frac{2RT}{E_a} \right) \right] - \left( \frac{E_a}{RT} \right),$$

where  $\alpha$  = fraction decomposed at temperature  $T$ ;  $\varphi$  is the heating rate;  $E_a$  is the activation energy for decomposition reaction;  $R$  is the universal gas constant and  $A$  is the Arrhenius frequency factor. Now we can obtain a plot (as shown in Fig. 2) from this linear kinetics equation by taking  $\ln[-\ln(1-\alpha)/T^2]$  on y-ordinate and  $1000/T$  on x-ordinate which gives a line with slope  $E_a/R$  and it follows the first-order kinetics (Table 4).

$E_a$  was calculated by multiplying the universal gas constant value ( $R = 8.314 \text{ J.mol}^{-1} \cdot \text{K}^{-1}$ ) with the slope of the above plots with a slope of the above plots with a correlation coefficient ( $R^2$ ) greater than 0.98.  $E_a$  of PET was found to be 243.1 kJ/mole. This value is in comparison with the reported value of 203–355 kJ/mole for PET [18].  $E_a$  and  $\ln A$  for neat polyesters were found to be in the following order: PET < PTT < PBT, whereas  $E_a/\ln A$  is in the order PET > PTT > PBT. The ratio of  $E_a/\ln A$  was used to characterize the thermal stability of nanocomposites. The lower ratio of  $E_a/\ln A$  indicates lower thermal stability [19]. This shows that PET is having higher thermal stability that PTT followed by PBT. Similar observation was made from the 5 wt. % loss data as given in Table 3. Upon introduction of nanofillers in PET, increase in the ratio of  $E_a/\ln A$  was higher than the neat PET. In the case of PTT and PBT nanocomposites, the increase is insignificant than the neat polyesters. Upon comparison of M2 nanocomposites of polyesters,  $E_a/\ln A$  ratio decreased as follows: PET >> PTT > PBT, indicating PET containing 2 wt.% of f-MWCNT was more thermally stable than the corresponding nanocomposite of PTT and PBT. Similar observation was found in the nanocomposite containing 2 wt.% of GO in polyesters. Among the hybrid nanocomposites in a particular polyester, there was not much difference in the ratio of  $E_a/\ln A$ , indicating the thermal stability remains same. This observation matches with the observation made from 5 wt.% loss during thermal degradation in nitrogen.



**Fig. 2** Plot of  $\ln[-\ln(1-\alpha)/T^2]$  versus  $1000/T$  for the thermal degradation of **a** PET, **b** PTT and **c** PBT and its nanocomposites

**Table 4** (a) Kinetics characteristics of PET and its nanocomposites

Sample code	$E_a$	$\ln A$	$E_a/\ln A$	$R^2$
	(KJ/mole)			
PET	243.1	27.65	8.8	0.989
M2	246.1	26.71	9.2	0.984
G0.5M1.5	219.8	23.62	9.3	0.991
G1M1	226.1	24.80	9.1	0.992
G1.5M0.5	219.1	23.52	9.3	0.985
G2	236.0	26.48	8.9	0.993

(b) Kinetics characteristics of PTT and its nanocomposites

PTT	264.2	33.5	7.9	0.996
M2	265.4	33.6	7.9	0.996
G0.5M1.5	256.3	32.1	8.0	0.988
G1M1	251.5	31.3	8.0	0.989
G1.5M0.5	252.3	31.4	8.0	0.995
G2	253.4	31.6	8.0	0.998

(c) Kinetics characteristics of PBT and its nanocomposites

PBT	283.5	37.00	7.7	0.998
M2	266.7	34.06	7.8	0.998
G0.5M1.5	270.2	34.42	7.9	0.998
G1M1	286.1	37.34	7.7	0.995
G1.5M0.5	278.7	36.11	7.7	0.997
G2	261.8	33.19	7.9	0.998

## 4 Conclusions

The density studies proved that the PET, PTT and PBT nanocomposites were having loose structure except few compositions of PBT nanocomposites. The positive values of activation energy indicate that the polyester degradation process is a nonspontaneous reaction. PET was found to be more thermally stable than PTT and PBT. In the case of 2 wt.% of f-MWCNT or GO, the trend remained same. Hybrid nanofiller content has no effect on the thermal stability of the particular polyester.

**Acknowledgements** The authors would like to express their gratitude to Dept. of Chemicals and Fertilizers, Govt. of India under the scheme of establishing, Centres of Excellence (CoE) for their financial support.

## References

1. Marshall I, Todd A (1953) The thermal degradation of polyethylene terephthalate. *Trans Faraday Soc* 49:67–78. <https://doi.org/10.1039/TF9534900067>
2. Jenekhe SA, Lin JW, Sun B (1983) Kinetics of the thermal degradation of polyethylene terephthalate. *Thermochim Acta* 61:287–299. [https://doi.org/10.1016/0040-6031\(83\)80283-4](https://doi.org/10.1016/0040-6031(83)80283-4)
3. Al-Mulla A (2012) Enthalpy-entropy compensation in polyester degradation reactions. *Int J Chem Eng* 2012:782346. <https://doi.org/10.1155/2012/782346>
4. Kaur M, Kaur H, Kukkar D (2018) Synthesis and characterization of graphene oxide using modified Hummer's method. *AIP Conf Proc* 1953:30180. <https://doi.org/10.1063/1.5032515>
5. Tzavalas S, Drakonakis V, Mouzakis DE, Fischer D, Gregoriou VG (2006) Effect of carboxy-functionalized multiwall nanotubes (MWNT - COOH) on the crystallization and chain conformations of poly(ethylene terephthalate) PET in PET—MWCNT nanocomposites. *Macromolecules* 39:9150–9156. <https://doi.org/10.1021/ma0613584>
6. Swain P (2013) Physical and mechanical behavior of Al<sub>2</sub>O<sub>3</sub> filled jute fiber reinforced epoxy composites. *Int J Curr Eng Technol* 2:67–71. <https://doi.org/10.14741/ijcet/spl.2.2014.13>
7. Paszkiewicz S, Nachman M, Szymczyk A, Spitalsky Z, Mosnacek J, Roslaniec Z (2014) Influence of expanded graphite (EG) and graphene oxide (GO) on physical properties of PET based nanocomposites. *Polish J Chem Technol* 16:45–50. <https://doi.org/10.2478/pjct-2014-0068>
8. Krishnan PSG, Kulkarni ST (2009) Polyester resins. In: Deopura BL, Alagirusamy R, Joshi M, Gupta B (eds) *Polyesters and polyamides*. Woodhead Publishing Limited, UK, Chapter 1, pp 3–40. <https://doi.org/10.1533/9781845694609.1.3>
9. Zhou T, Wang X, Liu XH, Lai LZ (2010) Effect of silane treatment of carboxylic-functionalized multi-walled carbon nanotubes on the thermal properties of epoxy nanocomposites. *Express Polym Lett* 4:217–226. <http://ndl.ethernet.edu.et/bitstream/123456789/72813/1>
10. Safaei MR, Goshayeshi HR, Chaer I (2019) Solar still efficiency enhancement by using graphene oxide/paraffin nano-PCM. *Energies* 12:10. <https://doi.org/10.3390/en12102002>
11. Maurya S, Purushothaman M, Krishnan PSG, Nayak SK (2013) Effect of nano-calcium carbonate content on the properties of poly(urethane methacrylate) nanocomposites. *J Thermoplast Compos Mater* 27:1711–1727. <https://doi.org/10.1177/0892705712475011>
12. Praveen S, Krishnan PSG, Purushothaman M, Nayak SK (2021) HDI based poly(Urethane Methacrylate) nanocomposites containing NanoCaCO<sub>3</sub>: preparation and properties. *Polymer Sci Peer Rev J* 1:522. <https://doi.org/10.31031/PSPRJ.2021.01.000522>
13. Pundir A, Krishnan PSG, Nayak SK (2017) Effect of nanocalcium carbonate content on the properties of PLA nanocomposites. *J Compos Bio Polym* 5:26–33. <https://doi.org/10.12974/2311-8717.2017.05.01.4>
14. Venkatachalam S, Nayak SG, Labde VJ, Gharal PR, Rao K, Kelkar AK. Degradation and recyclability of poly (Ethylene Terephthalate). In: Saleh HEM (ed). <https://doi.org/10.5772/48612>
15. Martin-Gullon I, Esperanza M, Font R (2001) Kinetic model for the pyrolysis and combustion of poly-(Ethylene Terephthalate) (PET). *J Anal Appl Pyrolysis* 58:635–650. [https://doi.org/10.1016/S0165-2370\(00\)00141-8](https://doi.org/10.1016/S0165-2370(00)00141-8)
16. Kelsey DR, Kiibler KS, Tutunjian PN (2005) Thermal stability of poly(trimethylene terephthalate). *Polymer (Guildf)* 46:8937–8946. <https://doi.org/10.1016/j.polymer.2005.07.015>
17. Coats AW, Redfern JP (1965) Kinetic parameters from thermogravimetric data. II. *J Polym Sci Part B Polym Lett* 3:917–920. <https://doi.org/10.1002/pol.1965.110031106>
18. Das P, Tiwari P (2019) Thermal degradation study of waste polyethylene terephthalate (PET) under inert and oxidative environments. *Thermochim Acta* 679:178340. <https://doi.org/10.1016/j.tca.2019.178340>
19. Andricic B, Kovacic T, Perinovic S, Grgic A (2008) Thermal properties of poly(L-lactide)/calcium carbonate nanocomposites. *Macromol Symp* 263:96–101. <https://doi.org/10.1002/masy.200850312>

# Residual Stress Analysis of Additively Manufactured and Post Processed Inconel 718



O. V. Mythreyi and R. Jayaganthan

**Abstract** The aim of the present work is to assess the impact of postprocessing on the residual stress distribution of additively manufactured Inconel 718 alloy. The samples were manufactured through laser–powder–bed–fusion (LPBF) and subjected to a combination of heat treatments and shot peening. The microstructural changes were studied using SEM/EDS and the residual stress profile was measured in all the conditions using XRD diffraction technique. It was seen that residual stress present in the as built condition was tensile in nature, whereas the postprocessed samples were found to contain compressive stresses. The tensile residual stress is primarily caused by the temperature gradients arising due to the repeated heating—cooling cycle in the printing process. This stress becomes compressive stress when the samples are subjected to shot peening, due to the strain hardened layers introduced by the impact of the repeated bombardment of balls. Additionally, the presence of multiple phases in the heat-treated samples also contribute to the overall stress depths.

**Keywords** LPBF · Inconel 718 · Residual stress · Heat treatment · Shot peening

## 1 Introduction

Inconel 718 is a super alloy known for its outstanding mechanical strength, structural stability at elevated temperature, creep and corrosion resistance, making it an ideally suited alloy for oil and gas industrial applications [1, 2]. End-part manufacturing and employing this alloy is currently explored via laser–powder–bed–fusion (LPBF), one of the promising techniques in the additive manufacturing family [3]. In this method, layer by layer melting of metallic powder is executed by laser power that scans directionally based on geometry of the required component [4]. Typically, the component is then subjected to a set of postprocessing procedures to relieve residual stresses, enhance microstructural and surface integrity [5]. The literature on

---

O. V. Mythreyi (✉) · R. Jayaganthan

Department of Engineering Design, Indian Institute of Technology Madras Chennai, Chennai 600036, India

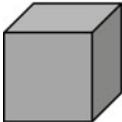
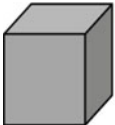
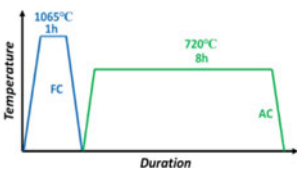

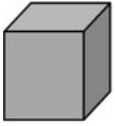
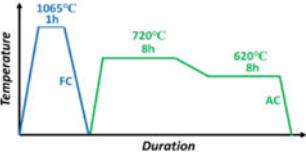

e-mail: [ed18d003@smail.iitm.ac.in](mailto:ed18d003@smail.iitm.ac.in)

the influence of various postprocessing treatments on the residual stress in LPBF-fabricated Inconel 718 is limited [6]. Hence, the current work is focused to understand the microstructure evolution and residual stress development in LPBFed Inconel 718 samples subjected to both thermal and surface postprocessing treatments. EBSD micrographs were used to substantiate the compressive stresses developed in the alloy due to postprocessing treatments.

## 2 Materials and Methods

A detailed description of processing parameters and compositional details is discussed in our earlier work [1]. The postprocessing condition adopted in the current work is detailed in Table 1.

**Table 1** Postprocessing steps adopted

<p>As received – LPBF + no postprocessing involved</p>	<p><b>AR – AS RECEIVED</b></p> <p>LPBFed In718</p> 
<p>T1 – LPBF + solutionizing + single ageing + shot peening</p>	<p><b>T1 – POST PROCESSING ROUTE 1</b></p> <p>LPBFed In718</p>  <p>+</p>  <p>+</p> 
<p>T2 – LPBF + solutionizing + double ageing + shot peening</p>	<p><b>T2 – POST PROCESSING ROUTE 2</b></p> <p>LPBFed In718</p>  <p>+</p>  <p>+</p> 



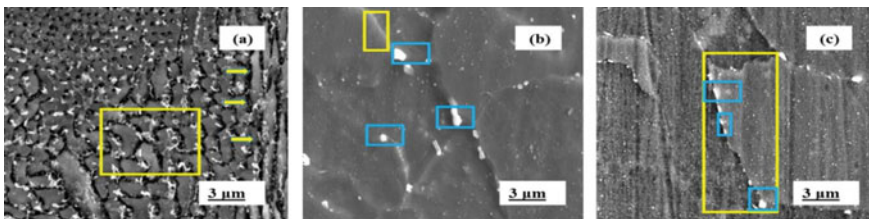
### 3 Microstructural Analysis

#### 3.1 Scanning Electron Microscopy (SEM)

The SEM images of all three specimen conditions are presented in Fig. 1a–c. In the AR condition, the cellular structure (indicated in yellow), typically occurring in LPBF process, is observed [7]. Certain dispersed precipitates of undefined morphology are found to be a network spread across the specimen representing possibly the Laves phase [8]. As indicated by the arrow marks, the dendritic growth parallel to the build direction can also be noticed. In the T1 condition, the cellular boundaries have completely vanished, and the grain boundary is beginning to appear, as indicated in yellow. In addition, clearly visible secondary precipitate formation is observed, highlighted in blue. From the morphology and previous studies, it can be deduced to be metallic carbide and  $\gamma'$ . After the T2 treatment, it can be seen that grain boundary formation is more clear with a fine distribution of metallic carbides deposited on the grain boundary (as indicated in yellow and blue) [9]. Hence, it can be stated that the process of solutionizing and ageing has led to reduction in Laves phase and has released the secondary precipitates into the matrix.

#### 3.2 Electron Backscattered Diffraction (EBSD)

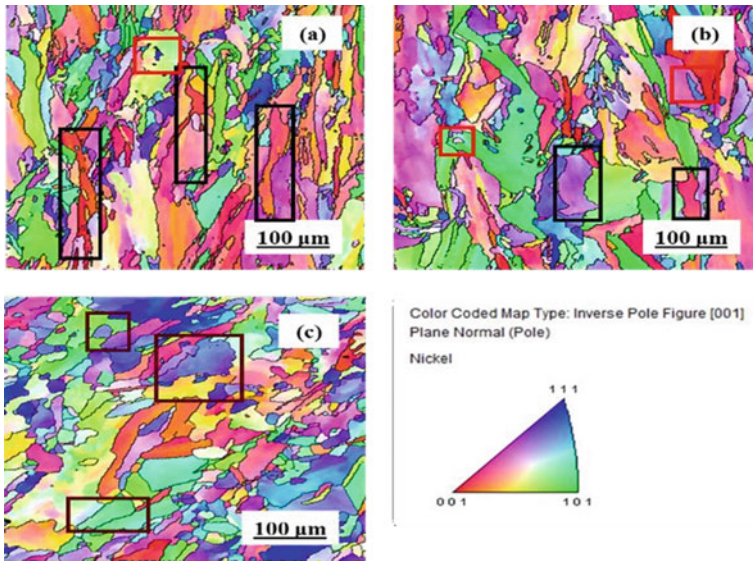
Figure 2a–c represents the EBSD images of all three specimen condition. In Fig. 2a, it is clear that vertical growth of the dendrite structure has resulted in long grains mostly oriented parallel to the build direction, indicated in black. The colour coding is predominantly in red, indicating that the grains in the AR condition follow the (001) plane. This indicates a strong goss component, also slightly impacted by coming from the cube component (101) [10]. This could be due to the finer grain formation, indicated in red in Fig. 2a. The structure is found to be inhomogeneous, with both long and fine grains present. After the samples are subjected to solutionizing and single ageing, it can be seen in Fig. 2b that the grains look more equiaxed after recrystallization. Cube component (101) is found to be more dominant in the T1 condition.



**Fig. 1** SEM images in etched condition of **a** AR **b** T1 **c** T2

A combination of equiaxed and fine grains are found, as indicated in black and red. In the T2 condition, after a two-step ageing treatment, it can be observed in Fig. 2c that most of the grains have become equiaxed due to recrystallization, as indicated in maroon. The predominant texture component is the (111) component. Due to multistage heat treatment process, the linear grains have transformed to equiaxed nature.

As seen from Table 2, it can be seen that conditions AR and T1 contain grain sizes closer to each other (58.06 and 52.64  $\mu\text{m}$ ). In the T2 condition, due to prolonged exposure to heat treatment and subsequent recrystallization, the microstructure is equiaxed and fine-grained. The misorientation angle is found to be closer in AR and T2 conditions around 16, while T1 is at 12.42.



**Fig. 2** EBSD images of **a** AR **b** T1 **c** T2

**Table 2** EBSD measurands for all three specimen conditions

Measurand	AR	T1	T2
Grain size ( $\mu\text{m}$ )	58.06	52.64	35.52
Misorientation	16.20	12.42	16.41

**Table 3** Residual stress values of all conditions

Specimen condition	Residual stress value (MPa)
AR	(+) 74.5 ( $\pm 15$ )
T1	(-) 809.1 ( $\pm 17$ )
T2	(-) 682.2 ( $\pm 15$ )

## 4 Residual Stress Analysis

Residual stress in LPBFed components are primarily due to the thermal gradients caused by the rapid heating and cooling [11]. They can also be induced by solidification induced transformation and precipitating phases. Compressive stresses are found to be beneficial and tensile residual stresses usually are detrimental. XRD-based testing was carried out to determine the magnitude and nature of the residual stress and the influence of the postprocessing steps is also investigated.

In the AR condition, the tensile stress is observed to +74.5 Mpa, indicating it tensile in nature, given in Table 3. Due to the rapid heating and cooling that takes place across multiple layers, stress begins to build up in LPBFed components. The interaction between the solidified layer and the molten pool of the next layer also creates stress in the part geometry. The presence of this stress component is conducive for easier crack propagation, thereby leading to a poorer fatigue life. In the post-processed condition, it can be seen that tensile stress has become compressive in nature. This could have occurred due to two reasons. Firstly, the process of solutionizing and ageing has resulted in a material condition populated with precipitates that exert stress on the matrix  $\gamma'$  and metallic carbide particles establish an incoherent relationship with the  $\gamma$  matrix, thereby resulting in heterogeneity in the microstructure. Subsequently, this leads to an increase in the stress levels within the matrix. Secondly, the repeated bombardment of the peening balls creates hardened layers in the near surface region. This surface plastic deformation, combined with the surface roughness reduction caused by shot peening [1], leads to an improvement in fatigue strength. Compressive stress level at this magnitude is highly helpful in preventing crack growth within the component. Hence, it can be concluded that the adopted postprocessing treatments are suitable in inducing favourable stresses in LPBFed Inconel 718.

## 5 Conclusion

- LPBFed Inconel 718 in the as received condition is distinguished by cellular structure and long grain dendritic growth parallel to the build direction.
- Solutionizing and ageing treatments lead to release of secondary precipitates,  $\gamma'$  and metallic carbides, and recrystallization resulting equiaxed grain structure.

- Residual stress has transformed from tensile to compressive through the post-processing steps. Shot peening is also found to contribute to the development of compressive residual stress in the Inconel 718.
- The adopted treatment methods have led to microstructural improvement and a favourable stress profile.

This work presents insight in to the material response of LPBFed Inconel 718 when subjected to a combination of thermal and surface treatments and helps in designing an optimized postprocessing route for this material.

## References

1. Mythreyi OV et al (2020) Corrosion study of selective laser melted IN718 alloy upon post heat treatment and shot peening. *Metals* 10(12):1562
2. Mythreyi OV et al (2021) Machine-learning-based prediction of corrosion behavior in additively manufactured inconel 718. *Data* 6(8):80
3. Froes FH, Dutta B (2014) The additive manufacturing (AM) of titanium alloys. *Adv Mater Res* 1019:19–25. <https://doi.org/10.4028/www.scientific.net/AMR.1019.19>
4. DebRoy T, Wei HL, Zuback JS, Mukherjee T, Elmer JW, Milewski JO et al (2018) Additive manufacturing of metallic components—process, structure and properties. *Prog Mater Sci* 92:112–224. <https://doi.org/10.1016/j.pmatsci.2017.10.001>
5. Kumar S, Pityana S (2011) Laser-based additive manufacturing of metals. *Adv Mater Res* 227:92–95. <https://doi.org/10.4028/www.scientific.net/AMR.227.92>
6. Lesyk DA et al (2020) Post-processing of the Inconel 718 alloy parts fabricated by selective laser melting: effects of mechanical surface treatments on surface topography, porosity, hardness and residual stress. *Surf Coat Technol* 381:125136
7. Wang Z, Guan K, Gao M, Li X, Chen X, Zeng X (2012) The microstructure and mechanical properties of deposited-IN718 by selective laser melting. *J Alloys Compd* 513:518–523. <https://doi.org/10.1016/j.jallcom.2011.10.107>
8. Li X, Shi JJ, Wang CH, Cao GH, Russell AM, Zhou ZJ et al (2018) Effect of heat treatment on microstructure evolution of Inconel 718 alloy fabricated by selective laser melting. *J Alloys Compd* 764:639–649. <https://doi.org/10.1016/j.jallcom.2018.06.112>
9. Li J, Zhao Z, Bai P, Qu H, Liu B, Li L et al (2019) Microstructural evolution and mechanical properties of IN718 alloy fabricated by selective laser melting following different heat treatments. *J Alloys Compd* 772:861–870. <https://doi.org/10.1016/j.jallcom.2018.09.200>
10. Holland S, Wang X, Fang XY, Guo YB, Yan F, Li L (2018) Grain boundary network evolution in Inconel 718 from selective laser melting to heat treatment. *Mater Sci Eng A*. <https://doi.org/10.1016/j.msea.2018.04.045>
11. Mirkoohi E, Li D, Garmestani H, Liang SY (2021) Residual stress modeling considering microstructure evolution in metal additive manufacturing. *J Manuf Process* 68:383–397. <https://doi.org/10.1016/j.jmapro.2021.04.041>

# Determination of Crystallinity of Natural Fibers—A Study with Spectroscopy



Akula Komuraiah, B. Satish Kumar, K. Shanker, N. Shyam Kumar,  
and B. Durga Prasad

**Abstract** The materials people use have a significant impact on their quality of life. A composite material, which revolutionized human life, is one such material. The traditional composites offered a provoking conversation starter to the innovator about its superfluity. The natural composite materials were the focus of the inventors' efforts to address pollution issues. The natural resin serves as the binding agent and the natural fiber serves as the reinforcing agent in the natural composite material. It is helpful to be familiar with the properties of natural fibers in order to comprehend the properties of natural composites. The regular fiber is made out of cellulose, hemi celluloses, lignin, gelatin, and waxes. There are crystalline and amorphous regions in the fiber. The translucent district contains the cellulose and shapeless area is made out of hemi celluloses. The fiber's strength increases with the crystallinity. The purpose of this paper is to demonstrate that the structure and composition of natural fibers are linked. The goal is to determine the natural fiber's crystallinity using FT-IT and Raman spectroscopy. Paul Garside and Paul Wyeth gave the equation to find proportion of lignin content to cellulose proportion and crystallinity. The ratios of intensities  $I_{1595}$  to  $I_{1105}$ ,  $R = (I_{1595})/(I_{1105})$  from FTIR spectra, are used to calculate the lignin content. This recipe didn't give the adequate qualities. According to the results of this study, the content  $K_1$  should be included in the formula as  $R = (I_{1595})/(K_1 \times I_{1105})$ . The intensity ratios of  $I_{1094}$  and  $I_{1121}$  are used to

---

A. Komuraiah (✉)

Department of Mechanical Engineering, Kamala Institute of Technology and Science,  
Karimnagar, Telangana, India

e-mail: [akulako@gmail.com](mailto:akulako@gmail.com)

B. S. Kumar

Department of Mechanical Engineering, Vignana Bharathi Institute of Technology, Hyderabad,  
India

K. Shanker

Principal, Kamala Institute of Technology and Science, Karimnagar, Telangana, India

N. S. Kumar

Principal, Warangal Institute of Technology and Science, Warangal, Andhra Pradesh, India

B. D. Prasad

Professor, JNTU, Anantapur, Andhra Pradesh, India

determine the crystallinity,  $R = (I_{1094}/I_{1121})$ . Additionally, the introduction of K2,  $R = "I_{1094}/(K2 I_{1121})."$  modifies this. The constant K3,  $R = "I_{1094}/(K3 \times I_{1121}),"$  is introduced from the Raman spectra.

**Keywords** Raman spectroscopy · FTIR spectroscopy · Crystallinity of natural fibers · Composition of natural fibers · Structure of natural fibers

## 1 Introduction

The natural composites have many advantages. They are easy to dispose, clean for environment, recyclable and provide employment to the rural farmers, etc. About 60% of the fibers are used to make a composite laminate and 40% of resin used. The use of natural composites is increasing day by day. The significance of natural fibers as crucial structural components cannot be overlooked, such as the case of coir fiber which can serve as an alternative to steel. It is an important structural material like the steel. The properties of the natural fibers highly influence the properties of the composites. The natural fibers like jute, coir, hemp, banana, cotton, etc., are widely used in making the natural composites. Each fiber has its unique composition and structure. The main constituents of the natural fibers are cellulose, hemi celluloses, lignin, pectin, and waxes. These constituents are in different compositions in natural fibers. The dissimilarity in properties among various natural fibers stems from disparities in their composition and structure. The difference in their composition makes the difference in structure and hence in its properties.

FTIR is an effective method for analyzing how inter and intramolecular hydrogen bonds occur in cellulose. A substantial association between the type of hydrogen bonds and physical properties (such as solubility and hydroxyl) may be established because of the extensive database, mechanical characteristics, reactivity, and crystallinity of cellulose. The capacity to precisely examine hydrogen bonds has led to an increase in the use of FTIR for examining natural fiber flaws, degradation, and material changes after modification (e.g., dislocation of hemp fiber).

The IR spectrum was created when infrared radiation entered a sample and was selectively absorbed at particular frequencies. The electric dipole moment of the molecule will change in response to infrared radiation. Raman spectroscopy, on the other hand, is dependent on the molecule's capacity to polarize electrically. As a result, Raman and IR spectroscopy are complementary to one another.

## 2 Literature Review

Chemically modified fibers were characterized by Fourier transformed infrared spectroscopy (FTIR) and  $^{13}\text{C}$  nuclear magnetic resonance spectroscopy ( $^{13}\text{C}$  NMR) [1]. Smith. B et al proposed that the "modular" elongation mechanism is responsible for imparting toughness to natural fibers, it can be tested with atomic force microscope (AFM) [2]. Nils Almqvist et al. recorded the X-ray beam diffraction

with a Scintag PADX diffractometer, utilizing  $K\alpha$ -radiation from a copper focus to inspect talc tablets [3]. Norma Aurea Rangel-Vázquez and Timoteo Leal-García with FTIR showed that the after salinization in rice husk fiber will give explicit properties to the fiber relying upon the subsequent functional gatherings. In addition, they stated that the properties will determine the polymeric matrix for composite preparation [4]. The structure of natural fibers can be studied using either FTIR or Raman spectroscopy [5]. According to Katja Kavkler and Andrej Damser, both FTIR and Raman spectroscopy are appropriate for evaluating structural changes in cellulosic fibers [6]. According to J. L. Lopez, M. Sain, and P. Cooper, X-ray photoelectron spectroscopy can be used to measure chemical changes in the composite's materials in order to understand how chemical transformations on the material surface work [7]. A natural fiber's morphology, percentage of crystallinity, and thermal stability can all be determined using SEM and X-ray diffractometer [8]. Scanning electron microscopy (SEM), X-ray diffraction, and TGA/DTA methods were used to examine the morphology, crystallinity, and thermal stability of the modified ramie fibers. When synthetic polymers are grafted onto ramie fibers, the surface becomes rough, but biologically modified ramie fibers have a more supply and smooth appearance as a result of the removal of gum and other impurities from the fibers' surface [9].

### 3 Microstructure of Natural Fiber

Generally, the fibers are classified based on the sources from which they are extracted. The bast fibers, leaf fibers, seed fibers are the possible ways of classifying the fibers.

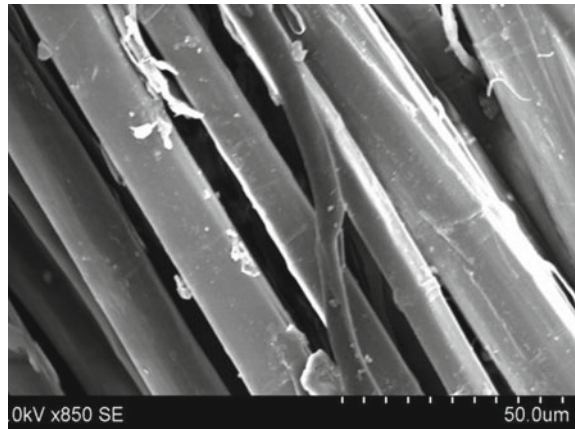
The main components of the plant fibers are cellulose, hemicelluloses, lignin, pectin, and waxes. There may be other chemical components in negligible quantities. These components constitute the properties of the natural fibers.

The cell wall of the natural fiber has a complex structure. The cell walls are rigid multi-layered structure having middle lamella, primary P, and secondary wall S. The secondary wall consists of sub layers S1, S2, and S3. Each layer consists the components cellulose, hemicelluloses, and lignin. The lignin is distributed in middle lamella and primary wall. S2 layer gives greatest contribution to the strength of the natural fiber. The fibers are shown in SEM images in Figs. 1 and 2.

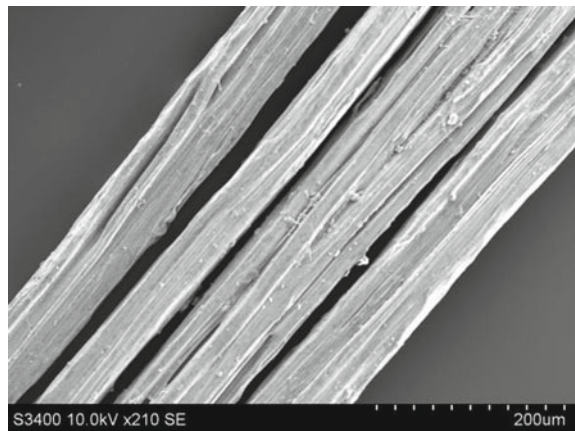
### 4 Spectroscopy of Natural Fibers

Ordinary methods to decide reference values for mohair yield, vegetable matter substance, fiber diameter, and level of medullated and kemp strands were directed. Each fleece sample's mohair characteristics were predicted using equations that linked NIR spectra to reference values for yield and diameter parameters [10]. There are a few drawbacks with conventional methods of characterizing these fibers such as microscopy and staining: The techniques depend vigorously on experience as they by and large produce subjective information and may require the abstract examination

**Fig. 1** SEM image of flax fibers



**Fig. 2** SEM image of hemp fiber



of results [11]. Yongliang Liu examines latest advancement in applying the Fourier change infrared (FTIR) spectroscopic procedure to describe these distinctions, to segregate youthful filaments from mature strands, to evaluate fiber development and crystallinity, and furthermore to disentangle the band tasks in translucent and undefined celluloses [12]. Anna Kicinska-Jakubowska in the paper review of Natural Fibers, Part I–Vegetable Fibers explained the SEM images of various fibers [33].

#### **4.1 FTIR Spectroscopy**

The outcomes affirmed the from Raman spectroscopy as an integral asset to scientific fiber assessment. Estimations could be performed straightforwardly on mounted fibers without experiencing a lot of obstruction from the mounting medium or the



cover glass [13]. The natural fiber's constituents were qualitatively identified using Fourier transform infrared (FTIR) spectroscopy [14]. Three chemical treatments were applied to green coconut fiber, a lignocellulosic material from Brazil's northeast coast: NaOCl, NaOCl/NaOH or H<sub>2</sub>O<sub>2</sub>, SEM, FTIR, XPS, TGA, and other analyses were used to investigate the effects of these treatments on the structure, composition, and properties of the fibers. According to FTIR and wettability results, treatment with H<sub>2</sub>O<sub>2</sub> is the most effective for removing waxy and fatty acid residues, as demonstrated by SEM, but it does not alter the chemical composition of the surface. The chemical composition and FTIR analyses showed that the fibers treated with NaOCl/NaOH had less hemicelluloses. As a result, this fiber had more cellulose exposed and had less thermal stability [15]. A solid calcium complexant obliterates the gelatin/calcium complex present on the outer layer of fibers. The infrared spectra indicate that calcium pectates are always present at the fiber surface, but their altered structure prevents calcium binding [16].

## 4.2 Raman Spectroscopy

Raman spectroscopy can examine the samples in glass/plastic container. Small particles as small as 1 micro m can be tested with Raman spectroscopy. Raman measurements are insensitive to water. So, Raman spectroscopy became a useful and powerful tool. It can provide molecular structure information to complement infrared analysis. It can be used to characterize both natural and synthetic fiber. Fibers of different structures show different spectra and can be easily analyzed. Slight variation in composition or structure can be differentiated easily with the spectra. Raman spectra will provide a rapid, non-destructive, and non-contact technique [24].

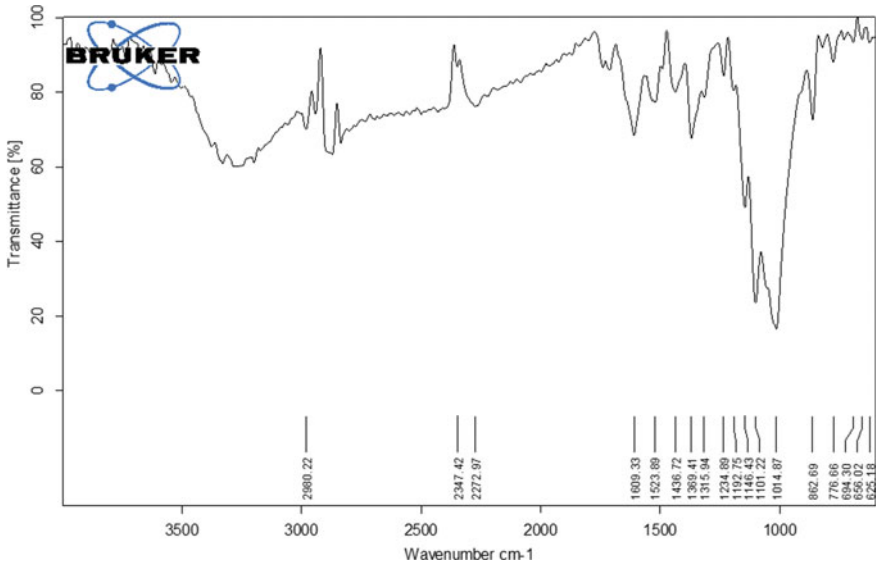
## 5 Materials and Methods

### 5.1 Preparation of Natural Fibers

The natural fibers are collected from the market where they are sold by agricultural farmers. These fibers are used to make ropes, brushes for use.

### 5.2 FTIR Spectroscopy

The influence pattern is obtained from a two-beam interferometer, the difference in path between the beams is changed. When tested with Fourier transformation, a spectrum is obtained.



**Fig. 3** FTIR spectroscopy of coir fiber

### 5.3 RAMAN Spectrometer

FT-RAMAN spectrometer is a multi-RAM, standalone model. The spectral range is  $4000\text{--}50\text{ cm}^{-1}$ . The laser source is Nd: YAG 1064 nm. The spectrometer has a large sample compartment to accommodate different sample formats, from powders to liquids in vials.

### 5.4 Results of FTIR Spectroscopy (Graphs)

The FTIR spectroscopy analysis of coir fiber, jute fiber, and hemp fiber was carried out at the Sophisticated Analytical Instruments Facility (SAIF) IIT Madras (Figs. 3, 4 and 5).

### 5.5 Graphs of Raman Spectroscopy

The Raman spectroscopy is conducted at SAIF, IIT Madras, India (Figs. 6, 7 and 8).

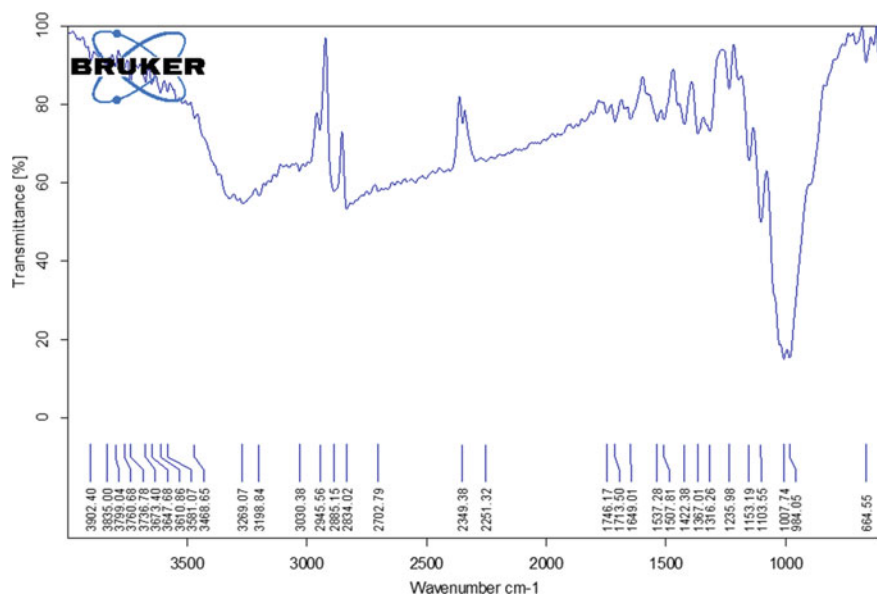


Fig. 4 FTIR spectroscopy of jute fiber

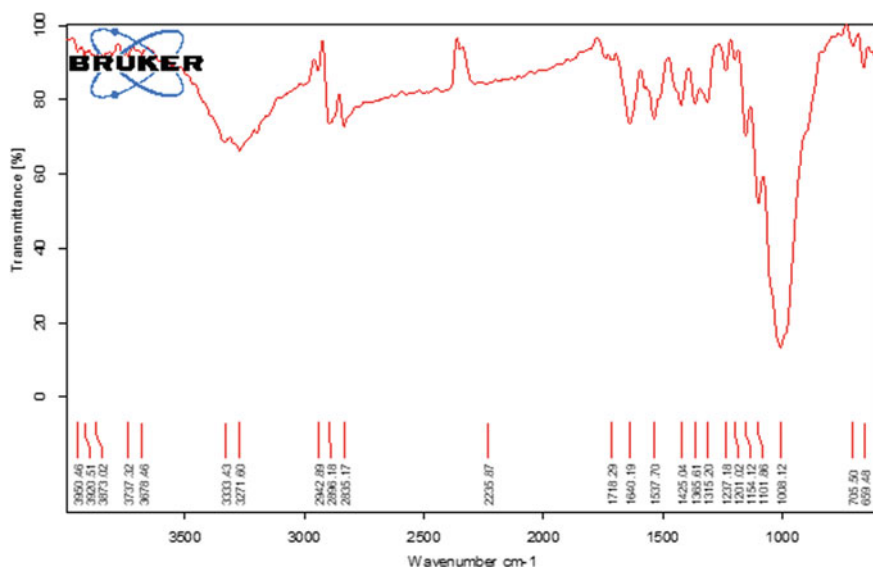


Fig. 5 FTIR spectroscopy of hemp fiber

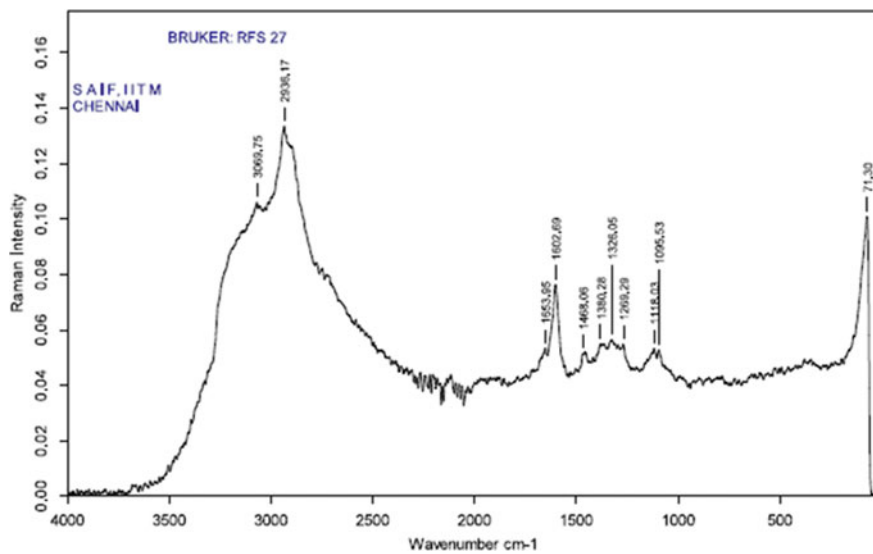


Fig. 6 Raman spectroscopy of coir fiber

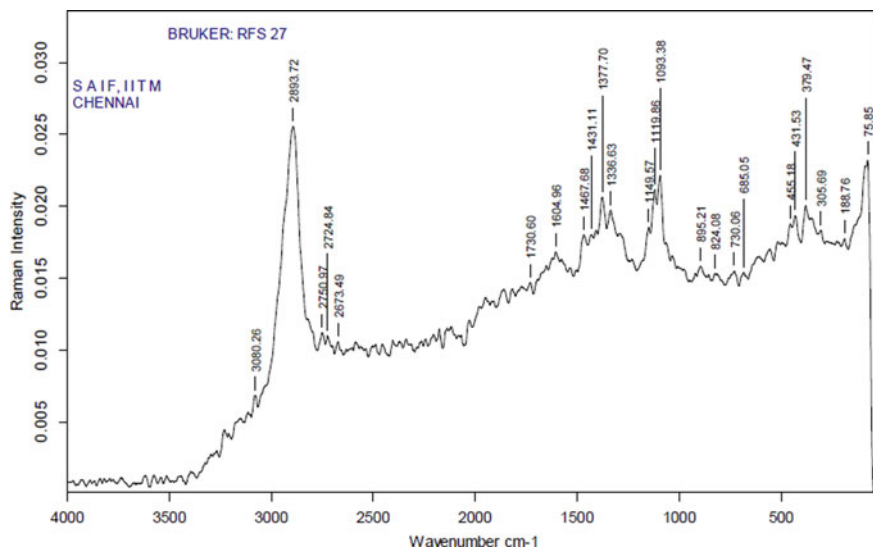


Fig. 7 Raman spectroscopy of hemp fiber

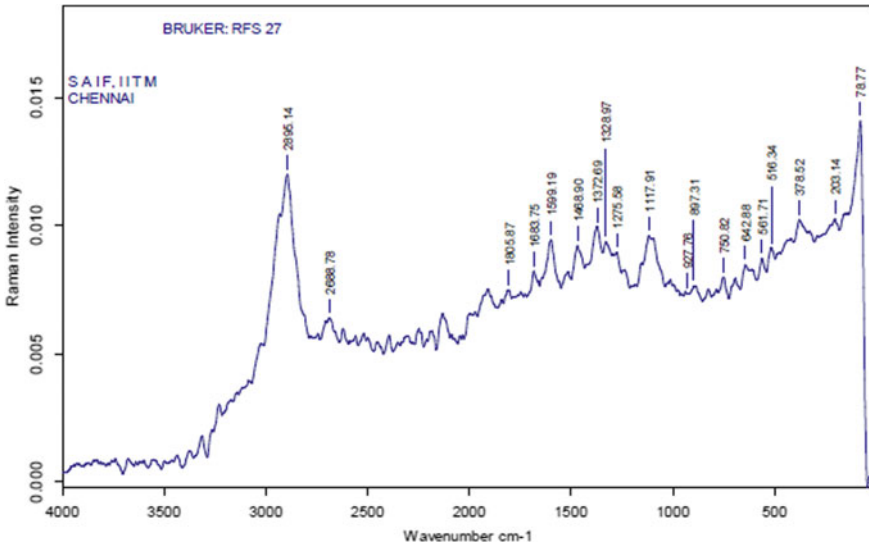


Fig. 8 Raman spectroscopy of jute fiber

## 6 Results and Discussion

### 6.1 Peak Positions and Assignment of Wave Number to the Chemical Groups in Natural Fibers From the Literature

Many researchers have studied the peak position with respect to wavenumber were studied for different natural fibers, few important are discussed in the Table 1.

### 6.2 Applications of FTIR—Determination of Structure

Fourier change infrared (FTIR) spectroscopy is utilized to get infrared (IR) spectra of inorganic and natural materials. This method estimated the IR radiation retention or conveyance by the example material against its frequency or wave numbers. The structure of molecules vibrates when the material is exposed to IR radiation [22].

The presence of cellulose, lignin, and polysaccharides in this fiber is confirmed by FTIR analysis. When used to make composites, the microstructural analysis of *S. trifasciata* fiber reveals the presence of surface irregularities that ensure a strong bond between the fiber and the matrix [23].

**Table 1** Peak positions and assignment of wave number to the chemical groups in natural fibers from the literature

	Fiber	Ficus religiosa leaf fibers	Alfa fiber	Raw wood	Coir	Sisal fiber	Sansevieria trifasciata fiber
	Work done by and reference	Obi Reddy et al. [19]	Benyahia [17]	Obi Reddy et al. [19]	Choudhury [14]	Hamdan et al. [20]	Bin Bakri [23]
1	OH stretching of alpha cellulose	3435	3359.8	3300–4000	3422–3398	3400	3421
2	Alkyl CH stretching	2930	2916.2		2928–2924	2900	2941
3	–C = O stretching of hemicellulose carbonyl stretching	1740	1731.9	1734	1730	1700	
4	C = C stretching of lignin	1631	1654.8	1600	1674	1650	
5	Auromatic skeletal vibration of benzene ring in lignin	1510				1500	1659
6	CH <sub>2</sub> bending						1542
7	CH deformation (methyl and methylene)	1459				1450	
8	CH in plane deformation with aromatic ring stretching	1430				1400	
9	CH bending of lignin	1380				1350	
10	OH in-plane bending						1337
11	CH <sub>2</sub> wagging	1319	1454			1300	
12	CH bending of hemicelluloses	1257					

(continued)

**Table 1** (continued)

	Fiber	Ficus religiosa leaf fibers	Alfa fiber	Raw wood	Coir	Sisal fiber	Sansevieria trifasciata fiber
	Work done by and reference	Obi Reddy et al. [19]	Benyahia [17]	Obi Reddy et al. [19]	Choudhury [14]	Hamdan et al. [20]	Bin Bakri [23]
13	Asymmetric C–O–C stretching of lignin	1159	1253.6		1052–1020		
14	Vibration of glucose rings	1120					
15	Symmetric C–O stretching of lignin	1050				1000	
16	CH stretching (–glycosidic linkages between the mono saccharides)	878				850	
17	Number of peaks in FTIR graph	13	6		5	12	

### 6.3 Applications of FTIR—Determination of Chemical Components

To find the lignin content Paul Garside and Paul Wyeth [11] gave formula with the intensities ratios,  $R_1$  and  $R_2$  where  $R_1 = I_{1595}/I_{1105}$ ,  $R_2 = I_{1595}/I_{2900}$ ,  $R_1$  gives the lignin to cellulose ratio,  $R_2$  gives the lignin to organic material ratio (Table 2).

### 6.4 Applications of Raman Spectroscopy

Raman spectroscopy as a non-damaging procedure is regularly used to examine a notable or measurable material. Additionally, it is a very useful technique for testing modified and functionalized textile materials [30]. Uses of Raman spectroscopy in the existence sciences have included evaluation of biomolecules, hyperspectral sub-atomic imaging of cells and tissue, clinical conclusion, and others.

**Table 2** Determination of  $R_1$  and  $R_2$  from the spectroscopic experiments done in this work and of the literature

S.N	Name of the fiber	I1105	I1595	I2900	$R_1 = \frac{I1595}{I1105}$	$R_2 = \frac{I1595}{I2900}$	Work done by and reference
1	Coir	58	76	79	1.310	0.962	From this work
2	Jute	80	95	97	1.188	0.979	From this work
3	Hemp	88	95	97	1.080	0.979	From this work
4	Cotton	15	10	12	0.66	0.83	Fan et al. [26]
5	Cotton	91	98	97	1.07	0.98	Cho [18]
6	Cotton	95	97	98	1.005	0.99	Pike technologies spectroscopic creativity [25]
7	Coir	85	83	87	0.97	0.94	Brigida [15]
8	Coir	95	97	98	1.02	0.99	Yue [27]
9	Coir	107.5	102.5	108	0.95	0.940	Choudhury [14]
10	Raw wood	52.5	60	62	1.14	0.96	Obi Redd et al. [19]
11	Ficus religiosa leaf fibers	64	68	72	1.04	0.944	Cordeiroa et al. [21]
12	Ficus religiosa leaf fibers	40	60	62	1.5	0.96	Liu [12]
13	Alfa fiber	45	98	54	2.17	1.81	Obi Redd et al. [19]
14	Sisal fiber	9	2.4	1.6	0.26	1.5	Hamdan et al. [20]
15	Flax	44	62	59	1.34	0.95	Mullik [28]

The natural fiber spectra, as observed by Luiz Claudio Ferreira et al. [13], exhibit various bands that are characteristic of cellulose structural units. This is primarily due to the fact that these fibers contain a significant amount of cellulose, approximately 70%. However, coconut fiber, also known as coir, contains a higher proportion of lignin than cellulose, resulting in a distinct spectra compared to other fibers. Specifically, the spectra of coir displays weaker cellulose bonds.

### 6.5 Crystallinity Estimation by Raman Spectroscopy

Thus, the ratio  $R = I1094/I1121$  has been used to estimate the crystallinity of the natural fiber [31] (Table 3).



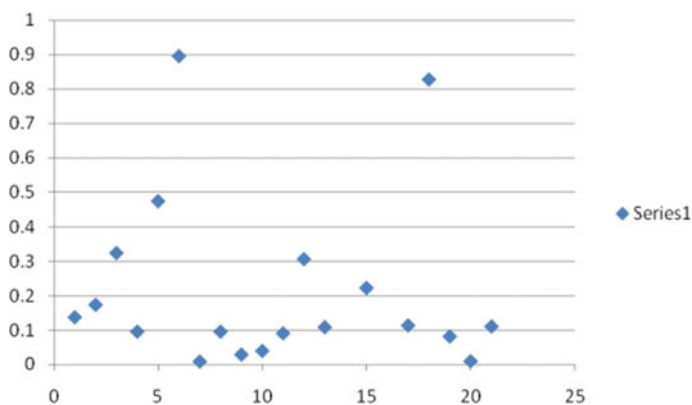
**Table 3** Crystallinity of natural fibers

S. N	Name of the fiber	I1094	I1121	$R = I_{1094}/I_{1121}$	Crystalline %	Work done by and reference
		(Relative intensities from graphs)				
1	Coir	44	46	0.957	95.652	From this work
2	Jute	62	76	0.816	81.579	From this work
3	Hemp	94	96	1.021	97	From this work
4	Cotton	13	21	0.619	61.905	Tze [31]
6	Brown cotton	35	38	0.921	92.105	Lepot [13]
7	Blue cotton	30	36	0.833	83.333	Lepot [13]
8	Undyed cotton	40	43	0.930	93.023	Lepot [13]

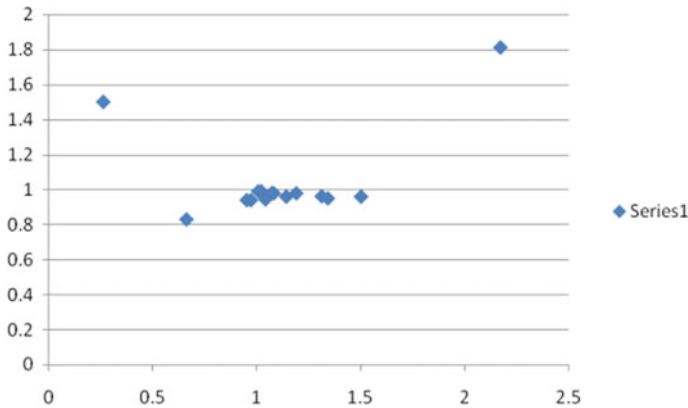
## 7 Conclusion

The composition and properties of normal filaments rely upon many elements like the geographic area, time of the growth, nature of the soil, accessibility of the water content to plant, the piece of the plant from which the fiber is separated, and the strategy for extraction. M. Prabhu and A. Vijay [33] had explained of different techniques for testing the regular strands to track down the construction (Figs. 9 and 10).

The results of this work were inconsistent. The results of the spectroscopy are not exactly comparable with those found in the published literature. The reason for this is that various analysts provided data on natural fibers from all over the world. Natural fibers vary worldwide in terms of their properties and composition. So the



**Fig. 9** Graph of  $R_1$  and  $R_2$  from spectroscopic analysis Table 1



**Fig. 10** Graph of R1 and R2 from analytical values of based on chemical composition

results gained are extraordinary. Be that as it may, the information might be helpful for making examinations.

The composing focus on shows that expecting a comparative fiber is focused on by the different researchers, they will not get the tantamount qualities. This demonstrates the deviation from the normal strands, e.g., the fibers cotton and coir were focused on various subject matter experts, and at this point they don't get comparable q values.

The spectroscopy can uncover even the littlest contrasts in the organization.

The presence of cellulose, hemicelluloses, lignin, gelatin, and waxes can be related to the spectroscopy diagrams. In any spectra, the absence of hemicelluloses and lignin may be confirmed if the bands at  $1368\text{ cm}^{-1}$  and  $1363\text{ cm}^{-1}$  disappear. Mizi [25] discovered that these bands are assigned to an in plane  $-\text{CH}$  bond.

Three fibers were retested using FRIR and Raman spectroscopy in this work. Due to the fact that the hemp and jute were obtained from agricultural farmers, the spectroscopy results do not align with the literature. Both of these fibers are unprocessed. They were not treated or subjected to a chemical process. They might have high lignin content.

The R1 and R2 ratios can be used to determine the amount of lignin. The plot of these proportions can give one of a kind locale of reverberation fiber. The fibers with a high lignin content will be plotted at the top right of the graph, while the fibers with a low lignin content will be plotted on the left side bottom.

According to Lepot [13], there are a number of issues when drawing conclusions from the Raman spectra. From it, partial conclusions can be drawn. The dye but not the fiber can be seen in the dyed fibers' Raman spectra. On the off chance that the force of the color is frail, elevated degrees of fluorescence can give significant spectra. The Raman range is extremely quick and safe method. It can be used to make comparisons.

The most gently lignified filaments are tracked down the higher upsides of the proportions. The pattern numerous does not follow writing values.

The FTIR images' R1 ratio does not match the values found in the literature. According to the data from the fibers, only one out of seven fibers agreed with the values. Here, it is proposed to alter the recipe of R1 to present steady, so the scientific qualities can be gotten. The equation

$$R1 = \frac{I1595}{I1105}$$

$$R1 = \frac{I1595}{K1 \times I1105},$$

where K1 is constant depends on the type of fiber, geographic location of the plant growth, season of the plant growth, the fiber extraction process, and the part of the plant from which the fiber is extracted.

By trial and error method the K values are found.

For the hemp fiber K = 6, for cotton K = 8, for coir, K = 7,

$$K1 = Kf \times Kg \times Ks \times Kp$$

R2 can be found from formula.

Kf = fiber type constant, Kg = geographical location constant,

Ks = season constant,

Kp = plant part constant;

$$R2 = \frac{I1595}{I2900}.$$

The R2 values of coir are similar in both analytical and spectra methods. For other fibers it is different, here the constant K<sub>2</sub> is introduced.

From trial and error method, the K<sub>2</sub> values for jute = 9, hemp = 25, flax = 34,

$$K2 = KfxKgxKsxKp.$$

In the graph of R1–R2 from the analytical values, the points seem to be arranged in a straight line with slope 1, but from the graph of spectroscopic values they seem to be arranged in different way, the values scattered to find the crystallinity, the formula from Raman spectroscopy used is

$$R3 = \frac{I1094}{I1121}.$$

This formula can be modified as

$$R3 = \frac{I1094}{K3xI1121}$$

From trial and error method, K3 values for coir = 3, jute = 1.6.

$$K3 = KfxKgxKsxKp.$$

**Acknowledgements** We thank Dr. M. Mohan Rao, Director CCMB (Center for Cellular and Molecular Biology), Hyderabad, India for allowing us to take the SEM (Scanning Electron Microscope) images. We also thank Mr. Saad M. Ahsan for helping us to take SEM images, SAIF, Indian Institute of Technology, Madras, India for FTIR analysis and SAIF, Indian Institute of Technology, Madras, India for Raman analysis.

## References

1. Favaro L, Ganzerli TA, De Carvalho NMeto AGV, da Silva ORRF, Radovanovic E (2010) Chemical, morphological and mechanical analysis of sisal fiber-reinforced recycled high density polyethylene composite. *Express Polym Lett* 4(8):465–473
2. Smith B, Schäffer T, Viani M et al (1999) Molecular mechanistic origin of the toughness of natural adhesives, fibres and composites. *Nature* 399:761–763
3. Almqvist N, Thomson NH, Smith BL, Stucky GD, Morse DE, Hansma PK (1999) Methods for fabricating and characterizing a new generation of biomimetic materials 1. The first and second authors contributed equally to this work. *Mater Sci Eng C* 7(1):37–43
4. Rangel-Vazquez NA, Leal-García T (2010) Spectroscopy analysis of chemical modification of natural fibers. *J Mex Chem Soc* 54(4):192–197
5. Abdul Khalil HPS, Suraya NL (2011) Anhydride modification of cultivated kenaf bast fibers: morphological, spectroscopic and thermal studies. *Bio Resour* 1122–1133
6. Kavkler K, Demsar A (2012) Applications of FTIR and Raman Spectroscopy to qualitative analysis of structural changes in cellulosic fibers. *Tekstilec letn* 55, st 1, str 19–31
7. Lepoz JL, Sain M, Cooper P (2006) Performance of natural fiber plastic composites under stress for outdoor applications: effect of moisture, temperature and ultraviolet light exposure. *J Appl Polym Sci* 99:2570–2577. Wiley Periodicals Inc.
8. Paquin R, Colomban P, Nano mechanics of single kerton fibers: A Raman study of the helix-β sheet transition and water effect. *J Raman Spectrosc* 38950:504–514
9. Kalia S, Sheoran R, Mittal H, Kumar A (2013) Surface modification of ramine fibers using microwave assisted graft co-polymerization followed by *Brevibacillus parabrevis* pretreatment. *Adv Mat Lett* 4(10):742–748
10. Coleman SW, Lupton CJ, Pfeiffer FA, Minikhiem DL, Hart SP (1999) Prediction of clean mohair, fiber diameter, vegetable matter, and medullated fiber with near-infrared spectroscopy. *J Anim Sci* 77(10):2594–2602. <https://doi.org/10.2527/1999.77102594x>. PMID: 10521017
11. Garside P, Wyeth P, Identification of cellulose fibers by FTIR Spectroscopy 1: Thread and single fiber analysis by attenuated total reflectance. *Stud Conserv* 48(4):269–275. [eprints.soton.ac.uk/.../cellulose\\_I\\_updated](http://eprints.soton.ac.uk/.../cellulose_I_updated). University of Southampton Winchester Campus, Park Avenue, Winchester, S 023 8DL
12. Liu Y (2013) Recent progress in fourier transform infrared (ftir) spectroscopy study of compositional, structural and physical attributes of developmental cotton fibers. *Materials* 6:299–313. <https://doi.org/10.3390/ma6010299>. ISSN 1996–1944
13. Lepot L, De Wael K, Gason F, Gilbert B (2008) Applications of raman spectroscopy to forensic fibre cases. *Sci Justice* 48:109–117. Elsevier

14. Choudhury R, Fabrication and characterization of raw and dewaxed coir fiber reinforced polymer composites a thesis submitted for partial fulfillment of the requirements for the degree of master of science in Physics, Roll no. 410ph2122, IIT Roorke, India
15. Brígida AIS, Calado VMA, Gonçalves LRB, Coelho MAZ (2010) Effect of chemical treatments on properties of green coconut fiber. *Carbohydr Polym* 79:832–838
16. Le Troedec M et al (2007) Physio chemical modifications of the interactions between hemp fibers and a lime mineral matrix: impacts on mechanical properties of mortars. In: 10th international conference of the European Ceramic society, B Verlin, pp 451–456. ISBN 3-87264-022-4
17. Benyahia A, Merrouche A, Rokbi M, Kouadr Z (2013) Study the effect of alkali treatment of natural fibers on the mechanical behavior of the composite 21ème congrès français de mécanique bordeaux, 26 au 30 août 2013
18. Cho L-L (2007) Identification of textile fiber by Raman micro spectroscopy. *Forensic Sci J* 6(910):55–62
19. Obi Reddy K, Uma Maheswari C, Jeevan Prasad Reddy D, Guduri1 BR, Varada Rajulu A (2010) Properties of Ligno-cellulose Ficus Religiosa leaf fibers. *Int J Polym Technol* 2(1). Serial publications, India
20. Hamdan S, Rahman MR, Ahmed AS, Islam MS, Thermo gravimetric analysis and dynamic Young's modulus measurement of N, N-dimethyla cetamid impregnated wood polymer composites (WPC), pp 1–14
21. Cordeiroa N, Gouveiaa C, Moraesb AGO, Amicob SC (2011) Natural fibers characterization by inverse gas chromatography. *Carbohydr Polym* 84:110–117. Elsevier
22. Sharma S (2013) Preparation, charecterization and Cr(Vi) adsorption behaviour study of poly(acrylic acid) grafted Ficus caricabast fiber. *Adv Mat Lett* 4(4):271–276
23. Bin Bakri MK et al (2016) Comparative study of functional groups in natural fibers: fourier transform infrared analysis (FTIR). In: International conference on futuristic trends in engineering, science, humanities, and technology (FTESHT-16). Gwalior, ISBN: 978–93–85225–55–0
24. Kanimozhi M (2011) Investigating the physical characteristics of sansevieria trifascicata fiber. *Int J Sci Res Publ* 1(1):1–4. IJSRP.Org
25. Nezafeirropoulos, Engineering the fibre matrix interface in Natural-fibre composites 2008, Woodhead Publishing Limited Properties and performance of natural-fibre composites, Chapter 3, pp 128–162
26. Fan M, Dai D, Huang B (2012) Fourier transform infrared spectroscopy for natural fibres, fourier transform—materials analysis. Salih S (ed) InTech. Available from: <http://www.intechopen.com/books/fourier-transform-materials-analysis/fourier-transform-infraredspectroscopy-for-natural-Fibers>. ISBN: 978-953-51-0594-7
27. Yue Y, A comparative study of cellulose i and ii fibers and nano crystalsa thesis submitted to the graduate faculty of the louisiana state university and agricultural and mechanical college in partial fulfillment of the requirements for the degree of master of science in the school of renewable natural resources
28. Mullik SS, Fabrication and characterization of alkali treated natural fibre reinforced polymer composites dept. of physics national institute of technology, Roorke
29. George J et al, Surface modification to improve the impact performance of natural fibre composites. [www.iccm-central.org/.../site/.../pap319.p.](http://www.iccm-central.org/.../site/.../pap319.p.), Dept of MTM, katholieke University Leuven, Belgium
30. Shipp DW et al, Raman spectroscopy: techniques and applications in the life sciences. *Adv Opt Photon*. <https://core.ac.uk/download/pdf/80838463.pdf>
31. Adebajo MO, Frost RL, Klopogge JT, Kokot S (2006) Raman spectroscopic investigation of acetylation of raw cotton. *Spectrochim Acta Part A Mol Biomol Spectrosc* 64(2):448–453

32. Tze WTY (2007) Evaluation of load transfer in the cellulosic-fiber polymer interphase using a micro-raman tensile. *Wood Fiber Sci* 39(1):184–195
33. Kicinska-Jakubowska A (2012) Review of natural fibers. part i—vegetable fibers. *J Nat Fibers* 150–167
34. Prabhu M, Vijay A (2018) Design and analysis of helmet using palmyra fiber. *Int Res J Eng Technol (IRJET)* 05(05)

# Studies on Thermal, Mechanical, and Morphological Properties of Aged XLPE Cables



Priya Selvamany, Gowri Sree Varadarajan, Naresh Chillu,  
Ramanujam Sarathi, Rengaswamy Jayaganthan, and Raman Velmurugan

**Abstract** The cross-linked polyethylene (XLPE) cable plays a crucial role as an insulating material in power transmission and distribution systems. Considering the adverse effects of aging on reliability and lifespan, the present study investigates the thermal, mechanical, and surface morphological characteristics of high-voltage XLPE power cables that have been exposed to chemical and hydrothermal aging. The mechanical properties of the specimens under consideration were evaluated and analyzed using impact strength experiments. It is found that, at room temperature, with XLPE specimen treated from unaged to chemical aging, the impact strength decreases from  $233.3 \text{ kJ m}^{-2}$  to about  $192.31 \text{ kJ m}^{-2}$ , and the elongation at break decreases from 187.74% to about 114.06%. When performing the impact test with hydrothermal aging, the impact strength and the elongation at break further reduce to  $71.43 \text{ kJ m}^{-2}$  and 100.2%, respectively. Surface profiles of unaged and aged materials are studied using atomic force microscopy and surface roughness is calculated consequently. The formation of pits on the surface of aged samples was visible in the AFM images. AFM analysis revealed a significant difference in the pattern of the average surface roughness and topography of XLPE insulation aged in chemical and those aged in hydrothermal. It will be demonstrated that a decrease in contact angle is related to increased specimen weight and surface roughness. For the specimens

---

P. Selvamany (✉) · G. S. Varadarajan  
Division of High Voltage Engineering, College of Engineering, Guindy Campus, Anna University,  
Chennai 600025, India  
e-mail: [priya.gdv@gmail.com](mailto:priya.gdv@gmail.com)

N. Chillu  
School of Electronics Engineering, VIT-AP University, Amaravati, Andhra Pradesh 522237, India

R. Sarathi  
Department of Electrical Engineering, Indian Institute of Technology Madras, Chennai 600036,  
India

R. Jayaganthan  
Department of Engineering Design, Indian Institute of Technology Madras, Chennai  
600036, India

R. Velmurugan  
Department of Aerospace Engineering, Indian Institute of Technology Madras, Chennai 600036,  
India

studied, the experimental results revealed an inverse relationship between surface roughness and contact angle. The thermal stability of aged specimens was further tested and analyzed to compare them with their unaged counterparts. XLPE materials were examined qualitatively for their applicability as an effective insulating material in the high-voltage insulation environment.

**Keywords** Aging · Cross-linking · Impact energy · Thermogravimetric analysis · AFM

## 1 Introduction

Owing to their mechanical, thermal, and electrical properties, cross-linked polyethylene (XLPE) cables are used as insulating material in transmission and distribution cables [1, 2]. Cross-linked polyethylene cable insulation is a composite material with XLPE as a polymer matrix and various additives and fillers. XLPE is subjected to different stresses such as thermal, mechanical, and environmental stress during operation, which affects its reliability [2]. Thermal aging causes structural and material property deterioration, as assessed by techniques such as differential scanning calorimetry (DSC) and thermo gravimetric analysis (TGA) [2–4]. XLPE crystallinity rises slightly due to recrystallization from laid-off segments at low temperatures (80 and 100 °C) aging [2]. The base XLPE polymer is organic in nature and has poor thermal stability. The cable system causes an increase in temperature during a short circuit or other malfunction during the power system operation. As a result, the thermal stability of polymer materials is an important consideration when choosing cables [3]. It is vital to investigate the thermal aging performance of XLPE to ensure cable protection and reliability [5]. Thermal aging of XLPE was considered to be a chain reaction involving free radicals and peroxides [6]. Despite the fact that many hypotheses state that water drastically influences cable lifetime, S. V. Nikolaevic highlighted that water enters the XLPE cable insulation and inhibits defected areas such as voids or contaminants [7]. Micro cracks form around these mechanically stressed imperfection areas as a result of Maxwell stress [7]. After a period of hydrothermal aging, the degradation in mechanical and electrical properties of XLPE leads to the transformation of physical and chemical structures [8, 9]. Water in the cable insulation (XLPE) is required for the formation of the water tree, which is a pre-breakdown phenomenon [10], and these intertwined defects on buried cables across the country are currently unavoidable [11].

Extruded cross-linked polyethylene (XLPE) submarine cables are typically designed to withstand challenging conditions such as thermal stress, anchoring, water pressure, salt mist, and chemical corrosion [12]. These submarine cables, which are buried under the seabed (~1–3 m) and laid nearshore under shallow water (~200 m), are abundant sources of hydrogen sulfide in the sea area [12, 13]. As a result of the reaction of copper conductors with the chemical ingredient forming copper sulfide crystals, sulfide deterioration and water permeation are two additional issues that



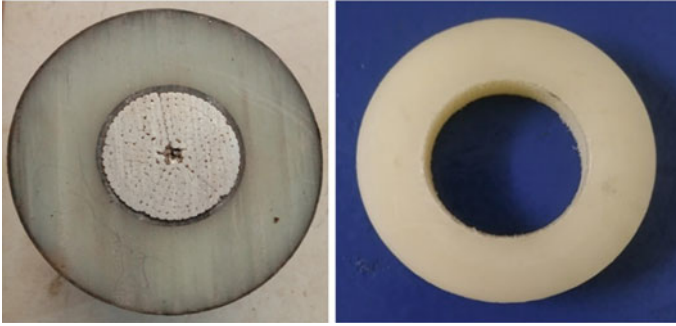
reduce insulator performance [13, 14]. The dielectric performance of ionic solutions is significantly affected [15]. The micro-indenter test emphasizes structural changes in macromolecular chains and crystalline morphology due to the elastic property of XLPE [16]. Tensile strength, Young modulus, impact strength, flexural strength, and percent elongation of XLPE were used to investigate mechanical properties [8, 17, 18]. Atomic pressure microscopy (AFM) is a powerful and reliable high-resolution method for visualizing spherulite morphology [19, 20]. For aged insulation surface structure, the contact angle and surface roughness measurement were correlated [8, 19]. Despite the fact that AFM studies have been conducted in the past, it is believed that the first steps have been taken to use AFM for quantitative analysis of underground cable insulation aging on its morphology [20].

Hence, the insulation will eventually fail mechanically and electrically due to water permeation and sulfide infection. The main motive of this study is to describe the deterioration of XLPE-insulated cables caused by water permeation and copper sulfate ( $\text{CuSO}_4$ ) electrolyte contagion. Thus, research focused on systematic techniques based on a review of the relevant literature. The current study aims to determine the effects of aging of insulation materials using a combination of analytical techniques. Therefore, the list of experimental studies were carried out to understand the various aging scenarios using techniques, namely (a) XLPE molecular structural changes with thermogravimetry (TG) method replication of the degree of deterioration, (b) mechanical impact strength by impact test, and (c) atomic force microscopic (AFM) examination of insulation. These studies have significantly aided in the accurate prediction of XLPE aging behavior. As a result, it is emphasized that current findings should be regarded as preliminary and inspiration for future research.

## 2 Materials and Methods

### 2.1 Specimen Aging Scenario

In this study, samples were peeled from a high-voltage single-core aluminum cable (230 kV, 1200 mm<sup>2</sup>) as shown in Fig. 1 with a specimen thickness of 0.3 mm using a specially designed cable cutting tool to achieve optimal surface smoothness. On XLPE samples, two aging conditions were used: hydrothermal aging at 80 °C, and a 1 M solution of copper sulphate ( $\text{CuSO}_4$ ) aging was incorporated at room temperature with a relative humidity of 50% for 250 h. The samples were taken out and their weight gain was measured every 30 min until saturation. After the saturation state, the weight gain was measured every four hours until any deviation persisted. Thermal, mechanical, and morphological investigations were performed on the samples because these aging scenarios could affect the various measurements.



**Fig. 1** 230 kV XLPE cable sample

## **2.2 Thermal Characterization**

Differential thermogravimetry analysis (TGA/DTG) was carried out on the specimens with the help of SDT-Q600 TA instruments. The weight of the empty crucible is  $214.4 \pm 0.1$  mg, while the mass of the samples is  $15.9 \pm 0.05$  mg. Utilizing sample filled alumina crucible, the weight loss of the specimen due to thermal decomposition was determined. The sample was heated from room temperature ( $27^\circ\text{C}$ ) to  $600^\circ\text{C}$  at a constant heating rate of  $10^\circ\text{C}/\text{min}$  maintaining a constant argon gas flow at a pressure of 200 kPa. The record data from the instrument was used to analyze the residual weight of samples as well as the weight derivative with respect to time and temperature. The degradation onset temperature ( $T_{5\%}$ ) was determined at 5% mass loss. The maximum degradation temperature ( $T_{\text{max}}$ ) was calculated at the peak of the first derivative of the TGA curve.

## **2.3 Mechanical Properties**

The Izod impact testing (as per ASTM D-256 standard) was carried out using Frank bacon model machine with a maximum capacity of 30 J. The measurements were taken for at least five samples of each specimen at room temperature. Stress efforts such as notches/cracks, high strain rates, extra loading, and low-test temperature all have an effect on the toughness of the material structure [18]. The impact test was performed in this work to understand the material property due to aging.

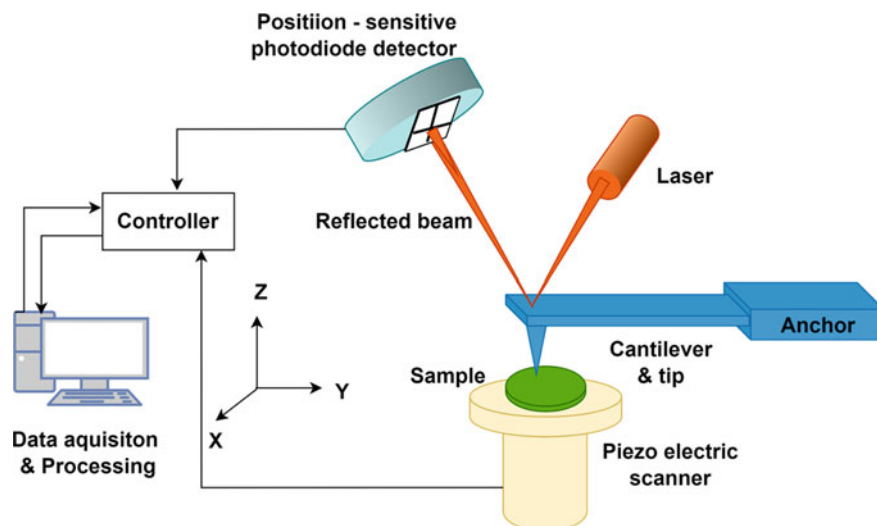


Fig. 2 Schematic illustration of the AFM imaging process

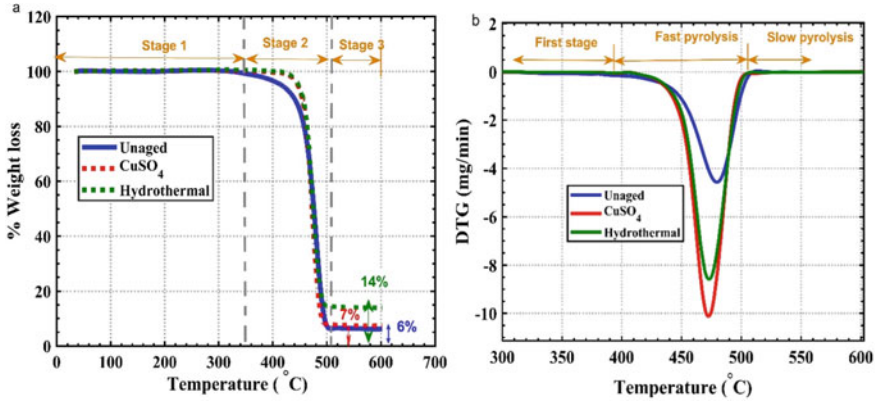
## 2.4 Examination of the Surface Topography Using an Atomic Force Microscope

The topography and roughness values of the XLPE insulation obtained from the surface of the specimens were characterized by AFM using AFM: A. P. E Research SRL system coupled with a flexure scanner in non-contact scanning mode under ambient conditions (temperature 25 °C and relative humidity 50%), as depicted in Fig. 2. The average surface roughness was evaluated by analyzing the three-dimensional (3D) height image exploiting a scan area of 30  $\mu\text{m} \times 30 \mu\text{m}$  with the Gwyddion software.

## 3 Results and Discussion

### 3.1 Thermogravimetric Analysis

Figure 3a, b show graphical representations of the TGA/DTG thermogram of various XLPE samples. The pyrolysis of the sample has progressed through several stages as the temperature rises. According to the results in Fig. 3a, the thermal degradation curve follows nearly the same path as the unaged specimen. The TGA curve of hydrothermally aged XLPE differs slightly but not significantly from that of  $\text{CuSO}_4$ . At stage 1 of Fig. 3a, no mass variation was observed for all XLPE specimens between 50 and 360 °C, owing to the volatilization of additives and by-products. The main



**Fig. 3** a TGA thermograms of XLPE decomposition; b DTG profile during pyrolysis of XLPE

stage of the pyrolysis process is stage 2 which is exemplified in Fig. 3a because most of the thermal weight loss in the XLPE cable specimen occurred at this stage from 360 °C to 508 °C. As a result, the weight loss rates for unaged, CuSO<sub>4</sub>, and hydrothermal specimens were 93.83, 92.82, and 86.25%, respectively. The weight loss rate is the differential weight loss per unit time at a given temperature that is calculated from differential thermogravimetry (DTG) profiles. Because of the fast pyrolysis during stage 2, the weight loss rate is rapid, resulting in a weight reduction of the sample when compared with the initial weight.

Following this stage, there was a constant and slow weight loss from 508 °C to 600 °C, which was attributed to “slow pyrolysis” and could be a thermal continuity of decomposition of material with high molecular weights. The inorganic content of the hydrothermal specimen is approximately 14 wt% higher than the unaged specimen during stage 3 in Fig. 3a. The residue value of the chemically aged specimens is approximately the same as that of the unaged specimens. When heated to 600 °C in argon, the inorganic content does not burn away and remains as residue after TGA testing. The plot of unaged and even-aged XLPE samples shows a good thermal behavior of single-step decomposition representing material homogeneity.

The phase of the derivate plot (DTG) from Fig. 3b of the thermal process’s first stage of weight loss was attributed to specimen moisture loss, resulting in low weight loss during this stage. The second stage is similar to fast pyrolysis exposed to rapid weight loss, with the most notable peak at 479.6 °C for unaged, 472.8 °C for CuSO<sub>4</sub>, and 473.2 °C for the hydrothermally aged specimen in the fast pyrolysis stage. Higher the decomposition temperature, the greater the thermal stability of the unaged XLPE cable. However, there was a slight deviation in peak temperature for aged specimens in this study. Table 1 summarizes the thermal stability results before and after aging. The weight loss rate at 360, 400, and 508 °C are the main criteria used in this study to determine the thermal stability of the aged specimen. With aging, the degradation onset temperature (T5%) of XLPE (Table 1) increased. CuSO<sub>4</sub> specimen raises T5% by 7 °C, while hydrothermal specimen raises T5% by 8 °C. The interaction between

**Table 1** Summary of thermal stability for XLPE samples obtained from TGA/DTG curves

Samples	Degradation onset temperature ( $T_{5\%}$ ) ( $^{\circ}\text{C}$ )	Maximum degradation temperature ( $T_{\text{max}}$ ) ( $^{\circ}\text{C}$ )	Weight loss rate (mg/min)		
			360 $^{\circ}\text{C}$	400 $^{\circ}\text{C}$	508 $^{\circ}\text{C}$
Unaged	416.4	479.6	0.07	0.16	0.06
CuSO <sub>4</sub>	446.2	472.6	0.02	0.05	0.06
Hydrothermal	447.9	473.2	0.01	0.04	0.01

carbonyl and hydroxyl groups has been linked to increased thermal stability (i.e., hydrogen bonding interactions).

As a result, the thermal stability of XLPE specimens was evaluated by comparing their decomposition temperatures. The decomposition temperature of XLPE cable insulation decreased with age, reducing the thermal stability of the aged specimen. The temperature of decomposition decreased with CuSO<sub>4</sub> and increased with hydrothermal aging compared with the unaged sample. In this study, hydrothermal and CuSO<sub>4</sub> aging both have moderate thermal stability in comparison with the unaged XLPE.

### 3.2 Impact Strength Analysis

Impact strength is frequently regarded as a defining measure of material toughness. The impact-tested XLPE specimen is discussed for comparison, and the effects of aging on mechanical properties are clearly depicted in Table 2. The energy required to fracture an unnotched specimen is measured using this impact test facility. However, in this study, every specimen demonstrates an unbreakable enactment. Under the given impact energy of 30 J, these specimens are reported as non-break (nb). It was concluded that the unnotched specimens attain barely invisible impact damage and had no major significant effect on the impact strength of the XLPE after aging. The impact energy and impact strength of unnotched Izod's decrease scientifically with CuSO<sub>4</sub> and hydrothermally aged samples compared with unaged specimen. For the cross-linked polyethylene material, a dramatic change in the impact strength is observed when the material undergoes this aging mechanism. Compared with the unaged specimen, the elongation at break decreases significantly with hydrothermal aging, and this is probably attributed to the suppression of mobility and orientation of the molecular chains during elongation. But compared with hydrothermal, the XLPE copper sulfide aging causes the elongation at break increases because of the decrease in crystallinity and increase in ductility. However, the presence of oxidation during hydrothermal aging, combined with cross-link bonds, causes a loss of ductility in the polymer prior to failure, as well as a decrease in tensile strength and elongation at break. The unaged specimen had an average impact strength of 233.3 kJ m<sup>-2</sup>, CuSO<sub>4</sub> had an average impact strength of 192.31 kJ m<sup>-2</sup>, and hydrothermal aging

had an average impact strength of  $71.43 \text{ kJ m}^{-2}$ . Under impact testing conditions, a  $\text{CuSO}_4$  aged sample demonstrates brittleness when compared with a hydrothermal specimen. When two aging scenarios are compared, the chemically aged specimen is slightly more ductile, and the impact strength of the chemically cross-linked XLPE sample increases significantly at room temperature due to a decrease in crystallinity, lamellar thickness, and crystallite size, as well as an increase in ductility [17].

The unaged XLPE is expected to absorb 0.7 J of large amounts of impact energy.  $\text{CuSO}_4$  and hydrothermal samples have impact strengths of about 0.5 and 0.2 J, respectively. The difference in impact strength between the aged and unaged samples is most likely due to the presence of small tiny cracks. The addition of water with thermal aging to the XLPE results in a 69.38% decrease in impact strength from  $233.3 \text{ kJ m}^{-2}$  for the unaged sample to  $71.43 \text{ kJ m}^{-2}$  for the hydrothermal sample. The addition of chemical aging to the XLPE affects both its toughness and stiffness. Because XLPE is rubber elastic in nature, the results strongly suggest that unaged causes material toughness.

Tensile strength and elongation at break (EAB) appear to be higher for  $\text{CuSO}_4$ -aged material than for hydrothermally aged material, according to previous tensile test results [8]. When the sample is hydrothermally aged, the materials become more cross-linked and the polymer chains become restrained, resulting in a lower EAB. Because the few crosslinks present have little effect on the ability of the chains to align in the stress direction, the EAB was moderately affected in  $\text{CuSO}_4$  at very low cross-link densities [8]. The results of the impact test, flexural test, and tracking time of the aged HDPE material discovered that materials with high toughness/stiffness increase the material's tracking time [18]. As a result of the experimental findings in the literature, it is confirmed that the unaged XLPE samples with higher impact energy results to validate that the unaged materials have high toughness/stiffness, which will promote the tracking time of the insulating material [18, 21].

**Table 2** Effect of laboratory-aged samples on their mechanical properties

Samples	Impact strength ( $\text{kJ m}^{-2}$ )	Impact energy unnotched (J)	Tensile strength* (MPa)	Elongation at break* (%)	Toughness ( $\text{J/m}^3$ )
Unaged	233.33 <sup>z</sup>	$0.7 \pm 0.04$	9.14	187.74	15.88
$\text{CuSO}_4$	192.31 <sup>z</sup>	$0.5 \pm 0.01$	9.55	114.06	9.09
Hydrothermal	71.43 <sup>z</sup>	$0.2 \pm 0.02$	8.73	100.2	7.57

\* Adapted from [8]; <sup>z</sup>No break

### 3.3 Topological Analysis

The AFM was used to investigate the surface morphology and roughness. It is used to reveal impurities, protrusions, or in-homogeneities on the XLPE specimens' surface [3]. A three-dimensional topographic scan of the XLPE samples is shown in Fig. 4. Table 3 gives the average surface roughness of XLPE with various aging criteria. Wettability is one of the most basic surface properties of materials. An approach based on the contact angle is presented for determining and evaluating the wettability behavior of XLPE materials. The deviation from the measured average roughness is less than 3% for all samples. The surface roughness of the hydrothermally aged specimen is increased by 23%, but the surface roughness of the CuSO<sub>4</sub> aged samples is increased by only 7% after chemical aging. Significant surface micro roughness is observed in the industrial manufacturing process of unaged high-voltage cables using 3D AFM images (Fig. 4a). As a result, it is emphasized that the quality of the virgin sample of highly defected regions with intensified peaks is responsible for local discharges. This will result in local breakdown and an increase in leakage current [2]. It is also concluded that the surface roughness of the hydrothermally aged sample plays a larger role in the mechanism of premature failure. Surface roughness variations in CuSO<sub>4</sub> can change the sample's surface energy.

Contact angle measurements from previous studies were considered, and pressure on the XLPE surface with work of adhesion,  $W_A$ , was calculated using Eq. (1) [22, 23]:

$$W_A = (1 + \cos\theta)\gamma_{LV}, \tag{1}$$

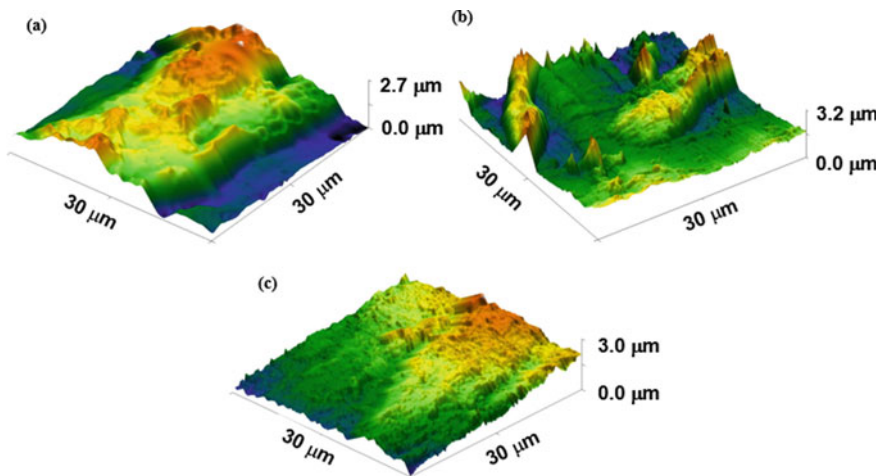


Fig. 4 AFM 3D images of XLPE insulations a Unaged; b CuSO<sub>4</sub>; c Hydrothermal

**Table 3** Measurements of the surface roughness and contact angle for the XLPE samples

Samples	Average surface roughness ( $\mu\text{m}$ )	Contact angle ( $\theta$ ) <sup>a</sup>	Work of adhesion ( $\text{mJ}/\text{m}^2$ )
Unaged	1.163	$88^\circ \pm 3.73^\circ$	75.35
CuSO <sub>4</sub>	1.246	$78^\circ \pm 6.22^\circ$	87.95
Hydrothermal	1.432	$56^\circ \pm 6.22^\circ$	113.52

<sup>a</sup>Adapted from [8]

where  $\gamma_{LV}$  and  $\theta$  denote the water surface tension (72.81 mN/m) and contact angle, respectively. Table 3 summarizes the effect of the various aging results and their wetting characteristics such as work of adhesion, total surface free energy, and interfacial free energy. In comparison with hydrothermally aged specimens, the static contact angle increases moderately with salt concentrated aging of the polymer, resulting in a more non-polar surface. It indicates that the hydrophobicity of CuSO<sub>4</sub> was significantly increased, resulting in a decrease in surface free energy. For the hydrothermal specimen, the contact angle decreases and the work of adhesion increases. Typically, adhesion work is related to polymer matrix interaction. The changes in the polymer matrix are defined in terms of crystallinity, polymer structures, etc., the segments and chains in the polymer matrix molecules can adopt a variety of unique configurations. The increase in the hydrophilic nature of the hydrothermal specimen is due to insufficient polymeric matrix bonding, which increases the work of adhesion. As a result, a correlation was discovered between surface roughness, wettability, and contact angle. Finally, it was discovered that surface roughness and contact angle variation had an inverse relationship and were validated with a literature survey [19]. The relation between surface roughness and surface wettability is explained through the surface energy of the specimen, where the higher surface roughness sample holds higher surface energy, which results in lower contact angle measurements. When the results were analyzed, it was discovered that the contact angle values near the hydrophobic surface value approached the hydrophilic values as the surface roughness increased.

## 4 Conclusions

The conclusions accrued based on the study are the following:

- (1) The TGA/DTA results show that the hydrothermal and chemical aging mechanism of these XLPE materials remains constant across a temperature range of 50–360 °C. A good correlation was found between the formation of decomposition products on the atomic scale and the reduction in mechanical properties (macromolecular scale) for each aged specimen.



- (2) The temperature-independent impact behavior of XLPE, as well as the relationship between impact performance and structure, are investigated in this work. Chemical and hydrothermal aging in XLPE reduces impact strength and elongation at break.
- (3) The impact response of all XLPE samples shows a non-catastrophic failure. Moreover, the hydrothermal aging decreased the toughness of the overall insulation of the cable.
- (4) AFM results revealed that during  $\text{CuSO}_4$  aging, ion diffusion is inadequate in the XLPE matrix, resulting in less surface roughness compared with hydrothermal aging. An inverse relationship was noticed between the measured contact angle and surface roughness.

**Acknowledgements** The author wishes to thank Tamil Nadu Generation and Distribution Corporation Ltd., (TANGEDCO) for providing cable samples.

## References

1. Zhao Y, Han Z, Xie Y, Fan X, Nie Y, Wang P, Liu G, Hao Y, Huang J, Zhu W (2020) Correlation between thermal parameters and morphology of cross-linked polyethylene. *IEEE Access* 8:19726–19736. <https://doi.org/10.1109/ACCESS.2020.2968109>
2. Zhang Y, Hou Z, Wu K, Wang S, Li J, Li S (2020) Influence of oxygen diffusion on thermal aging of cross-linked polyethylene cable insulation. *Materials (Basel)* 13:2056. <https://doi.org/10.3390/ma13092056>
3. Melo Nobrega A, Barreira Martinez ML, Alencar de Queiroz AA (2013) Investigation and analysis of electrical aging of XLPE insulation for medium voltage covered conductors manufactured in Brazil. *IEEE Trans Dielectr Electr Insul* 20:628–640. <https://doi.org/10.1109/TDEI.2013.6508767>
4. Qin S, Liu R, Wang Q, Chen X, Shen Z, Hou Z, Ju Z (2022) Study on the molecular structure evolution of long-term-operation XLPE cable insulation materials. *Energy Rep* 8:1249–1256. <https://doi.org/10.1016/j.egy.2021.11.212>
5. Li J, Li H, Wang Q, Zhang X, Ouyang B, Zhao J (2016) Accelerated inhomogeneous degradation of XLPE insulation caused by copper-rich impurities at elevated temperature. *IEEE Trans Dielectr Electr Insul* 23:1789–1797. <https://doi.org/10.1109/TDEI.2016.005142>
6. Seguchi T, Tamura K, Kudoh H, Shimada A, Sugimoto M (2015) Degradation of cable insulation material by accelerated thermal radiation combined aging. *IEEE Trans Dielectr Electr Insul* 22:3197–3206. <https://doi.org/10.1109/TDEI.2015.004880>
7. Nikolajevic SV, Drca R (2001) Effect of water on aging of XLPE cable insulation. *Electr Power Syst Res* 60:9–15. [https://doi.org/10.1016/S0378-7796\(01\)00147-X](https://doi.org/10.1016/S0378-7796(01)00147-X)
8. Selvamany P, Varadarajan GS, Chillu N, Sarathi R (2022) Investigation of XLPE cable insulation using electrical, thermal and mechanical properties, and aging level adopting machine learning techniques. *Polymers* 14:1614. <https://doi.org/10.3390/polym14081614>
9. German-Sobek M, Cimbala R, Kiraly J (2013) Influence of aging and water treeing to degradation of XLPE insulation. *Starnutie Elektroizol Systémov* 8:26–30
10. Selvamany P, Varadarajan GS (2022) Understanding of pulse voltage response analysis for degradation in XLPE cable using equivalent circuit model. *J Electr Eng Technol* 17:2951–2962. <https://doi.org/10.1007/s42835-022-01071-w>

11. Li J, Zhao X, Yin G, Li S, Zhao J, Ouyang B (2011) The effect of accelerated water tree aging on the properties of XLPE cable insulation. *IEEE Trans Dielectr Electr Insul* 18:1562–1569. <https://doi.org/10.1109/TDEI.2011.6032825>
12. Wang W, Yan X, Li S, Zhang L, Ouyang J, Ni X (2021) Failure of submarine cables used in high-voltage power transmission: Characteristics, mechanisms, key issues and prospects. *IET Generation, Transm Distrib* 15:1387–1402. <https://doi.org/10.1049/gtd2.12117>
13. Fukuda T, Irie S, Fujiki S, Hisatsune T (1980) A new method for the prevention of water and sulfide penetration and deterioration of cross-linked Polyethylene (XLPE) insulated submarine power cables. *IEEE Trans Power Appar Syst* 2094–2101
14. Anelli P, Motori A, Ghinello I, Mazzanti G, Montanari GC (1997) Electrical properties for diagnosis of sulfide-tree growth in cables under dc stress. In: *IEEE conference on electrical insulation and dielectric phenomena*, pp 292–295. <https://doi.org/10.1109/CEIDP.1997.634616>
15. Promvichai N, Boonraksa T, Marungsri B (2019) The ionic solutions effects to degradation on XLPE insulated underground cable with environmental model. *GMSARN Int J* 13:12–25
16. Suraci SV, Fabiani D, Xu A, Roland S, Colin X (2020) Aging assessment of XLPE LV cables for nuclear applications through physico-chemical and electrical measurements. *IEEE Access* 8:27086–27096. <https://doi.org/10.1109/ACCESS.2020.2970833>
17. Ren Y, Sun X, Chen L, Li Y, Sun M, Duan X, Liang W (2021) Structures and impact strength variation of chemically crosslinked high-density polyethylene: effect of crosslinking density. *RSC Adv* 11:6791–6797. <https://doi.org/10.1039/D0RA10365A>
18. Sarathi R, Chandrasekar S, Giri VS, Venkateshaiah C, Velmurugan R (2004) Analysis of surface degradation of high-density polyethylene (HDPE) insulation material due to tracking. *Bull Mater Sci* 27:251–262. <https://doi.org/10.1007/BF02708514>
19. Naresh C, Parameswarreddy G, Kumar AV, Jayaganthan R, Subramanian V, Sarathi R, Danikas MG (2022) Understanding the dielectric properties and electromagnetic shielding efficiency of zirconia filled epoxy-MWCNT composites. *Eng Res Express* 4:15008. <https://doi.org/10.1088/2631-8695/ac4a4a>
20. Robertson C, Wertheimer MR, Fournier D, Lamarre L (1996) Study on the morphology of XLPE power cable by means of atomic force microscopy. *IEEE Trans Dielectr Electr Insul* 3:283–288. <https://doi.org/10.1109/94.486780>
21. Sarathi R, Das S, Venkateshaiah C, Yoshimura N (2003) Investigations of growth of electrical trees in XLPE cable insulation under different voltage profiles. In: *Annual report conference on electrical insulation and dielectric phenomena*, pp 666–669. <https://doi.org/10.1109/CEIDP.2003.1254942>
22. Jose JP, Abraham J, Maria HJ, Varughese KT, Thomas S (2016) Contact angle studies in XLPE hybrid nanocomposites with inorganic nanofillers. *Macromol Symp* 366:66–78. <https://doi.org/10.1002/masy.201650048>
23. Li W, Shi Q, Xiao W (2015) Investigation on thermal aging of HVDC XLPE. In: *Proceedings of 5th international conference on advanced design and manufacturing engineering*. Atlantis Press, Paris, France, pp 428–432. <https://doi.org/10.2991/icadme-15.2015.86>

# Numerical Investigation of Vertical Roller Mill Operation Using Discrete Element Method



Vinoth Dhanasekaran, Velmurugan Ramachandran,  
Praveenkumar Vijayakumar, and Harikrishnan Krishnamoorthy

**Abstract** A vertical roller mill (VRM) is a grinding equipment used for the size reduction of minerals, cement, and ceramics. The capacity of the VRM depends not only on the grinding material properties but also on the operational parameters of the VRM. This study investigated the effect of table speed (mill speed), roller and table gap, dam ring height, and rolling resistance of material using the discrete element method in an industrial-scale VRM. Simulation results showed that the rolling point is moved near the outer diameter of the grinding table as the mill speed increased. This behavior matches the previous experimental analysis carried out in a lab-scale VRM. The grinding force increases when mill speed is reduced. This is due to the lowered centrifugal force acting on the particles. Increasing the gap between the roller and table reduced the grinding forces required for performing the compaction. An increase in the dam ring facilitated the higher particle bed and raised the grinding force and power consumption. The roller speed is not influenced by the gap between roller and table and dam ring height when other parameters are kept constant. Increased rolling resistance increases the force and power required for grinding. When higher rolling resistance is applied due to particle shape complexity at less mill speed, more vertical force is exerted on the roller, and the roller speed is insensitive to rolling resistance. This study provides the basis for further experimental investigations on industrial-scale VRM and supports the design optimization of the VRM.

**Keywords** Powder technology · Discrete element method · Vertical roller mill · Comminution

---

V. Dhanasekaran (✉) · V. Ramachandran  
Department of Aerospace Engineering, Indian Institute of Technology Madras, Chennai 600036,  
India  
e-mail: [ae18s019@smail.iitm.ac.in](mailto:ae18s019@smail.iitm.ac.in)

V. Ramachandran  
e-mail: [ramanv@iitm.ac.in](mailto:ramanv@iitm.ac.in)

P. Vijayakumar · H. Krishnamoorthy  
Department of Mechanical Engineering, Indian Institute of Technology Madras, Chennai 600036,  
India

## Nomenclature

$F_n$	Normal contact force
$F_\tau$	Tangential contact force
$K_{nl}$	Contact stiffness during loading
$K_{nu}$	Contact stiffness during unloading
$K_\tau$	Tangential stiffness
$K_r$	Rolling stiffness
$M_r$	Rolling resistance moment
$R_r$	Rolling radius
$s_n$	Overlap value
$s_\tau$	Tangential relative displacement
$\lambda$	Dimensionless constant
$\mu$	Frictional coefficient
$\mu_r$	Rolling resistance coefficient
$\omega_{rel}$	Relative angular velocity

## 1 Introduction

In processing plants, size reduction of raw materials is an energy-intensive operation. A vertical roller mill is a grinding equipment for many industries such as minerals, cement, and ceramics. It is also used to grind slag and nonmetallic ores. The VRM decreases the number of equipment in the grinding circuit by combining the drying, crushing, grinding, and particle segregation in one unit [1]. The energy-efficient operation and proven benefits over other grinding equipment like ball mills and autogenous mills attracted the interest of using VRM in mineral industries.

The successful operation of the VRM is not only affected by grinding material properties such as mechanical and contact properties and the shape of particles but also depends on the operational parameters like mill speed, roller and table gap, and dam ring height.

Numerical simulations applying the discrete element method (DEM) are for computing the motion and collisions of particles. DEM effectively optimizes the equipment design and operating conditions in various industries. Mishra et al. [2] studied the ball mill using two-dimensional DEM. The authors validated that the power and torque estimated by the DEM code correspond to the experimental result. The mill speed and filling were varied, and the torque required to drive the mill and power was predicted.

Mishra et al. [3] conducted the motion analysis of particles in ball mills using DEM. The results predicted the motion of two arbitrary particles, charge profile similar to the laboratory ball mill. Effect of lifter bar shapes on charge motion is identified.

Cleary [4] simulated the industrial-scale ball mill of 5 m diameter using DEM to predict the motion of particles, power, torque, and liner wear by varying the mill speed and material parameters. Influence of mill speed and contact properties on power draw and the effect of particle shape on charge motion were predicted.

Bian et al. [5] demonstrated the accuracy of DEM over empirical formulas in calculating ball mill torque and power consumption for various mill speeds and lifter configurations using experiments.

Cleary et al. [6] developed a methodology for scale-up of a HICOM mill using DEM considering mechanical and process requirements. The relation between speed, power draw, and mill height scaling factor was developed.

Eichler et al. [7] analyzed the roller compaction chamber using DEM to understand the powder behavior. Velocity profile, pressure, and porosity predicted by DEM are in good quantitative agreement with experimental data. Chen et al. [8] developed and validated a FEM-DEM model of an impact roller to predict the soil displacements, peak pressures at each pass, and energy delivered.

Liu et al. [9] simulated and validated the capability of DEM to estimate the product particle size distribution, throughput, crushing rate, and power draw of the lab-scale VRM for various material and operational parameters.

The present study investigated the effect of mill speed, roller and table gap, dam ring height of an industrial-scale VRM, and rolling resistance of particles using DEM. In this simulation, DEM is utilized to estimate the forces exerted on the roller and the rotational speed of the roller during the grinding of limestone.

## 2 Methodology

### 2.1 Vertical Roller Mill

The VRM shall have three or four rollers and a table. The rollers were pressed against the ore and table using hydraulic cylinders during operation. The table is rotated by an external drive train, and rollers are counter-rotated due to the friction between the roller and material. The feed chute leads the feed material onto the grinding table. The centrifugal force generated due to the table rotation accelerates the feed material toward the gap between roller and table. Feed material is ground by the combination of shear and compressive forces. The ground material flows over the dam ring and mixes with the gas stream coming through the nozzle ring. The gas stream carries the material to the separator for further segregation. The fine material leaves the mill, and coarser material is diverted to the grinding table by the separator. This process is carried out until the required product size is achieved.

The VRM investigated in this study has a roller diameter of 3000 mm and a width of 1000 mm. The outer diameter of the table is 5000 mm, and the maximum dam ring height is 200 mm. The influence of the gas stream in the grinding zone is not considered to simplify the simulation.

## 2.2 Numerical Simulation

### 2.2.1 Modeling

Three-dimensional models of the VRM were created using the computer-aided design tool SolidWorks, and RockyDEM software (version 4.5.2) is used to carry out the DEM simulation. In the DEM simulation, Newton's second law is used to calculate the behavior of limestone. For calculating the contact force in the normal direction, hysteretic linear spring model [10, 11] was utilized. In this model, contact stiffnesses and overlaps were used to calculate the normal force (Fig. 1).

$$\Delta s_n \geq 0; F_n^t = \min(K_{nl}s_n^t, F_n^{t-\Delta t} + K_{nu}\Delta s_n), \quad (1)$$

$$\Delta s_n < 0; F_n^t = \max(F_n^{t-\Delta t} + K_{nu}\Delta s_n, \lambda K_{nl}s_n^t), \quad (2)$$

$$\Delta s_n = s_n^t - s_n^{t-\Delta t}, \quad (3)$$

where  $F_n^t$  and  $F_n^{t-\Delta t}$  are the normal contact forces at time  $t$  and  $t - \Delta t$ , respectively.  $\Delta t$ ,  $\Delta s_n$  are respectively the calculated time step and the change in contact normal overlap.  $s_n^t$  and  $s_n^{t-\Delta t}$  are the normal overlap values at time  $t$  and  $t - \Delta t$ , respectively.  $K_{nl}$  and  $K_{nu}$  are the contact stiffness values during loading and unloading, respectively.

The linear spring coulomb limit model [11] was utilized to calculate the contact forces acting in tangential direction. In this model, the tangential force cannot exceed the coulombs limit. So, the tangential contact force is given by:

$$F_\tau^t = \min(|F_{\tau,e}^t|, \mu F_n^t) \frac{F_{\tau,e}^t}{|F_{\tau,e}^t|} \quad (4)$$

$$F_{\tau,e}^t = F_\tau^{t-\Delta t} - K_\tau \Delta s_\tau, \quad (5)$$

where  $F_\tau^{t-\Delta t}$  is the tangential contact force at time  $t - \Delta t$ ,  $F_{\tau,e}^t$  is the purely elastic tangential contact force at time  $t$ ,  $\Delta s_\tau$  is the relative displacement in tangential direction at time  $t$ , and  $K_\tau$  is the tangential stiffness.

Rolling resistance is the force that resists the body's motion when it rolls on a surface. In RockyDEM, rolling resistance is adapted as a moment that opposes the rolling motion of a particle. In this investigation, the rolling resistance moment is calculated using type C: linear spring rolling limit model [11].

$$M_r^t = \min(|M_{r,e}^t|, M_{r,lim}) \frac{M_{r,e}^t}{|M_{r,e}^t|} \quad (6)$$

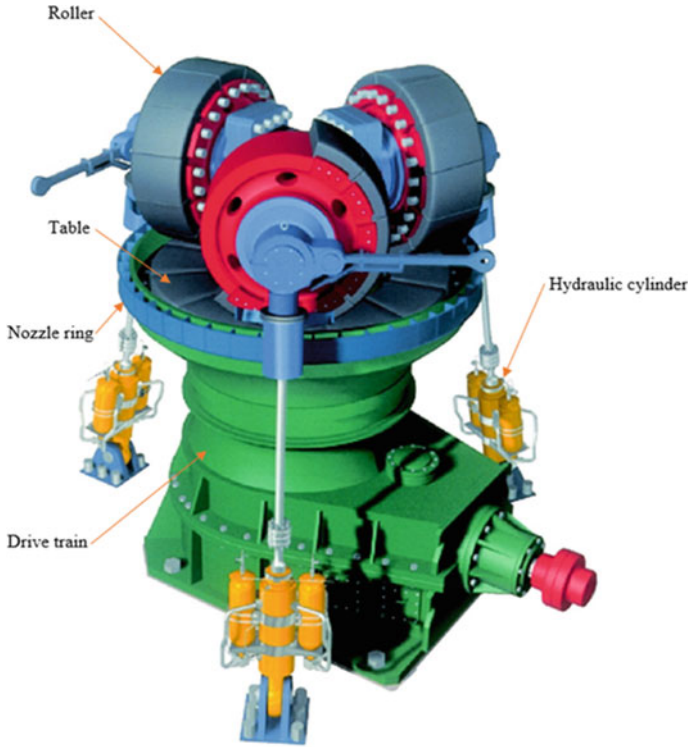


Fig. 1 Main parts of a typical vertical roller mill [12]

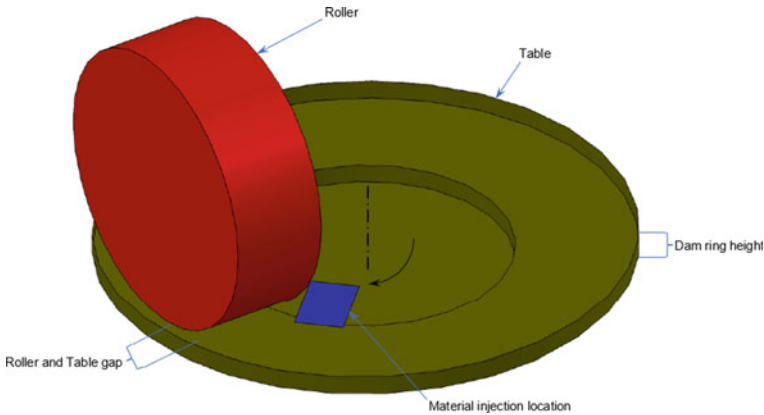
$$M_{r,e}^t = M_r^{t-\Delta t} - K_r \omega_{rel} \Delta t \quad (7)$$

$$M_{r,lim} = \mu_r R_r F_n, \quad (8)$$

where  $M_{r,e}^t$  is the purely elastic rolling resistance moment and  $M_{r,lim}$  is the limiting rolling moment value.  $K_r$  and  $\omega_{rel}$  are the rolling stiffness and relative angular velocity vector, respectively.  $\mu_r$  and  $R_r$  are rolling resistance coefficient and rolling radius, respectively.

The three-dimensional model consists of a roller and a table. Cylindrical periodic domain about Y-axis was applied to the model to reduce the simulation time. Figure 2 shows the three-dimensional model used for simulation. Table rotation was achieved by creating a rotation type motion frame with uniform angular velocity about Y-axis. To model the rotation of the rollers due to friction forces arising from material motion, free-body rotation type motion frame was created about the roller X-axis.

The Young's modulus, shear modulus (obtained by uniaxial compression test), and contact parameters (measured by drop and sliding plate tests) were collected from the study by Qin et al. [13]. The physical and contact properties are presented



**Fig. 2** Simulation model of an industrial-scale vertical roller mill

**Table 1** Physical and contact properties for numerical simulation

Young's modulus of limestone	Pa	$5.23 \times 10^8$
Bulk density of limestone	$\text{kg/m}^3$	1400
Poisson's ratio of limestone		0.25
Young's modulus of steel	Pa	$1 \times 10^{11}$
Density of steel	$\text{kg/m}^3$	7850
Poisson's ratio of steel		0.3
Friction coefficient between particles		0.77
Restitution coefficient between particles		0.208
Friction coefficient between particle and steel		0.61
Restitution coefficient between particle and steel		0.557

in Table 1. Ore particle sizes ranges from 30 to 50 mm. The particles were injected continuously in front of the roller.

### 2.2.2 Simulation

The simulation was performed by changing the mill speed from 20 to 30 rpm, the gap between the roller and table from 60 to 100 mm, and the dam ring height from 140 to 200 mm. The duration of each simulation is 10 s, and the steady-state is reached after 5 s. Figure 3 shows the particle interaction with the roller and the table.

Grinding force is one of the critical design parameters of the VRM. These values are obtained from the simulation by measuring the force acting on the Y-direction (vertical force) and Z-direction (horizontal force) of the roller axis. The rolling point in a VRM is a diameter at which the roller translational velocity is the same as the



**Fig. 3** DEM simulation of a vertical roller mill

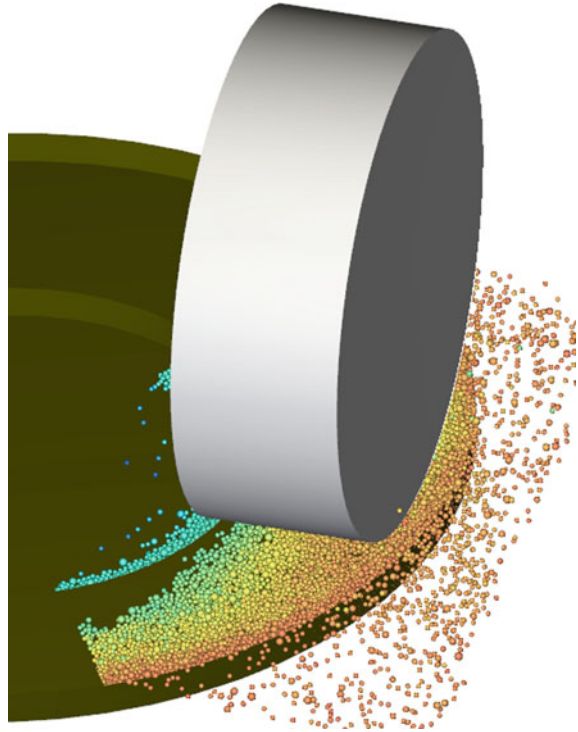


table translational velocity. At rolling point, materials undergo pure compression, and in the other portion of the table, materials experience compression and shear. Roller speed is measured during the simulation to calculate the rolling point. The rolling point shall predict the location of high-pressure zone in the grinding table [12].

In DEM, the particle's shape is essential to accurately predict the behavior. So complex and realistic shapes are being utilized in simulations. However, complex particle shapes require more computation time to predict their behavior. To speed up the simulation that involves complex-shaped particles, spherical shapes are used. To compensate the shape simplification, suitable rolling resistance can be added to the contact of spherical particles [14]. Raw ore from different mines shall have different shapes. To investigate the effect of changes in particle shapes, multiple simulations were conducted by changing the rolling resistance coefficient from 0.1 to 0.2.

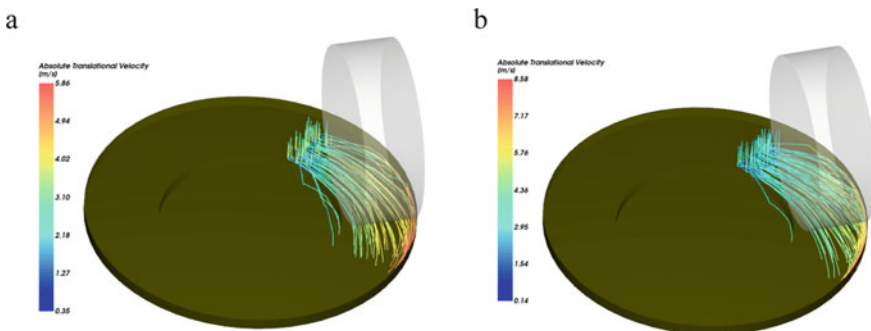
### 3 Results and Discussions

#### 3.1 Influence of Mill Speed

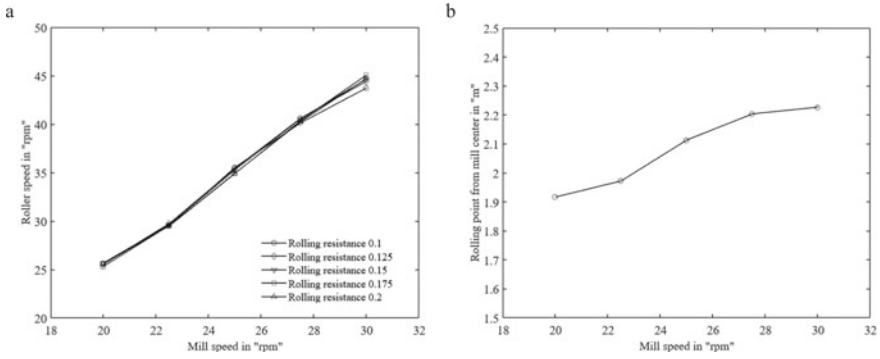
To identify the significance of mill speed, simulations were conducted at five different mill speeds from 20 to 30 rpm in steps of 2.5 rpm. Translational velocity induced in the particles at different mill speeds are shown in Fig. 4. At a mill speed of 20 rpm and rolling resistance of 0.15, the maximum translational velocity of particles is 5.86 m/s, which is 46% lesser than the maximum translational velocity at 30 rpm. This is due to the lesser centrifugal force and angular velocity of the particles.

The roller speed and rolling point at various mill speeds are shown in Fig. 5. Simulation results show that there is no influence of rolling resistance on the roller speed, hence the rolling point is calculated by taking the average roller speed at different coefficients of rolling resistance. At low speeds, the particles flow near the inner diameter of the table, which widens the compression zone, and the rolling point is located near to the mean diameter of the table. As table speed increases, the centrifugal force makes the sloped grinding bed and the compression zone becomes small and the rolling point is placed near to the table's outer diameter. This phenomenon matches the experimental investigation carried out by Jensen et al. [12].

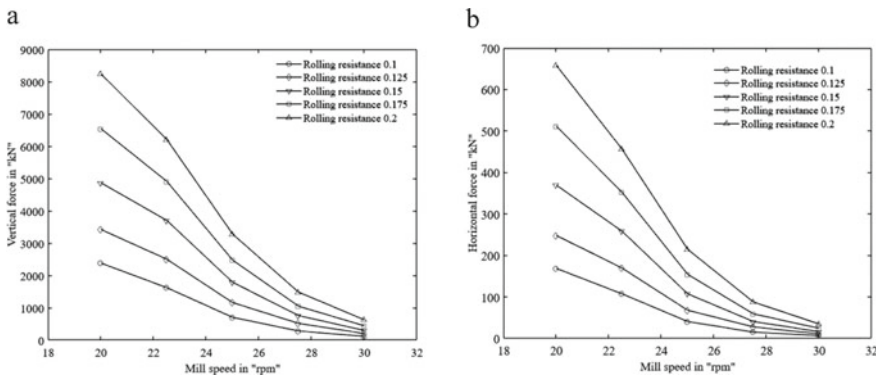
The resulting forces in the vertical and horizontal directions due to changes in rolling resistance and the mill speed are summarized in Fig. 6. Lesser mill speed and increase in rolling resistance aid the formation of a larger compression zone, resulting in higher forces on rollers. Based on the rolling resistance of the particle, the minimum acceptable mill speed needs to be identified for the safe operation of the VRM.



**Fig. 4** Trajectory of particles in the table at various mill speeds. **a** Mill speed—20 rpm; **b** Mill speed—30 rpm



**Fig. 5** Influence of mill speeds on **a** Roller speed; **b** Rolling point



**Fig. 6** Force generated due to compaction at various mill speeds. **(a)** Vertical force; **(b)** Horizontal force

### 3.2 Effect of the Roller and Table Gap

In VRM, it is impossible to maintain a particular gap between the table and roller during operation. However, the VRM can be stopped using mechanical or hydraulic systems at minimum gap. The equipment needs to be designed considering the minimum allowable gap. The simulation is carried out with a roller and table gap from 60 to 100 mm.

The effect of the gap between the roller and the table was summarized in Fig. 7. Less gap between the roller and table requires higher material compression, resulting in high force and power consumption. This behavior was already documented in the literature by West [15] using analytical formula. The roller and the table gap does not affect the speed of the roller when other parameters are kept constant.

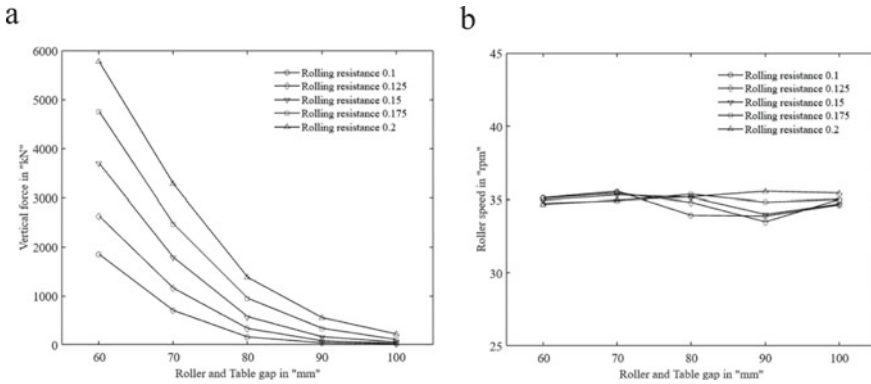


Fig. 7 Effect of the gap between the roller and table on (a) Vertical force; (b) Roller speed

### 3.3 Influence of the Dam Ring Height

The dam ring facilitates the needed bed formation during the operation of the VRM. Simulations were performed by changing the dam ring height from 140 to 200 mm. The influence of the dam ring height on induced vertical forces and roller speed is shown in Fig. 8. Higher dam ring height increases the upstream material bed thickness in front of the roller, increasing the grinding force requirements. Similar to gap between the roller and table, changes in dam ring height do not affect the roller speed.

In general, increasing rolling resistance increases the force induced on the roller during grinding. The effect of particle shape is more at low mill speeds when compared with the reduced roller and table gap and increased dam ring height. The roller speed induced by friction is unaffected by the particle shape parameters.

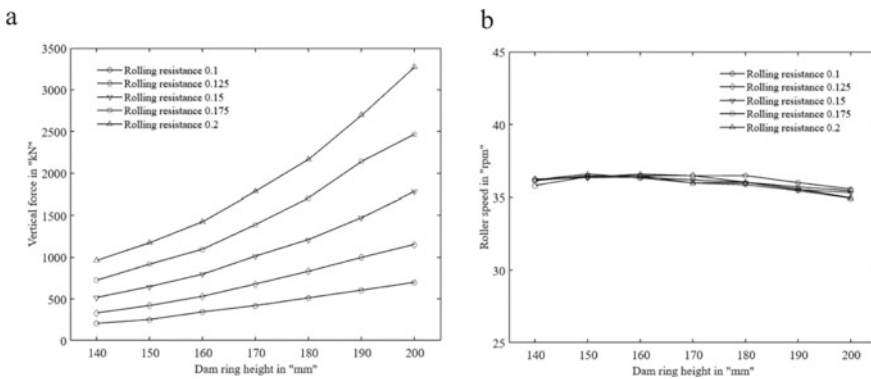


Fig. 8 Influence of dam ring height on (a) Vertical force; (b) Roller speed

## 4 Conclusion

An industrial-scale vertical roller mill has been developed and successfully simulated employing the discrete element method. Analysis of the VRM to many operational parameters shows trends that are in qualitative agreement with the industrial practice. The simulation results showed that the rolling point is moved near the outer diameter of the grinding table as the mill speed increased. This behavior matches the previous experimental analysis carried out in a lab-scale VRM. The grinding force increased when the mill speed or gap between the roller and table was reduced. An increase in dam ring height results in a thicker material bed and increases the forces acting on the roller and table. However, the gap or the dam ring height does not affect roller speed. The influence of particle shape is more at lower mill speeds than the roller and table gap and changes to dam ring height. The roller speed resulting from the frictional force is insensitive to the rolling resistance of the material. This study provides the basis for further experimental investigations on industrial-scale VRM and supports the design optimization of the VRM.

## References

1. Pareek P, Sankhla VS (2021) Review on Vertical Roller Mill in Cement Industry and its performance parameters. *Mater Today: Proc* 44:4621–4627. <https://doi.org/10.1016/j.matpr.2020.10.916>
2. Mishra BK, Rajamani RK (1992) The discrete element method for the simulation of Ball Mills. *Appl Math Model* 16:598–604. [https://doi.org/10.1016/0307-904x\(92\)90035-2](https://doi.org/10.1016/0307-904x(92)90035-2)
3. Mishra BK, Rajamani RK (1990) Motion analysis in tumbling mills by the discrete element method. *Kona Powder Part J* 8:92–98. <https://doi.org/10.14356/kona.1990016>
4. Cleary PW (1998) Predicting charge motion, power draw, segregation and wear in ball mills using discrete element methods. *Miner Eng* 11:1061–1080. [https://doi.org/10.1016/s0892-6875\(98\)00093-4](https://doi.org/10.1016/s0892-6875(98)00093-4)
5. Bian X, Wang G, Wang H, Wang S, Lv W (2017) Effect of lifters and mill speed on particle behaviour, torque, and power consumption of a tumbling ball mill: experimental Study and DEM simulation. *Miner Eng* 105:22–35. <https://doi.org/10.1016/j.mineng.2016.12.014>
6. Cleary PW, Owen PJ (2016) Using DEM to understand scale-up for a HICOM® Mill. *Miner Eng* 92:86–109. <https://doi.org/10.1016/j.mineng.2016.03.004>
7. Eichler C, Pietsch-Braune S, Dosta M, Schmidt A, Heinrich S (2022) Micromechanical analysis of roller compaction process with DEM. *Powder Technol* 398:117146. <https://doi.org/10.1016/j.powtec.2022.117146>
8. Chen Y, Jaksa MB, Kuo Y-L, Scott BT (2021) Discrete element modelling of the 4-sided impact roller. *Comput Geotech* 137:104250. <https://doi.org/10.1016/j.compgeo.2021.104250>
9. Liu C, Chen Z, Zhang W, Mao Y, Xu P, Xie Q (2022) Analysis of vertical roller mill performance with changes in material properties and operating conditions using DEM. *Miner Eng* 182:107573. <https://doi.org/10.1016/j.mineng.2022.107573>
10. Walton OR, Braun RL (1986) Viscosity, granular-temperature, and stress calculations for shearing assemblies of inelastic, frictional disks. *J Rheol* 30:949–980. <https://doi.org/10.1122/1.549893>
11. ESSI Rocky, Release 4.5.2, DEM Technical Manual. ESSI Rocky DEM, S.R.L., 2021

12. Jensen LRD, Fundal E, Møller P, Jespersen M (2011) Wear mechanism of abrasion resistant wear parts in raw material Vertical Roller Mills. *Wear* 271:2707–2719. <https://doi.org/10.1016/j.wear.2011.03.018>
13. Qin R, Fang H, Liu F, Xing D, Yang J, Lv N et al (2019) Study on physical and contact parameters of limestone by DEM. *IOP Conf Ser: Earth Environ Sci* 252:052110. <https://doi.org/10.1088/1755-1315/252/5/052110>
14. Zhou L, Chu X, Xu Y (2017) DEM investigation on characteristics of rolling resistance for modelling particle shape. *EPJ Web Conf* 140:05005. <https://doi.org/10.1051/epjconf/201714005005>
15. West MP (1991) Process Mechanics of vertical roller mill comminution grinding. *J Eng Ind* 113:381–387. <https://doi.org/10.1115/1.2899711>

# Effect of Gamma Irradiation on Mechanical and Thermal Properties of 3D-Printed PLAs



V. Yogeshwaran, J. Chandradass, M. Chinnapandi, and R. Velmurugan

**Abstract** Polylactic acid (PLA) is a popular 3D printing material with a high decomposition rate and is used in various environmentally friendly applications such as biomedical and food-grade packaging. This work is focused on studying the properties of 3D-printed PLA samples irradiated with gamma radiation at the dosages of 5, 10, and 15 K Gy using cobalt-60 gamma irradiation and is examined for the mechanical and thermal properties. The layer thickness of 0.4 mm and a rectilinear infill pattern with a 100% density is used. Mechanical properties such as tensile, flexural, and Izod impact properties are studied. Dynamic mechanical analysis (DMA), differential scanning calorimetry (DSC), dilatometer, and thermal conductivity are used to study thermal stability. The effect of gamma irradiation on these mechanical and thermal properties is studied, and these studies show that gamma irradiation affects the mechanical and thermal properties of PLA.

**Keywords** Fused deposition modeling · Layer thickness · Infill pattern · Mechanical properties · Thermal properties · Gamma irradiation

## 1 Introduction

Making polymers with any complex form is easy and affordable with fused deposition modeling. 3D printing is a popular technique for fabricating three-dimensional solid objects from a digital design. It is widely popular in many applications in the modern production sector. Paritala et al. [1] discuss the advantages of additive manufacturing over traditional production. This approach involves designing the product and sending the designs to the shop floor for the prototype's production. In comparison, additive manufacturing uses CAD software to design and innovate the product

---

V. Yogeshwaran · J. Chandradass (✉)

Centre for Automotive Materials, Department of Automobile Engineering, SRM Institute of Science and Technology, KTR Campus, Chengalpattu, India  
e-mail: [chandraj@srmist.edu.in](mailto:chandraj@srmist.edu.in)

J. Chandradass · M. Chinnapandi · R. Velmurugan

Department of Aerospace Engineering, Indian Institute of Technology, Madras, India

© The Author(s), under exclusive license to Springer Nature Singapore Pte Ltd. 2024  
R. Velmurugan et al. (eds.), *Dynamic Behavior of Soft and Hard Materials, Volume 3*, Springer Proceedings in Materials 36, [https://doi.org/10.1007/978-981-99-6259-4\\_29](https://doi.org/10.1007/978-981-99-6259-4_29)

335

conceptually. Using additive manufacturing, 3D-based CAD models can take the operation models [2]. AM techniques, which are being employed in a variety of industries for a variety of purposes, have many advantages. In every aspect of daily life, AM applications are visible. Many AM techniques are employed for different applications and different materials, and our attention is mostly on approaches based on extrusion (FDM). It is possible to manage the porosity and size of the final product using an extrusion-based additive manufacturing approach in which the material is selectively distributed in a nozzle layer by layer. This procedure can be used to create a variety of products out of diverse materials, including metals, ceramics, highly filled polymers, and multiple materials, for use in different industries such as automotive, aerospace, biomedical, construction, and retail sectors [3–5]. The challenges of employing composite natural polymers, such as PLA and bioglass for medical applications were discussed by Brezulier et al. [6]. Polylactic acid (PLA) is a promising family of plastics created through the chemical processing of bio-derived monomers [7–9]. PLA has appealing properties because it is derived from renewable resources, is an alternative resource of use as biodegradable, and has low manufacturing costs [10, 11].

Priya et al. [12] investigated the physicochemical and mechanical properties of PLA and ABS materials. FDM processing was used, with four distinct layer heights of 0.1–0.4 mm, and two infill patterns. The impact of low frequency (20 Hz) on the thermal and mechanical properties of the two different thermoplastic polymers, ABS, and PLA (triangular and rectilinear), is studied. It has been observed that the triangle infill pattern PLA has higher tensile and flexural characteristics at a layer height of 0.1 mm. Both PLA and ABS materials' mechanical properties deteriorate with increasing layer thickness.

Chikkanna et al. [13] have studied the effect of thermal annealing on the preparation of PLA-fused filaments under static and dynamic flexural loads. A 15 min annealing period at 110 °C showed improved flexural properties. Compared with non-annealing PLA, the storage modulus at 60 °C rose more than 24.33 times.

Aydin et al. [14] presented the stress–strain curves of printed PLA material using the 2D digital image correlation (DIC) method. Tensile specimens with 100% infill ratios were produced using a 3D printer and tested in uniaxial tensile tests in different ranges of strain rates. As a result, the average ultimate tensile stress increased as the test speed increased. The effects of print orientation, material age, infill, shells, and slicer operations on the material's mechanical properties resulted in a significant drop in average strains when the test speed increased. It has been observed that the DIC technique was helpful for strain measurement. Several applications where plastic components are utilized involve various kinds of radiation. Gamma sterilization facilities and radiotherapy equipment for use in medicine are two examples. To guarantee that the polymer parts can maintain their integrity and perform as intended even after being subjected to gamma radiation, it is vital to investigate the effects of gamma radiation on their properties. Depending on the polymer, the desired property, the type, and the pace of radiation exposure, changes in the microstructural, macrostructural, and mechanical properties may result from radiation exposure. Studies on the



effect of radiation on the characteristics of various polyethylene polymers have been conducted [15–18].

Alsabbagh et al. [19] have shown that the structural behavior of HDPE after gamma irradiation is improved when compared with unexposed PLA. However, the structural behavior of HDPE after gamma irradiation is inferiorly presented by hydrogen bonds compared with neat PLA. This is because of the effect of gamma irradiation on HDPE and PLA at higher dosages.

Subrata et al. [20] have studied the mechanical properties of the hybrid composition of jute and glass fiber, in polyester resin and demonstrated higher strength than neat jute polyester and neat glass polyester in the presence of 1% gamma irradiation. Polymer blends or rice husk fiber have high tensile and modulus properties at low doses of gamma radiation (below 50 kGy) but quickly degrade thermally at larger doses of radiation such as 150 kGy [21].

Food safety and biomechanical characterization studies were carried out by Harrell et al. [22] and found the negative effects of gamma irradiation. Free hydroxyl radicals and other radiotoxic are produced when gamma radiation is applied.

This study identifies the effect of PLA on the mechanical and thermal characteristics of printed PLA when subjected to gamma irradiation. The PLA samples are exposed to gamma irradiation of doses 5, 10, and 15 kGy, and its effects on thermal and mechanical properties are studied.

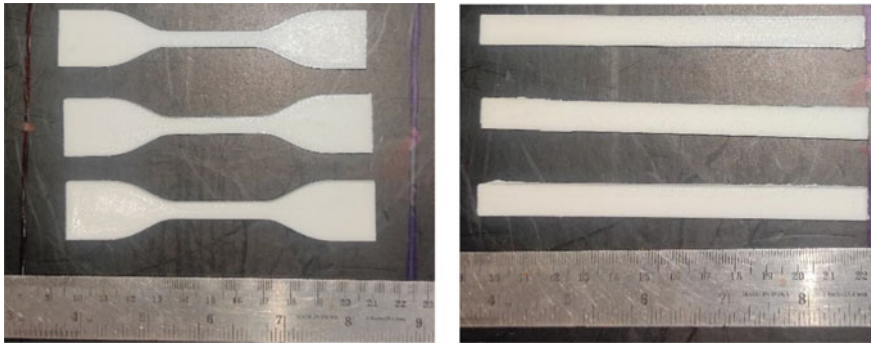
## 2 Materials Selection and Specimen Preparation

3D-printed specimens are modeled as per the ASTM with the help of Solid Works CAD software and are prepared using a 3D-printing machine, Flash Forge, Creator Pro 2. Samples are printed using PLA filament, which is widely available in the market. The specification of the printing specimen is given in Table 1.

Three sets of samples are printed for mechanical and thermal characterization studies. Also, each test specimen was printed and treated with gamma irradiations of 5, 10, and 15 kGy.

**Table 1** D3 specimen printing specifications

Description	Parameters
Filament type	PLA
The nozzle size	0.4 mm
Slice	Standard
Extruder temperature	210 °C
Platform temperature	40 °C
Infill density	100%
Diameter of the filament	1.7 mm
Pattern type	Linear



A) Tensile specimens

B) Flexural specimens

**Fig. 1** Tensile and flexural specimens as per ASTM standards

## 2.1 *Experimental Procedures*

### 2.1.1 Mechanical Characterization

Using the Kalpak universal testing machine, with a capacity of 20 kN, tensile tests as per ASTM D638 (type IV) and three-point bending tests as per ASTM D790 are carried out. The crosshead speed used for these experiments is 2 mm/min.

The gauge length and width for the tensile tests on the dog-bone-shaped specimens are 33 and 6 mm, and the three-point bending rectangular specimen's gauge length and breadth of 50 and 12.7 mm are used and are shown in Fig. 1.

### 2.1.2 Compression Test

A  $13 \times 13$  mm cuboid specimen is 3D printed for the compression test as per ASTM D3410. Compression tests are carried out on the servo-controlled hydraulic compression testing machine (BLUE STAR) with a 40 T capacity to study the compressive strength of the neat PLA material. The crosshead speed is 2 mm/min, and its speed can be adjusted manually.

## 2.2 *Thermal Characterization*

Four testing techniques are used to study the thermal properties of PLA: differential scanning calorimetry, dynamic mechanical analyzer, light flash apparatus (LFA), and dilatometer.

### **2.2.1 Differential Scanning Calorimetry**

DSC is used to find the melting point and glass transition temperature of the material.

### **2.2.2 Light Flash Apparatus 467**

Light flash apparatus 467 hyper mesh by NETZSCH, Germany equipment is used to find the material's thermal conductivity, specific heat, and thermal diffusivity. The samples are disc-shaped, the size is 25.4 in diameter, and the thickness is 3 mm. As the temperature increases, the diffusivity decreases, and at 35 °C, the conductivity and specific heat increase.

### **2.2.3 Dynamic Mechanical Analyzer (DMA)**

The dynamic mechanical analyzer (DMA 242D) by NETZSCH, Germany machine is equipment with a three-point bending fixture. This gives the properties as a function of temperature and frequency and is used to find the viscoelastic properties of the 3D-printed sample. The sample size is 11.5 mm in width and 40 mm in length, and the studies are done at a heating rate of 3 k/min with a 1 Hz frequency. The material behavior is studied in terms of loss modulus ( $E''$ ), loss factor ( $\tan \delta$ ), and storage modulus ( $E'$ ).

### **2.2.4 Dilatometer**

To study the linear coefficient of thermal expansion, the material is tested in the dilatometer supplied by Visva Ceramics, Chennai. The dimensions of the specimens are  $40 \times 10 \times 3.4$  mm in length, width, and layer thickness, respectively. Through the linear curve of the thermal strain and the temperature, the thermal expansion coefficient is obtained between 300 and 600 °C.

## **3 Result and Discussion**

The mechanical and thermal behavior of virgin PLA and gamma irradiation PLA are discussed in this part.

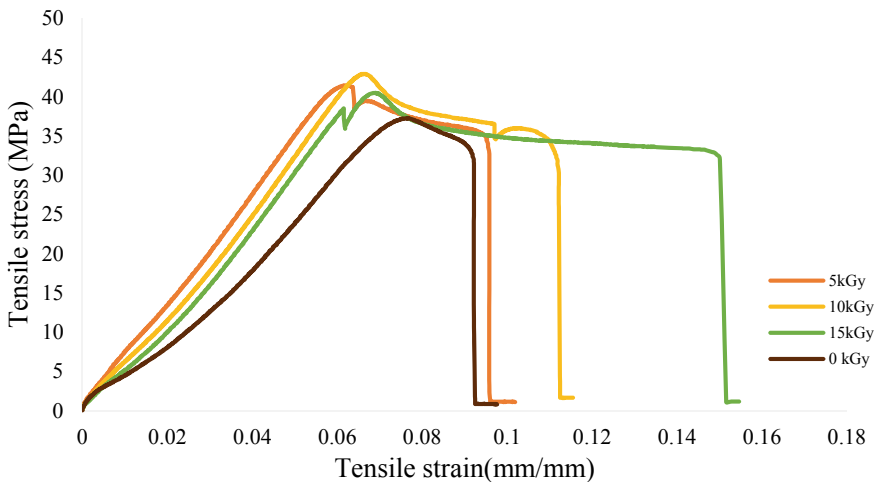
### 3.1 Tensile Strength

The infill density can affect the strength of the 3D-printed specimen, and infill density can lead to changes in the structure (micro, macro) of the 3D part. The type IV dog-bone-shaped specimen is designed in Solid Works following ASTM standard D3039, and the diagram is converted to stereolithography (STL) file format for 3D printing. The sample is printed using a linear infill pattern with 100% density. Table 2 shows the average result obtained during tensile testing is 35.15 MPa, which is high compared with previous literature data mentioned below. The tensile strength of a 0.4 mm layer thickness with a linear pattern is 35.15 MPa, higher than that obtained from the rectilinear pattern (30.43 MPa) as reported in the literature [12]. The PLA gamma irradiation strength is high compared with pure PLA. The gamma effect of PLA significantly improves the strength compared with pure PLA by 21% (Table 2).

For the 10 kGy-treated specimen, the strength is 42.8 MPa, for the 5 kGy sample, it is 40.42 MPa, and 15 kGy the strength is 40.47 MPa, respectively. Increasing the doses of gamma irradiation increased the tensile strength and modulus significantly.

**Table 2** Tensile strength of PLA samples with different percentages of gamma irradiation doses

S. no.	Gamma irradiation %	Tensile strength (MPa)
1	0	35.15
2	5	40.42
3	10	42.8
4	15	40.47



**Fig. 2** Stress–strain curve obtained in PLA and PLA gamma irradiation doses 5, 10, 15 kGy

### 3.2 Flexural Test

For flexural testing, rectangular samples are kept in a three-point fixture of the UTM machine. The flexural modulus ( $E_f$ ), flexural strength ( $\sigma_f$ ), and strain ( $\varepsilon_f$ ) are given by the expressions.

$$E_B = \frac{L^3 m}{4bd^3} \tag{1}$$

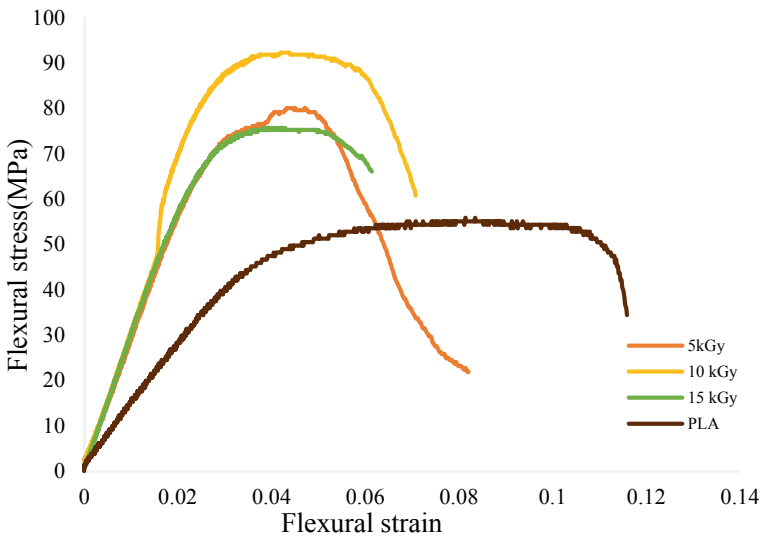
Here, m is obtained from the initial slope of a straight-line region of the load–deflection curve of the bending test

$$\sigma_f = \frac{3PL}{2bd^2} \tag{2}$$

$$\varepsilon_f = \frac{6bd}{L^2} \tag{3}$$

Here, L is the length of the specimen, b is the width, and d is the depth of the specimen. All the samples are subjected to different doses of gamma irradiation, and the load–displacement curve can be obtained by using the expressions (2) and (3), the stress–strain curves are obtained and are shown in Fig. 3.

The flexural strength obtained during the test is 55.85 MPa for pure PLA and 91.85 MPa for gamma irradiation at 10 kGy, 79.17 MPa for 5 kGy, and 75.23 MPa



**Fig. 3** Comparison of bending stress–strain of PLA with gamma irradiation PLA of doses 5, 10, 15 kGy

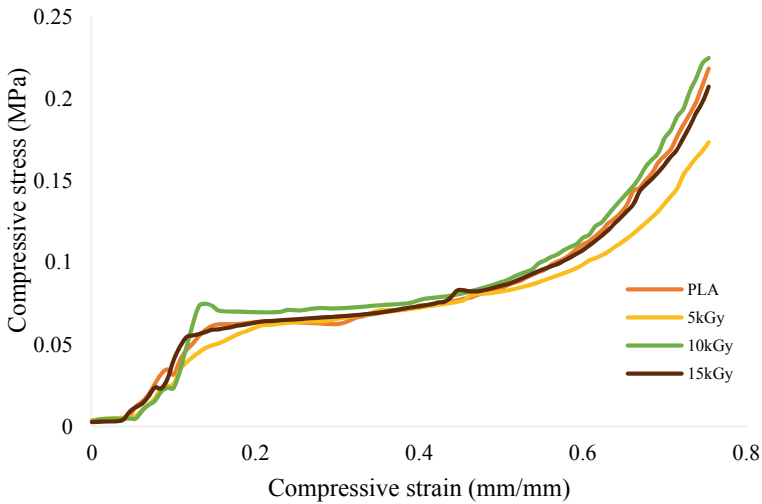
**Table 3** Flexural strength of PLA samples with different percentages of gamma irradiation doses

S.No	Gamma irradiation %	Flexural strength (MPa)
1	0	55.85
2	5	79.17
3	10	91.85
4	15	75.23

for 15 kGy. The results obtained from experiments show improvement compared with virgin materials (Table 3).

### 3.3 Compression

In compression tests, the printed specimens were compressed by applying the force of the hydraulic control system in UTM at the rate of 2 mm/min. Specimen shape is changed by applying compressive force. Figure 4 shows the stress and strain curves obtained from compression tests for various dosages of irradiated PLA samples. When compared with a 10 kGy irradiated specimen, pure PLA has a lower value, which shows that the irradiated PLA specimen’s property is improved.



**Fig. 4** Compression specimen stress–strain curve pure PLA and PLA gamma irradiation different doses

### 3.4 Izod Impact

The specimens' length, width, and thickness for impact tests are 65, 12.7, and 3.1 mm, respectively. The pendulum swings down to hit the specimen and breaks the specimen. Izod impact tests are done with a 25 J pendulum released from a height of 0.91 m. The result shows that the value of PLA is 15.24 kJ, which is not different from the values of gamma irradiation-treated PLAs. Hence impact strength is not different by gamma irradiation.

## 4 Thermal Characterization

This section presents and discusses the viscoelastic properties of PLA studied from DMA. The  $T_g$  values are measured with DSC and thermal conductivity, and specific heat capacity are obtained using LFA apparatus, and linear coefficient of thermal expansion is obtained from dilatometer.

### 4.1 Dynamic Mechanical Analyzer

DMA is used to get the storage modulus ( $E'$ ), loss modulus ( $E''$ ), and loss factor ( $\tan \delta$ ) under a dynamic loading environment. The loss factor shifts to higher values for virgin PLA compared with the irradiated sample, which shows that the material is degraded due to irradiation at a higher temperature (Fig. 5).

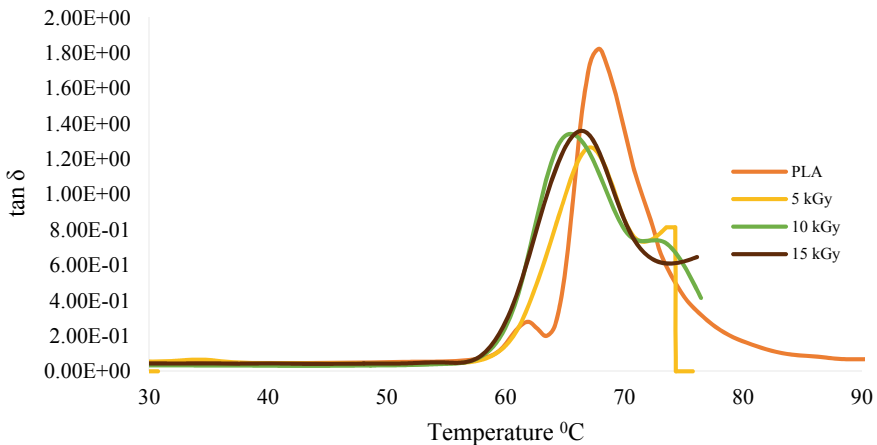


Fig. 5 Loss factor ( $\tan \delta$ ) over the temperature PLA and gamma irradiation PLA

The material's capacity to absorb energy is represented by a storage modulus, whereas a loss modulus represents energy dissipation. Evaluating these two stiffness characteristics under sinusoidal thermal loading circumstances is crucial. The material's glass transition temperature ( $T_g$ ) can be calculated from the ratio of  $E''$  to  $E'$ , which is the peak temperature for the loss factor [12, 23]. The result shows a reduction in storage modulus due to gamma irradiation (Fig. 6).

Figure 7 demonstrates the storage modulus of the pure PLA and different doses of gamma-treated samples as a function of temperature. Pure PLA exhibits  $T_g$ , liquid flow, and cold crystallization behavior. The gamma irradiation-treated curve also shows the same pattern as pure PLA. Compared with gamma-irradiated PLA, the storage modulus is high for pure PLA. This result matches very well with DSC results. The reduction in  $T_g$ ,  $E'$ ,  $E''$  values was observed with gamma irradiation in samples compared with neat PLAs.

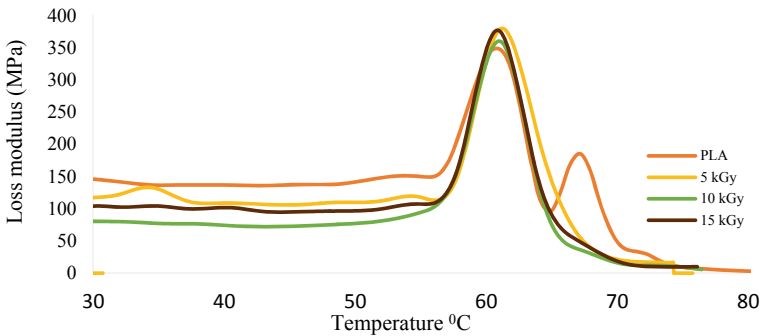


Fig. 6 Loss modulus over the temperature PLA and PLA with gamma irradiation different doses

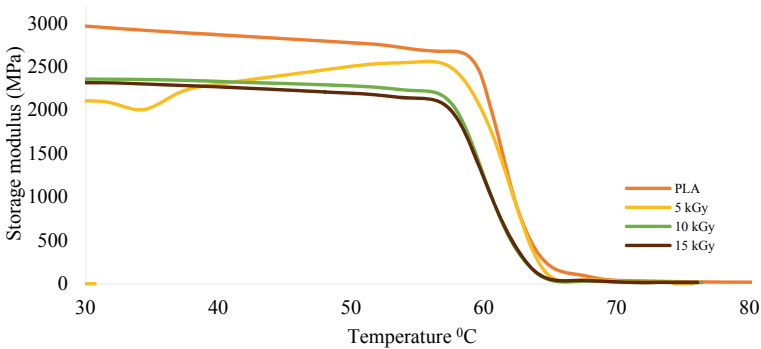
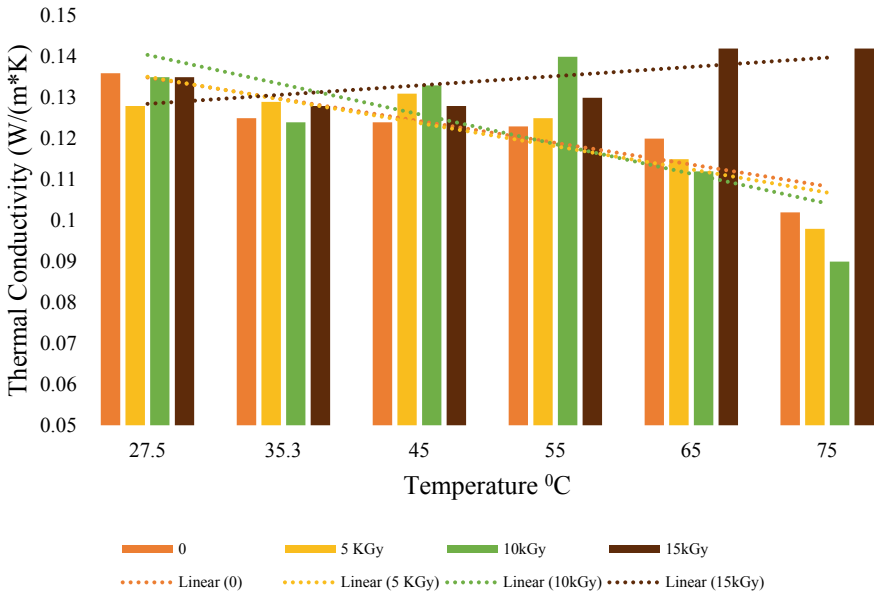


Fig. 7 Storage modulus over the temperature PLA and PLA with gamma irradiation different doses





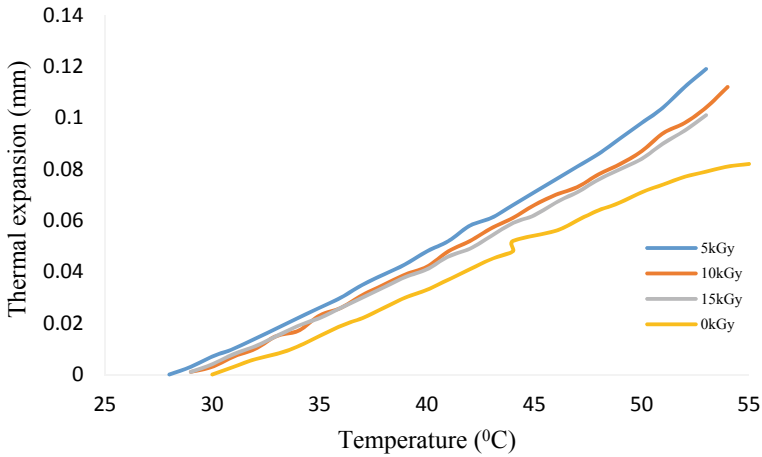
**Fig. 8** Thermal conductivity of PLA with gamma irradiation in different doses

### 4.2 Light Flash Apparatus (LFA) 467

Figure 8 shows the thermal conductivity of PLAs with and without gamma irradiation. The conductivity values of pure PLA show a decreasing trend with temperature, and PLA at 15 kGy dose shows an increasing trend which means that gamma irradiation stabilizes the molecular structure and increases the conductivity.

### 4.3 Thermal Coefficient of Expansion

The thermal coefficient of thermal expansion from room temperature to up to 60 °C is obtained from the specimen exposed to different doses of gamma irradiation. However, there is not much difference in the thermal expansion at various doses, but the gamma irradiation sample is slightly higher than the PLA pure sample, as shown in Fig. 9 (Table 4).



**Fig. 9** Thermal expansion vs temperature PLA and gamma irradiation-treated PLA

**Table 4** Linear coefficient of thermal expansion with PLA and gamma-treated PLA

S. no.	Specimen	Linear coefficient of thermal expansion ( $10^{-5}/^{\circ}\text{C}$ )
1	Neat PLA	5.94
2	PLA for 5 kGy	9.96
3	PLA for 10 kGy	8.59
4	PLA for 15 kGy	8.88

## 5 Conclusions

Mechanical and thermal characterization of PLA and gamma-irradiated PLA are carried out to investigate the effect of gamma irradiation on 3D-printed PLA.

The tensile values of PLA are compared with the values of gamma-irradiated samples. The strength increases with the increase of doses as the irradiation brings the molecules closer; hence, the tensile value is improved.

The flexural strength of PLA with high doses is higher than that of neat PLA.

Thermal conductivity is also increased with the increase in gamma dosage.

No significant difference in load resistance was observed for PLA and irradiated PLA in compression.

An increase in the thermal coefficient of expansion is observed with irradiation.

In dynamic mechanical analysis, reduction in storage modulus, loss modulus, and transition temperature is observed with irradiation of PLA samples.

## References

1. Paritala PK, Manchikatla S, Yarlagadda PK (2017) Digital manufacturing-applications past, current, and future trends. *Procedia Eng* 174:982–991
2. Holmström J, Holweg M, Khajavi SH, Partanen J (2016) The direct digital manufacturing (r) evolution: definition of a research agenda. *Oper Manag Res* 9(1):1–10
3. Srivastava M, Rathee S (2021) Additive manufacturing: recent trends, applications and future outlooks. *Prog Addit Manuf* 1–27
4. Mandala R et al (2022) A short review on fused deposition modeling 3D printing of bio-based polymer nanocomposites. *J Appl Polym Sci* 139(14):51904
5. Zhang H, Mao X, Du Z, Jiang W, Han X, Zhao D, Han D, Li Q (2016) Three dimensional printed macroporous polylactic acid/hydroxyapatite composite scaffolds for promoting bone formation in a critical-size rat calvarial defect model. *Sci Technol Adv Mater* 17(1):136–148
6. Brézulier D, Chaigneau L, Jeanne S, Lebullenger R (2021) The challenge of 3D bioprinting of composite natural polymers PLA/Bioglass: trends and benefits in cleft palate surgery. *Biomedicines* 9(11):1553
7. Garlotta D (2001) A literature review of poly (lactic acid). *J Polym Environ* 9(2):63–84
8. Jem KJ, Tan B (2020) The development and challenges of poly (lactic acid) and poly (glycolic acid). *Adv Ind Eng Polym Res* 3(2):60–70
9. Hamad K, Kaseem M, Yang HW, Deri F, Ko YG (2015) Properties and medical applications of polylactic acid: a review. *Express Polym Lett* 9(5)
10. Patel RM (2016) Polyethylene. In: Wagner JR (ed) *Multilayer flexible packaging*, 2nd edn. Elsevier, pp 17–34
11. Ayadi A, Kraiem D, Bradai C, Pimbert S (2012) Recycling effect on mechanical behavior of HDPE/glass fibers at low concentrations. *J Thermoplast Compos Mater* 25:523–536
12. Priya MS, Naresh K, Jayaganthan R, Velmurugan R (2019) A comparative study between in-house 3D printed and injection molded ABS and PLA polymers for low-frequency applications. *Mater Res Express* 6(8):085345
13. Chikkanna N, Krishnapillai S, Ramachandran V (2022) Static and dynamic flexural behaviour of printed polylactic acid with thermal annealing: parametric optimisation and empirical modelling. *Int J Adv Manuf Technol* 119(1):1179–1197
14. Aydin M, Özkan ÖZ (2018) Application of digital image correlation technique to tensile test for printed PLA specimens. *Int J 3D Print Technol Digit Ind* 2(2):1–7
15. Naikwadi AT, Sharma BK, Bhatt KD, Mahanwar PA (2022) Gamma radiation processed polymeric materials for high performance applications: a review. *Front Chem* 10
16. West C et al (2019) Effects of gamma irradiation upon the mechanical and chemical properties of 3D-printed samples of polylactic acid. *J Manuf Sci Eng* 141(4)
17. Sadighzadeh A, Azimzadeh Asiabi P, Ramazani A, Ghoranneviss M, Salar Elahi A (2015) Characterization of gamma irradiated low and high density polyethylene using the FTIR and DSC technique. *J Inorg Organomet Polym Mater* 25(6):1448–1455
18. Moez AA, Aly SS, Elshaer YH (2012) Effect of gamma radiation on low density polyethylene (LDPE) films: optical, dielectric and FTIR studies. *Spectrochim Acta Part A Mol Biomol Spectrosc* 93:203–207
19. Klepac D, Ščetar M, Baranović G, Valić S (2014) Influence of high doses  $\gamma$ -irradiation on oxygen permeability of linear low-density polyethylene and cast polypropylene films. *Radiat Phys Chem* 97:304–312
20. Alsabbagh A, Abu Saleem R, Almasri R, Aljarrah S, Awad S (2021) Effects of gamma irradiation on 3D-printed polylactic acid (PLA) and high-density polyethylene (HDPE). *Polym Bull* 78(9):4931–4945
21. Das SC, Paul D, Grammatikos SA, Siddiquee MA, Papatzani S, Koralli P, Islam JM, Khan MA, Shauddin SM, Khan RA, Vidakis N (2021) Effect of stacking sequence on the performance of hybrid natural/synthetic fiber reinforced polymer composite laminates. *Compos Struct* 276:114525

22. Chen RS, Ab Ghani MH, Ahmad S, Mou'ad AT, Gan S (2021) Tensile, thermal degradation and water diffusion behaviour of gamma-radiation induced recycled polymer blend/rice husk composites: experimental and statistical analysis. *Compos Sci Technol* 207:108748
23. Harrell CR, Djonov V, Fellabaum C, Volarevic V (2018) Risks of using sterilization by gamma radiation: the other side of the coin. *Int J Med Sci* 15(3):274